Rainfall Variability and Trends over the Greater Horn of Africa

zur
Erlangung des akademischen Grades eines Doktors
der Naturwissenschaften
von der KIT-Fakultät für Physik
des Karlsruher Instituts für Technologie (KIT)
genehmigte Dissertation

vorgelegt von

M.Sc. Larisa Seregina

Tag der mündlichen Prüfung: 19. Juni 2020
Referent: Prof. Dr. Joaquim Pinto
Korreferent: Prof. Dr. Andreas Fink

5. Juni 2021

Preface

The PhD candidate confirms that the research presented in this thesis contains significant scientific contributions by herself. This thesis reuses material from the following publications:

Seregina, L. S., A. H. Fink, R. van der Linden, N. A. Elagib, and J. G. Pinto (2019). A new and flexible rainy season definition: validation for the Greater Horn of Africa and application to rainfall trends. *International Journal of Climatology*, 39(2), 989–1012, doi:10.1002/joc.5856.

Seregina, L. S., A. H. Fink, R. van der Linden, J. G. Pinto, and C. Funk (2021). Using seasonal rainfall clusters to explain the interannual variability of the rain belt over the Greater Horn of Africa. *International Journal of Climatology*, 41 (Suppl. 1): E1717–E1737, doi:10.1002/joc.6802.

The abstract and chapters 1, 2, 3, 4, 6 and the Appendix reuse material from Seregina et al. (2019). Secondly, the abstract and chapters 2, 3, 5 and 6 reuse material from Seregina et al. (2021).
In all cases, the design, implementation of the research, data analysis, interpretation of the results, and manuscript preparation were solely performed by the candidate with advice from Joaquim G. Pinto and Andreas H. Fink and comments from all co-authors during the manuscript preparation.
The candidate confirms that appropriate credit has been given within the thesis where reference has been made to the publications of others.

Abstract

The Greater Horn of Africa (GHA) experiences a high interannual variability of seasonal rainfall, which frequently manifests itself in drought and flood events. In addition, future changes of rainfall over the GHA may have the potential for initiating negative socioeconomic developments. Therefore, an understanding of atmospheric and oceanic interactions like e.g., coupled ocean-atmosphere modes in the Indian and Pacific Oceans, and their influence on patterns of the seasonal rainfall variability is essential for estimating future changes and establishing appropriate adaptation strategies. The aim of this work is to contribute to the description and understanding of the seasonal and interannual variability of rainfall over the GHA.

The GHA is located in the equatorial latitudes but it is mostly separated from the rest of the African continent by two mountainous massifs that considerably influence the weather and climate of the region. The complex topography and some of the world's largest lakes contribute to a multitude of local rainfall climates. However, since the mountains reduce the intrusions of westerly winds from the moist Congo Basin, particularly the eastern lowlands are mostly arid with two distinct rainy seasons during boreal spring and autumn. In the northwest and south of the GHA, the two seasons merge into one lasting approximately from June to September and October to April, respectively.

In recent decades, the different rainy seasons exhibited diverging trends. Particularly, rainfall in the boreal spring season, which has historically been the primary agricultural season, has been declining abruptly since the late 1990s. Theories trying to explain this decline range from interactions with regional circulation features, like enhanced warming of the nearby Indian Ocean and deserts, to global shifts of the tropical circulation embedded in the decadal variability of the Pacific Ocean. The current work attempts to disentangle the various factors of rainfall climate variability in the different rainy seasons and how they alter the migration of the tropical rain band (TRB). The approach is centered around the question, whether the observed negative rainfall trends were driven by an overall reduction of moisture or by changes in the migration of the TRB.

In the first part of this work, a novel and flexible rainy season definition is introduced in order to identify the rainfall seasonality, the onset, cessation and duration of the rainy seasons, and the associated uncertainties from rainfall time series. This approach enables to delimit coherent parts of the region with a comparable seasonality and to quantify trends of the respective rainy seasons. The definition is applied to the Climate Hazards InfraRed Precipitation with Stations (CHIRPS) satellite-based product and to an extensive set of ground-based measurements from the Karlsruhe African Surface Station Database (KASS-D). The results demonstrate a strong agreement with known seasonal dynamics in the region and the commonly used calendric 3-month periods. Compared to the latter definitions, an added value is found for the novel approach, since it also captures local rainfall features and facilitates evaluations across rainfall seasonality borders. The trend analysis shows a wetting trend in central Sudan and western and northeastern Ethiopia for the boreal summer season as well as in eastern and southeastern Ethiopia, Somalia and northern Kenya for the boreal autumn season. A drying trend in Tanzania and the Democratic Republic of Congo can be detected. Both kinds of trends are regionally associated with changes in rainy season cessation.

CHIRPS and station trends mostly agree across the GHA but differ in coastal and topographically complex regions and regions with an unstable rainfall seasonality.
In the second part, interannual variations of the seasonal cycle of the TRB are analyzed using two statistical indices. The Seasonal Location Index (SLI) is a continuous index that extracts the seasonal migration of the TRB associated with daily rainfall patterns using a principal component analysis. The Rainfall Cluster Index (RCI) is a discrete index that describes the seasonal cycle as a succession of six characteristic rainfall patterns defined through a cluster analysis. In combination, both indices capture the full seasonal cycle of the TRB supporting interpretations of the interannual variations and trends. Two rainy seasons, the Msimu Rains in December–March and the Long Rains in March–May, are analyzed in detail in order to identify characteristic circulation patterns and potential correlations to large-scale forcing mechanisms. The Msimu Rains are dominated by two patterns with opposite rainfall characteristics between the Congo Basin and Tanzania. The associated circulation anomalies in moisture flux and divergence indicate variations in the location of the TRB originating from an interplay between low-level air flows from the Atlantic and Indian Oceans, and tropical and subtropical teleconnections. The peak month April of the Long Rains shows a complex composition of five patterns, which is tightly connected to intraseasonal and interannual variability of latitudinal locations of the TRB. A persistent location of the TRB near the equator, evidenced in a high number of days near the multi-year mean SLI-value, is associated with wet conditions over equatorial East Africa. These conditions go along with frequent occurrence of a pattern related to increased sea surface temperature in the nearby Arabian Sea and an anomalously weak Walker circulation. Dry Long Rains are associated with strong and frequent latitudinal variations of the TRB position partly related to tropical-extratropical interactions in both hemispheres. The composition of patterns indicates a late onset and intermittent rainfall. The results and links to the various forcing mechanisms offer new opportunities to understand recent variability and trends in the GHA region.

Kurzzusammenfassung

Am erweiterten Horn von Afrika (engl. "Greater Horn of Africa", GHA) gibt es eine hohe Jahr-zu-Jahr Variabilität der saisonalen Niederschläge, die sich häufig in Dürre- und Überschwemmungsereignissen äußert. Darüber hinaus können zukünftige Veränderungen der Niederschläge über dem GHA das Potenzial haben, negative sozio-ökonomische Entwicklungen zu begünstigen. Daher ist ein Verständnis der atmosphärischen und ozeanischen Wechselwirkungen, wie z.B. der gekoppelten Ozean-Atmosphären-Modi im Indischen und Pazifischen Ozean, und ihres Einflußes auf die Muster der saisonalen Niederschlagsvariabilität wesentlich für die Abschätzung zukünftiger Veränderungen und die Festlegung geeigneter Anpassungsstrategien. Ziel dieser Arbeit ist es, einen Beitrag zur Beschreibung und zum Verständnis der saisonalen und interannuellen Variabilität des Niederschlags über dem GHA zu leisten.
Das GHA befindet sich in den äquatorialen Breitengraden, ist jedoch vom Rest des afrikanischen Kontinents durch zwei Bergmassive abgetrennt, welche das Wetter und Klima der Region erheblich beeinflussen. Die komplexe Topographie und einige der größten Seen der Welt tragen zu einer Vielzahl von lokalen Niederschlagsklimaten bei. Da die Berge den Einfluss westlicher Winde aus dem feuchten Kongobecken reduzieren, sind vor allem die östlichen Tiefländer meist trocken mit zwei unterschiedlichen Regenzeiten im borealen Frühjahr und Herbst. Im Nordwesten und Süden des GHA verschmelzen die beiden Regenzeiten zu einer, die ungefähr von Juni bis September bzw. Oktober bis April dauert.
In den letzten Jahrzehnten wiesen die verschiedenen Regenzeiten unterschiedliche Trends auf. Vor allem die Niederschläge in der borealen Frühjahrssaison, die historisch gesehen die wichtigste landwirtschaftliche Saison ist, sind seit Ende der 1990er Jahre abrupt zurückgegangen. Theorien, die versuchen, diesen Rückgang zu erklären, reichen von Wechselwirkungen mit regionalen Zirkulationsmustern, wie der verstärkten Erwärmung des nahe gelegenen Indischen Ozeans und der Wüsten, bis hin zu globalen Verschiebungen der tropischen Zirkulation, die in der dekadischen Variabilität des Pazifischen Ozeans eingebettet sind. In der vorliegenden Arbeit wird versucht, die verschiedenen Faktoren der Klimavariabilität des Niederschlags in den verschiedenen Regenzeiten zu entwirren und herauszufinden, wie sie die Wanderung des tropischen Regenbands (engl. "Tropical Rain Band", TRB) verändern. Der Ansatz konzentriert sich auf die Frage, ob die beobachteten negativen Niederschlagstrends durch eine allgemeine Verringerung der Feuchtigkeit oder durch Veränderungen in der Wanderung des TRB verursacht wurden.
Im ersten Teil dieser Arbeit wird eine neuartige und flexible Definition der Regenzeiten vorgestellt, um die Niederschlagssaisonalität, den Beginn, das Ende und die Dauer der Regenzeiten, sowie die dazugehörigen Unsicherheiten aus den Niederschlagszeitreihen zu ermitteln. Dieser Ansatz ermöglicht es, zusammenhängende Teile der Region mit einer vergleichbaren Saisonalität abzugrenzen und Trends der jeweiligen Regenzeiten zu quantifizieren. Die Definition wird auf das satellitengestützte Produkt "Climate Hazards InfraRed Precipitation with Stations" (CHIRPS) und auf einen umfangreichen Satz bodengestützter Messungen aus der "Karlsruhe African Surface Station Database" (KASS-D) angewandt. Die Ergebnisse zeigen eine starke Übereinstimmung mit der bekannten saisonalen Dynamik in der Region und den üblicherweise verwendeten kalendarischen Dreimonatsperioden. Im Vergleich zu den letztgenannten Einteilungen

ergibt sich ein Mehrwert durch den neuartigen Ansatz, da er auch lokale Niederschlagsmerkmale erfasst und Auswertungen über die Grenzen der Niederschlagssaisonalität hinweg erleichtert. Die Trendanalyse zeigt einen Feuchtetrend im Zentralsudan und in West- und Nordost-Äthiopien für die boreale Sommersaison sowie in Ost- und Südost-Äthiopien, Somalia und Nordkenia für die boreale Herbstsaison. Ein Trockentrend ist in Tansania und der Demokratischen Republik Kongo festzustellen. Beide Arten von Trends sind regional mit Veränderungen der Endzeitpunkte der Regenzeit verbunden. CHIRPS- und Stationstrends stimmen in den meisten Fällen innerhalb des GHA überein, unterscheiden sich jedoch in Küsten- und topographisch komplexen Regionen, sowie Regionen mit einer instabilen Niederschlagssaisonalität.
Im zweiten Teil werden die interannuellen Variationen des saisonalen Zyklus des TRB unter Verwendung zweier statistischer Indizes analysiert. Der "Seasonal Location Index" (SLI) ist ein kontinuierlicher Index, der mit Hilfe einer Hauptkomponentenanalyse die saisonale Wanderung des TRB in Verbindung mit täglichen Niederschlagsmustern darstellt. Der "Rainfall Cluster Index" (RCI) ist ein diskreter Index, der den saisonalen Zyklus als eine Abfolge von sechs charakteristischen Niederschlagsmustern beschreibt, die durch eine Clusteranalyse definiert werden. In Kombination erfassen beide Indizes den vollständigen saisonalen Zyklus des TRB, was die Interpretation der zwischenjährlichen Schwankungen und Trends unterstützt. Zwei Regenzeiten, die "Msimu"-Regenzeit im Dezember–März und die "Long Rains" im März–Mai, werden im Detail analysiert, um charakteristische Zirkulationsmuster und potenzielle Korrelationen zu großräumigen Antriebsmechanismen zu identifizieren. Die Msimu-Regenzeit wird von zwei Mustern mit entgegengesetzten Niederschlagscharakteristiken zwischen dem Kongobecken und Tansania dominiert. Die damit verbundenen Zirkulationsanomalien im Feuchtefluss und in der Divergenz deuten auf Variationen in der Lage des TRB hin, die aus einem Wechselspiel zwischen unteren Luftströmungen aus dem Atlantischen und Indischen Ozean sowie tropischen und subtropischen Wechselwirkungen entstehen. Die Analyse für den April, dem Monat mit den stärksten Niederschlägen der Long Rains, zeigt eine komplexe Zusammensetzung von fünf Niederschlagsmustern, die eng mit der intraseasonalen und interannuellen Variabilität der Positionen des TRB, insbesondere entlang der Breitengrade, verbunden ist. Eine dauerhafte Lage des TRB in Äquatornähe, die sich in einer hohen Anzahl von Tagen in der Nähe des mehrjährigen mittleren SLI-Wertes äußert, ist mit feuchten Bedingungen über dem äquatorialen Ostafrika verbunden. Diese Bedingungen gehen mit dem häufigen Auftreten eines bestimmten Musters einher, welches mit einer erhöhten Meeresoberflächentemperatur in der Arabischen See und einer verminderten Walker-Zirkulation zusammenhängt. Trockene Long Rains sind mit starken und häufigen Schwankungen der TRB-Position entlang der Breitengrade assoziiert, die teilweise auf tropisch-extratropische Wechselwirkungen in beiden Hemisphären zurückzuführen sind. Die relativen Verhältnisse der vorkommenden Muster deuten auf ein spätes Einsetzen und unterbrochene Regenperioden hin. Die Ergebnisse und Verbindungen zu den verschiedenen Antriebsmechanismen bieten neue Möglichkeiten, die Variabilität und Trends der letzten Dekaden in der GHA-Region zu verstehen.

Contents

1 Introduction

The Greater Horn of Africa (GHA) consists of eleven countries (cf. Figure 1.2) with a total population of approximately 365.5 million people, which is more than one third of the African total population (United Nations, 2019). In recent years, this region exhibited a higher average economic growth rate compared to the African continent with three countries among the top ten fastest growing in the world (ADBG, 2019). However, this growth is fragile due to socio-economic and environmental factors. Socio-economic factors like regional conflicts lead to migration and increased refugee flows. Environmental factors include land degradation, land overuse and removal of forest cover (ADBG, 2019). In addition, approximately 30% of economy consists of agriculture with a high proportion of smallholders and with limited access to irrigation and fertilizers (ADBG, 2019). Thus, the economy of GHA strongly depends on seasonal rainfall and hydrological extremes have the potential of spillover effects on food (in)security, health, infrastructure, migration flows and various conflicts.
Unfortunately, the GHA experiences a high interannual variability of seasonal rainfall, which is driven by a variety of influences like coupled ocean-atmosphere modes in the Indian and Pacific Oceans. One of the most severe droughts in the recent decades during the years 2010–2011 affected more than twelve million people (Dutra et al., 2013; WMO, 2016). The drought resulted from the successive failure of the October–November 2010 and March–May 2011 rainy seasons and was partly linked to a strong La Niña event (Lyon and DeWitt, 2012). Despite of an alert of the Famine Early Warning Systems Network (FEWS NET) in summer 2010, especially Somalia and adjacent areas of northern Kenya exhibited major humanitarian impacts including stock and crop losses, food and water shortages and large-scale famine with estimated 258 000 excess deaths (Funk, 2011; WMO, 2016). Although drought was the main trigger, secondary impacts including conflicts, population displacement and an increase in food and fuel prices led to a serious humanitarian crisis (Funk, 2011; IASC, 2012). Similar drought conditions also reccurred in the years 2016-2017 (UNOCHA, 2017).
On the other side, persistently wet conditions and prolonged rainy seasons can lead to floods and landslides, but also enhance insect infestation of disease-transmitting mosquitos or crop pests like desert locusts. Desert locusts are able to change their behavior and morphology in response to favorable meteorological conditions, and transform itself from a harmless solitarious individual to part of a cohesive swarm (Steedman, 1990). These swarms can reach up to 80 million of members, which cross wide distances and devour as much as 1.8 million metric tons of green vegetation per day (World Bank, 2020). Due to its ability to reproduce rapidly, migrate long distances, and devastate crops, the desert locust is categorized as the most dangerous of all migratory pests in the world (Cressman, 2016). Widespread or unusually heavy rains over several months in adjacent areas create favorable breeding conditions for desert

locusts. In case, an outbreak or multiple outbreaks at the same time are not controlled, an upsurge can evolve. Uncontrolled upsurge can further develop into a plague, when two or more regions are affected (WMO and FAO, 2016). During February 2020, approximately 10.25 million of 24.7 million of already food insecure people across the GHA were living in areas affected by desert locusts in Ethiopia, Kenya and Somalia (UNOCHA, 2020). Regionally, the projected damages reach several billion US Dollars (Figure 1.1). According to World Bank (2020), the current locust population could grow 400 times larger by June 2020 and spread to new areas, disrupting food supply and threatening livelihoods if no action is taken.

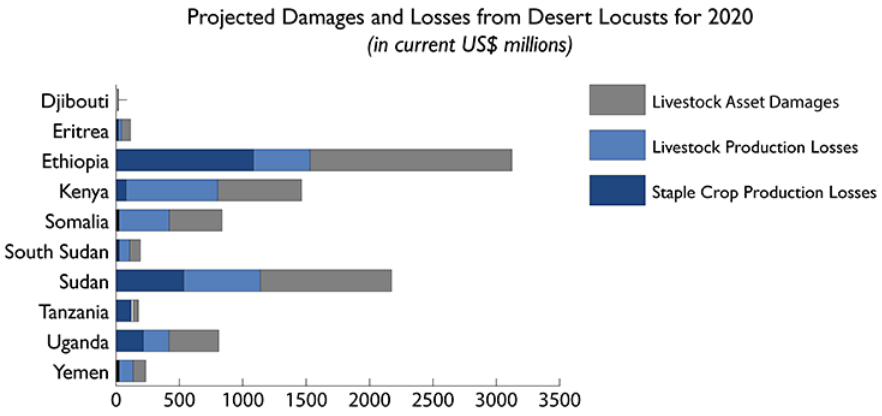

Figure 1.1: Projected damages and losses from desert locusts for 2020. Chart: S. D'Alessandro/World Bank, used under Creative Commons Attribution 4.0 International License (CC BY 4.0). Available at `https://blogs.worldbank.org/voices/locust-plague-fighting-crisis-within-crisis`

The large proportion of the economy dependent upon rain-fed agriculture means that future changes in rainfall over GHA have high potential for destructive socioeconomic consequences. Thus, understanding atmospheric and oceanic dynamics and interactions of the seasonal rainfall over GHA is crucial for estimating changes in future projections and establishing appropriate adaptation strategies.
Large parts of the low-lying Horn of Africa region are unique in several aspects. Through its topography, the rainfall climate in these parts is almost completely isolated from the rest of the African continent except of a narrow corridor in the Turkana Valley in northwestern Kenya (Figure 1.2). In contrast to the rest of the near-equatorial Africa, the region is arid to semiarid (e.g., Nicholson, 1996). In addition, the annual rainfall cycle is characterized by two distinct wet seasons across large parts of the region even in its northern latitudes located well north of the equator at approximately 12°N. Elsewhere at this latitudes, rainfall occurs almost entirely as a single wet season during June–September (Liebmann et al., 2017). Such kind of seasonality with two distinct rainy seasons is usually restricted to a latitudinally narrow band at the equator due to the biannual migration of the Intertropical Convergence Zone (ITCZ, e.g., Liebmann et al., 2012, their Figure 6). Beyond the consensus that an interplay between the topography, low-level moisture flows, ocean–atmospheric interactions and ocean upwelling results in this unique regional climate conditions, the atmospheric dynamics and rainfall variability over are not fully understood (Liebmann et al., 2017).

The March–May rainy season has historically been the major rainfall and primary agricultural season for most of the GHA. Since 1980s the rainfall has decreased with a significant and abrupt decline after 1999, but a partial recovery occurred since the late 2000s (Williams and Funk, 2011; Lyon and DeWitt, 2012; Lyon and Vigaud, 2017; Wainwright et al., 2019). In contrast, global climate model projections show a trend towards overall increased rainfall, while regional climate models project diverging trends: this contradiction was named the 'Eastern African climate change paradox' (Lyon and Vigaud, 2017; Wainwright et al., 2019). This issue questioned the reliability of the climate projections and their usability for planning and implementing suitable adaptation measures (Lyon and DeWitt, 2012; Wainwright et al., 2019). The present work contributes to the description and understanding seasonal and interannual variability of rainfall over the GHA. In particular, it attempts to disentangle the various factors of rainfall climate variability in the different rainy seasons and how they affect the migration of the ITCZ (alternatively known as "Tropical Rain Band", TRB, Nicholson, 2018).

1.1 Topics of this work

The aim of this thesis is to investigate possible causes of rainfall variability over GHA on spatial and intraseasonal to interannual time scales. The overarching task is to explore how the migration of the ITCZ over the GHA reflects interannual variability and trends of seasonal rainfall. One fundamental question is to explore, whether the observed rainfall trends resulted through an overall reduction of moisture, convergence of moisture and thus rainfall, or with changes in the migration of the ITCZ. The former case would indicate that either the advection of moisture to the GHA is reduced, or the region exhibits an increased divergence of moisture flows, increased atmospheric convective stability and thus, decreasing rainfall. Thus, such trends could be not exclusively restricted to a particular period in the seasonal cycle. The latter case would imply that a negative trend at particular location results from a fast progression of the ITCZ associated with later onset and earlier cessation dates of the respective rainy season as indicated by (Lyon and Vigaud, 2017). This "acceleration" might be compensated by a prolonged rainy season in another part of the region and/or another rainy season. The follow-up task is to investigate the appropriate atmospheric and oceanic conditions that contribute to the variability of the ITCZ migration. This approach contributes to the understanding of the relative contribution of the various drivers of rainfall variability over the GHA. Therefore, ground-based measurements, measurements from instruments aboard satellites and reanalyses are employed to focus on two different steps:

1. Development of an objective definition of rainy seasons and to quantify trends for the whole GHA.
2. Identify consistent rainfall patterns over the region and estimate their interannual variability and potential causes and links to sea surface temperature (SST) and teleconnection patterns.

The first step includes an objective classification of rainfall seasonality and the timing of the rainy seasons over the GHA from long-term measurements. Generally, full-

month periods are used to define rainy seasons. For example, the rainfall amount and corresponding long-term trends rainy seasons in equatorial East Africa are estimated using March–May (MAM) and October–December (OND) totals, respectively (e.g. Maidment et al., 2015; Cattani et al., 2018). For Ethiopia, studies use the periods of February–May (FMAM) and June–September (JJAS) for two rainy seasons Belg and Kiremt, respectively (Segele and Lamb, 2005; Bekele-Biratu et al., 2018), while the relevance of the seasons for the agriculture may vary regionally. Similarly, in Tanzania three periods of rainy seasons are defined, since northern parts of the country experience two rainy seasons in MAM and OND, whereas in the south and western parts the two seasons merge into one lasting from October/November to April. Thus, a novel and objective approach to resolve onset and cessation dates on supranational scale is introduced and applied for the GHA to classify the variety of climatological periods of rainfall. Using this classification, a first analysis of interannual variability and trends of seasonal rainfall totals and onset and cessation dates is performed. So far, trends of rainfall totals were only evaluated for calendric rainy seasons systematically and thus only for distinct subregions of the GHA. Trends of onset and cessation dates have not been subject of studies on rainfall over GHA so far.

In the second step, the interannual variability and trends of spatial and temporal rainfall patterns over the GHA are investigated. The main assumption of this chapter is that rainfall variability arises from delayed or accelerated meridional migration of the ITCZ, resulting in an anomalous position of the ITCZ compared to the climatology. In this chapter, two statistical indices are introduced that represent the seasonal location of the ITCZ over the region and the associated characteristic spatial rainfall patterns. With the focus on the merged October/November–April rainy season in southern and western Tanzania and the MAM rains in equatorial East Africa, anomalous ITCZ locations and related circulation characteristics on intraseasonal to decadal time scales are analyzed. By considering various synoptic- to large-scale atmospheric fields and fields of sea surface temperature (SST), potential explanations for atypical rainy season outcomes are proposed.

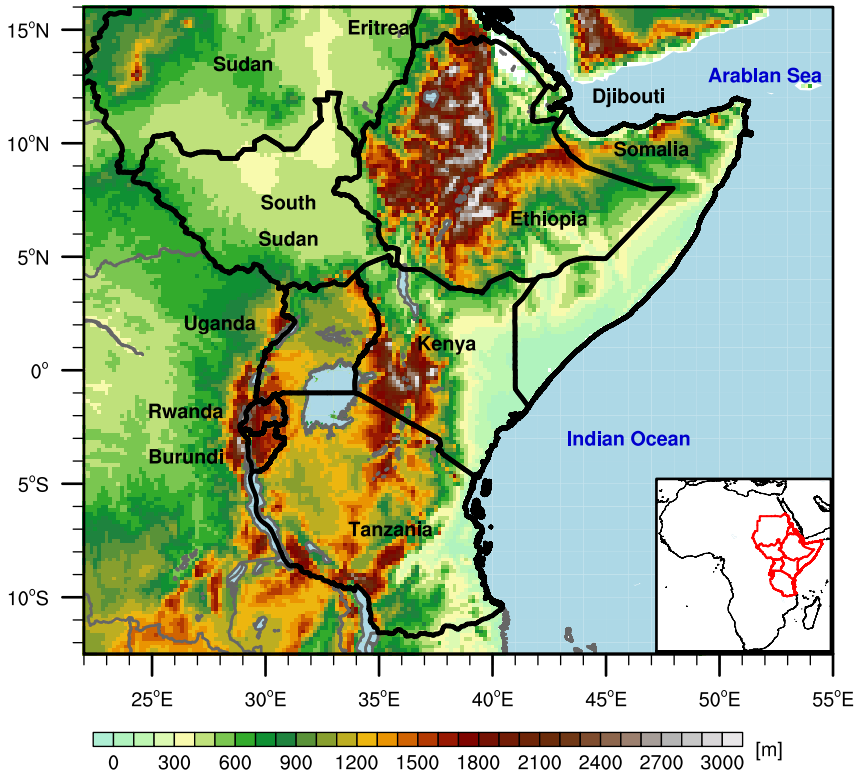

Figure 1.2: Map of the Greater Horn of Africa (GHA). The colors reflect the topography in meters above sea level. The included countries are denoted by black borders. The location of the region on the African continent is denoted by red lines in the inset in the lower right corner.

2 Literature review

In the following chapter, the state of research concerning the rainfall climate and its variability is described. This chapter is divided into three main sections: the first section introduces the region, its topography and climate including the rainfall climatology and some general aspects of the regional circulation. In the second section, general aspects of the tropical atmospheric circulation are discussed. In addition, the role of these aspects on the rainfall climate and its variability including some approaches to explain the recent rainfall trends are briefly summarized. The third section describes global modes of variability associated with modifications of the sea surface temperature and the tropical circulation resulting in rainfall anomalies over the GHA. Since each of the rainy seasons is affected in different ways by the variations of the latter modes and exhibits different rainfall trends, each of the rainy seasons is summarized in the last section.

2.1 Geography and regional climate

Geography
The GHA encompasses the countries Sudan, Eritrea, Ethiopia, Djibouti, South Sudan, Somalia, Kenya, Uganda, Rwanda, Burundi and Tanzania. This region covers a large latitudinal range extending from approximately 12 ° S to 20 ° N and encompasses a complex topographic structure with the highest mountains in Africa and some of the world's largest lakes (Figure 1.2). In addition, the lowest point of the continent, Lake Assal in Djibouti (153 m below mean sea level), is located within this region. The Ethiopian Highlands form the largest continuous mountainous massif on the African continent and range from 1500 m up to 4550 m at its highest peak Ras Dashen. In the equatorial parts, the East African Highlands encompass the Mount Kenya (5199 m) and Mount Kilimanjaro (5895 m), the highest peaks of the African continent. The two massifs are separated by the 300 km wide Turkana depression at the border between Kenya and South Sudan, which connects the Nile River Basin in the north-west with the lowland plains of eastern Ethiopia, Kenya, Somalia and Tanzania. The western part of the region encompasses the East African Lakes including Lake Tanganyika and Lake Victoria. Lake Victoria is the third largest lake and the second-largest freshwater lake worldwide. Lake Tanganyika is the second-deepest and second-largest freshwater lake by volume worldwide. These topographic features are related to the East African Rift System, an approximately 5000 km long divergent boundary between the Nubian and Somalian tectonic plates, which extends from the Red Sea and the Gulf of Aden to northern Mozambique (Saria et al., 2014). The north-south oriented topography

isolates the GHA from the rest of the African continent while partly forming a barrier between humid and arid climate zones according to the Köppen-Geiger classification (e.g. Peel et al., 2006; Beck et al., 2018, Figure 2.1). Since the highlands mostly prevent westerly intrusions of moisture from the Congo Basin (Hills, 1979; Nicholson, 1996), large parts of the region are characterized as semi-arid (Nicholson, 1996; Yang et al., 2015), which is exceptional for their location deep in the tropics.

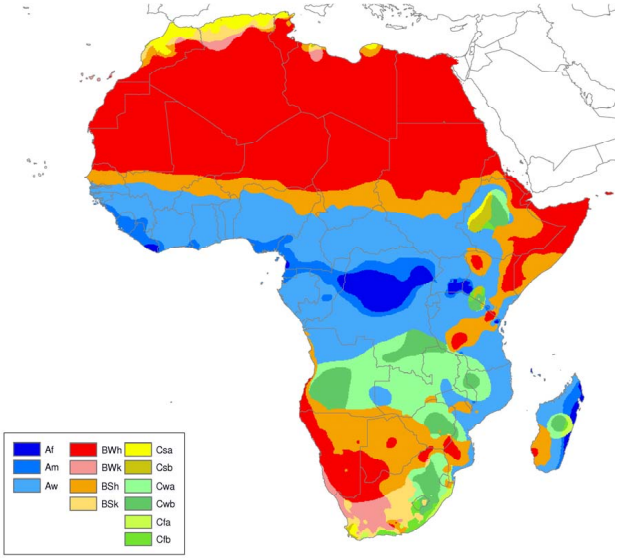

Figure 2.1: Köppen-Geiger climate type map of Africa. Blue colors depict classes with tropical climates, while red and orange colors mark classes with arid climates. Green and yellow depict temperate climates. souce: Peel et al. (2006)

Rainy seasons

Due to its location near the equator, the seasonal cycle of rainfall over the GHA is tightly associated with the migration of the ITCZ, which passes over the GHA twice a year, and the associated convective precipitation processes. Still, topographic variations further modulate the local climates contributing to their considerable spatial heterogeneity (Nicholson, 1996). To a first approximation, the migration stages of the seasonal rainfall can be separated into four phases: two solstitial positions during the respective high sun periods December to March (DJFM, Figure 2.2a) and June to September (JJAS, Figure 2.2c), and two distinct equinoctial periods in boreal spring (March to May, MAM, Figure 2.2b) and autumn (October to December, OND, Figure 2.2d). According to these phases, the GHA can be subdivided into two regions exhibiting one rainy season during each of the solstitial phases, and one region with two rainy seasons during each of the transition periods with little to no precipitation in between (cp., e.g. Liebmann et al., 2012; Yang et al., 2015; Dunning et al., 2016). The primary agricultural season of the dual-season region in the boreal spring is usually considered as the "Long Rains", while the secondary season in boreal autumn is referred to as the "Short Rains". The respective names for the solstitial rainy seasons in JJAS and DJFM in this work are adopted from locally used names, i.e. "Kiremt" in Ethiopia and "Msimu" in southern and western Tanzania, respectively.

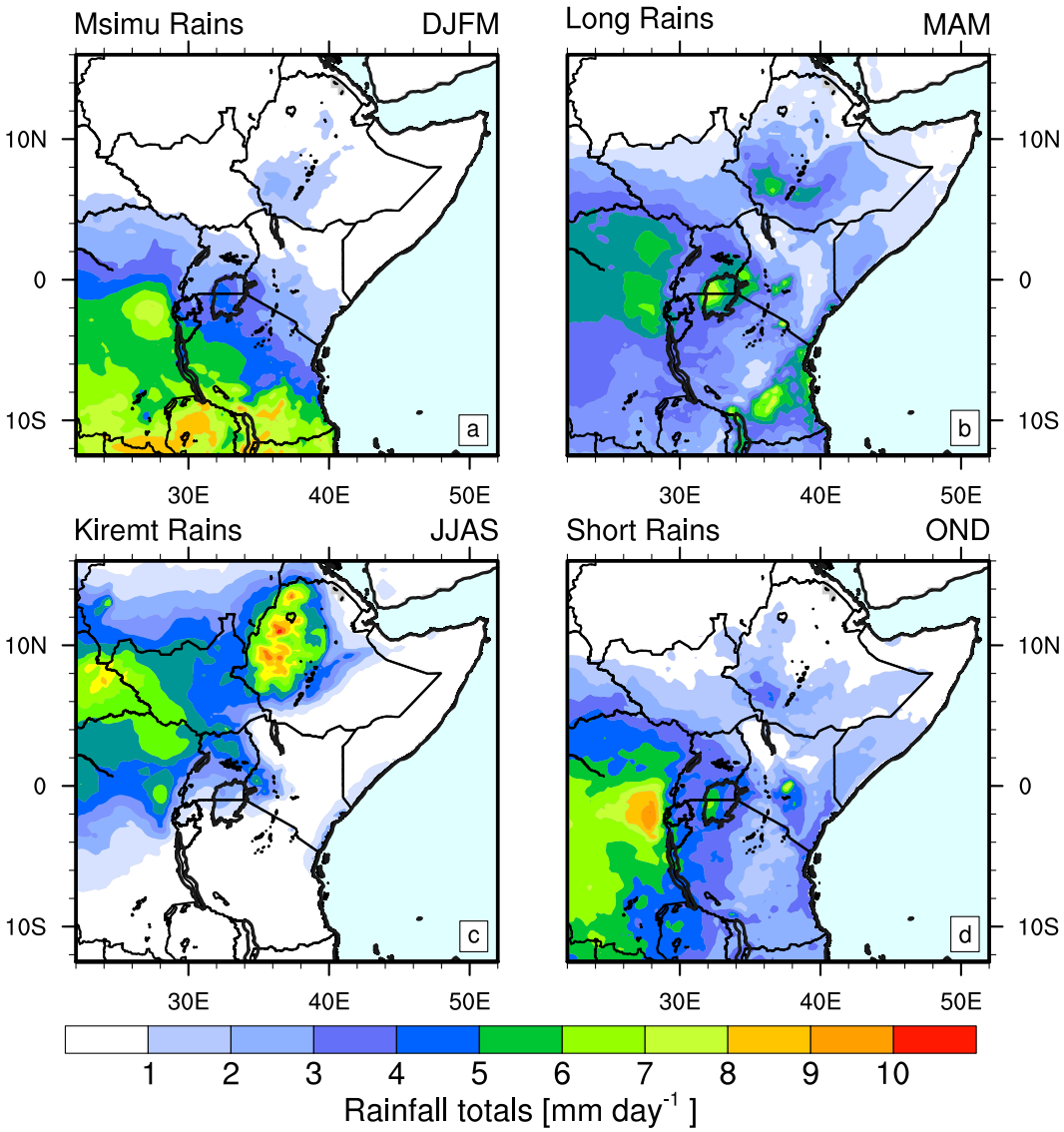

Figure 2.2: Mean daily rainfall totals for each of the rainy seasons over the GHA based on daily rainfall estimates from Climate Hazards Precipitation with Stations (CHIRPS) for the period 1981–2018.

Regional circulation

The regional low-level circulation consists basically of three major air flows from northeast, southeast and west. The northeasterlies and the southeasterlies dominate the circulation most of the year and are connected to the monsoon systems of India and south-central Africa, respectively. While transporting air masses from the Arabian Peninsula, the northeasterly flow is almost parallel to the shoreline and associated with cool and dry conditions. The southeasterlies are part of the so-called Somali- or Findlater Jet (Findlater, 1966, 1969, 1977), which maintains the Indian summer monsoon circulation. During its mature stage in boreal summer, the southeasterly flow is parallel to the coast at the equator whereas it turns east north of 2 ° N and transports moisture away from GHA towards India. An additional smaller westerly branch, which is referred as Turkana Jet, partly redirects the flow through the Turkana Channel towards South Sudan and western Ethiopia (Nicholson, 2016). Both easterly

flows are divergent and lead to subsidence and inversions in the mid-troposphere. These conditions act like a lid on the lower troposphere and cap convection over the lowlands. Only on the luv-side of the highlands orographic convection can occur. Thus, the highlands and plateaus act as both centers of convection and barriers for transcontinental flows. Humidity and rainfall are mostly associated with confluence from north- and southeast due the passage of the ITCZ and occasionally westerly flow from the Congo Basin (Nicholson, 1996; Finney et al., 2019). Indeed, model experiments without topography (Fig. 1a in Chou and Neelin (2003)) demonstrated that the GHA would be much wetter during the boreal summer due to the enhanced low-level westerlies in the simulation, which bring moist air from the interior of Africa (Yang et al., 2015). The variability in strength of the westerlies explain the large mostly east-west gradients in annual rainfall: mountainous areas in western Ethiopia, Rwanda, Burundi, Uganda and western Tanzania receive the highest rainfall amounts of more than 1200 mm m^{-2}, smaller portions of Ethiopia, Kenya and Tanzania range at ca. 800 mm m^{-2}, while the most arid parts in the northeast have to go with less that 200 mm m^{-2} per year (Nicholson, 1996).

Somali Jet and seasonal progression

The onset and progression of the rainy seasons coincide with the evolvement and northward progression of the Somali-Jet (Findlater, 1966, 1969, 1977; Riddle and Cook, 2008; Riddle and Wilks, 2013). This jet is located in the lowest 3 km of the troposphere and extends from the northern tip of Madagascar across the East African Lowlands over the Arabian Sea towards India (Findlater, 1977). Findlater (1969) showed that its origin was in the trade-wind easterlies over the southern Indian Ocean. After crossing the equator along a narrow longitudinal belt over the Somalia coast near the East African mountains, the jet turns east and transports moisture into the Indian region (Findlater, 1977). The development of the jet consists of four main stages: southeasterly flow south of the equator, meridional jet around the equator near the east coast of Africa, southwesterly flow between 55 ° E and the coast of Africa north of the equator and zonal westerly winds with a maximum around 10 ° N extending from the Arabian Sea to India (Chakraborty et al., 2009). Riddle and Cook (2008) provided a slightly different categorization: they separated the stages into an easterly phase "pre-jet" phase, a meridional phase, when only the meridional branch of the Somali-Jet is present, and a fully formed Somali-Jet including the branch across the Arabian Sea. The convergence of moist southeasterly flow from the Indian Ocean associated with the lowest (easterly) stage of the Somali Jet and the northeasterlies coincide with the Msimu Rains in boreal winter over Tanzania. Further strengthening of southeasterly and meridional component towards the equator marks the progressing onset of the Long Rains over equatorial East Africa, while the establishment of the zonal branches in Arabian Sea terminates the Long Rains. The retreat of the Somali Jet from October to December mark the progression of the Short Rains across equatorial East Africa.

2.2 General aspects of the tropical circulation

In the following section, the main aspects of the tropical circulation and their effect on the seasonal cycle of rainfall over the GHA are discussed. This section is built up from global-scale to regional-scale circulation patterns. Usually, the global-scale tropical circulation is split up in a zonal and meridional component, which is attributed to the influence of the Walker and the Hadley circulations (as in e.g., Schwendike et al., 2015). Their theory and some of the most relevant features for this work are described in the current section.

The driving force of the atmospheric circulation is an uneven distribution of solar heating over the globe, which is greatest near the equator and least at the poles. This imbalance is caused by the inclination of the Earth's ecliptic. On an Earth without rotation, this constellation would result in one circulation cell on each hemisphere. Abundant solar energy at the equator would warm the low-level air parcels and force them to ascent, while the energy deficit in the polar regions would result in cooling and descending air parcels. To reduce this strong equator-to-pole temperature and pressure gradients, the atmosphere and oceans transport parcels in the upper levels polewards and the low-level parcels back towards the equator (e.g. Peixoto and Oort, 1992). This circulation reduces energy gradients across the hemispheres and contributes to an meridional energy balance.

In the rotating reference frame of the Earth, the so-called Coriolis force generates additional acceleration of fluid parcels. The Coriolis force deflects longitudinally moving parcels to the right in the northern and to the left in the southern hemisphere. Its amplitude depends on the traveling speed and latitude. Due to this additional forcing, the equilibrium between the pressure gradient and Coriolis force is reached at the subtropical latitudes and produces two main upper-tropospheric westerly jets. These Polar and Subtropical Jets limit the meridional heat transport and lead to three global circulation cells: the Hadley Cell, the Ferrel Cell and the Polar Cell (e.g. Peixoto and Oort, 1992). Whereas the circulation of Hadley and the Polar Cell can be considered as thermally direct, the Ferrel circulation is a thermally indirect, i.e. driven by eddy forcing (e.g. Peixoto and Oort, 1992). Since the GHA is located in the tropical latitudes, the Hadley Cell is the most relevant for this region and is described below in subsection 2.2.1.

An additional factor of the tropical circulation at the Earth is the inhomogeneous land-water distribution, which leads to topographic variability, differences of heat capacity and differential heating. Due to the Earth's rotation and the resulting Coriolis force, the trade winds are oriented from north-east/east to south-west/west in the northern and from south-east/east to north-west/west in the southern hemisphere pushing sea water towards the western boundaries of the ocean basins. The influence of northerly/southerly components decreases with the weakened Coriolis force near the equator. As the ocean water warms during the transport, the result is a convergence and downwelling of relatively warmer surface water in the west and divergence and upwelling of cooler surface waters in the eastern parts of the oceans. The most prominent examples are the Pacific Warm Pool located to the east of the Maritime Continent and the Atlantic Warm Pool including the Gulf of Mexico and the Caribbean Sea. This east-west gradient in sea surface temperatures leads to a zonal atmospheric response with increased ascent, low pressure and increased convection in the western

ocean basins and subsidence, high pressure and dry conditions in the east. Temperature contrasts between land and ocean additionally enhance the circulation. This zonal equatorial circulation is known as the Walker Circulation, which is further discussed in subsection 2.2.2.

2.2.1 The Hadley Circulation

The Hadley circulation is the primary feature of meridional heat and moisture transport of the tropical atmosphere (e.g. Peixoto and Oort, 1992). It extends roughly from 15° in the summer hemisphere to 30° in the winter hemisphere, centered close to the equator (ca. 10° in the winter hemisphere). The structure of the Hadley Cell is defined by equatorward flow close to the surface in the tropics, an upward branch close to the equator, return poleward flow at the upper troposphere, and a downward subsiding branch at the subtropics (e.g. Peixoto and Oort, 1992). The region of strong ascent is known as the ITCZ. The maximum north-south extent of its migration determines the northernmost locations of the Earth's regions with tropical climates. Its boundaries are hot and dry regions containing most of the world's deserts due to the dominance of the subsiding branch of the Hadley circulation (e.g. Peixoto and Oort, 1992). The north- and southeasterly low-level flow over the global oceans is known as the trade winds, whereas over south Asian and west African landmasses the monsoon winds are of greater importance.
The location of both branches is constantly varying. On temporal scales, the variability arises due to seasonal cycles of solar insolation and the natural interannual variability of the atmosphere. On spatial scales, differential heating, gradients in heat capacity between land and ocean surfaces and also topography modify the regional circulation patterns. The seasonal transition of the meridional circulation from the southern to the northern hemisphere (and back) leads to a reversal of the direction of the Coriolis force and thus, a change in wind direction. In the northern hemisphere, the southeasterly winds turn toward north-east, while in the southern hemisphere the opposite occurs. As long as the transfer takes place over ocean surface, the displacements of the ITCZ are rather small of few degrees. However in monsoon regions, differential heating capacities of land and ocean are very important features of the circulation (e.g. Wallace and Hobbs, 2006). When intense solar radiation hits land, its energy is absorbed and transferred as heat directly back into the atmosphere. In contrast, increased solar radiation over the ocean results in predominately downward mixing and storage in deeper ocean layers. This differential heating forces a built-up of so-called thermal low pressure systems over land that enhance the monsoon winds and shift the ITCZ toward land regions. In regions where continents are located near the equator, this causes the ITCZ to shift farther off the equator during the respective summer season (e.g. Wallace and Hobbs, 2006).
Over the African continent, the influence of the Hadley circulation is obvious through the West African Monsoon. However, the high topography of the GHA forms a meridional barrier for westerly flow and thus, mostly prevents advection of moisture at low levels (Yang et al., 2015). In addition, the change of southeasterly winds to southwesterlies by forming the Somali-Jet during boreal summer transports moisture away from the GHA and is an important feature of the Indian Monsoon circulation (e.g. Yang et al., 2015). A similar drying effect of the GHA occurs in austral summer.

2.2.2 The Walker Circulation

Besides the latitudinal variations, interseasonal and interannual variability on zonal scale affect the intensity of monsoon circulations and thus, the amount of associated seasonal rainfall. This variability is tightly connected to changes of the land-sea temperature gradient, which itself is modified by the Walker circulation. The Walker circulation can be regarded as the zonal counterpart of the Hadley circulation and transports heat and moisture longitudinally along the equatorial belt. The circulation is driven by pressure gradients across the tropical belt, which mostly arise from deep convection, zonal variations of sea surface temperature through wind stress and fluxes of heat and moisture (e.g. Peixoto and Oort, 1992). The most dominant component is the Pacific cell, which consists of a rising branch over the western, and subsidence over the eastern part of the Pacific Ocean (Figure 2.3). In its neutral state, predominately easterly winds in the lower and westerly winds at the upper troposphere maintain the circulation. Similar circulations with a smaller extent can also be identified over the Indian Ocean as well as the Atlantic, mostly interacting with the neighboring continents Africa and America (e.g. Peixoto and Oort, 1992; Cook and Vizy, 2016). The east–west pressure gradient associated with the Walker circulation undergoes an irregular variability on seasonal intraseasonal and interannual timescales, which is often coupled with the oceanic modes like the El Niño Southern Oscillation or the Indian Ocean Dipole (section 2.3.1) and is thus an integral part of the global climate system.

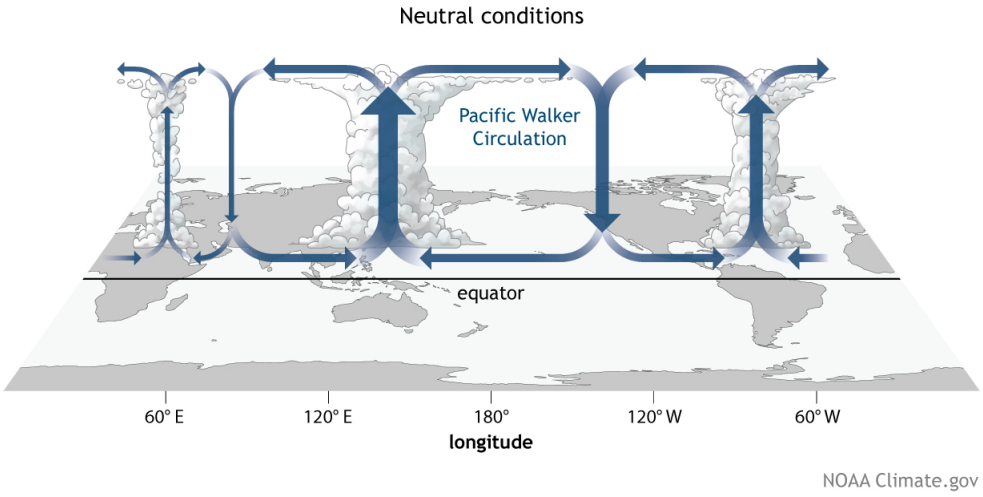

Figure 2.3: Global Walker circulation during neutral conditions centered over the Pacific Ocean. Ascending branches over the maritime continent, central Africa and south America are indicated by enhanced convections. source: NOAA Climate.gov

The mostly arid rainfall conditions over the GHA can also be explained by the structure of the Walker Circulation over the Indian Ocean and Africa. Whereas the ascending branch of the Indian Ocean Walker Cell is usually located over the Maritime Continent, the western Indian Ocean is located under the descending branch, which prevents deep convection during the boreal summer and autumn seasons. The ascending branch of the Congo-Atlantic Walker circulation is located over the Congo Basin in agreement with the humid climate of equatorial western Africa (Cook and Vizy, 2016). However,

the subsidence of the descending branch can trigger secondary circulations on synoptic scales, which are relevant for the extent of the northward migration of the ITCZ and enhanced Hadley circulation. For example, strong subsidence over the eastern Atlantic tend to enhance rainfall over the Sahel and vice versa (e.g. Cook and Vizy, 2016). The Sahel rainfall increase during anomalously strong subsidence is attributed to an enhanced meridional surface temperature gradient and surface confluence over the Sahel. While the subsidence at the coast of the GHA reduces rainfall, it feeds the Indian monsoon system via the Somali-Jet (e.g. Halpern and Woiceshyn, 1999, 2001; Camberlin and Philippon, 2002). A comparable effect of the West African Monsoon is considered on the Ethiopian June-September rainy season (e.g. Diro et al., 2011). Since changes in location and strength of one circulation cell affect the neighbors, fluctuations of the Walker Circulation can lead to extreme weather conditions in different parts of the world. The most common fluctuations arise from El Niño events every two to seven years. This mode of variability is introduced in section 2.3.1.

Changes in the structure of the Walker circulation, in particular the Indian and Pacific Walker Cells, are often used to explain the Eastern African climate change paradox. For instance, Funk et al. (2008), Funk et al. (2014) and Williams and Funk (2011) attribute the decline of the MAM rainfall over the GHA to a westwards shift of the of the Indian Ocean Walker Cell, which results in increased ascend and rainfall over the southern tropical Indian Ocean and enhanced subsidence near the intersection of Somalia, Kenya and Ethiopia, and a decrease in convection over parts of the Ethiopian highlands and Sudan. Funk et al. (2008) links the increased rainfall over the Indian Ocean to reduced onshore moisture transports into Kenya, Somalia and Ethiopia, and potentially enhanced dry northerly flows out of the Sahara. Williams and Funk (2011) attribute this shift to a disproportionately rapid warming in the central and eastern Indian Ocean since 1980. The climate projections, which show increased GHA precipitation during the MAM season, assume an overall weakening of the Walker Circulation due to a reduced SST gradients as a response to anthropogenic global warming.

Other hypothesis support a shift of Pacific decadal variability (PDV) to its cold phase in 1998-1999 that lead to a shift of the Walker circulation of the Indian Ocean (Lyon and Vigaud, 2017; Bahaga et al., 2019). According to this explanation, the drying trend is not a continuous development but a rather abrupt decline from 1998-1999 onwards (Lyon and DeWitt, 2012; Lyon, 2014a; Bahaga et al., 2019). Lyon and DeWitt (2012) and Bahaga et al. (2019) also emphasizes that in terms of rainfall variance, interannual variations at time scale of less than ten years account for the majority of MAM rainfall, while decadal variations contribute 10%. Negative trends at segments of approximately ten years start around the year 2000. Analysis of change points in different atmospheric parameters also show a shift likely occurring around this year. The enhanced ascending branch was identified over the western tropical Pacific centered near 135 °E (the Pacific warm pool region). The Eastern African climate change paradox might be then a result from a mismatch of timescales, between decadal scale variability and distinct, longer-term climate changes in East Africa arising from anthropogenic global warming.

However, a major caveat of this explanation concerns the seasonality aspect of the Walker circulation. Particularly near the East African coast, the upwelling of cold water, which is a major driver of the Walker circulation, is only present from boreal summer to autumn (Hastenrath, 2000; Liebmann et al., 2017), although a modulation

of subsidence over Eastern Africa by upper level easterlies over the Indian Ocean has also been proposed (Liebmann et al., 2017).

2.2.3 The Intertropical Convergence Zone and the Tropical Rain Belt

In the current climate, 32% of the globally accumulated annual rainfall falls within a latitudinal range from 10°S to 10°N in a narrow band of heavy precipitation (Kang et al., 2018). A quick view on a climatological map over the tropics likely shows a belt of annual rainfall maxima at approximately 7°N. Although the time-averages of solar insolation peak at the geographic equator, the Earth's climate has regionally pronounced asymmetries especially in the eastern tropical Pacific and Atlantic Oceans (Philander et al., 1996). Over the Atlantic and Pacific Oceans, the maximum latitudinal extension lies at 9°N in the northern and 2°N in the southern hemisphere summer, whereas over the Indian Ocean and adjacent land areas the maximum poleward edges lies at 20°N and 8°S, respectively (Schneider et al., 2014). This large extent is attributed to variations of the dominating South Asian Monsoon circulations (Gadgil, 2003; Schneider et al., 2014).
Embedded in the Hadley circulation, the ITCZ is maintained by convergence of trade winds near the surface and migrates following the sun towards the hemisphere that warms relative to the other (Schneider et al., 2014; Nicholson, 2018). While fed with heat and moisture, this process leads to an ascent of air masses, cooling, condensation and precipitation from deep convective clouds. Beyond the meridional transport, the ITCZ can also interact zonally with the Walker circulation and the associated circulations in the underlying oceans (e.g. Cook and Vizy, 2016; Freitas et al., 2017). However, this description supports the image that 1) the pressure minimum, wind convergence and rainfall maximum are collocated with each other and, 2) the maximum cloudiness is roughly collocated with maximum rainfall, and 3) due to the maximum cloudiness, the longwave radiation is at a minimum at that location (Nicholson, 2018). For this reason, the terms "Intertropical Convergence Zone" was frequently used interchangeably for the seasonal location of maximum rainfall, as well as the location of the associated dynamics like convergence of trade winds, equatorial low pressure trough or lines of cloud clusters (Nicholson, 2018). However, this understanding neglects differences in the structure of the ITCZ between oceans and continents and particularly regional variations over the African continent. Over northern subsaharan Africa, the surface ITCZ instead represents the zone where the northeasterlies and southwesterly monsoon flow.s converge. An important aspect of the ITCZ in this region is that the convergence of the flows is located several degrees farther to the north than the zone of convection and rainfall (Nicholson, 2018). Therefore, the zone of convergence of surface flows (often called "Intertropical Discontinuity", ITD) should be regarded separately from the zone of maximum rainfall. Although both of them shift latitudinally with the seasons and exhibit an interannual variability, they fluctuate independently from each other (Grist and Nicholson, 2001). For equatorial Africa, Nicholson (2018) has shown that the ITD stays north of the equator over the whole year, whereas the rainfall belt migrates towards 20 °S. For these reasons, the term "Tropical Rain Band" (TRB) for the zone of maximum rainfall is used in this work,

whereas the ITCZ refers only to the whole system including ITD and TRB.
Over most of the year, there is a strong difference between the mean location of the TRB over the Atlantic and the Indian Oceans. This spread is associated with the regional topography over the GHA and the resulting rainfall circulation patterns over equatorial Africa. Over the GHA, three air masses are involved: the northeasterly and the southeasterly monsoon flows and the Congo air masses from the west. Thus, depending on the season, two convergence zones prevail over and around the GHA. Besides the TRB, the so-called Congo Air Boundary (CAB) separates the westerlies from the Congo Basin and the southeasterlies from the Indian Ocean (e.g. Nicholson, 1996). However, the low-level westerlies are mostly blocked by topography and thus, only the upper levels of the CAB occasionally reach the GHA (Hills, 1979; Nicholson, 1996). The TRB is mostly formed by the dry northeasterlies related to the Asian winter monsoon and moist southeasterlies from the southwestern Indian Ocean. The latter forms the basis of the annually recurring Somali-Jet (cf. paragraph 2.1). This means, that low-level convergence can only occur as long as the zonal branch is not developed and the flow brings moisture towards the GHA. An increase of low-level moisture increases the moist static energy near the surface and weakens the atmospheric stability, which dominates the atmospheric thermal conditions over the rest of the year (Yang et al., 2015). The amount of moisture is connected to the SSTs in the western Indian Ocean. Yang et al. (2015) demonstrated that the off-coast SST annual cycle is closely related to that for GHA precipitation. The SSTs are higher during the rainy seasons than in the dry seasons and are highest during April as the peak month of the Long Rains. During boreal summer, the westerly branch of the Somali-Jet contributes to enhanced upwelling and cooler SSTs in the western Indian Ocean, which leads to higher atmospheric stability. Thus, the atmosphere is generally conditionally stable throughout the year but the degree of instability follows the precipitation annual cycle, that is, less stable during the rainy seasons and more stable during the dry seasons and least stable during the Long Rains (Yang et al., 2015). The degree of instability during the rainy seasons can still be increased through higher SST values associated with e.g. IOD events (section 2.3.1) or with enhanced westerlies from the Congo Basin due to e.g. MJO (section 2.3.2).

2.2.4 Semi-permanent Low Pressure Systems

One key component of rainfall variability over the GHA is the variability of seasonal, semi-permanent low pressure systems over the African continent and the Arabian Peninsula. These systems are built and maintained by temperature differences between the continent, with maxima in the deserts, and the surrounding oceans, and minima related to upwelling regions and cold currents. Such heat lows (also known as thermal lows or thermal troughs) are persistent climatological features during the summer seasons of the respective hemispheres in subtropical arid and semi-arid regions with high insolation and low evaporation (e.g. Rácz and Smith, 1999, and references therein). They belong to the class of so-called warm-core vortices with the cyclonic circulation being strongest at near-surface levels and decaying with height, partly even becoming anticyclonic where the low extends radially outward (Spengler and Smith, 2008). The relevant systems over the GHA are the Angola Low over the plateau region to the east of the Angolan and Namibian highlands in austral spring and summer, the Arabian

Low and to a lesser extend the West African Heat Low in the boreal spring, summer and autumn seasons. During the respective summer seasons, the lows drive the moist flows from the coasts towards the dry inland areas, as well as the dry subtropical winds across the deserts. Both kinds of flow converge in the region of the heat lows along the Intertropical Discontinuity. Over northwestern Africa, this zone consists of the dry Harmattan and moist monsoon flow (e.g. Lavaysse et al., 2009). In the Indian pre-monsoon system, these are the dry Shamal and the flow associated with the zonal branch of the Somali-Jet along the Arabian coast (Rashki et al., 2019). Over southern Africa, the convergence originates from moisture fluxes from the western Indian and southeastern Atlantic Oceans (Rouault et al., 2003; Cook et al., 2004; Vigaud et al., 2007, 2009; Hermes and Reason, 2009). Over the African continent, this convergence results in a baroclinicity of the dry and hot continental air and colder and moist air from the oceans that is an important driver for the African Easterly Jets (AEJs) in both hemispheres. While the wind maximum of the AEJ-North can be detected throughout the year at 700 hPa, the weaker AEJ-South persist only during austral spring from September to November with a maximum at 600 hPa (Nicholson and Grist, 2003; Lavaysse et al., 2009; Kuete et al., 2020). Over West Africa, the baroclinicity is also responsible for instabilities of the waveguide, which results in African Easterly Waves (AEWs, Thorncroft and Blackburn, 1999).

However, similar characteristics were also observed for other warm core vortices like the tropical low (Spengler and Smith, 2008). Their similarities involve the role of surface friction in the two types of vortices, each having strong inflow in a shallow boundary layer. The essential difference between the two types of vortices is the way in which the warm core is maintained: in the heat low it is primarily a result of diabatic heating in a deep, dry convective boundary layer, whereas in the tropical low it is a result of moist deep convection in conjunction with enhanced surface moisture fluxes (Spengler and Smith, 2008). Due to specific regional features, the influence of pure surface thermal forcing in the development the Angola Low has recently been questioned. Recent studies on the Angola Low have demonstrated that during the peak of austral summer, the heat low moves southward towards the Kalahari desert, while cyclonic vorticity remains over the Angola Low region through moist processes reminiscent of tropical lows (Munday and Washington, 2017; Howard and Washington, 2018; Howard et al., 2019). The transition from the heat low to the tropical low mode typically occurs in December, although heat low circulations can occasionally occur throughout the whole season (Howard and Washington, 2018).

On the seasonal scale, the core pressure of the respective low is an indicator of the intensity of the rainy season. Evan et al. (2015) partly attributed the recovery of the drought in the Sahel to the deepening of the Sahara Heat Low. During wet austral summers (January–March; JFM) there is a 10% increase in the strength of the Angola Low, while dry JFMs are associated with a 20% decrease in strength of the Angola Low in southern Africa (Cook et al., 2004). At the intraseasonal timescale, intensification of the Angola Low favors wet spells over South Africa, southern Angola and southern Namibia (Rouault et al., 2003; Cook et al., 2004; Reason and Jagadheesha, 2005; Hermes and Reason, 2009). However, the position of the Angola Low plays a role in its modifications of the moist processes and rainfall anomalies. Crétat et al. (2019) analyzed preferred states of the Angola Low and their effect on the regional circulation. Their refined view on the Angola Low resulted in three main states that are robust across three reanalyses: anomalously weak Angola Low, near-climatological state with

slight zonal shifts and anomalously strong Angola Low with meridional shifts. Crétat et al. (2019) also noted that in particular, anomalously weak, northward and southward Angola Low states depict significant vorticity anomalies throughout the troposphere, which confirms that the Angola Low cannot be regarded only as a thermal low driven by surface heating and dry convection. Dunning et al. (2018) indicated in their analysis of 29 CMIP5 climate models that the deepening of the Sahara Heat Low and Angola Low might contribute to shift of the timing of rainy season onset and cessation dates particularly over equatorial and southern Africa in the future.

2.3 Global modes of variability over GHA

In the following section, some global and remote-scale patterns, which affect the rainfall variability of the GHA, are introduced.

2.3.1 El Niño Southern Oscillation and Indian Ocean Modes

The El Niño Southern Oscillation (ENSO) is a coupled periodic mode of SSTs ("El Niño") and the overlying atmospheric pressure ("Southern Oscillation") across the equatorial Pacific Ocean. The name of the SST mode originated from South American fisherman who noticed that the warm up of coastal waters occurred often around Christmas. They referred to the warming as "El Niño", (Spanish term for a boy child) in connection with the religious holiday (e.g. Peixoto and Oort, 1992; Wallace and Hobbs, 2006; Schoenwiese, 2003). The "Southern Oscillation" or large-scale changes in sea level pressure across Indonesia and the tropical Pacific were discovered by Sir Gilbert Walker at the beginning of the twentieth century (e.g. Peixoto and Oort, 1992; Wallace and Hobbs, 2006). However, it was not until the late 1960s, that the coupling between the oceanic and atmospheric parts was accepted in the scientific community (e.g. Peixoto and Oort, 1992).
ENSO is one of the most important climate phenomena due to its effect on the global atmospheric circulation, which in turn, influences temperature and precipitation across the globe. It is also a quasi-periodic phenomenon that tends to reccur every 2-7 years (Diaz and Markgraf, 2000). The considerably slow evolution of the respective ENSO mode often facilitates the prediction of several months in advance of its strongest impacts on weather and climate. Though ENSO is a single climate phenomenon, it has three modes, it can be in: the two opposite phases, "El Niño" and "La Niña", and "Neutral" as the middle of the continuum (e.g. Peixoto and Oort, 1992; Diaz and Markgraf, 2000). The El Niño mode is associated with a reduced upwelling and a deepening of the equatorial thermocline in the eastern Pacific and an enrichment of anomalously warm water near the coast of South America (Figure 2.4). The warm anomaly leads to decreased sea-level pressure and increased ascent in the eastern Pacific, which leads to enhanced convection in the east-central Pacific and western coast of South America. On the other side, convection over the western Pacific is suppressed. Reverse conditions, i.e. a stronger upwelling in the eastern Pacific, increased sea-level pressure and subsidence are referred to as La Niña and are associated with dryness in the eastern and wetness in the western Pacific (Figure 2.4).

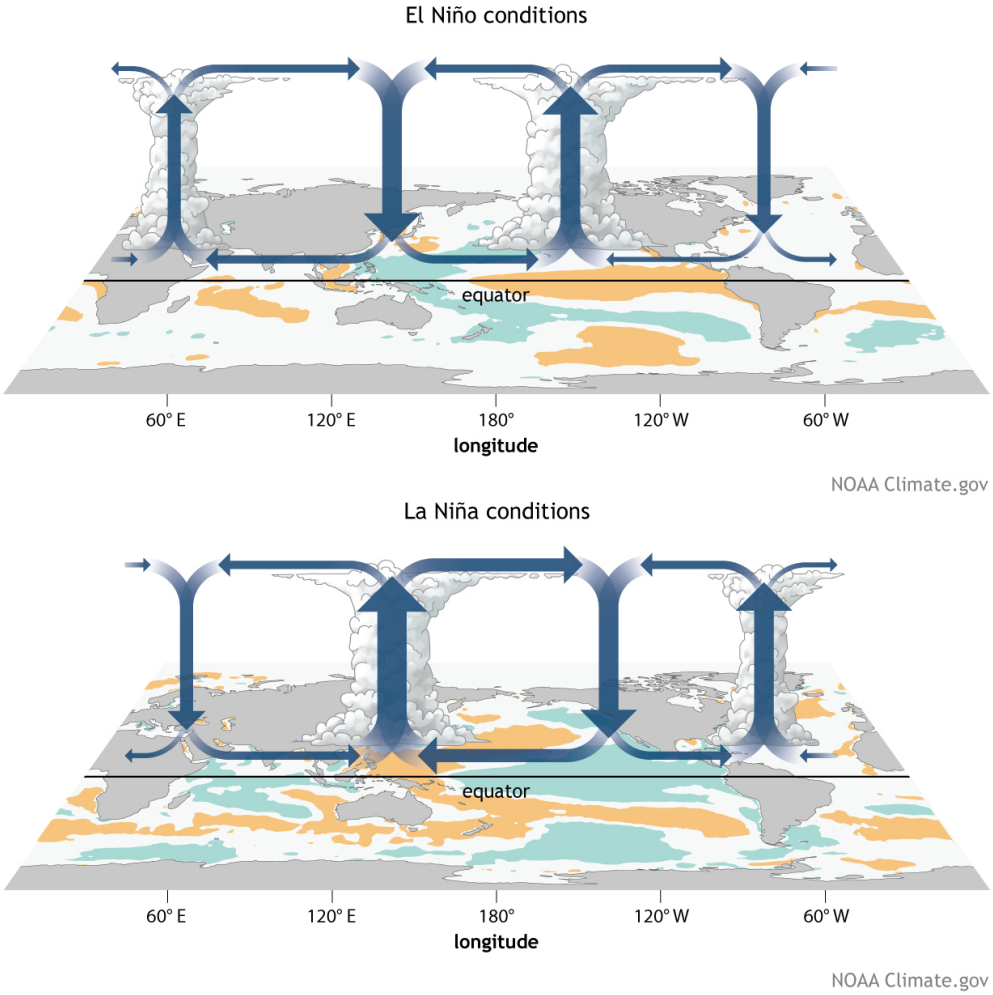

Figure 2.4: Generalized Walker Circulation (December-February) anomaly during El Niño (above) and La Niña (below) events, overlaid on map of average sea surface temperature anomalies. Positive SST anomalies in the central and eastern Pacific (orange) during El Niño events induce an anomalous ascending branch of the Walker Circulation east of 180°, while the descending branches shift to the Maritime continent and northern South America. Negative SST anomalies in the central and eastern Pacific Ocean (blue) and positive SST anomalies over the western Pacific Ocean during La Niña events enhance the ascending branch of the Walker circulation over the Maritime Continent and the descending branch over the eastern Pacific Ocean. Enhanced rising motion is also found over northern South America, while enhanced sinking motion is found over eastern Africa. source: NOAA Climate.gov

Thus, the El Niño mode counteracts the average seasonal SST gradients, which feed the Walker circulation over the Pacific Ocean. Supposing no further effects from other modes of variability, reduced SST gradients in the equatorial Pacific also weaken the Walker circulation of the neighboring Walker cells in the Indian Ocean and over the American continent (Peixoto and Oort, 1992). Preceding effects of an El Niño event include a weakened Hadley circulation with reduced core pressure of the subtropical pressure belt and weaker trade winds particularly in the southern Pacific. Thus, the impact of ENSO affects not only the tropical but also the midlatitudes making ENSO a global phenomenon (Figure 2.5 Peixoto and Oort, 1992). Weak Walker circulation

lead to a strong latitudinal energy gradient with high values at the equator and a stronger decrease in the poleward direction. These conditions re-strengthen the Hadley circulation and the latitudinal transport of energy that strengthens the subtropical pressure belt and the trade winds. Further amplification can initiate La Niña conditions (Peixoto and Oort, 1992; Schoenwiese, 2003).

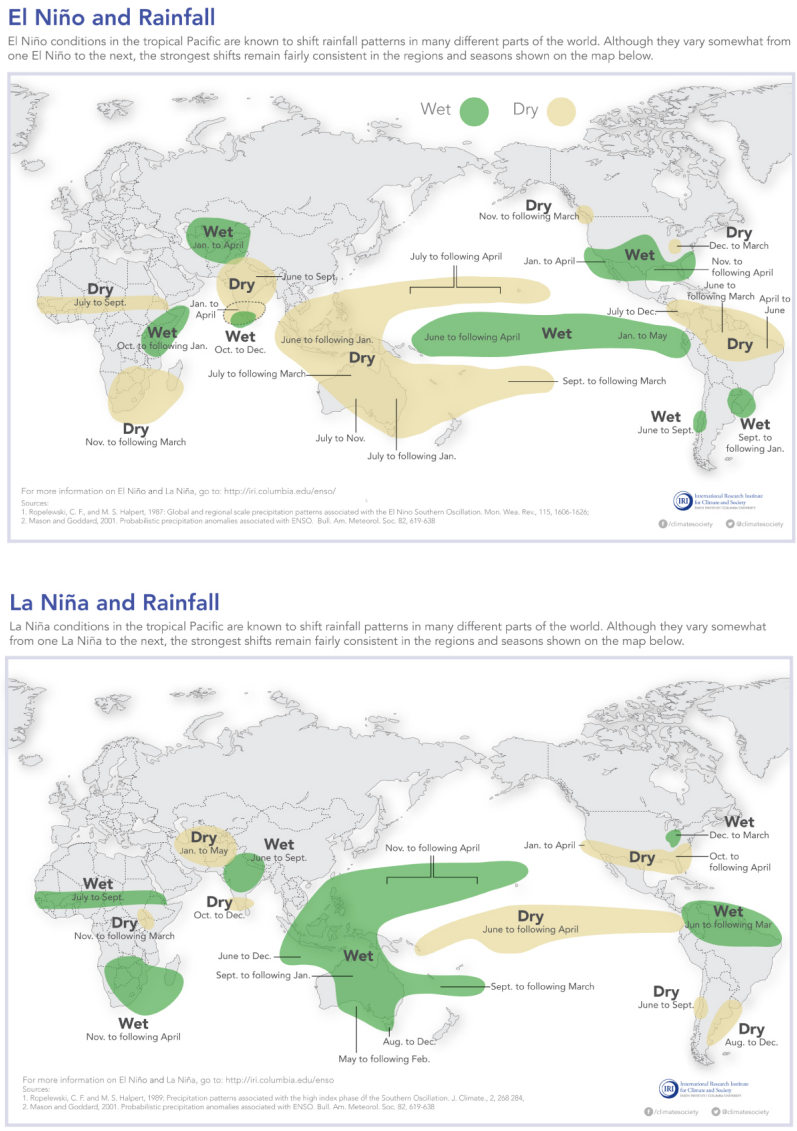

Figure 2.5: Schematic representation of typical ENSO-related rainfall anomalies over the globe. Green areas enclose regions with positive rainfall anomalies relative to the climatology, while brown regions exhibit negative rainfall anomalies. The approximate period of anomalies is also shown for the respective regions. source: IRI data library, adopted from Ropelewski and Halpert (1987).

Despite of these general pattern, it can only be used to predict a tendency of how much rain will fall in a particular region in any particular summer. In fact, the strongest El Niño event in the 20th Century (1997-1998) had little effect on the Indian monsoon rainfall or precipitation over southern Africa (Kumar et al., 2006; Blamey et al., 2018).

On the other hand, this event accounted for extreme rainfall during the Short Rains over GHA (MacLeod and Caminade, 2019).
While the ENSO patterns were originally described as east-west patterns, there are further "flavors", which in turn differ in their location of SST anomalies and the changes in the Walker Circulation. Thus, the widely known El Niño pattern is usually referred as "canonical El Niño", "cold tongue (CT) El Niño" (Kug et al., 2009, 2010), or "eastern Pacific El Niño" (Yeh et al., 2009; Kao and Yu, 2009; Yu and Kim, 2010b,a), while the second pattern is called "El Niño Modoki" (Ashok et al., 2007; Weng et al., 2007), "dateline El Niño" (Larkin and Harrison, 2005), "Central Pacific El Niño" (Yeh et al., 2009; Kao and Yu, 2009; Yu and Kim, 2010b,a) or "warm pool (WP) El Niño" (Kug et al., 2009, 2010) according to the location of the warm SST anomaly. The flavors are not distinct, but rather a continuum, i.e. one El Niño event can occur in different types during multiple phases of its development (Yu and Kim, 2010b; Zhang et al., 2019). Depending on the position and timing of the SST anomaly, the change in the Walker circulation can affect different regions and rainy seasons.
Besides ENSO, similar modes also exist over the Atlantic and Indian Oceans. The former is often referred as "Atlantic Niño" or "Atlantic Equatorial Mode" and shows weaker growth rates (Zebiak, 1993; Keenlyside and Latif, 2007). Except for the Ethiopian Kiremt Rains, where non-stationary relationships exist, this mode is less relevant for rainfall over GHA (Bahaga et al., 2019). Over the Indian Ocean, the phenomenon is often referred as "Indian Ocean Dipole" (IOD, Saji et al., 1999) or "Indian Ocean Zonal Mode" (IOZM, Black et al., 2003). The positive phase of IOD is characterized by a tongue of positive SST anomalies over the Arabian Sea, while negative anomalies prevail over southeastern Indian Ocean and the Maritime Continent (Figure 2.6). The associated Walker circulation shows an anomalously ascending branch over the Arabian Sea and subsidence over the Maritime Continent (Figure 2.6). The reverse conditions apply to the negative IOD phase. Recent studies also identified an alternative "flavor" of the IOD (IOD Modoki, Endo and Tozuka, 2016), which shows, analogous to ENSO Modoki, different teleconnection patterns compared to the "canonical IOD".

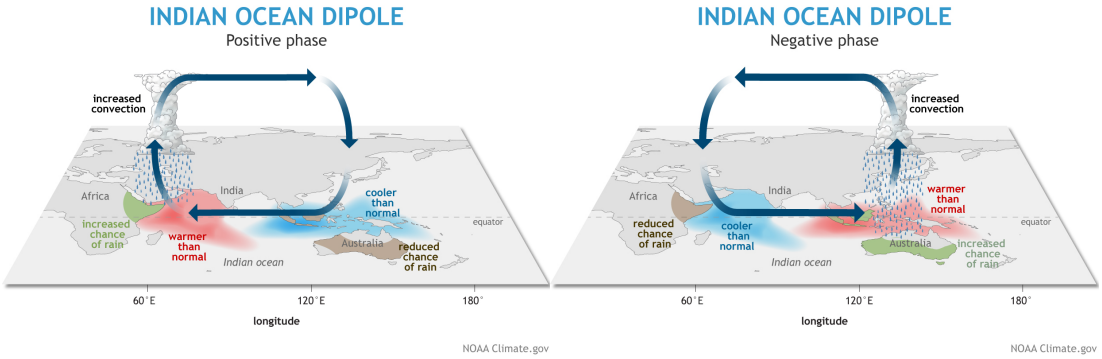

Figure 2.6: SST and Walker circulation anomalies associated with the different IOD phases. Left: Positive phases of the Indian Ocean Dipole are characterized by negative SST anomalies west of Indonesia and positive SST anomalies in the western Indian Ocean. The SST anomalies alter the atmospheric circulation in the Indian Ocean region leading to wetter conditions over eastern Africa and drier conditions over Indonesia and Australia. Right: The negative phase favors the opposite pattern. source: NOAA Climate.gov

As many positive IOD events occur in the same season as ENSO events, there is a consensus that an intercorrelation between the two phenomena exists (Baquero-Bernal et al., 2002; Black et al., 2003; Stuecker et al., 2017; Bahaga et al., 2019). This interaction may occur through the Walker Circulation to the west and/or via the Indonesian through-flow of the warm tropical ocean waters from the Pacific into the Indian ocean. Still, a small fraction of IOD events occur independently of ENSO events (e.g. Black et al., 2003; Stuecker et al., 2017). Black et al. (2003) indicate that the relationship between ENSO and IOD is not linear and a strong ENSO forcing is needed to initiate an IOD event. Fan et al. (2017) argue that the timing of the El Niño development determines if a positive IOD event occurs during the same season. According to their results, due to different atmospheric responses over the Indian Ocean to the eastern Pacific warming between early and late summer, early-onset ENSO is associated with subsequent strong IOD development, whereas late-onset ENSO forces only marginal SST anomalies in the equatorial western Indian Ocean.
Emerging from the question of the independence of ENSO and IOD modes in the Indian Ocean, the follow-up discussion arises on which is the more important mode for rainfall over the GHA. Goddard and Graham (1999) and Latif et al. (1999) argue that the SST anomalies induced by the co-occurring positive IOD in 1997/1998 were essential for simulating the correct rainfall response over eastern, central, and southern Africa. Blamey et al. (2018) and MacLeod and Caminade (2019) compared the most recent El Niño 2015/2016 event with previous events 1982/1983 and 1997/1998 in terms of rainfall and circulation anomalies over eastern and southern Africa. Both studies emphasize that despite the high magnitude of the three events, the impacts on rainfall differed. Particularly, the recent El Niño event did not cause exceptionally high rainfall anomalies, while some parts even experienced a drier than average season (MacLeod and Caminade, 2019). The authors attribute these effect to a positive but weaker IOD phase compared to previous El Niño events (such as the 1997 event) and thus, to a smaller reduction in the strength of the Indian Ocean Walker-type circulation. Partial correlation analysis at decadal scales in Bahaga et al. (2019) point to a leading role of the IOD on the East African Short Rains.

2.3.2 Madden-Julian Oscillation

The Madden-Julian oscillation (MJO) is a tropical disturbance, which is responsible for a large part of rainfall variability in the tropics at a time scale of 30 to 60 days with globally extending impacts (Madden and Julian, 1971, 1972, 1994). MJO events appear typically as a large-scale convective system that emerges over the Indian Ocean and propagate eastward to the Pacific Ocean at a speed of $\approx$ 5 m s-1 (Weickmann et al., 1985; Knutson et al., 1986; Zaitchik, 2017). Over the central Pacific, it loses convective coupling and propagates at higher speed through the cooler eastern Pacific. Sometimes it re-arises as a convective feature over the tropical Atlantic and Equatorial Africa (Madden and Julian, 1971, 1994; Zhang, 2005; Zaitchik, 2017). It affects precipitation variability in both tropical and extratropical regions year-round, but the seasonal peaks are typically in boreal winter and spring and to a lesser extend in boreal summer (Hendon and Salby, 1994; Zhang and Dong, 2004; Donald et al., 2006; Zhang, 2013; Zaitchik, 2017). Despite of its name, the duration of one cycle is not uniform and time between active phases, convective strength, and speed of

propagation may vary from event to event (Zaitchik, 2017). Thus, as noted by Zhang (2005), the MJO is more an episodic mode of intra-seasonal variability rather than a regular oscillation.

Briefly, the MJO consists of an "active phase" and a "suppressed phase". The "active phase" is characterized by a convective core, which itself is composed of a number of small scale systems of deep convection. This phase shows convergence of wind in the lower levels and divergence aloft (e.g. Zhang, 2005; Zaitchik, 2017). Reverse conditions can be observed in the "suppressed phase" like weak convection and surface divergence. Both phases are dynamically linked to each other and propagate eastwards while producing a convection dipole that can cover a large part of the global tropics (Figure 2.7). Large-scale heating anomalies can initiate equatorial Kelvin waves and equatorial Rossby waves, which can play an important role in rainfall dynamics remote from the main locations of the MJO in the Indian and Pacific Oceans (e.g. Zaitchik, 2017).
The initiation and propagation of the MJO core has been subject to extensive research, but currently there is no single theory, which can explain all of the observed aspects of this mode. Early studies hypothesized that MJO events result from stationary intraseasonal oscillations (Yasunari, 1979), but neither statistical analysis nor simulations of stationary oscillations supported this mechanism (Yamagata and Hayashi, 1984). Another early approach focused on wind-induced surface heat exchange (Matsuno, 1966). Here, strengthened winds to the east of a tropical convective core could enhance evaporation and favor eastward migration of the convective core (Emanuel, 1987; Neelin et al., 1987). However, observations of surface winds during strong MJO events are inconsistent with this theory (Zaitchik, 2017).
Recent studies agree that the MJO initiation occur over the eastern Indian Ocean approximately ten days before a convective core of an active MJO event can be detected (e.g. Straub, 2013; Zhao et al., 2013; Mei et al., 2015). Zhao et al. (2013) categorized two hypotheses of MJO initiation: The tropical origin hypothesis is based on a forcing from a preceding MJO event that circumnavigates around the global tropics. The previous propagating MJO may induce local changes in the air-sea-moisture fluxes over the moist and warm Indian Ocean and thus trigger convection after it passes the African continent. Orographic lifting over eastern Africa may enhance the convective effect. The extratropical origin theory assumes a forcing from mid-latitude Rossby waves and baroclinic eddies, which transport momentum and energy while propagating towards the equator. Zhao et al. (2013) could identify a marked increase of the lower-tropospheric moisture and temperature, which is caused through horizontal advection, over the western Indian Ocean prior to the convection initiation. The authors found that the local wind anomaly is closely linked to the forcing of a negative heating anomaly over the eastern Indian Ocean. This heating implies that the local precursor signals are mainly set up by the preceding suppressed-phase MJO in the form of a Rossby wave response, or by an extratropical trigger from the southern hemisphere. Similar results were obtained by Mei et al. (2015): they identified three types of an MJO initiation processes. The moisture-leading process in the lower levels describes an increase of lower-tropospheric moisture, which induces a convectively unstable stratification and MJO convection onset over the western Indian Ocean resulting from advection of moisture from a preceding MJO suppressed phase. A second process results from phase leading of lower-tropospheric ascending motion, which promote

latent heat release and trigger MJO convection. The third process involves forcing from midlatitude perturbations. Rossby wave train signals in the upper troposphere extend from the midlatitudes to the tropical Indian Ocean a few days prior to an MJO initiation.

Zaitchik (2017) distinguished between three mechanisms of MJO influence on Africa: (1) direct influence of the MJO convective core, as it passes over Africa; (2) synoptic influence of the convective core when it is located in or near Africa; (3) remote teleconnections communicated via dry Kelvin and/or Rossby waves emanating from the MJO convective region. For the austral summer rains, mechanisms and even the magnitude of MJO modulation on this region are poorly characterized. Studies mostly focus on indirect synoptic effects of the MJO on rainfall over southern Africa (Zaitchik, 2017). Pohl et al. (2007) found that the impact of MJO over southern Africa is out of phase with convective anomalies in equatorial Africa. The dry phase of the MJO induces a secondary cycle of convection, which propagates from the Congo Basin over southern Africa and arrives over Zimbabwe and southern Tanzania prior to the convective core of the following cycle (Pohl et al., 2007). Possible interpretations of this effect might be that the MJO core influences the intensity of rainfall associated with tropical-temperate troughs as they pass through Africa or interactions of the convection dipole between the Southwest Indian Ocean and Southern Africa when the MJO is located near the African continent (Pohl et al., 2007; Oettli et al., 2014; Hart et al., 2013a).

Since equatorial East Africa is located relatively close to active MJO convective regions in the Indian Ocean the emphasis has been on the direct influence of the MJO convective core or on the synoptic effects of MJO convection. Pohl and Camberlin (2006a) noted the direct influence of the MJO convective core through destabilization of the atmosphere as it passes over the region. Still, it takes several days for this destabilization to induce enhanced convection. In addition, synoptic-scale mechanisms modify convection over East Africa (Figure 2.7, phases 2–3). Berhane and Zaitchik (2014) identified a dynamical link between MJO convection in the Indian Ocean and southeasterly winds entering the East African highlands. This leads to an MJO influence on convection due to thermodynamic and convergence effects of altered low level winds. In the coastal regions, different mechanisms are suggested: Pohl and Camberlin (2006a) indicate that MJO leads to changes in stratiform precipitation along the coast through changes of the strength of trade winds. Berhane and Zaitchik (2014) identify a Walker Circulation response with enhanced subsidence occurring over the East African coast when the MJO convective core is located over the Maritime Continent.

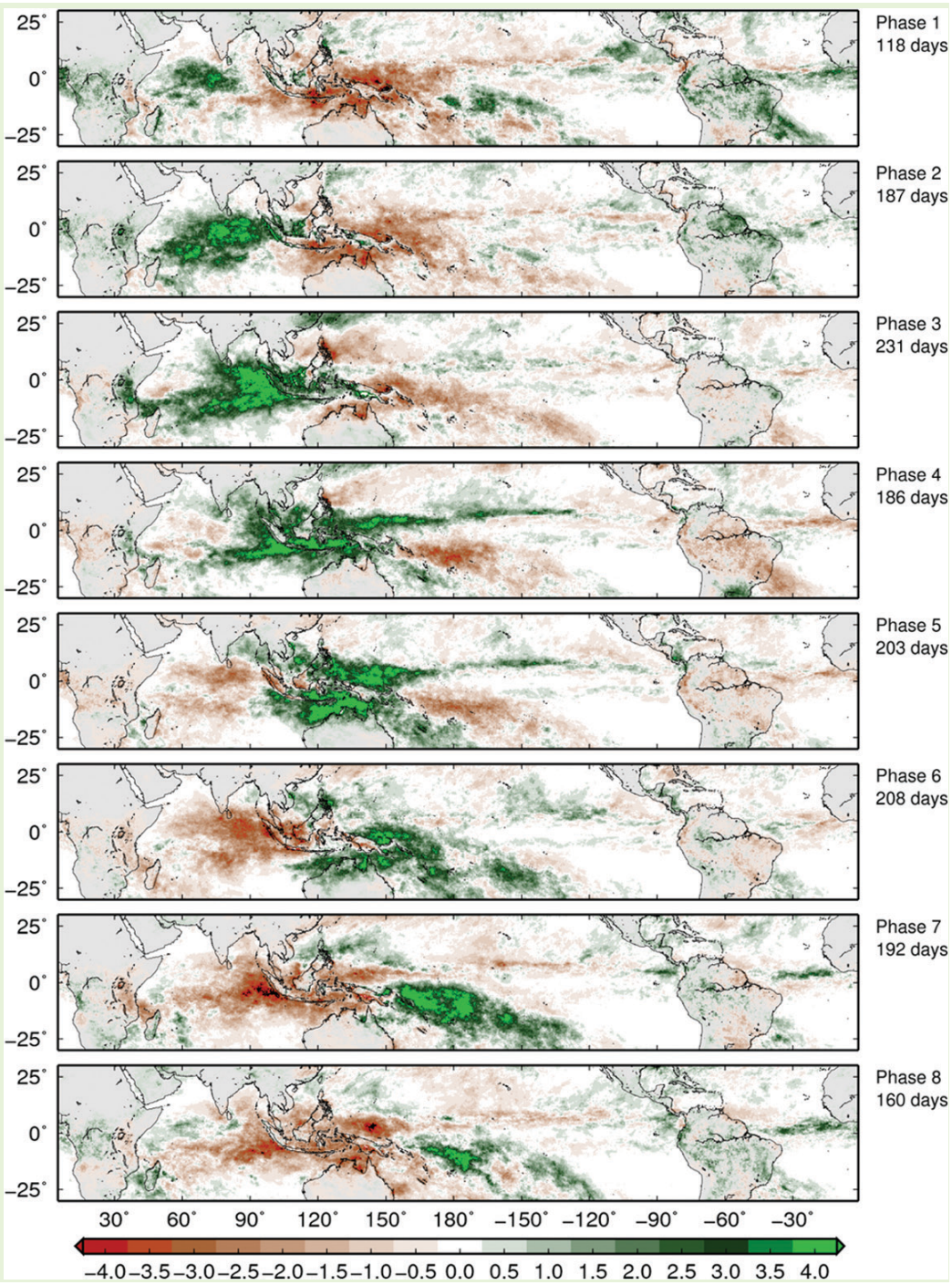

Figure 2.7: Composites of intraseasonal (30–90 days) rainfall anomalies per MJO-phase estimated from TRMM [mm day^{-1}] during the November–April season for the period 1998–2012. source: Zhang (2013)

2.3.3 Tropical-extratropical interactions

Particularly at the northern and southern edges of the GHA, rainfall variability can be affected by extra-tropical systems from higher latitudes propagating towards the equator. In an early case study, Habtemichael and Pegley (1974) analyzed the causes of an Eritrean wet spell in April 1970 and found a strong southward band of convection extending from the sub-tropical jet stream to 10°N, which was fed by moisture from lower tropospheric south-easterly winds flowing across the southern Red Sea. Camberlin and Philippon (2002) found systematic interactions between midlatitude circulation in the Northern Hemisphere spring and early season precipitation of the Long Rains. They emphasize that both low-level and upper-level circulation features are involved. The circulation anomalies at the lower levels are associated with reduced easterlies or even westerly winds and anomalous convergence, while the convergence in the upper levels is reduced. Westerly winds are major initiators of low-level moisture convergence, reduced atmospheric stability and rainfall over the GHA during the Long Rains (Finney et al., 2019). In their analysis of the Ethiopian spring rainy season (locally termed "Belg"), Bekele-Biratu et al. (2018) pointed out multiple features that contribute to the enhancement of tropical–extratropical interactions and moisture surpluses. They include a presence of a mid- to upper-level cyclonic trough over the Red Sea that penetrates southward, the presence of an area of upper-level positive anomaly of potential vorticity cut-off north of Ethiopia and an elongated area of anomalous upper-level divergence across the Horn of Africa. As a seasonal link, Bekele-Biratu et al. (2018) have shown a relationship to negative phases of the North-Atlantic Oscillation (NAO). The latter is associated with a southerly position of the midlatitude jet stream over the Mediterranean Sea (Hurrell et al., 2013).
Over southern Africa, tropical-extratropical interactions are known to account for a significant proportion of seasonal rainfall. The region around southern Africa and the southwestern Indian Ocean is one of three known preferred locations for this kind of interactions in the southern hemisphere. This "hotspot" is referred as the South-Indian Convergence Zone (SICZ) but, unlike its counterparts in the Atlantic and Pacific, persists only during the austral summer months (Cook, 2000; Hart et al., 2018). During so-called tropical-temperate trough (TTTs) events, northwest–southeast oriented migratory bands of clouds and rain on the leading edge of upper-tropospheric waves link tropical convection with transients in the southern midlatitudes (e.g. Todd and Washington, 1999; Macron et al., 2014). Midlatitude Rossby waves seem to be a necessary condition for TTT development, but only 41% of the Rossby waves occurring in austral summer are associated with a convective activity link between the tropics and the midlatitudes (Macron et al., 2014). Besides of a sufficient strength and extension of the Rossby waves towards the lower latitudes, strong positive moist static energy anomalies and lower-tropospheric instability off the South African east coast provide latent heat to initiate a TTT approximately two days prior to its development. Developments of TTTs also coincide with moisture convergence over southern Africa, due to a intense Angola Low that links westerly moisture fluxes from the Atlantic basin toward southern Africa and easterly fluxes from the nearby Indian Ocean and Mozambique Channel. Fluxes are then forced to deviate southward, hereby causing the poleward transport of momentum (Todd and Washington, 1999; Fauchereau et al., 2009; Macron et al., 2014). A warm southwestern Indian Ocean due to e.g. positive

Subtropical SST dipole events (Behera and Yamagata, 2001) or La Niña conditions, provides favorable conditions for such latent heat anomalies (e.g. Fauchereau et al., 2009; Manhique et al., 2011). Hart et al. (2018) found that La Niña events are also associated with a higher probability of the occurrence of the subtropical jet near southern Africa compared to El Niño conditions.
Depending on the location of the SICZ, Tanzania can be affected by opposed rainfall conditions related to the occurrence of TTTs. North-east of a TTT, dry conditions prevail, since anti-cyclonic flow transports cold air masses from the subtropics towards the Angola Low region (Fauchereau et al., 2009; Manhique et al., 2011). An eastward shift of the system can lead to enhanced convection over southern Tanzania (c.f. cluster 7 in Fauchereau et al., 2009).

2.4 Interannual Variability and Trends of the Rainy Seasons

In the previous sections, the general circulation of the tropics and the regional climatic conditions over the GHA were introduced. Furthermore, the main global modes of rainfall variability, which affect the GHA, were reviewed. In the following section, the main four rainy seasons are discussed with the focus of their interannual variability, recent trends and how each of the rainy seasons responds to the global modes.

2.4.1 Long Rains

The Long Rains in MAM correspond to the period when the TRB crosses the equator during its migration from the southern into the northern hemisphere. There is a northern protrusion of the Long Rains into southeastern Ethiopia, where they are known as "Belg" often starting already in February (e.g. Camberlin and Philippon, 2002; Bekele-Biratu et al., 2018, Figure 2.2b). Compared to the Short Rains (section 2.4.2), this rainy season accounts for the higher proportion of the total annual rainfall and posseses a high reliability, making it the major agricultural season in East Africa (e.g. Camberlin and Okoola, 2003; Wainwright et al., 2019). However, the Long Rains show a weak spatiotemporal coherence, which also varies from month to month (Camberlin and Philippon, 2002; Zorita and Tilya, 2002; Nicholson, 2017). This may result from multiple 'jumps' that are characteristic for the northward migration of the TRB over eastern Africa (Riddle and Cook, 2008; Riddle and Wilks, 2013). Both studies highlight that these jumps are connected with different stages in the development of the Somali Jet (c.f. section 2.1). Riddle and Cook (2008) showed that early stages of the Somali Jet (referred to as 'nascent') coincide with heavy rainfall over Ethiopia in April. This corresponds to the earliest two stages of the Somali Jet in section 2.1.
The major challenge regarding the Long Rains has been to understand its interannual variability and predictability, since no strong relationships to any large-scale modes of atmospheric or oceanic forcing could be identified (Hastenrath et al., 1993; Camberlin and Philippon, 2002; Liebmann et al., 2014; Nicholson, 2017). Particularly in March and April, several studies agree on a relationship between wet conditions and equatorial

westerly wind anomalies in the middle and lower troposphere over the Congo Basin (e.g. Okoola, 1999; Mutai and Ward, 2000; Zorita and Tilya, 2002; Finney et al., 2019). Westerlies are known to contribute to low-level convergence and less stability in the atmosphere over the GHA. Finney et al. (2019) attribute the westerlies to the passage of the MJO through eastern Africa and tropical cyclones in the western Indian Ocean. A relationship with the occurrence of tropical cyclones in the southwest Indian Ocean and deficient Ethiopian Belg Rains was also found at both interannual and intraseasonal timescales by Shanko and Camberlin (1998). Camberlin and Okoola (2003) have shown that a late start of the season was associated with positive SST and negative sea-level pressure anomalies over the southern Atlantic Ocean, while the reverse conditions and large-scale descend occur over the western Indian Ocean. This Walker-like circulation results in anomalous easterlies and divergence over East Africa preventing the meridional branch of the TRB of moving eastwards and favoring westerly winds. Towards the end of the Long Rains (May), positive correlations between inland Kenya and Uganda rainfall and low sea-level pressure and reduced divergence over the equatorial Indian Ocean are found, which are linked to the dynamics of the Indian monsoon (Camberlin and Philippon, 2002). Indeje et al. (2000) documented a relationship with the stratospheric quasi-biennial oscillation (QBO). Due to the diverse correlations and their non-stationarity, many studies recommended to analyze each month of the Long Rains separately (Camberlin and Philippon, 2002; Nicholson, 2017).

In the northern part of the GHA, tropical-extratropical interactions modify rainfall. Camberlin and Philippon (2002) and Bekele-Biratu et al. (2018) found interactions with anomalous ridge-trough patterns in the upper- and mid-troposphere. In this context, Bekele-Biratu et al. (2018) highlighted that the negative phase of the North-Atlantic Oscillation (NAO) favors the formation of such ridge-trough patterns in the lower latitudes, while the opposed phase leads to widespread dry conditions in northern parts of Ethiopia and Eritrea.

The effect of the MJO on the Long Rains is the only relationship, which is documented as robust and valid for the whole season (e.g. Pohl and Camberlin, 2006a,b; Berhane and Zaitchik, 2014; Nicholson, 2017; Bekele-Biratu et al., 2018; Finney et al., 2019). It should be noted that wet conditions predominately occur in the first half of the MJO cycle along the coast and in the second half of the MJO cycle in the highlands (Hogan et al., 2015). Pohl and Camberlin (2006b) demonstrated that the contrasting rainfall conditions in the two regions for the opposite MJO phases strongly correlate with the pressure gradient between the Indian and Atlantic Oceans. Pohl and Camberlin (2006a) also noted that the enhanced convection over East Africa lags several days the passage of the MJO convective core. In addition, synoptic-scale mechanisms modify convection over East Africa (Zaitchik, 2017). Many studies analyzed the relationship between the Long Rains and ENSO, but they have led to contradictory results. Works of Ogallo (1988); Hastenrath et al. (1993); Phillips and McIntyre (2000), based on different temporal and spatial scales, did not show any significant correlations between the Long Rains and either the atmospheric or oceanic components of ENSO. Nicholson (1996); Nicholson and Kim (1997) and Indeje et al. (2000) indicate that the relationship between Niño-3 SST and rainfall shifts: weak positive rainfall anomalies are found on the onset year of El Niño conditions, while more pronounced negative anomalies develop in the years after El Niño events. Moreover, Mutai and Ward (2000) emphasize that, whereas the March–April Southern Oscillation index (SOI) shows no

teleconnection signal in East Africa, in May some relationship between the convection anomalies and SOI can be observed. The authors also argue, that the relationship is established through modifications of SSTs and the Walker Circulation over the Indian Ocean. Preethi et al. (2015) emphasize that different modes of ENSO show partly opposing correlations with rainfall over GHA, and particularly the El Niño Modoki events induce significant enhancement in rainfall in the western GHA, namely western Kenya, Uganda, Rwanda and northwestern Tanzania.

The atmospheric teleconnections and dynamics of the Long Rains moved into the focus of research due to a downward trend of seasonal rainfall amounts and increased frequency of drought in the recent decades (Funk et al., 2008; Williams and Funk, 2011). Analysis of Lyon and DeWitt (2012) further concluded that the decline started abruptly around 1999. They also suggested that the decline is primarily forced by large-scale pattern of SST anomalies located in the equatorial Pacific Ocean, which is not explained by variability of ENSO. Their findings are in accordance with a diabatic cooling anomaly over the Indian Summer Monsoon and northern East Asian Summer Monsoon regions after the El Niño event 1997/1998 reported by Yun et al. (2010). Similarly, Vigaud et al. (2017) suggest that a more frequent dry regime in May since 1998/1999, associated with an earlier onset of the Indian summer monsoon and Somali jet, could account for a recent abrupt shift observed in GHA Long Rains. Further studies indicate that the decline in GHA Long Rains is associated with an increased SST gradient between the the western and eastern tropical Pacific (Lyon and DeWitt, 2012; Lyon, 2014a; Lyon et al., 2014b; Yang et al., 2014; Vigaud et al., 2017; Ummenhofer et al., 2018). This gradient leads to a a westward shift of the Walker circulation and a subsidence anomaly and drying over East Africa (Williams and Funk, 2011; Funk et al., 2014; Liebmann et al., 2014; Hoell et al., 2017). On the other hand, several studies argue that the observed drying can only be partly explained by SSTs (Liebmann et al., 2014; Hoell et al., 2017; Hua et al., 2018). Also, there is limited evidence for the Indian Ocean Walker Cell extending over the Horn of Africa, and an equatorial zonal circulation cell is not present in boreal spring (Liebmann et al., 2014, 2017). Camberlin and Philippon (2002) and Vellinga and Milton (2018) could not identify a large-scale Walker Cell over the Indian Ocean during the Long Rains. Instead, results of Vellinga and Milton (2018) and Wainwright et al. (2019) reveal a positive correlation between abundant Long Rains and the SST anomalies in the Arabian Sea, whereas a pole of negative SSTs in the eastern Indian Ocean could not be identified. Recently, Wainwright et al. (2019) proposed an alternative explanation for the decline of the Long Rains: they emphasize that the Long Rains decline is mainly attributed to a general shortening of the rainy season with a later onset and an earlier cessation rather than a decrease in the peak daily rainfall. The shortening is attributed to a faster movement of the TRB over Eastern Africa during the Long Rains and is a consequence of a stronger interhemispheric SST contrast in the western Indian Ocean during the whole January–August period. Wainwright et al. (2019) argue that enhanced warming of the deserts in the northern hemisphere and the associated earlier deepening of the Arabian Heat Low leads to an increased pressure gradient and hence to more rapid migration of the TRB. The month April, as the peak of the Long Rains, will be analyzed in more detail in chapter 4.

2.4.2 Short Rains

The Short Rains in OND correspond to the period when the TRB crosses the equator during its migration from the northern into the southern hemisphere. Compared to the Long Rains, the Short Rains show a larger degree of interannual variability, are less reliable (Hastenrath et al., 1993; Black et al., 2003) and have a larger impact on the society through changes in the regional hydrological cycle (Behera et al., 2005). They account for a large proportion to the annual rainfall amounts only in eastern equatorial latitudes (Nicholson, 1996). Indeed, crop failure in the Short Rains occurs as often as once every 3yr (e.g., Hutchinson 1992). The Short Rains reveal different regional circulation patterns compared to the Long Rains. Camberlin and Wairoto (1997) found a contrast between eastern and western parts of East Africa. While in the western parts rainfall is associated with westerly flow and moisture convergence, which is comparable to the Long Rains, easterly wind anomalies lead to rainfall in the eastern parts. This rainfall pattern resembles the MJO associations, which Pohl and Camberlin (2006a) also found for the Short Rains.
Studies generally agree on a relationship between the Short Rains, ENSO and IOD (e.g. Nicholson, 1996; Goddard and Graham, 1999; Indeje et al., 2000; Black et al., 2003; Liebmann et al., 2014; Lyon, 2014a; Lyon et al., 2014b). Positive IOD events are correlated with abundant rainfall over equatorial East Africa, while negative IOD events lead to drought conditions. The link is primarily established through a zonal shift of the Walker circulation over the Pacific and Indian Oceans. However, ENSO and IOD show an intercorrelation as well as individual modes of interannual variability. Statistical studies find a strong connection between ENSO and East African rainfall (e.g. Ropelewski and Halpert, 1987; Nicholson and Kim, 1997; Nicholson, 2017). Contrarily, atmospheric general circulation models suggest that the Indian Ocean SSTs exert a greater influence on the East African Short Rains than the Pacific SSTs (Goddard and Graham, 1999; Latif et al., 1999). Black et al. (2003) point out that only extreme positive IOD events lead to enhanced Short Rains. The major requirement is a reversal of the latitudinal SST gradient over the Indian Ocean, which leads to a persistent change in the Walker circulation. This reversal can be reached through a strong El Niño event, but other triggers should also be considered: for example, the positive IOD event in 1961 occurred without ENSO forcing. Thus, the question whether the Pacific or the Indian Ocean affects the East African Short Rains remains not fully solved. In addition, Preethi et al. (2015) emphasize opposed effects of El Niño Modoki compared to canonical ENSO events on the Short Rains. Preethi et al. (2015) and Bahaga et al. (2019) also argue that a co-occuring IOD events can enhance or reduce contrasting influence of the ENSO event on the Short Rains. Bahaga et al. (2019) also identified several change points in the decadal intercorrelation between ENSO and IOD with the last occurring during the 1980s. The authors interpret this change with the phase shift of the Pacific Decadal Oscillation and Interdecadal Pacific Oscillation. On the other side, Manatsa et al. (2016) link major long-term shifts in Short Rains to decadal shifts in the Southern Annular Mode (SAM). Their results emphasize that SAM modifies the circulation over the Indian Ocean through the strength and position of the Mascarene High, which is part of the subtropical high pressure belt, while the correlation to ENSO is less significant. However, unlike the Short Sains, the SAM exhibits a continuous rising trend since the early twentieth

century (Nicholson, 2017).
In contrast to the Long Rains and despite of several droughts, rainfall during the Short Rains reveal a positive trend in the recent decades (e.g. Liebmann et al., 2014; Schmocker et al., 2016; Nicholson, 2017). In particular, rainfall amounts over the eastern equatorial parts of the region have increased. Several studies ascribe this increase to a warming of the western Indian Ocean, which in turn weakened the atmospheric Walker circulation cell (e.g. Tierney et al., 2013; Liebmann et al., 2014; Nicholson, 2017).

2.4.3 Kiremt Rains

The solstitial rainy season of the boreal summer corresponds to the Kiremt Rains from June to September. This is the primary agricultural season in northern and western parts of Ethiopia, Sudan but also parts of South Sudan, western Kenya, and northern Uganda (Nicholson, 2017). Particularly the Ethiopian Highlands have a high impact on the regional rainfall distribution (Diro et al., 2011). Traditionally, it was assumed that these rains are related to the rainy season of the Sahel region and airflow from the Congo Basin and the Atlantic (Nicholson, 2017). However, a detailed analysis of moisture fluxes by Viste and Sorteberg (2013) has shown that the majority of released moisture in northern Ethiopia is related to the Red Sea and the Indian Ocean. Moisture from the latter source is able to reach Ethiopia via different pathways including the Congo Basin, the Turkana Channel and the Gulf of Aden.
Unlike for the Short Rains, El Niño events show associations with drought occurrence during the Kiremt season, while La Niña events tend to enhance rainfall (Seleshi and Zanke, 2004; Korecha and Barnston, 2007; Segele et al., 2009). Similar as for the Short Rains, the role of the SSTs in the Indian Ocean remains unclear. Korecha and Barnston (2007) showed that ENSO and Atlantic SSTs are the main modulators of the Kiremt Rains, while the effect of the Indian Ocean is less important. They argue that ENSO affects the northward-protruding meridional arm of TRB associated with rainfall in central and northern Ethiopia, depending on cross-equatorial northward flow of moist air. Bahaga et al. (2019) analyzed interannual to decadal teleconnections influencing the Kiremt Rains. They found that ENSO affects the Kiremt Rains mainly at timescales of below eight years in the recent decades. This relationship is particularly enhanced, when El Niño events coincide during warm phases of Interdecadal Pacific Oscillation. In addition, they identified a non-stationary relationship of the Kiremt Rains to the SSTs at the Guinea coast. This correlation changed from significantly negative to positive after in the 1960s, which coincides with a regime change of the West African monsoon in 1968 (e.g., Diatta and Fink, 2014; Nicholson, 2018).
Depending on the time period and observational data considered, various trends were documented for the Kiremt season. Rainfall during this rainy season decreased since the 1950s with a minimum in the 1980s, but a slight increase since the 1990s (Williams et al., 2012; Nicholson, 2017). Still, strong regional differences persist. Over the period 1965-2002, Seleshi and Zanke (2004) found particularly decreasing trends in Kiremt rainfall only for eastern and southern stations, while for stations in central, western and northwestern parts of Ethiopia no significant trends could be detected. For their study of trends in erosivity over GHA, Fenta et al. (2017) calculated rainfall trends of the Climate Hazards InfraRed Precipitation with Stations

(CHIRPS) satellite product for the period 1981-2016 and found increasing trends in parts of Sudan and northern Ethiopia. Similar results were obtained by Maidment et al. (2015) for the period 1983-2010 for three other satellite products. These patterns partly go along with positive vegetation trends in the Sahel (Herrmann et al., 2005). However, the evaluation of three satellite products by Cattani et al. (2018) in terms of trends of ETCCDI rainfall indices (Expert Team on Climate Change Detection and Indices; Alexander et al., 2006; Zhang et al., 2011) of Kiremt Rains for the period 1983-2015 found diverse and partly contradicting signals among the satellite products. Still, some significant signals towards a wettening over Uganda, South Sudan, and western Ethiopia could be identified. For Sudan, Elagib and Elhag (2011) emphasize that drought conditions in northern and central parts of Sudan still prevail, since rainfall there is less effective due to increasing temperatures and evaporation.

2.4.4 Msimu Rains

Less attention has been devoted to the boreal winter rainy season in Tanzania locally known as "Msimu Rains" (e.g. Herrmann and Mohr, 2011). These rains with their peaks from December to March are important for the southern and western parts of Tanzania. These rains show a decreasing trend over most parts of Tanzania and particularly over the lowlands in the south (Maidment et al., 2015; Fenta et al., 2017; Harrison et al., 2019). In contrast, rainfall amounts increase in southern and south-central Africa (Maidment et al., 2015), suggesting a shift of the seasonal circulation to the south-west. Shongwe et al. (2009) and Dunning et al. (2018) indicated that this decreasing trend might arise due to a late onset and/or earlier cessation of the rainy season. Dunning et al. (2018) interpreted this tendency as a response to the deepening of the Saharan Heat Low and the Angola Low.
In terms of atmospheric dynamics, the Msimu rains are part of the southern African solstitial rainy season. Therefore, the circulation consists of three main air streams: westerly moisture fluxes from the southeast Atlantic, humid north-easterlies from the northwestern Indian Ocean and temperate south-easterlies from the southern Mozambique Channel. On the synoptic scale, the interactions and convergence between these air streams is tightly connected to the variability of the Angola Low, TTTs and SST signals in the southern hemisphere. The above-mentioned enhanced westerly flow extends northward to the Congo Basin and can push the meridional branch of the TRB eastward into the southern GHA region. In connection with a passing upper-level wave from the mid-latitudes, the Angola Low can intensify and trigger the formation of TTTs (Todd and Washington, 1999). TTTs act as an important source of rainfall for southern Africa (Todd and Washington, 1999; Fauchereau et al., 2009). Depending on the position of the trough, convection over Tanzania can be suppressed (Manhique et al., 2011).
Various studies focused on the effect of ENSO on the latter features of the austral summer rainy season. Similar to the Short Rains, El Niño conditions increase rainfall over Tanzania, while La Niña is associated with droughts. This signal is opposed to the effect on the southern parts of Africa, where La Niña years are associated with above-average rainfall due to modulations of the SICZ (Manhique et al., 2011). Moreover, Harrison et al. (2019) found strong correlations between drought conditions

in southern Tanzania during the December-February season and La Niña-like conditions in the equatorial Pacific at interannual and decadal time scales. The authors explain this teleconnection by shifts in the tropical Walker circulations and modulations of the Rossby wave train in the southern hemisphere extra-tropics. However, the interactions between the Angola Low, TTTs and ENSO-like circulations on rainfall variability over southern Africa are not straight-forward and various other interactions and internal modes of variability can counteract the signals.

3 Data

A challenging aspect in studies on climate variability over the GHA is the lack of high-quality and high-density observational records. The gauge density in the region is low and in particular continuous long-term rainfall timeseries are rare. Ground-based measurement stations usually provide long-term rainfall time series, but the station network is sparse and uncoordinated. Although surface measurements are often referred as the "truth", they are point measurements and represent only a limited area. Particularly, tropical Africa has exhibited a substantial loss of rain gauges over the past several decades, with strongest decrease being observed across central equatorial Africa, which has lost over 90% of its gauges since the early 1980s (Washington et al., 2013; Diem et al., 2019). The density of available stations also depends on the country. While the gauge density in Ethiopia is relatively high (Dinku et al., 2014), the Democratic Republic of Congo (DR Congo), which is more than twice as large as Ethiopia and the second-largest country of the African continent, has just a few gauges (Washington et al., 2013). Another source of biases are (undocumented) changes of the station location and instruments as well as their maintenance that might lead to data gaps and inhomogeneity of the rainfall time series (e.g. Tsidu, 2012).
In the last decades, satellite estimates partly improved the situation, but the performance of their algorithms often depends on the availability of dense ground-based networks of rainfall measurements for calibration and validation. The performance of satellite algorithms varies depending on the respective product, region and rainfall type. Hirpa et al. (2010), Thiemig et al. (2012) and Cattani et al. (2016) provided evidence that satellite products, which considered station data for bias-correction, tend to outperform those products which did not. For western Uganda, Diem et al. (2019) could show that without adjustments of station data, satellite products can erroneously suggest dry-biased multi-decadal trends. The comparison of adjusted to non-adjusted trends partly even showed a reversal of trend sign for some rainy seasons. Other parts of the algorithm, like retrieval and interpolation, can also lead to large differences in accuracy of rainfall estimates depending on the regional climate and season (Nikulin et al., 2012; Sylla et al., 2013). Finally, due to stronger biases than for satellite estimates, reanalysis precipitation estimates are found to be less suitable for studying rainfall variability in Africa (Poccard et al., 2000; Maidment et al., 2013; Salih et al., 2018). Therefore, in this work reanalysis data is only used to study other variables than precipitation. Only few satellite products cover time periods of several decades at a high spatiotemporal resolution. The current chapter provides an overview on the data sets used in the following chapters.

3.1 KASS-D Observational Precipitation Database

The Karlsruhe African Surface Station - Database (KASS-D, Vogel et al. (2018)) offers an extended collection of long-term in-situ observations for the whole African continent on daily temporal resolution from various sources. In chapter 4, daily rainfall observations in the countries Ethiopia, Kenya, Rwanda, South Sudan, Sudan, Tanzania and Uganda for the time period 1983 to 2013 with a temporal data coverage of at least 75% were used. Elementary quality checks have been manually performed on the data sets. Several criteria were used to detect outliers: exceeded world record values, values with deviations of more than 200 mm to the daily rainfall distribution and values beyond nine times the 99th percentile were removed. The locations of the stations are displayed in Figure 4.1. A detailed list of the stations can be found in the supplementary material (Table S1).

3.2 CHIRPS

Only few satellite products combine decadal-long time series with a high spatio-temporal resolution. The Climate Hazards Group InfraRed Precipitation with Stations (CHIRPS, Funk et al., 2015a) data set utilizes both high-resolution satellite imagery and in-situ station data, and provides more than 30 years of daily rainfall estimates spanning the globe between 50° S and 50° N at 0.05 latitude-longitude resolution. This work uses version 2.0 with a 0.25 x 0.25 latitude-longitude resolution. The main disadvantage is the lack of coverage over the oceans. CHIRPS can be seen as a product of an underlying static rainfall climatology (CHPclim, Funk et al., 2015b) with several correcting factors (Figure 3.1). The underlying climatology contains input from historical station precipitation averages, historical thermal infrared satellite estimation averages and a global topographic grid.
In the first step of the CHIRPS algorithm, the pentad estimates based on thermal infrared temperatures are corrected through local regression between cold cloud top duration and Tropical Rainfall Measuring Mission (TRMM) 3B42 precipitation (Huffman et al., 2007). Missing satellite values are filled in using model forecasts from National Oceanic and Atmospheric Administration (NOAA) Climate Forecast System, version 2 (CFSv2; Saha et al., 2010). The infrared precipitation estimates are standardized with their long-term means over the period 1981–2012. In the second step, the product of the infrared estimates and CHPclim is bias-corrected using daily gauge observations. The incorporation of station data can improve the rainfall estimates in complex topographic regions, as the estimation of orographic rainfall is a substantial challenge for many satellite products (Diem et al., 2014b). Orographic rainfall often consists of so-called "warm rain", which means that the rain clouds do not build an iced cloud top. These clouds are not sufficiently captured by infrared sensors, which leads to underestimations of rainfall in high-altitude areas (Dinku et al., 2007, 2008). CHIRPS performed well in Ethiopia (Bayissa et al., 2017), Mozambique (Toté et al., 2015), Kenya (Kimani et al., 2017) and western Uganda (Diem et al., 2019). Toté et al. (2015) and Kimani et al. (2017) indicate that the station correction procedure in CHIRPS generally improves the overall rainfall estimate. CHIRPS shows a better estimation for annual rainfall totals and higher spatial differentiation of

rainfall Toté et al. (2015). Diem et al. (2019) emphasize that CHIRPS was the least biased and most accurate product in their study, which presumably resulted from the additional bias-correction with rain-gauge data. Kimani et al. (2017) demonstrated that CHIRPS performs better than other products in regions with multiple rainfall types. Both studies, Toté et al. (2015) and Kimani et al. (2017) detected a positive bias of CHIRPS in low rainfall events and rainy days.
Still, this approach can also lead to potential accuracy variations depending on the amount of available measurement sites. In case of CHIRPS, the blending procedure does not intend to tune the rainfall amount at the grid point towards the observational value or to reproduce the point observations exactly. Instead, the station data is an additional weighting factor, which contributes to the correction of CHPclim at a particular grid point for a specific time period. The CHIRPS product is used in chapter 4 for the time period 1981–2013 and in chapter 5 for the time period 1981–2018.

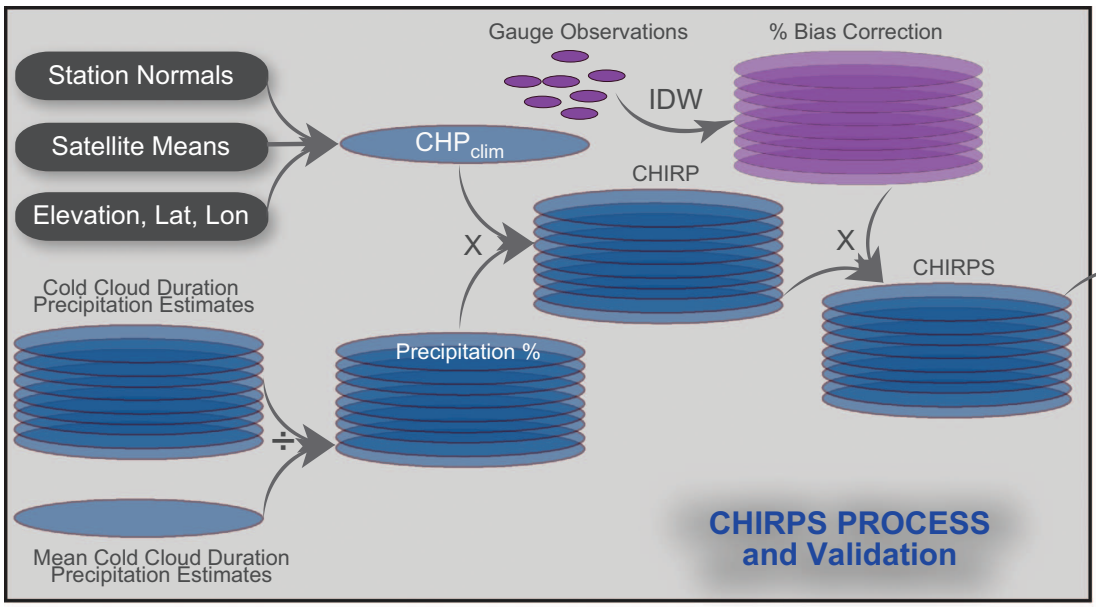

Figure 3.1: Graphical overview of the CHIRPS processing and validation algorithm. Blue components indicate estimation process, while purple components denote the bias correction. source: Funk et al. (2014)

3.3 ERA5-reanalysis

Large-scale atmospheric fields, including wind components and geopotential at different pressure levels, SSTs and vertically integrated water vapour flux and its divergence, were obtained from the fifth-generation European Centre for Medium-Range Weather Forecasts (ECMWF) reanalysis (ERA5). Compared to its predecessor ERA-Interim (Dee et al., 2011), ERA5 offers a higher spatio-temporal resolution and an improvement of the atmospheric model and data assimilation processes (Copernicus Climate Change Service (C3S), 2017). For chapter 5, the time period from 1981 to 2018 is used.

4 Mapping of rainfall seasonality and rainy seasons

The following chapter covers step 1 described in section 1.1, which encompasses the development of an objective definition of rainy seasons. This definition is applied for mapping the regional rainfall seasonality and the estimation of trends of rainfall totals as well as trends of onset, cessation and length of the rainy seasons. This chapter reuses material published in the International Journal of Climatology: Seregina et al. (2019).

4.1 Overview on commonly used rainy season criteria

Rainy seasons in the tropics are tightly connected to the seasonal migration of the TRB and associated convective processes. Depending to the location relative to the equator and the complex interplay of local factors (e.g. orography, water bodies and extensive coastal lowlands), regional circulation (e.g., the Somali and Turkana Jet) and remote forcings such as the Walker circulations and the IOD, parts of the GHA can experience one or more rainy seasons. In the near-equatorial subregion, the complex interplay of these different factors leads to a mostly bimodal rainfall distribution, with rainy seasons in boreal spring and autumn (e.g., Nicholson, 1996). In the northern and southern parts of the GHA, both seasons merge into one in boreal summer and winter, respectively. Generally, full-month periods are used to define rainy seasons. For example, the rainfall amount and corresponding long-term trends of the spring (autumn) rains are estimated using MAM (OND) totals (e.g., Maidment et al., 2015). An overview of the rainy seasons on national scale, including their local names, can be found in Table 4.1.

Table 4.1: Overview of national calendric rainy season periods.

Country	Rainy seasons	Local names	Remarks	Reference (e.g.)
Sudan	June - Sept./Oct.	—	—	Osman and Shamseldin (2002), Salih et al. (2018)
South Sudan	Apr. - Nov.	—	—	Osman and Hastenrath (1969), Osman and Shamseldin (2002)
Ethiopia	MAM JJAS	Belg Kiremt	Relevance of the seasons varies regionally	Segele and Lamb (2005) Bekele-Biratu et al. (2018)
Somalia	AM JAS ON	Gu Karan Deyr	 Northern parts Southern parts	Herrmann and Mohr (2011)
Kenya, Uganda	MAM OND	Long Rains Short Rains	Northern Uganda: unimodal	Phillips and McIntyre (2000) Camberlin and Philippon (2002)
Tanzania	MAM OND Oct./Nov. - Apr.	Masika Vuli Msimu	Northern parts: bimodal Southern and western parts: unimodal	Zorita and Tilya (2002) Camberlin and Philippon (2002)

However, a such calendric approaches neglect regional differences in the rainy seasons and/or they are only valid on national scale. In addition, calendric approaches neglect regional differences in the rainy seasons, particularly in regions where the rainfall seasonality transforms from a single-season regime into a dual-season regime and vice versa. Herrmann and Mohr (2011) visualized the complex patterns of rainfall seasonality over the GHA from gridded rainfall and land surface temperature products, where they also distinguished between dual-season regimes and regimes of single rainy seasons with multiple seasonal maxima. Thus, a flexible definition of rainy seasons, which also depicts these patterns of rainfall seasonality, would be desirable.

Various flexible rainfall onset criteria have been used to define rainy seasons in tropical monsoon regimes. Fitzpatrick et al. (2015) and Bombardi et al. (2019) categorized several criteria for monsoon detection in regional and local definitions. Regional definitions focus on the seasonal variation of large-scale dynamics and changes in atmospheric parameters on supranational scales. Such approaches tend to be constructed as monsoon indices, which transform characteristic regional-to-large-scale features of the monsoon circulation into a single time series (i.e. index) that reflects the large-scale development of the monsoon system (Bombardi et al., 2019). Such indices can be based on precipitation datasets, either from gauge measurements or satellite estimates, while others use outgoing long-wave radiation (Fontaine and Louvet, 2006; Garcia and Kayano, 2009), moist static energy (Vellinga et al., 2013), or a combination of mean sea level pressure and 850-hPa zonal wind data (Nguyen et al., 2011). In contrast, local onset definitions use data of single gauges or grid points without additional spatial information. Most of them are defined for specific local agronomic needs and use absolute thresholds of precipitation, which have to be reached or exceeded for a specific time period (e.g. Stern et al., 1982; Marteau et al., 2009; Yamada et al., 2013). However, absolute thresholds need to be adapted for different regions and sources of rainfall data to account for biases.

The variety of local climates in the GHA complicates the usage of agronomic onset definitions due to the topography but also due to loose links to both the West African and the Indian Monsoon systems (Nicholson, 2017). Moreover, the region is

inhomogeneous and seasonal rainfall amounts vary by several hundreds of mm m^{-2}. These variations complicate the usage of local onset definitions. The loose links to both the West African and the Indian Monsoon systems (Nicholson, 2017) and diverse local atmospheric circulation systems also complicate the use of regional onset definitions.

One solution by Liebmann and Marengo (2001) developed for South America uses accumulated daily rainfall anomalies to determine the onset of the rainy season. The onset and retreat are defined as the date of maximum accumulated rainfall deficit and excess in relation to the climatological daily mean rainfall, respectively. Liebmann et al. (2012) applied this criterion on various gridded products for the African continent. Although this method was also originally defined for unimodal rainfall distributions, Dunning et al. (2016) successfully adapted it for biannual rainfall regions by smoothing and splitting the time series between the climatological rainy seasons. This application is straight-forward and does not require fixed thresholds. However, it requires the a priori determination of the modality of the rainfall climate. Therefor it can only be used for past rainy seasons, and is thus limited in terms of operational use. Further requirements are complete datasets without gaps, since the latter can alter the seasonal and annual rainfall accumulations. In addition, limitations may occur during a given very poor or short rainy season, when almost all precipitation is below the long-term mean (Dunning et al., 2016).

Another approach to overcome these shortcomings is to standardize the input data. Wang and LinHo (2002) developed an onset criterion based on local timeseries of precipitation while retaining suitability for large regions. In their approach, the difference between the pentad (i.e. 5-day) rainfall average and the average of the climatologically driest month in a specific year has to exceed 5 mm to mark the start of the rainy season. To mark the end of the rainy season, the difference between the pentad rainfall average and the average of the climatologically driest month needs to fall below 5 mm. The threshold value was chosen to yield meaningful results for the monsoon region in East Asia. For West Africa, Sanogo et al. (2015) adapted the threshold to 2.4 mm in order to obtain results comparable to a local criterion. Still, this onset criterion is optimized for monsoon regions with a unimodal rainfall peak and less suitable for a bimodal rainfall distribution.

In the present chapter, a novel and flexible rainy season approach is introduced and applied to an extensive station data sample from KASS-D (Figure 4.1) and to CHIRPS, representing a gridded rainfall product. This criterion does not depend on total rainfall or seasonality of the rains and is applicable in near-real time. This approach was motivated for applications in climate, but not in an agronomic context. Using this new definition, trends and variability of rainfall for the GHA are reassessed. A second objective is to compare the rainy season definition between station and grid point data sets. In section 4.2, the rainy season definition is described and tested on three representative stations (red stars in Figure 4.1). Each of these stations was chosen to represent a common seasonality over the GHA. Regional peculiarities modifying the rainy seasons are additionally discussed. The following sections 4.3 and 4.4 present the results for different rainfall characteristics, including the rainfall seasonality, the onset and cessation of the rainy seasons. Sections 4.5 and 4.6 show applications on trends season rainfall totals and onset and cessation dates, respectively. A summary

and discussion of this chapter follows in section 4.7.

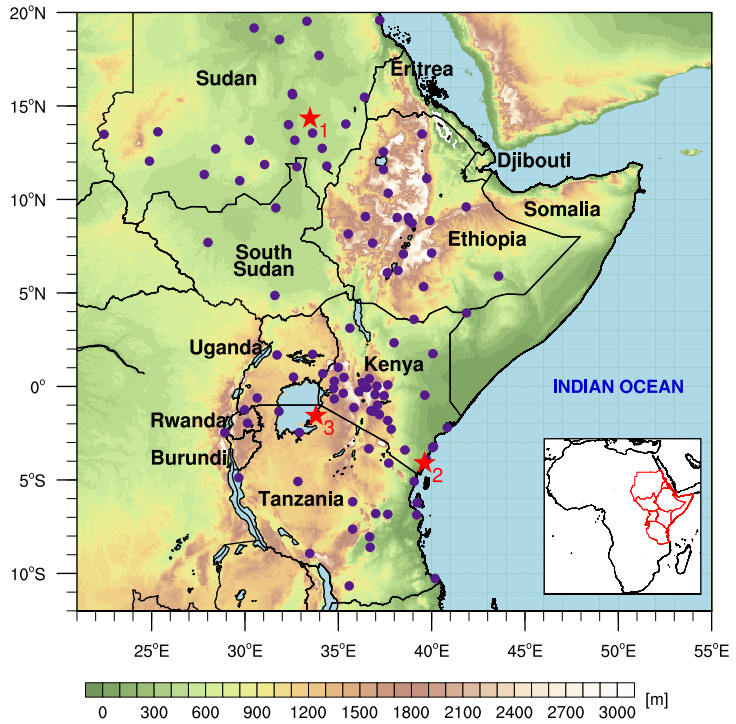

Figure 4.1: Area of investigation. Available KASS-D stations are marked by purple dots. The red stars and numbers indicate three exemplary stations (see section 4.2). The inset shows the geographic location of the area on the African continent. A complete list of the stations can be found in the Appendix, Table S1. © The authors and John Wiley & Sons Ltd, CC-BY.

4.2 Definition of the rainy season

The onset criterion of the rainy season used herein is based on the criterion proposed by Wang and LinHo (2002) for the monsoon region of Asia. Their approach used 5-days (pentad) averages of daily rainfall, which were standardized by the daily average of the climatologically driest month. In order to reduce the time series to the seasonal cycle, they truncated a Fourier series and kept only the first 12 Fourier harmonics for every single year. Finally, based on the inter-comparison of different climates in the Asian monsoon region, they defined a universal rainfall rate of 5 mm/day as a threshold for the monsoon onset. The start of the monsoon season in Asia is defined as the first pentad when the standardized pentad average of rainfall exceeds the threshold. Vice versa, the monsoon season ends when the standardized pentad average falls below this threshold. The method can be considered as a local onset definition since only the rainfall at the specific grid point or station is used. However, due to the standardization, the method can still be utilized on a supranational scale, thus enabling a comparison of rainy season characteristics.
For the following approach, several modifications to the onset criterion of Wang and LinHo (2002) were implemented. A low-pass Lanczos Filter (Duchon, 1979) replaced the Fourier truncation. Given that the magnitude of the 5-day rainfall rate differs

tremendously between the local rainfall climate zones at the GHA, it was a challenge to define an objective rainfall threshold, which is valid for every location in the region. While the threshold of Sanogo et al. (2015) of 2.4 mm/day for West Africa is valid for the humid rainfall zones in the GHA, a lower (higher) threshold needs to be determined for drier (wetter) regions. The following method defines individual thresholds for each location.

The general method consists of three steps (Figure 4.2). First, a Lanczos low-pass filter with a cut-off period of six pentads (i.e., 30 days) is applied to pentad averages of rainfall of every hydrological year of the station/grid point time series. The hydrological year needs to start in the dry season to bypass a splitting of continuous rainy seasons. A previous standardization by the monthly average of the climatologically driest month (as in Wang and LinHo, 2002) is not necessary.

In the second step, multi-year averages are computed, which are used to define a local threshold for the station/grid point. The threshold determines the onset and cessation dates and, thus, the climatological number of rainy seasons. The rainfall onset and retreat can be regarded as a point of inhomogeneity in the climatological time series. This point in the rainfall climatology is identified by using the homogeneity test of Alexandersson (1986), which results in one or multiple potential inhomogeneity points. Khaliq and Ouarda (2007) presented critical values for the test depending on different sample sizes that are used here as reference. Several cases had to be taken care of. If the test returns one critical inhomogeneity point, the rainfall value of this point is used as threshold. If the test returns multiple critical points, the lowest rainfall value is chosen. If none of the potential inhomogeneity points is critical, the nearest point to the critical value is used. A rainy season is defined as the period of at least five consecutive pentads which exceed the rainfall threshold. As mentioned above, the rainy season "regime" is thus the number of rainy seasons during one hydrological year. The onset and cessation of the rainy season are defined as the first and last pentad which exceed the rainfall threshold, respectively. Contrary to the widespread notion of uni-, bi- or trimodality of rainfall, the terms single-, dual- or triple-wet-season regimes following the terminology of Herrmann and Mohr (2011) are opted to use here. As a consequence, a single-wet-season may also be bimodal, if it contains two distinct rainfall peaks.

The uncertainty of the threshold value is estimated through a bootstrapping approach. This approach consists of creating a pool of random samples of pentad values at the change point. For every sample, the average threshold per sample is calculated. The 5^{th} and the 95^{th} percentiles of these averages set the interval of uncertainty of the threshold (grey box in Figure 4.2). These two additional thresholds are applied in the same way as the initial one to estimate the rainy seasons. These "alternative rainy seasons" may differ in terms of regime, onset and cessation dates. If the number of rainy seasons stays constant when using any of the threshold values, the regime can be considered as stable in the long term. Otherwise, the number of rainy seasons can vary depending on which threshold level is used. In such cases, the rainy season regime at the location cannot be determined unequivocally. This situation occurs when two rainy seasons repeatedly merge during wet years or one season fails during dry years. The confidence intervals of the onset and cessation of the rainy season are determined by applying the upper and lower threshold values to the climatology (orange hatching in Figure 4.2).

In the third step, rainfall onset and cessation dates for single years are determined. With

this aim, the climatological threshold and its confidence intervals were applied to the Lanczos-filtered pentad time series of the hydrological year of interest. All consecutive rainy pentads, which exceed the threshold, are grouped into blocks. Analogous to step one, the rainy seasons can be set as the first pentad of the first rainfall block that overlaps with the climatological rainy season. The cessation is set as the last pentad of the last rainfall block that overlaps with the climatological rainy season. This condition allows a rainy season to start earlier or end later than in the climatology. The uncertainty of the rainy season regime and time periods for the particular hydrological year can be determined analogously by applying the 5^{th} and the 95^{th} percentile bounds and the corresponding confidence intervals to the filtered time series.
The methodology is the same for every station and grid point. The number of rainy seasons is determined by the threshold in step two and is not assumed a priori. Isolated rainfall events or light rain from warm clouds, which are typical at the beginning or end of the season, can lead to higher uncertainties of the estimation of the rainy seasons. In such cases, the rain rates may lie between the lower and upper thresholds, leading to an uncertainty in the estimation of the rainfall onset pentad.

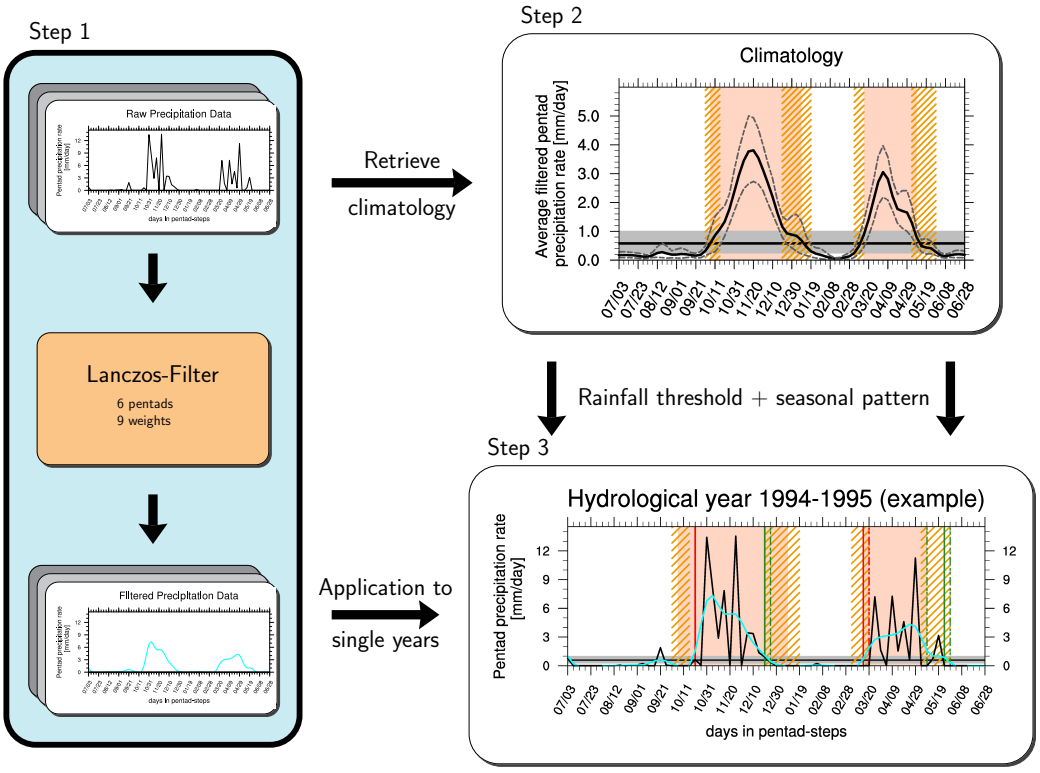

Figure 4.2: Illustration of the methodology to determine the onset of the rainy season, which consists of three steps (Section 4.2). Step 1: filtering; step 2: rainfall climatology and estimation of the rainy seasons; step 3: application to single years. A detailed explanation of the different lines is given in the caption of Figure 4.3. © The authors and John Wiley & Sons Ltd, CC-BY.

4.2.1 Representative examples

The performance of the rainy season criterion is visualized on three exemplary stations with distinct rainfall regimes (red stars in Figure 4.1). The first two examples correspond to the typical single-wet-season and dual-wet-season rainfall climatology, respectively. The third example introduces a station with an unstable rainfall regime.

Example 1: Wad Medani, Sudan The first example is the rainfall site Wad Medani, which is located at the Blue Nile in central-eastern Sudan (Figure 4.1). This regime can be characterized as a stable single-wet-season regime (Figure 4.3a) with the month January as the start of the hydrological year and the main rainy season during boreal summer. According to climatology, the period of the main rainy season can be generally expected from the end of June until the beginning of October. However, weak rainfall peaks can occur already in May and may extend the rainy season. The atmospheric mechanisms behind this early rainfall surge are not obvious. Nonetheless, rainfall events during this time period occur at several stations in the area, thus a regional atmospheric cause can be assumed (compare Figure S3a).
Two representative hydrological years illustrate the variability of the rainfall onset in Wad Medani. In 1991, no rainfall was measured in May or June (Figure 4.3b) and the rainy season onset can be sharply determined in the second pentad of July. The cessation of the rainy season in 1991 is estimated for the end of September although some weak rainfall below the rainfall thresholds occurs afterwards. In contrast, an early onset of the rainy season is detected in the year 2002 at the end of May (Figure 4.3c). The first wet period ends in mid-June and is followed by three dry pentads, until the main segment of the rainy season starts at the beginning of July. In the year 2002, the rainfall amounts in June are comparable to those of the main rainy season, thus these two rainfall periods cannot be strictly separated. Consequently, two onset dates are estimated: one at the end of May and one at the beginning of July. The interannual variability of these early rains leads to a high uncertainty in the estimation of rainfall onset dates for this station. Large uncertainties may cause false onsets in agronomic definitions.

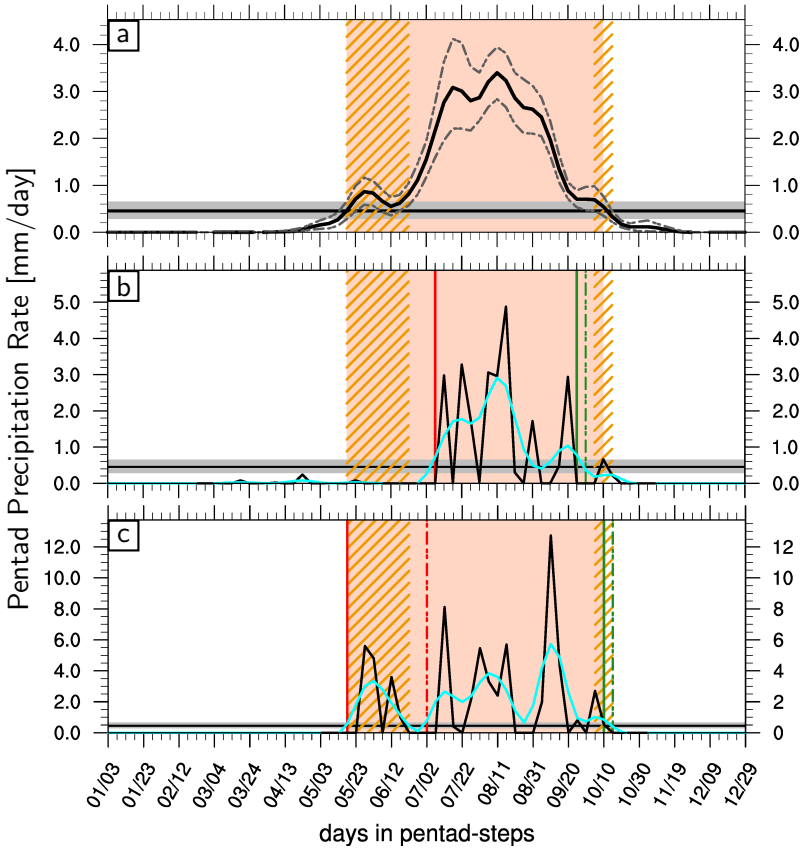

Figure 4.3: Climatology and two exemplary hydrological years for the measurement site Wad Medani, Sudan (33.5 °E, 14.4 °N, no. 1 in Figure 4.1). (a) Rainfall climatology in pentads. Hydrological years (b) 1991 and (c) 2002. Time resolution on the x-axes is pentads. The rainfall threshold, which determines the rainy season, is marked by the bold horizontal black line. The grey box denotes the confidence interval of the rainfall threshold. Orange boxes show the climatological rainy seasons including the confidence intervals (dashed orange boxes). Dashed grey lines in (a) show the 5% and 95% confidence intervals in the climatology. The onsets and cessations of the rainy season in (b) and (c) are marked by solid red and green vertical lines, respectively. The uncertainty of the onset (red) and withdrawal (green) are indicated by dashed vertical lines. For more details see text.

Example 2: Mombasa, Kenya The second example is Mombasa, which is located in the coastal region in southern Kenya (Figure 4.1). The driest month here is February, and the rainfall regime is dual-wet-season (Figure 4.4a). The regime can be considered as stable, since the rainfall rates during the dry season fall below all three threshold levels. The rainy seasons correspond to the "Long Rains" with a first rainfall peak during April/May and the "Short Rains" with a second weaker peak during October/November. However, the confidence intervals of both rainy season cessations are large due to the strong sea breeze (Camberlin and Planchon, 1997), which can (in case of the "Long Rains") extend the rainy season into boreal summer for up to a month or (in case of the "Short Rains") lead to an earlier onset of the rainy season.
The exemplary hydrological year 1999/2000 (Figure 4.4b) demonstrates the effect

of the sea breeze in combination with a dual-wet-season regime. The confidence intervals of the rainfall threshold separate each rainy season into a period of high rainfall (periods between red and first green dashed vertical lines) and a period with light rainfall events (periods between first and second dashed green lines). The former could correspond to a rainy season phase dominated by the TRB, whereas the latter could be attributed to the sea breeze related convection.

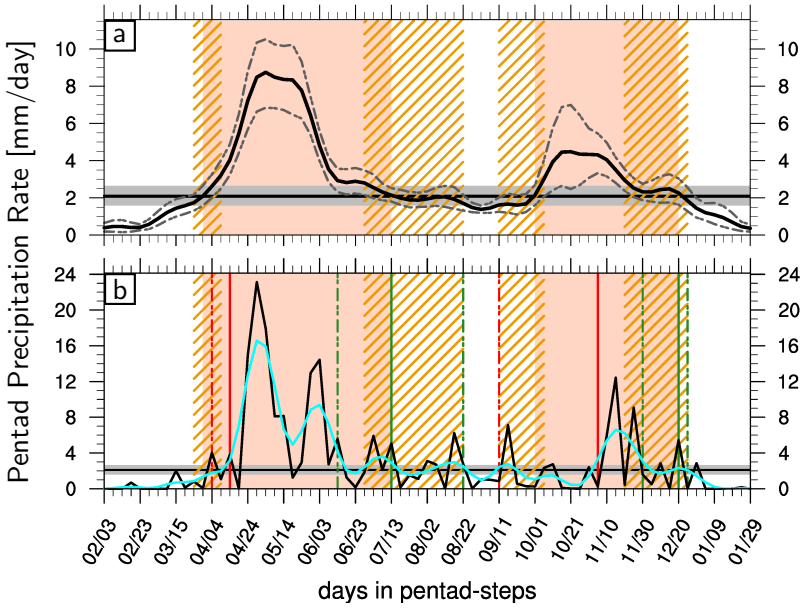

Figure 4.4: Same as in Figure 4.3, but for Mombasa, Kenya (39.6 °E, 4.0 °S, no. 2 in Figure 4.1) and for (b) hydrological year 1999/2000 in pentads. © The authors and John Wiley & Sons Ltd, CC-BY.

Example 3: Musoma, Tanzania The last example is Musoma, which is located at the shore of Lake Victoria in northern Tanzania (Figure 4.1), a humid region with an unstable rainfall regime. The rainfall climatology shows two seasonal rainfall peaks with a modest break (Figure 4.5a). The driest month of the climatology is July. The first rainy season starts at the beginning of October and usually reaches the rainfall maximum around the beginning of November. The second rainy season commences with a light rainfall peak at the beginning of February. In April, this season reaches the main peak whereas it terminates in the end of May. During the break in January, the rainfall rate in the climatology does not fall below the fifth percentile threshold, and thus depending on the threshold, the station regime can be classified as bimodal single-wet-season or dual-wet-season. The region has been classified by Herrmann and Mohr (2011) and Dunning et al. (2016) as a transition region between single-wet-season and dual-wet-season regimes.
The fluctuations of the regime are demonstrated by two exemplary hydrological years. In the hydrological year 1986/1987 (Figure 4.5b), two distinct rainy seasons can be identified. The first rainy season starts during the end of October and lasts until the end of December. This season is followed by a break, until the second rainy season begins in the first pentad of February. The cessation of the second rainy season is estimated at the beginning of June, which is considerably later than the climatology. In contrast, the hydrological year 2004/2005 (Figure 4.5c) is characterized by multiple

peaks and breaks. A late onset of the first rainy season at the end of October and a cessation of the second rainy season at the end of May can be identified. A separation of the two seasons is ambiguous due to a persistent rainfall period which occurs during the climatological break in January. This rainfall period can be attributed to both rainy seasons. The usage of the fifth percentile threshold leads to a single rainy season. By applying the climatological threshold, the period in January is added to the second season due to the partial overlap with its climatological occurrence. The 95th percentile threshold sets the onset of the second season to the beginning of March.

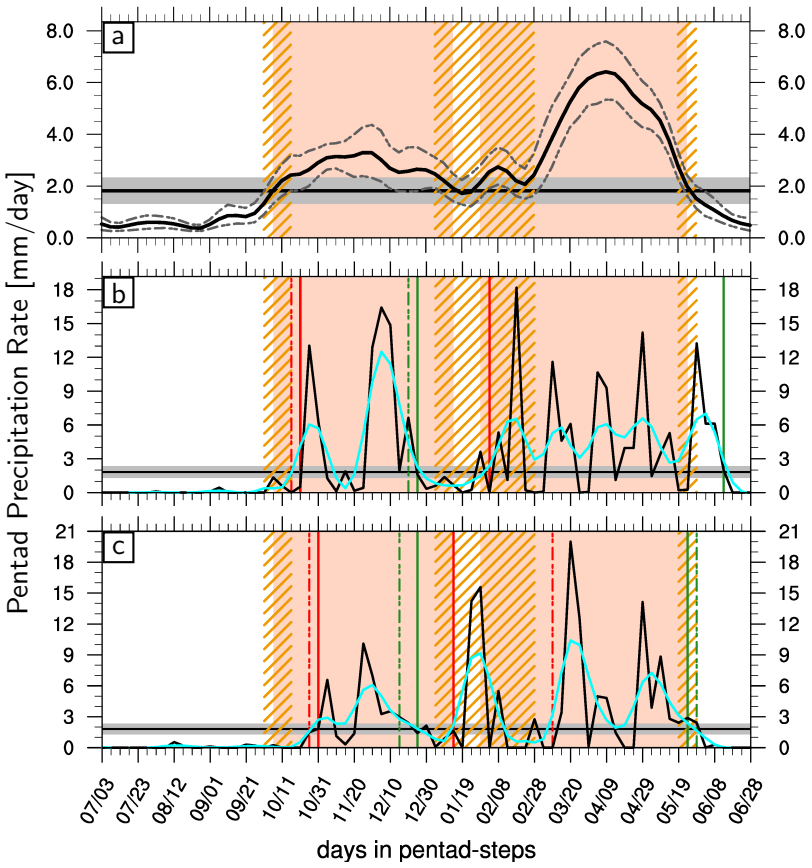

Figure 4.5: Same as in Figure 4.3, but for Musoma, Tanzania (33.8 °E, 1.3 °S, no. 3 in Figure 4.1) and for hydrological years (b) 1986/1987 and (c) 2004/2005 in pentads.

The above results provide evidence that the methodology permits a flexible and meaningful determination of the onset, cessation and duration of the rainy seasons for the study areas. The confidence intervals can be used for detection of critical periods with "false" onsets (5th percentile threshold) or selection of core periods (95th percentile threshold). Thus, the method is applied to the complete station database and gridded product in the next section.

4.3 Climatological rainfall regimes

In the first step, the region is classified according to the number of rainy seasons (Figure 4.6). The region can be subdivided into two large areas with single-wet-season rainfall regimes (yellow), two areas with dual-wet-season rainfall regimes (blue) and two small and spatially incoherent areas with a triple-wet-season regime in the Kenyan Highlands and near the coast of Eritrea and Sudan (orange). The triple-wet-season regime will only be briefly discussed. The two large single-wet-season rainfall areas cover the southern part of the region which includes most parts of Tanzania, Rwanda, and Burundi, and the northern part, which includes Sudan, South Sudan, western Ethiopia, and northern Uganda. The smaller subregion with a dual-wet-season regime includes a strip in Democratic Republic (DR) of the Congo, southern parts of Uganda and the Kenyan shore of Lake Victoria. The large dual-wet-season subregion includes most of Kenya, Somalia, southern and north-eastern Ethiopia, Djibouti, and southern Eritrea. At the border between different rainfall regimes, the areas are classified as unstable in the long term, i.e. the rainfall regime in these areas varies and/or cannot always be clearly categorized as single-wet-season or dual-wet-season. Triple-wet-season rainfall regimes are always unstable and can be seen as a special case of unstable regime. A single-wet-season regime can still show multimodal characteristics and contain multiple peaks and minima. Nonetheless, the rainfall rates during the periods of the minima prevail above the rainy season threshold and prevent a splitting into multiple rainy seasons. This case occurs in parts of e.g. the DR Congo or Tanzania and is confirmed by different peak months during the passages of the north-south meandering TRB (Figure S2). The regimes of the coastal areas of Somalia, Kenya and northern Tanzania are also classified as unstable. This region can vary between single-wet-season and dual-wet-season regimes due to the strong sea breeze effect (cf. Example 2 in section 4.2.1). In the desert area of north-western Sudan, the categorization is less reliable (Figure S1). In some regions, the comparison of station and grid point modalities reveals different classifications. These regions are classified as unstable in both grid point and station data. However, CHIRPS tends to overestimate the single-wet-season regimes and to underestimate dual-wet-season regimes. This tendency is obvious at the coast of Kenya and northern Tanzania and in the Ethiopian Highlands. In all cases, several station distributions are classified as dual-wet-season although the stations are located within CHIRPS grid points with single-wet-season regimes.

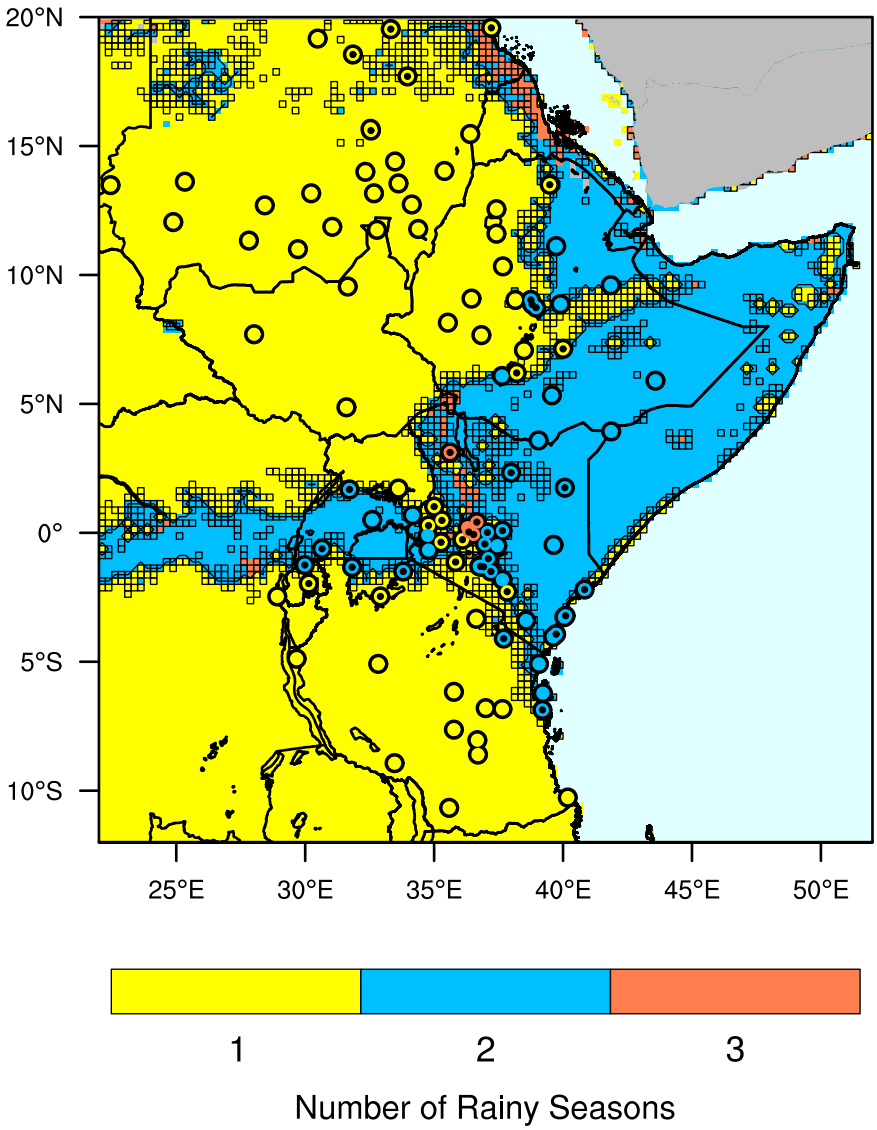

Figure 4.6: Classification of rainfall regimes in single-wet-season (1), dual-wet-season (2) and triple-wet-season (3). The colors indicate the climatological number of rainy seasons. Stations are marked by circles. Black boxes enclose grid points with climatologically unstable rainfall regimes. Black dots indicate stations with climatologically unstable rainfall regimes.

4.4 Comparison of rainy season definitions

The following section discusses the seasonal migration of the climatological rainy season onset and cessation estimates as determined in Step 2 of the new definition compared to calendric rainy season definitions. Depending on the sub-region and season, various calendric definitions are used in studies on rainfall variability. For the northern single-wet-season part of GHA, studies generally suggest that the main rainy season occurs during the boreal summer (June-July-August-September, JJAS, e.g. Camberlin (1995)). A more detailed overview on regional rainy season definitions

is given in Table 4.1. Figure 4.7a-c shows the respective onset, cessation, and seasonal length obtained using the climatological threshold of the northern areas with a single-wet-season regime. The sub-region shows a smooth and mostly zonal progression of the season in northward direction that can be mainly attributed to the circulation associated with the seasonally migrating TRB. Overall, the results derived from CHIRPS and station data agree well in the estimation of the seasonal rainfall characteristics. The onset and cessation dates as well as rainy season length are compared with the calendric definition in Figure 4.7d-f. Figure 4.7a shows that the onset of the rainy season can partly be expected in March for northern DR Congo and Uganda, and southern parts of South Sudan and Ethiopia. Farther north, in southern Sudan and western Ethiopia, the onset can be expected in April and May. In Ethiopia, this period is usually referred as "Belg Rains" (c.f. section 2.4.1). The calendric onset date of June 1st is met around 12 °N in the area of central Sudan and northern Ethiopia (Figure 4.7d). At the beginning of September, the cessation starts around 15 °N in northern Sudan, and reaches northern Uganda and DR Congo at the beginning of November (Figure 4.7b). In general, the assumption of the rainy season period as JJAS is valid only for Sudan (Figure 4.7f). For the single-wet-season areas farther south, large parts of the climatological rainy season are underestimated.
Figure 4.8 compares the rainy season definition and its uncertainties between station data and the nearest CHIRPS grid point. In most cases, the rainy season of the station matches the season of the grid point or deviates by few pentads (see also Figure S3a,d). In central-eastern Sudan, the station rainy season length is slightly prolonged compared to the CHIRPS estimation (Figure 4.7c, stations no. 9, 12, 13). Other discrepancies between stations and grid points can be located at near-equatorial latitudes where the rainfall regime is unstable (stations no. 58, 60, 67, 68). Several station regimes in the Kenyan and Ethiopian Highlands are characterized as single-wet-season, but the satellite estimations show different regimes. However, both estimations consistently show unstable rainfall regimes for these stations.

For the southern single-wet-season regimes, the climatological rainy season parameters are shown in Figure 4.9. Northern Tanzania is considered to experience two rainy seasons in MAM and OND (Camberlin and Philippon, 2002; Zorita and Tilya, 2002; Mapande and Reason, 2005). In the rest of the country, the calendric rainy season is assumed to occur from October to April (Zorita and Tilya, 2002; Mapande and Reason, 2005), which is considerably longer than in the northern part of the region. The progression of the onset and cessation reflects topographic conditions through an additional meridional component of propagation. The onset starts in DR Congo at the end of August and at the coast at the end of October. It progresses towards central and southern Tanzania until mid-November from both directions (Figure 4.9a). The cessation of the rainy season in the region starts in the middle of March in the south-west and progresses towards north and east until the middle of May (Figure 4.9b). The estimation of the rainy season from station data mostly agrees with the estimation from CHIRPS (Figure 4.9a, Figure 4.10). Slight differences in the cessation dates are found for some stations due to orographic rainfall (e.g. Kilombero region, Tanzania, 8.25 °S, 36.33 °E, Figure 4.9b, Figure 4.10, stations no. 106, 107) triggered through predominant south-easterly winds in May. In general, the flexible rainy season definition coincides with the calendric rainy season in most parts of the region. Some of the near-equatorial stations also show bimodal characteristics, which are partly

captured by CHIRPS (stations no. 75, 85, 87, 88). The difference in season length of the southern part compared to the northern part arises from the topography and the lower poleward extent.

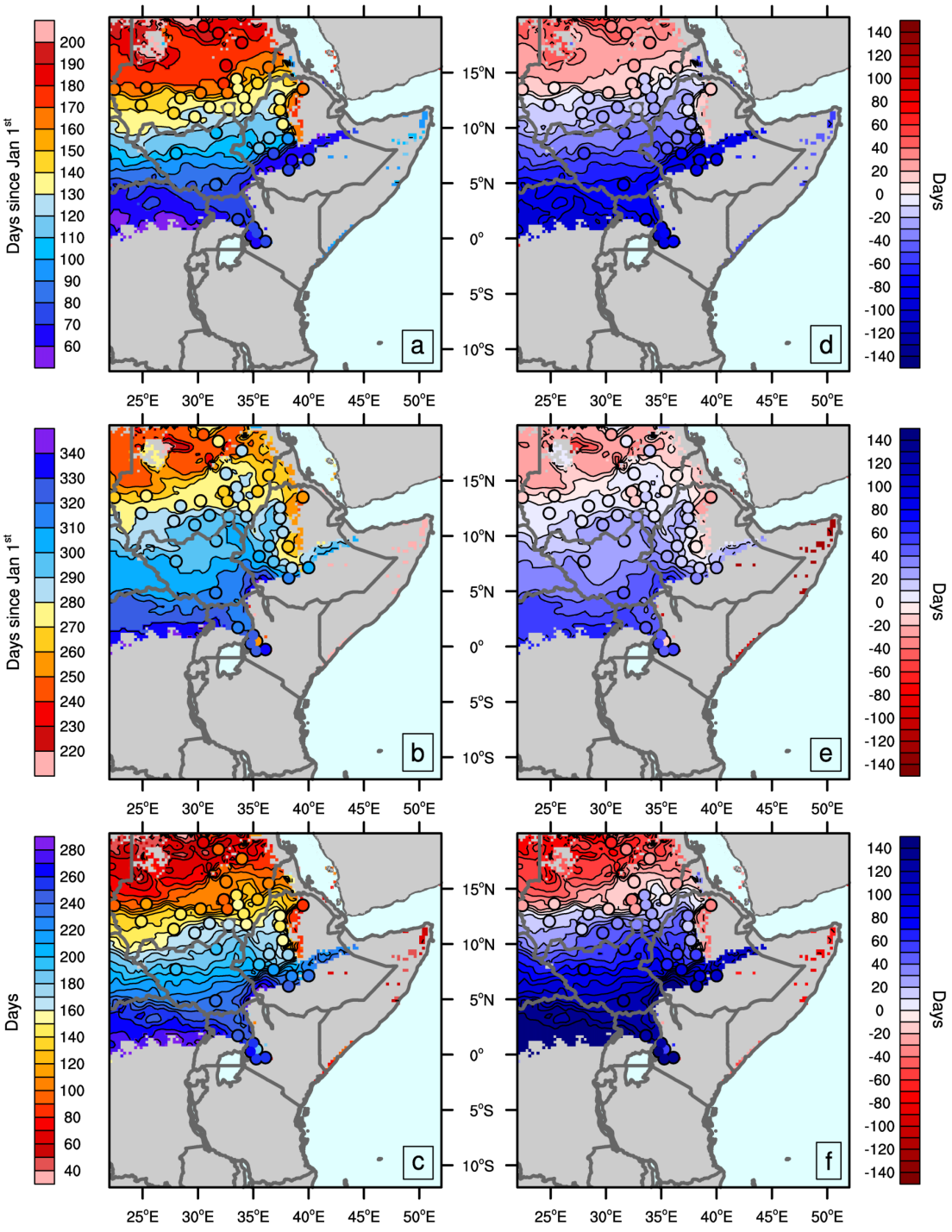

Figure 4.7: Progression of (a) the rainy season onset [days since Jan 1st], (b) the rainy season cessation [days since Jan 1st], and (c) the duration [days] of the rainy season for the northern region with a single-wet-season regime estimated from CHIRPS (contours) and station data (circles). (d,e,f) Difference of (a, b, c) with calendric definition of rainy season onset (d, i.e., June 1st), cessation (e, i.e., September 30th) and duration (f, i.e., 122 days).

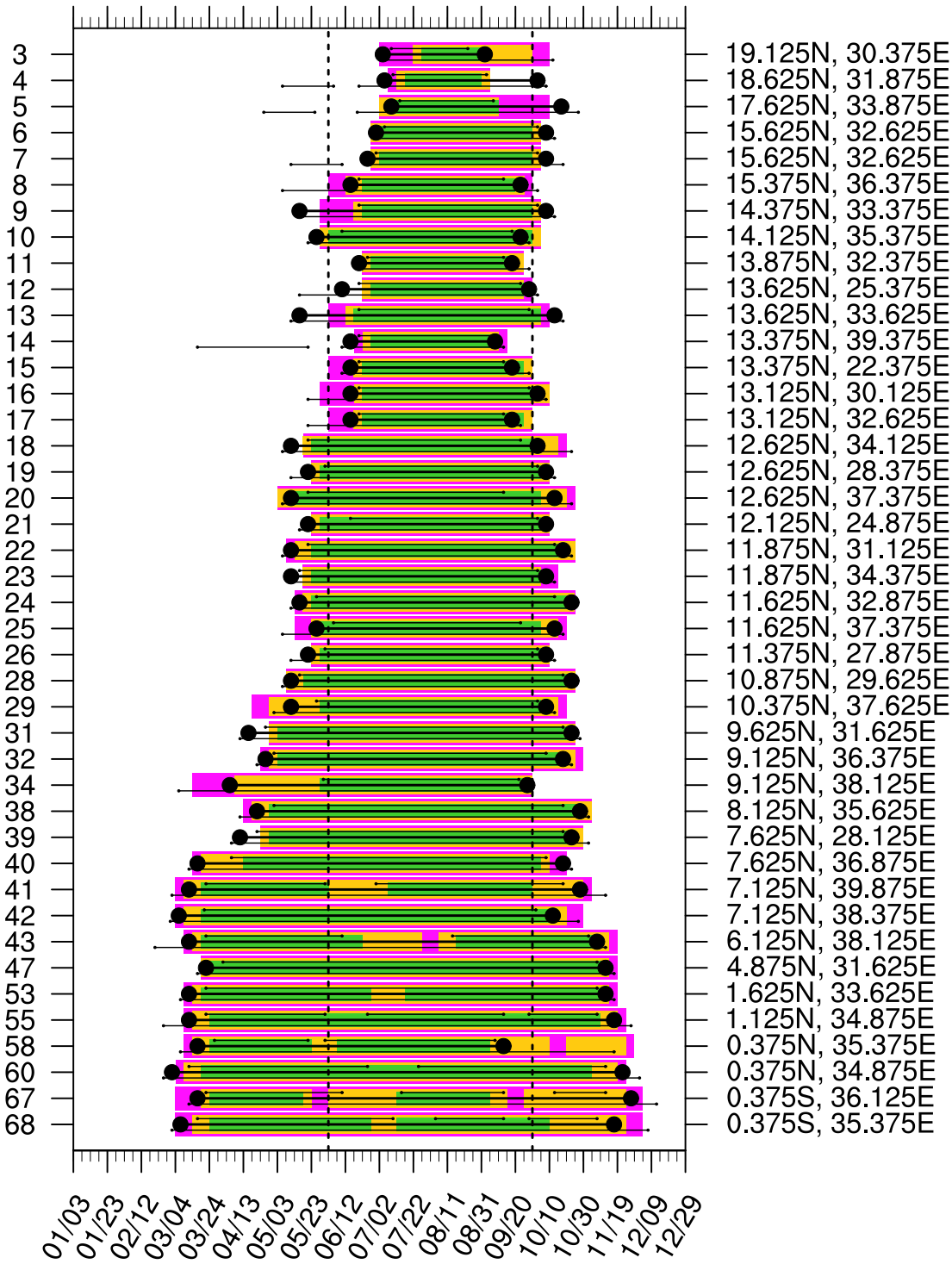

Figure 4.8: Comparison of rainy seasons at stations and satellite grid points for the northern region with a single-wet-season regime. Numbers of the stations are listed on the left side. Coordinates of the grid points are listed on the right side. Station rainy seasons are shown as horizontal black lines, with circles marking the onset and cessation of the rainy seasons. The uncertainty (5^{th} and 95^{th} percentile confidence interval bounds) is shown as thinner black lines below and above the average rainy season. The average grid point rainy season and its confidence interval bounds are shown as yellow, magenta and green bars, respectively. A complete list of the stations can be found in Table S1.

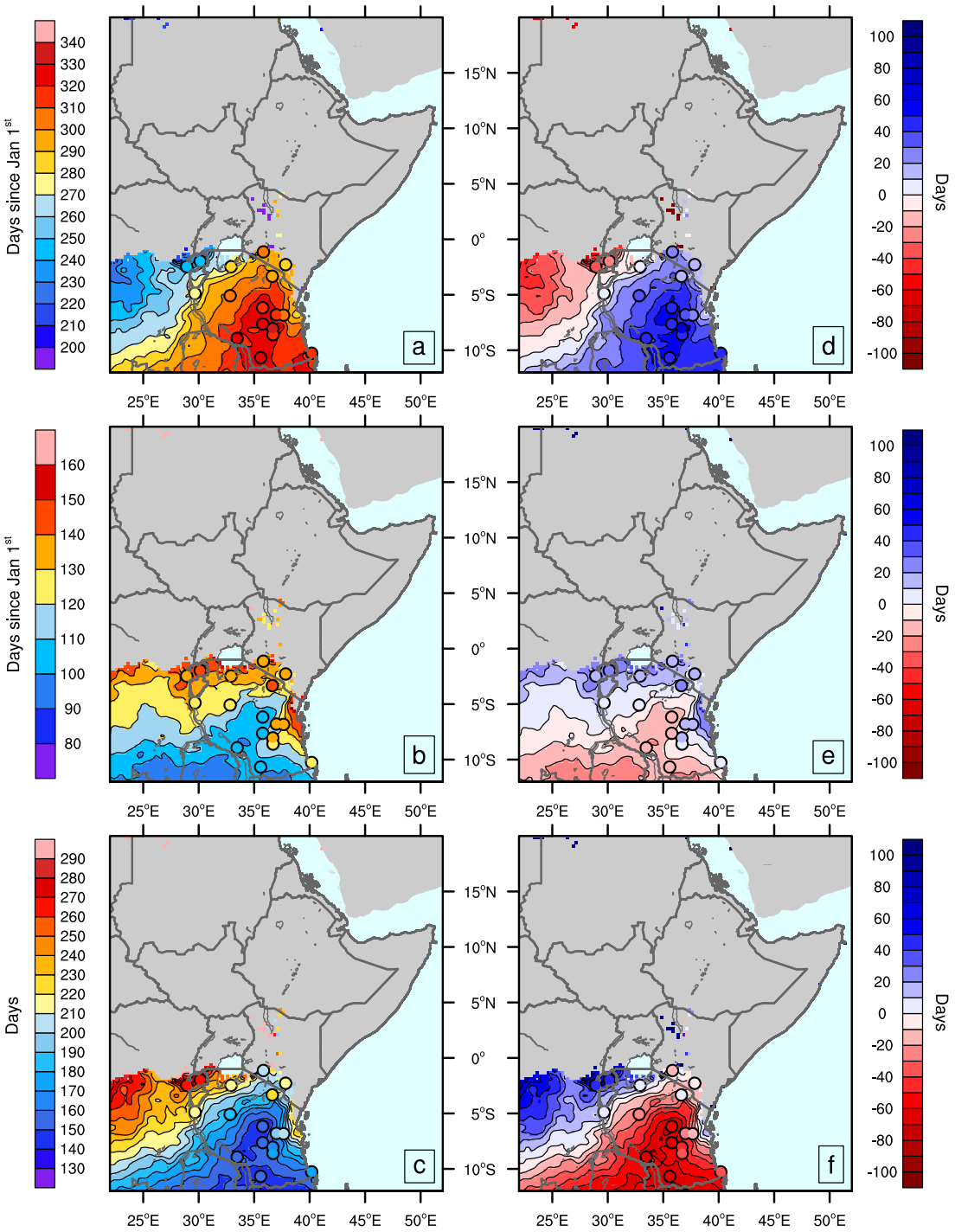

Figure 4.9: Same as Figure 4.7, but for the southern region with a single-wet-season regime and calendric definition of rainy season onset and cessation (i.e., October 1st, April 30th and 212 days).

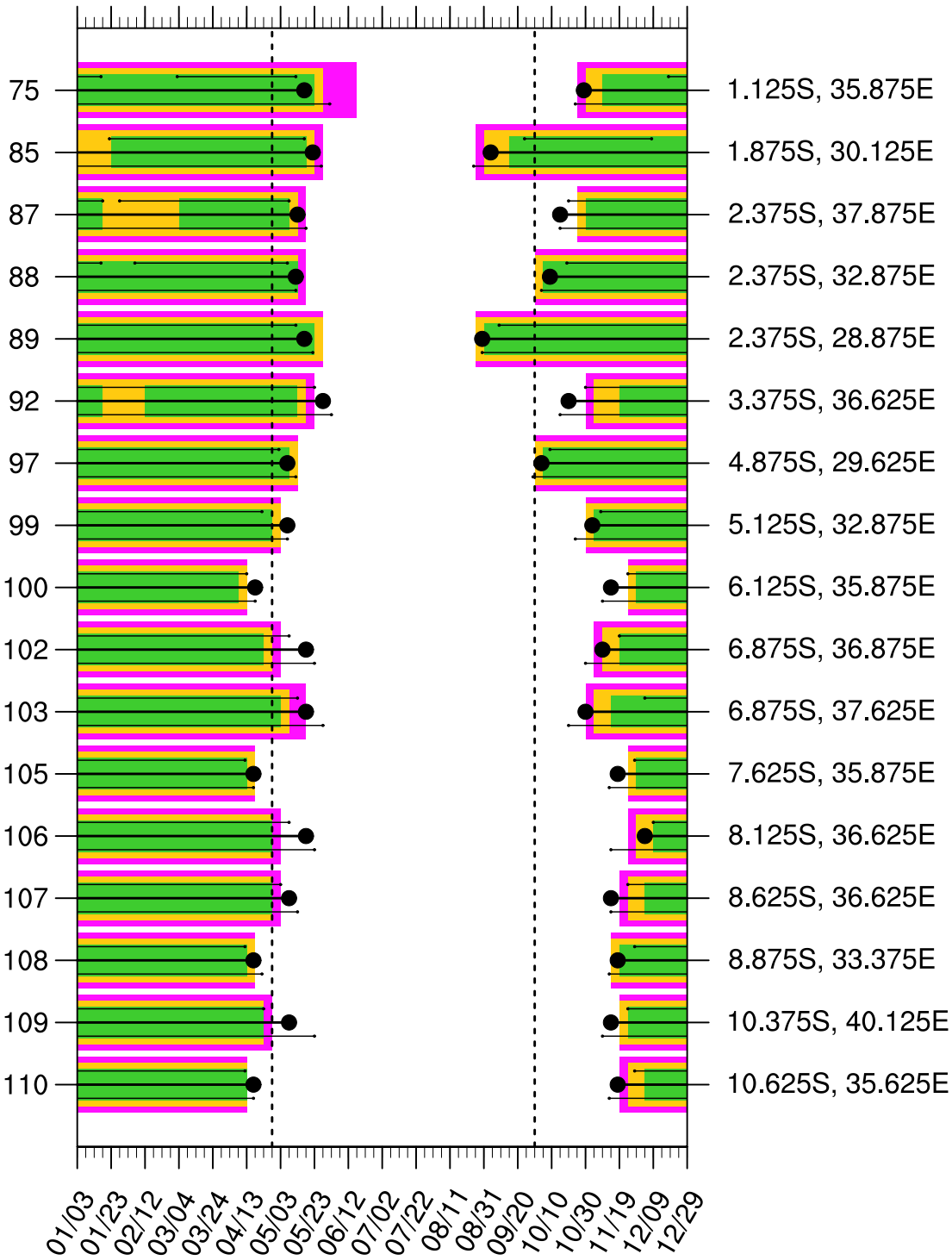

Figure 4.10: Same as Figure 4.8, but for the stations in the southern region with a single-wet-season regime. © The authors and John Wiley & Sons Ltd, CC-BY.

For the area with dual-wet-season regimes, the rainy seasons are commonly known as "Long Rains" (MAM) and "Short Rains" (OND; e.g. Nicholson (1996), cf. Table 4.1). The MAM-estimation for the Long Rains is valid for the lowland areas of Kenya, most of Somalia, and eastern Ethiopia (Figure 4.11). The onset progresses from the East African Highlands towards the Horn of Africa (Figure 4.11a). For the Kenyan Highlands and southern Uganda, the Long Rains start already in February. The cessation starts in

the Lowlands of Kenya and in north-eastern Ethiopia (Figure 4.11b). A later cessation of the Long Rains occurs at the Kenyan coast and at a strip at the north-western edge of the Kenyan Highlands. These features lead to a prolonged season compared to the calendric definition (Figure 4.11c,f).

The onset of the second rainy season progresses from north-west towards the Kenyan Lowlands and Somalia (Figure 4.12a). The cessation starts near the Horn of Africa and ends in the near-equatorial Highlands (Figure 4.11 b) In north-eastern Ethiopia, the season starts in July and ends in September, which corresponds well to the "Kiremt" (cf. Table 4.1, Segele and Lamb (2005)). Compared to the commonly used OND-definition, Uganda also experiences an earlier onset in July/August. The cessation in Uganda lies mostly in December (Figure 4.12b), thus the overall season is longer than three months (Figure 4.12f). The OND definition is valid for lower parts of Kenya. For higher elevated areas, the cessation lies in January, and thus is slightly later than in the OND-definition (Figure 4.12b,e).

The direct comparison between the station and grid point estimations for the sub-region shows consistent results for both, the station and the gridded product (Figure 4.13). A more detailed view on the uncertainties reveals that the CHIRPS estimation coincides with the station rainy season, when the season is well pronounced and the 95th percentile threshold is reached. Weakly pronounced rainy seasons or parts are often underestimated (as in case of the sea breeze, stations no. 86, 90, 94, 95). In case of modest or short breaks between two rainy seasons, CHIRPS tends to overestimate rainfall during the break, thus only one merged rainy season is estimated (e.g. Nairobi area, stations no. 77-no. 80). This tendency can also be confirmed by the triple-wet-season stations (Figure S4). Consequently, the border between the two main regimes is set to a different location in the CHIRPS estimation than in the station estimation. In Uganda and the Kenyan Highlands, the Short Rains can be equal to the Long Rains or even longer. Nonetheless, the Short Rains are usually associated with lower rainfall rates as compared to the Long Rains.

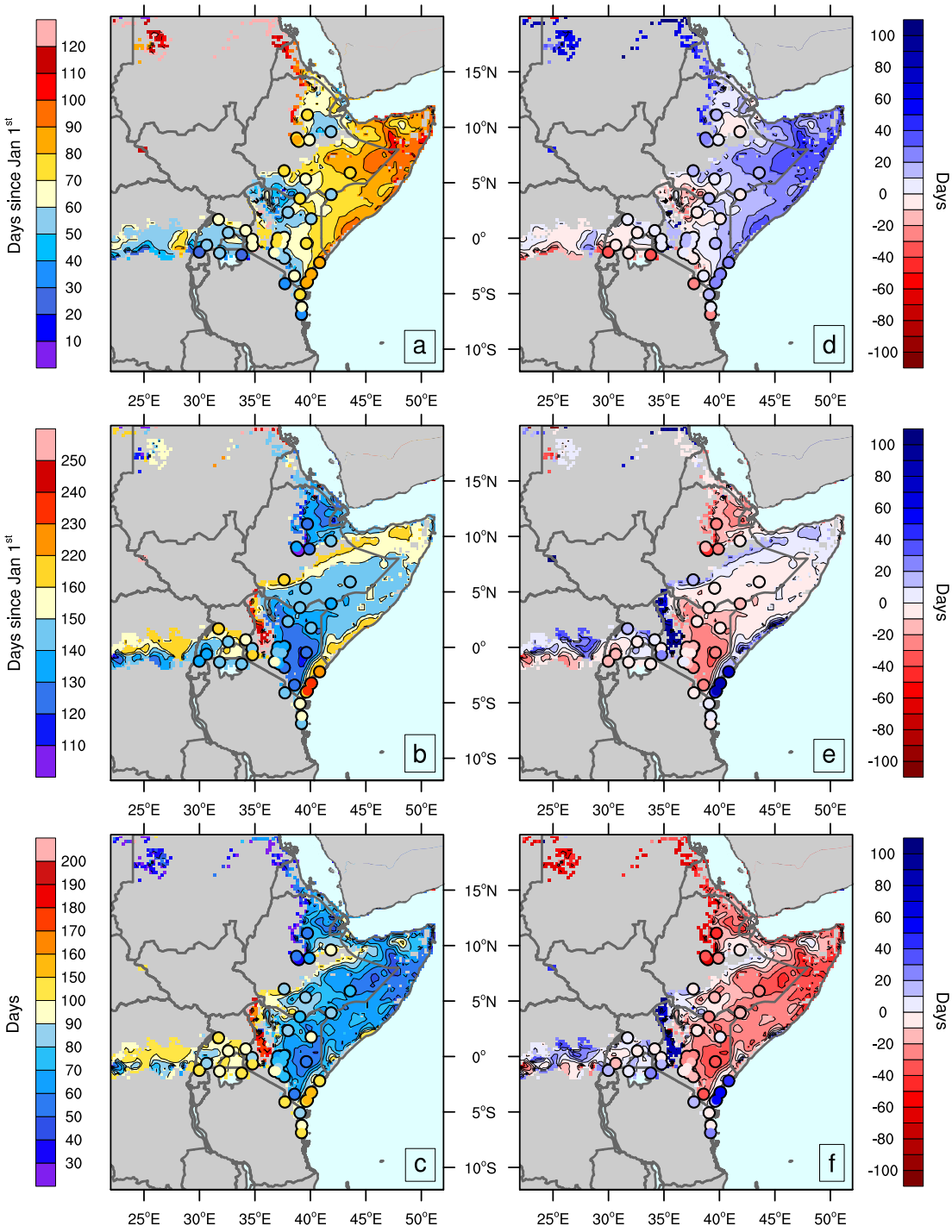

Figure 4.11: Same as Figure 4.7, but for Long Rains in the region with a dual-wet-season regime and calendric definition of rainy season onset and cessation (i.e., March 1st, May 31st and 92 days). © The authors and John Wiley & Sons Ltd, CC-BY.

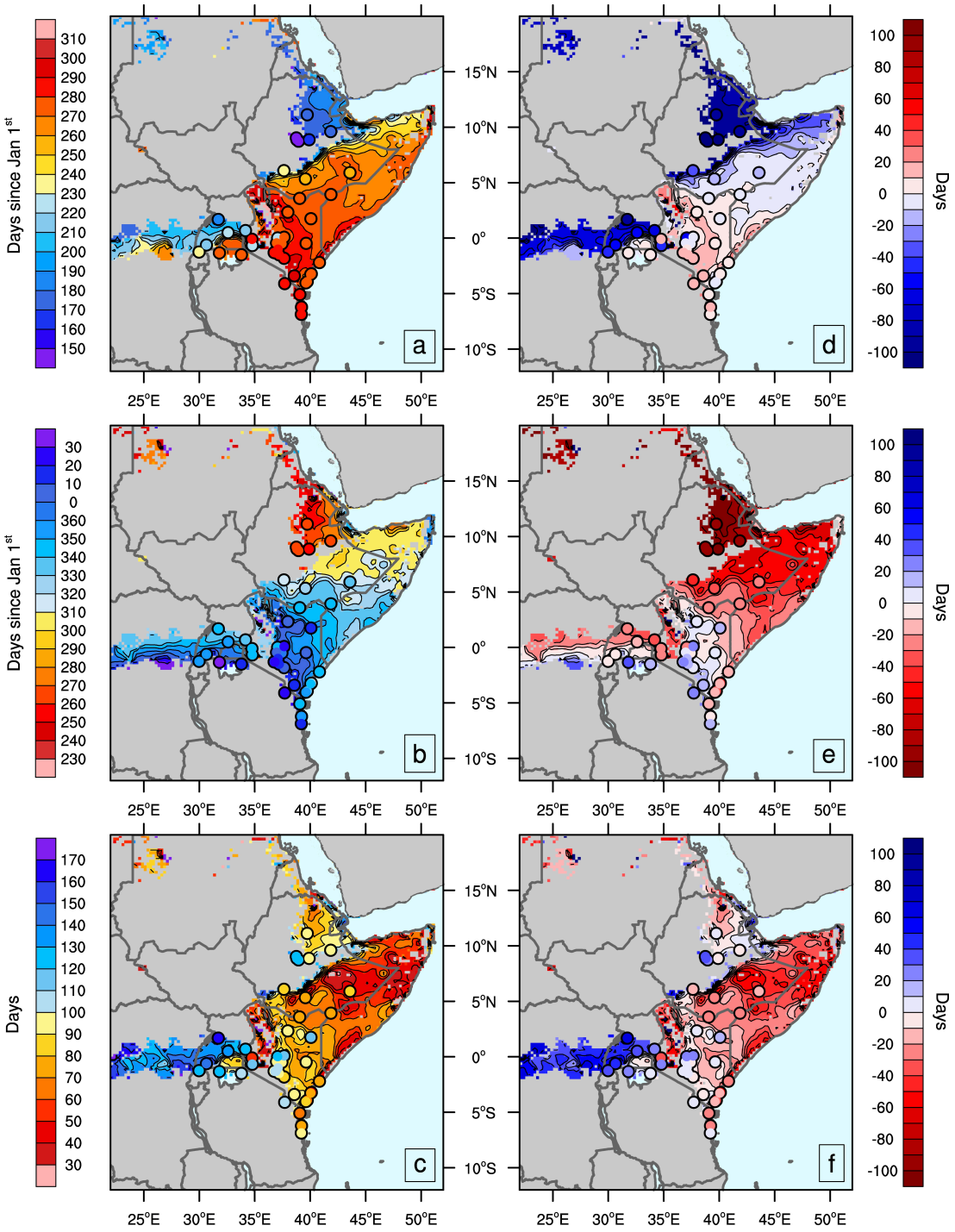

Figure 4.12: Same as Figure 4.7, but for Short Rains in the region with a dual-wet-season regime and calendric definition of rainy season onset and cessation (i.e., October 1st, December 31st and 92 days). © The authors and John Wiley & Sons Ltd, CC-BY.

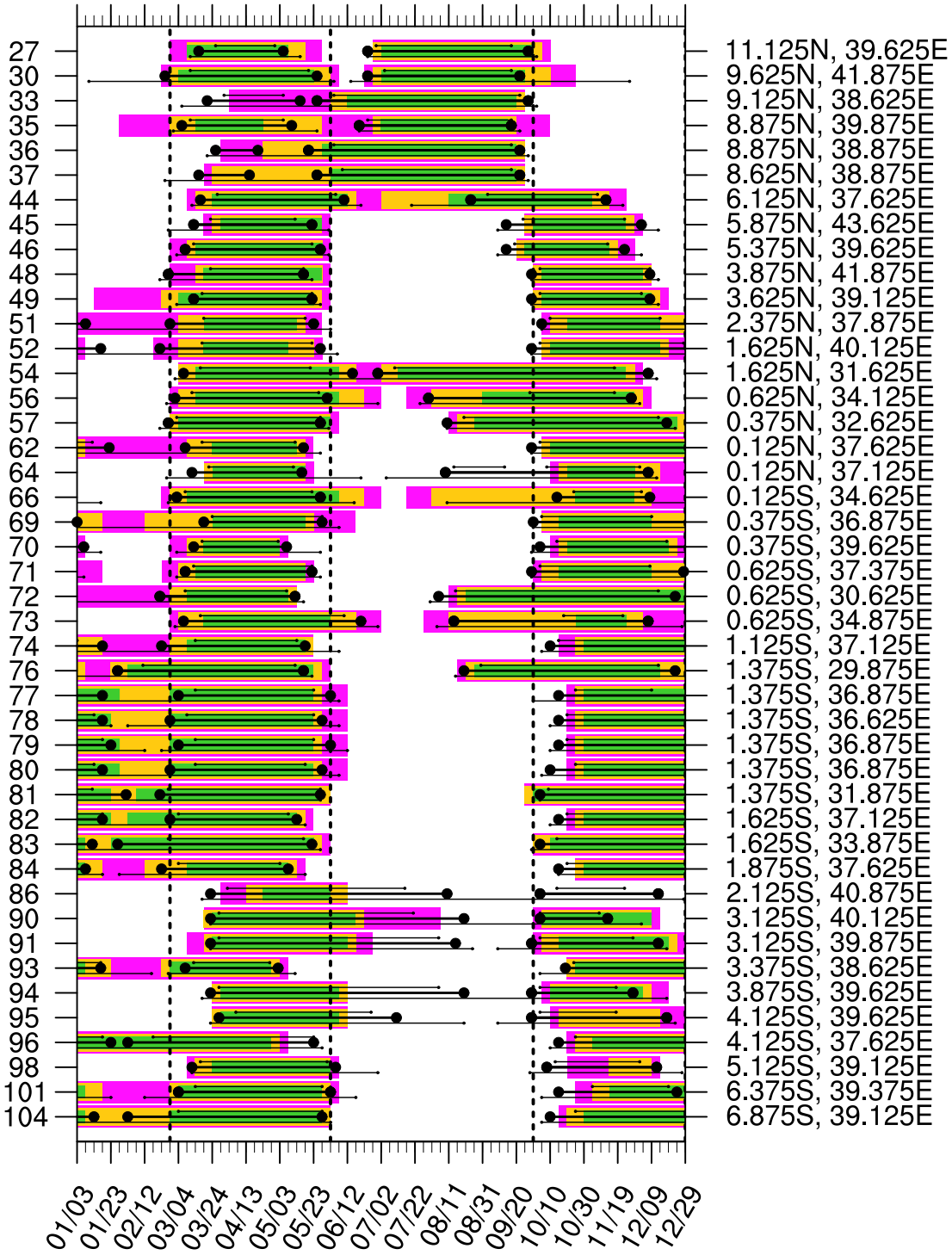

Figure 4.13: Same as Figure 4.8, but for the stations with a dual-wet-season regime.

4.5 Rainfall trends for flexible rainy season definition

The flexible rainy season definition can be applied to determine long-term trends of seasonal rainfall metrics (e.g. onset, cessation, rainfall amount). The adapted rainy season definition can lead to different trends in rainfall amount compared to those

obtained by using the calendric rainfall onset and cessation (i.e. MAM, OND). In case of the rainfall amount, two adjustment steps can be performed. The seasonal rainfall amount can be determined for the climatological rainy season (resulting from step 2, section 4.2, Figure 4.2) or for each individual rainy season in every hydrological year (resulting from step 3, section 4.2, Figure 4.2). However, the latter option can lead to complicated assignments in regions with unstable regimes and without an unequivocal distinction between the rainy seasons. Therefore, the trends of the rainfall amount are calculated using the non-parametric Mann-Kendall test and the Sen's Slope estimator (Hirsch et al., 1982) for the adjusted climatological rainy season from step 2 and for the calendric definition. In general, the spatial pattern of trends from station data agrees with the results from the gridded satellite product (Figures 4.14 and 4.15): Areas with single-wet-season regimes show a significant positive trend in central Sudan, western Ethiopia and north-eastern Uganda (Figure 4.14a). The trend for Tanzania and single-wet-seasonal areas of DR Congo is predominately negative and significant in DR Congo and southeastern Tanzania (Figure 4.14d). However, the trend sign over Ethiopia, eastern Uganda and western Tanzania is not coherent and some nearby stations reveal opposed trend signs (Figure 4.14a,d). For the Long Rains, the weak trend is coherently negative for the Kenyan lowlands and Ethiopia (Figure 4.15a) with only few significant station or grid point trends. The highest and significant trend magnitudes are estimated for the coastal region. The Kenyan Highlands and most stations in Uganda show a wetting trend. For Uganda, the satellite estimation does not underline this wetting trend. The Short Rains reveal a significant wetting trend for large parts of Ethiopia and Somalia (Figure 4.15d). Stations in these countries and in northern and coastal Kenya agree in the sign of the trend, but the trends are generally not significant. The coastal stations in northern Tanzania and parts of south-central Kenya point towards drier conditions. The drying is coherent with the trends in most parts of Tanzania (compare with Figure 4.14d). The trend from the flexible rainy season definition also agrees with the estimation from the calendric definition in terms of sign (Figure 4.14 and Figure 4.15b,e), but reveals an amplified trend magnitude (Figure 4.14c,f). The largest differences occur in regions which have a longer rainy season compared to the calendric definition. In case of the the region with dual-wet-season regimes (Figure 4.15c), there is a general consensus between the calendric and the flexible trend estimation for the Long Rains. The Short Rains reveal different trend estimates in north-eastern Ethiopia, the Kenyan Highlands and parts of Uganda due to a different timing of the second rainy season (Figure 4.15e-f). In general, the overall trend pattern of the flexible rainy season definition matches the trend pattern of the calendric method. Some regions disagree in trend patterns, like the north-eastern part of Ethiopia for the Short Rains and the Kenyan coast whose calendric definition needs to be adapted. The second rainy season in north-eastern Ethiopia usually occurs from July to September rather than in OND, thus the definition of Kenyan Short Rains does not fit here. In any case, the trend signal is more pronounced when applying the flexible rainy season criterion.

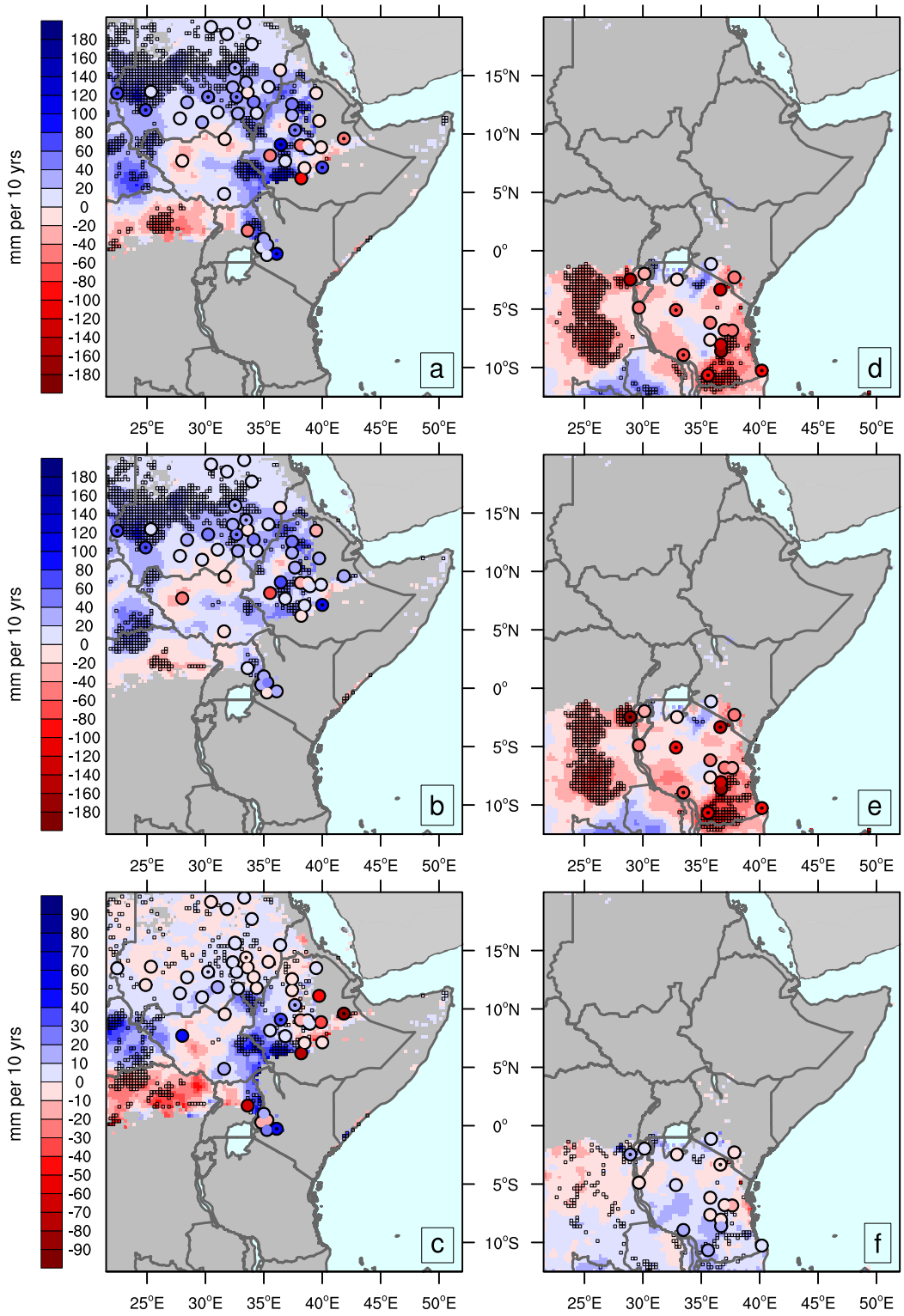

Figure 4.14: Rainfall trends (mm/10 years) based on (a) the flexible rainy season definition and (b) the calendric rainy season definition for the northern single-wet-season regime estimated from CHIRPS (colors) and station data (colored circles). Grid points and stations with significant trends at 5% level are indicated by black squares and dots, respectively. (c) Difference (a–b) in trends (colors) and significance (squares, dots) between the rainy season definitions. (d–f) Same as (a–c) but for the southern single-wet-season regime. Note that the label bar in (c, f) differs from those in (a–b, d–e).

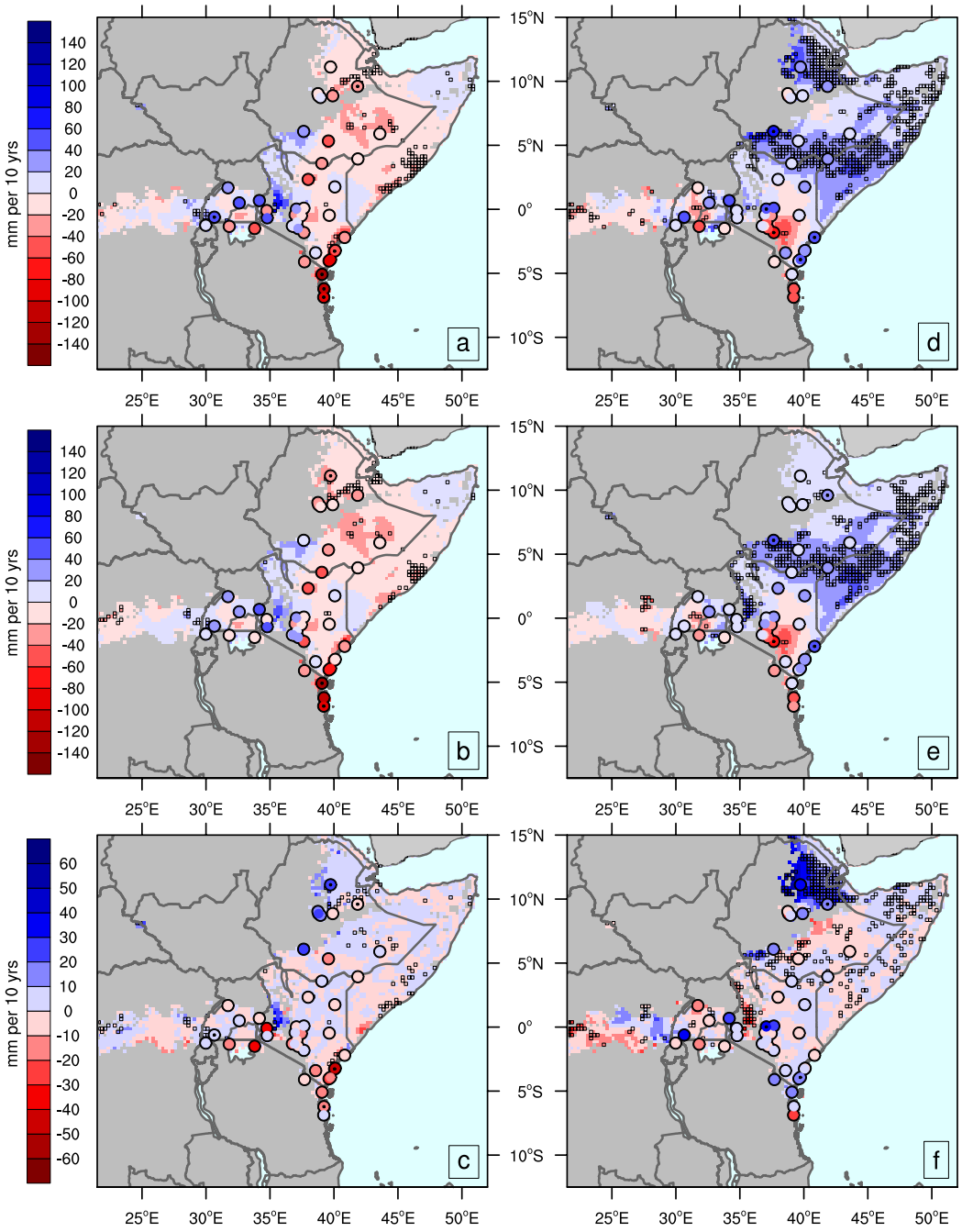

Figure 4.15: Same as Figure 4.14, but for the Long and Short Rains in the dual-wet-season regimes. © The authors and John Wiley & Sons Ltd, CC-BY.

4.6 Trends of onset and cessation dates

One important advantage of a flexible rainy season definition is to determine the onset and cessation of a particular rainy season irrespective of a strict climatological definition in order to quantify its interannual variability and trends. These results extend the analysis on trends in the GHA with additional metrics that describe the rainy season in more detail. For convention, a negative sign indicates a trend towards an earlier onset/cessation and vice versa. Figure 4.16 displays scores that indicate the significance of the trends of onset and cessation dates for the four main rainy seasons. The trend magnitudes can be obtained from Figure S5. For example, the highest score is obtained when the trend is significant at 5%-level for all three thresholds. Other combinations leading to lower scores are explained in Table 4.2. The scores can be regarded as a measure of sensitivity of the trends to the threshold level. The trend for the rainy season onset of the northern single-wet-season region (Figure 4.16 a) is predominantly not significant. In the northernmost parts of the region, the area is dry and the number of years with a detectable onset is reduced (cf. Figure S6a-b). In general, the results for stations are coherent with those for grid points. However, several stations in Sudan (stations no. 8, 16, 22, 24) and Ethiopia (stations no. 20, 34, 38, 42, 43) show insignificant delaying trends in the onset that are not depicted in CHIRPS. The trend for the cessation of the rainy season (Figure 4.16 b) reveals a negative sign in northern Congo, although no station observations are available to support this sign. A strong and robust positive trend region is located near the border between Sudan, South Sudan and Ethiopia, which is also found at several stations in the area (e.g. stations no. 22, 24). The trend pattern of the onset and cessation for the northern sub-region expands the results from Figure 4.14a-c, where a negative trend in the Congo and a positive trend in the rainfall amount in central Sudan has been shown. Still, the region with the positive trend in cessation is located south of the region with the increase in rainfall amount during the climatological rainy season. As for the onset, several stations in Ethiopia also show a negative trend in cessation, which is not confirmed by the grid point product. In the areas with a trend towards a delayed cessation, the climatological rainy season ends at the end of October or beginning of November. For the area with trends towards an earlier cessation in DR Congo, a climatological cessation at the beginning of December is estimated (Figure 4.7b). The southern area with single-wet-season regimes reveal a trend towards a later rainy season onset and earlier cessation in parts of central and southern Tanzania. The signal for the later rainy season onset (Figure 4.16 c) mostly prevails in the southern part of the country and is predominately not significant. Two stations in this region agree on the negative trend (one of which is significant at the 5%-level, stations no. 106, 107). The signal towards the earlier rainy season cessation (Figure 4.16 d) focuses on two strips through the central and coastal parts of Tanzania. This trend is emphasized by several stations in the region in both, sign and partly significance level. In the context of Figure 4.9d-f, the region can be divided into an area with a tendency towards a weaker rainy season with less rainfall in the south of Tanzania, and an area with a shorter rainy season without much rainfall decrease in central Tanzania. The climatological cessation in the areas with the latter trends is estimated for mid-April (Figure 4.9b). The pattern for the Long Rains can be described as weak and patchy, with only few local trends in onset and cessation. The onset based on CHIRPS outlines

weak tendencies towards an earlier onset in the mountainous region of western Kenya and Uganda (Figure 4.16 e). Conversely, the onset in northern Kenya, Somalia and Ethiopia tends to occur slightly later. The North-East of Ethiopia is exceptional here, featuring both a trend towards a later onset and a trend towards an earlier cessation (Figure 4.16 f). Generally, the trends for the cessation of the Long Rains show a more coherent and stronger pattern than for the onset. Here, the Kenyan coast, the North-East of Ethiopia and, with a weaker magnitude, the North-East of Kenya reveal trends towards an earlier cessation. The trends for grid points are more coherent in sign than those for stations, which often show no significant or opposing trends. The Kenyan Highlands and parts of Uganda show weak and incoherent trends towards a prolonged rainy season. The region with negative trends at the Kenyan coast and the southern country parts lie adjacent to the regions with the earlier cessation in Tanzania. The patterns also mirror the trends in rainfall sum (Figure 4.11a-c), as only few stations reveal significant trends in onset and cessation. The pattern of the Short Rains onset is dominated by a robust trend towards an earlier onset in northern Kenya, southern Ethiopia, and Somalia (Figure 4.16 g). Three stations in the region emphasize this trend (two being significant, stations no 48, 51). The trend of the cessation does not show a uniform pattern for the region (Figure 4.16 h). The results from CHIRPS shows a trend towards an earlier cessation, while the trends from stations only partly confirm this tendency. The Horn of Africa and eastern Ethiopia show a strong and robustly significant trend towards a later cessation of the rainy season. Gode (station no. 44), as the only available station in eastern Ethiopia, fits in this pattern and shows a significant trend of more than 2.5 pentads per decade (Figure S5h). Although the percentage of detectable OND-seasons is decreased at the Horn of Africa (Figure S6), the patterns coincides with the trends in rainfall sum, which were discussed in Figure 4.12d-f. The climatological onset and cessation of both regions with significant trends is estimated for the end of October or beginning of November, respectively (Figure 4.12a-b).

Table 4.2: Scoring rules for Figure 4.16.

$\sum$ of uniform trend signs	$\sum$ of significant trends at 5%-level	Score
$2 >$	0	0
$2 \leq$	0	++/ - -
$2 \leq$	1	1x significant
$2 \leq$	2	2x significant
3	3	3x significant

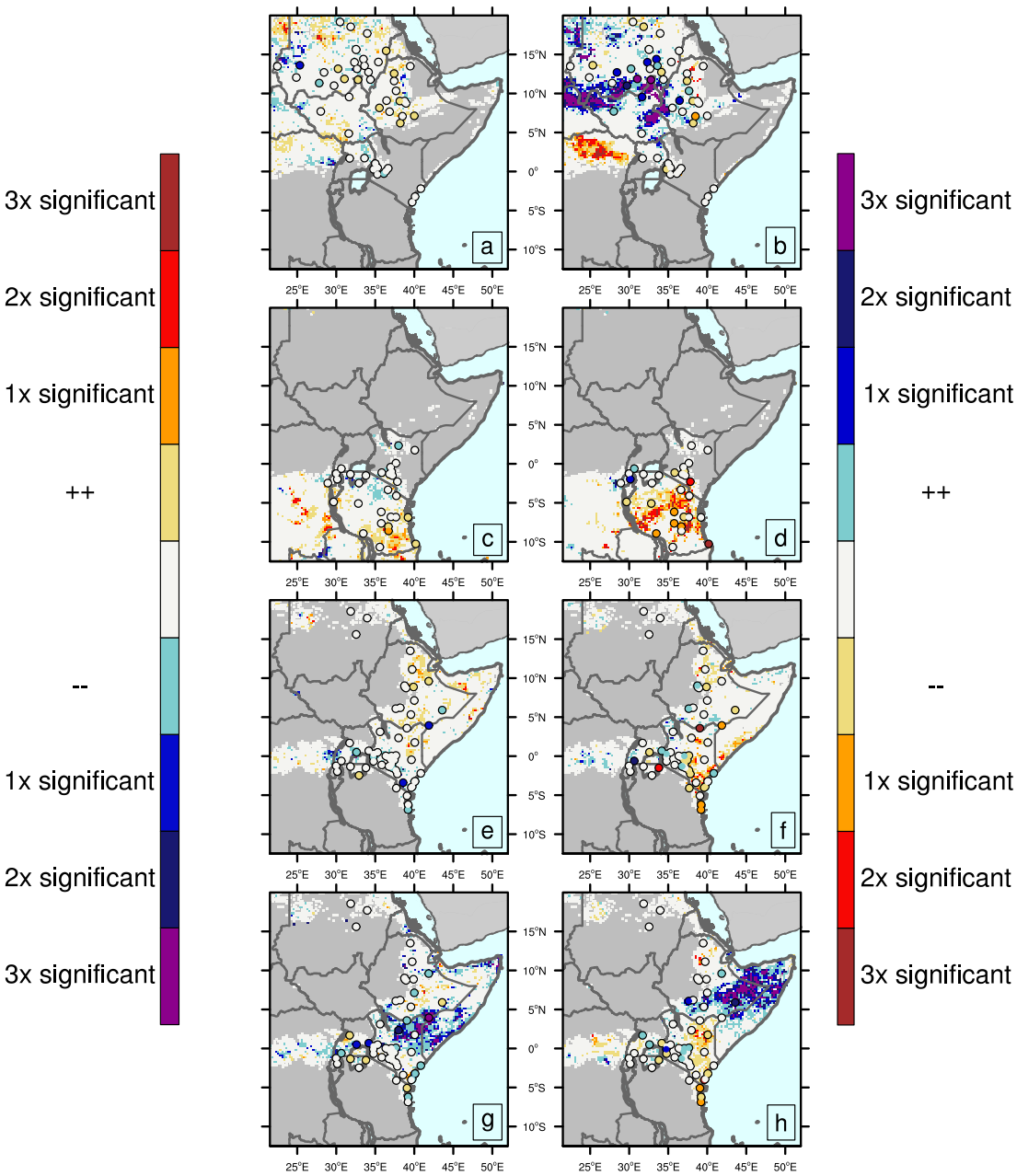

Figure 4.16: Onset (left) and cessation (right) trend significance scores based on the threshold levels of the flexible rainy season definition. Uniform trend signs of at least two threshold levels are required for a score of 1 (positive) and -1 (negative). Each significant trend at 5% level per threshold level increases (decreases) the score by 1. For more details, see Table 4.2. CHIRPS (colors) and station data (colored circles) are shown for (a–b) the northern single-wet- season regime, (c–d) southern single-wet-season regime and (e–f) Long Rains and (g–h) Short Rains in the dual-wet-season regimes.

4.7 Conclusions and Discussion

A novel method to determine the onset and cessation of rainy seasons across a wide range of GHA's climates has been developed, tested, and discussed for representative examples. It neither requires a priori assumptions on the number of the rainy seasons nor on suitable thresholds, and enables to estimate the stability of rainfall modes and uncertainties in onset and cessation dates in the GHA. The method was applied to estimate the seasonality and trends based on CHIRPS and station data for the period 1983–2013. The following main conclusions can be drawn:

1. The application of the method to three exemplary stations demonstrates the meaningfulness of the methodology for different rainfall regimes in spite of some peculiarities due to local effects. Unlike many previous methods, our approach can also estimate the uncertainty in the onset date, cessation date and duration of the rainy seasons.

2. The classification of seasonal regime (number of rainy seasons) for the GHA is in good agreement with previous results. The areas with low stability of rainfall seasons correspond to regions characterized by known disagreements in terms of rainfall regimes between different data sets and studies. Patterns of onset and cessation dates estimated by the new method are consistent with known regional characteristics of rainfall in the GHA, including, for example, the effects of coastlines and mountains.

3. The comparison of the adjusted climatology of rainy season onset and cessation to the traditional calendric definition (e.g., MAM and OND) reveals that the latter is only valid for a limited latitudinal and altitude range. Deviations can reach up to several months. Thus, the results provide evidence that the calendric definitions cannot always be assumed to be valid on supranational scale without appropriate adjustments.

4. The trends based on the adjusted and calendric rainy seasons do not differ in pattern, but the former possess a higher magnitude. Significant trends could be identified for the following regions: Central Sudan tends towards a wetter rainy season of constant length. In contrast, the southern part of Sudan reveals a trend towards a prolonged rainy season without significant changes in the rainfall sum. Tanzania can be divided into a southern area with a tendency towards a drier rainy season and less rainfall and a central area with a shorter rainy season. For the Long Rains, a trend towards a shorter rainy season with less rainfall can be observed in the eastern parts of the GHA. The Kenyan coast shows a consistent drying trend. For the Short Rains, a wetting trend is estimated for northern Kenya, eastern Ethiopia and Somalia.

5. Irrespective of the seasonality, the shortening of the rainy season is predominately found in areas with a climatological cessation in April. Areas with a climatological cessation during the end of October and beginning of November coincide with areas showing trends towards later cessation dates.

6. CHIRPS and the station data sets exhibit discrepancies in terms of rainfall seasonality, onset and cessation dates primarily in coastal areas and areas with

complex topography. A large area with differences in season regime between stations and the gridded product covers the border between regions with single-wet-season and dual-wet-season climates as well as climates with rains from warmer clouds. These differences can also be identified in the trend estimation.

While the seasonal pattern agrees well with previous studies Nicholson (1996); Herrmann and Mohr (2011); Yang et al. (2015); Dunning et al. (2016), differences to the first three studies may be attributed to the use of different data bases and classification criteria. For example, Nicholson (1996) only distinguished according the number of rainfall peaks. Herrmann and Mohr (2011) used a more detailed classification, which distinguished between the number of rainy seasons and the number of the associated peaks, resulting in a classification of up to eight classes. Comparing our results with those of Yang et al. (2015) and Dunning et al. (2016), several regions differ in terms of rainfall regime, namely, northeastern Ethiopia, the coastal and mountainous parts of Kenya and parts of Uganda. Dunning et al. (2016) characterized all of these regions as single-wet-season or dual-wet-season in different satellite data sets. The different assessment can be partially attributed to diverse algorithms of the satellite products and the underlying representation of the local conditions (e.g., topography). Additionally, Dunning et al. (2016) pointed out that the harmonic analysis may suggest a dual-wet-season regime at grid points where one of the wet seasons is weak and features low rainfall totals. Thus, and despite the classification as a dual-wet- season regime, only one rainy season can be clearly identified there. An additional reason can be the stability of the seasonality classes. At a particular location, this factor can lead to alternating seasonality classes in different years. Herrmann and Mohr (2011) pointed out that there is a gradient in temporal stability of the seasonality classification, which decreases from arid (stable) to humid (unstable) classes. The areas with differences in seasonality, when compared to Yang et al. (2015) and Dunning et al. (2016), coincide well with regions herein identified as of "unstable" classification. Observational studies on climate variability often use strict calendric time periods (e.g., MAM, OND), which may be valid at national scales and might lead to inaccuracies for enlarged areas. In some of the analyzed countries, calendric definitions also vary on subnational scale. On the contrary, modeling studies require basic information on rainy seasons for large (sub-)domains. The adjusted definition of rainy seasons captures all commonly used calendric definitions and agrees with patterns from supranational studies as derived by Liebmann et al. (2012) and Dunning et al. (2016). Consequently, the method can be applied in both observational and modeling studies. In contrast to anomaly-based methods like that applied by Dunning et al. (2016), the method introduced in the present study can also be used on sub-annual timescale and it can also be applied to forecast products. For the application in near-real time, the method either requires at least 20-day forecasts or tapering with at least four climatological pentad values. Unlike in Boyard-Micheau et al. (2013), the calibration can be implemented locally at the particular station/grid point. For example, the method is less reliable for regions without a clear seasonal cycle, like very arid (e.g., northern Sudan, parts of Puntland in Somalia) and very humid regions (e.g., DR Congo). In general, the method does not distinguish between rainfall events from local rainfall triggers (e.g., sea breeze) and large scale atmospheric processes (i.e., TRB), thus knowledge of local atmospheric conditions is always required. Compared to agronomic definitions (e.g., Philippon et al., 2015), the method leads to different results due to the different objectives.

Crop growth requires a minimum rainfall amount over a specific time period, thus their results can lead to longer rainy seasons in humid regions and shorter seasons in arid regions compared to the results of this study. In terms of observed trends, the analysis for the estimated rainy season onset and cessation enables a more detailed view on the development of the rainy seasons in the GHA. Overall, the trends of rainy season cessation are more robust, while onset trends show weaker magnitudes and varying significance. While the results suggest trends towards a more intense rainy season in central Sudan, trends in South Sudan and southern parts of Sudan suggest a prolonged rainy season due to a later cessation. Ethiopia reveals predominantly wetting trends in the western parts, despite of single stations with opposed trends. The rainy season tends to weaken and shorten in DR Congo, west-central Uganda and large parts of Tanzania. The results fit in well with the observed increase of greenness over eastern Sahel (e.g., Herrmann and Mohr, 2011) which is linked to the West African monsoon. Seleshi and Zanke (2004) detected both, a widespread (but insignificant) rainfall increase and dramatic decreases at single stations in Ethiopia. A recent drying trend is observed in west-central Uganda and DR Congo (Zhou et al., 2014; Diem et al., 2014a; Hua et al., 2016). For the dual-wet-season regimes of the GHA, the results point towards longer Short Rains, either due to a regionally earlier onset or a later cessation in the lowlands. A weaker reversed signal towards shorter Long Rains can be assumed for the same region. To date, several studies have identified an abrupt decline in the Long Rains since the end of the 1990s (e.g., Lyon and DeWitt, 2012; Maidment et al., 2015; Schmocker et al., 2016). Williams and Funk (2011) attributed the descending trend to a major shift in the Walker Circulation, which results in an increased subsidence over the GHA that leads to persistently drier atmospheric conditions. Several studies ascribe the increase of the Short Rains to an enhanced SST gradient of the Indian Ocean (e.g., Kabanda and Jury, 1999; Zorita and Tilya, 2002; Cook and Vizy, 2013; Liebmann et al., 2014). The region around Lake Victoria does not follow these trends irrespective of the regime. Several stations point towards wetter conditions, while CHIRPS does not underline these results. As the seasonal regime is unstable here, the region might require a more detailed analysis, which goes beyond the scope of this study. Further investigations could include a more detailed view on the seasonal stability and the associated trends. The comparison of CHIRPS and station data reveals recurring biases of the satellite product in particular subregions. In mountainous and coastal subregions, CHIRPS shows shortened rainy seasons due to well-known underestimations of "warm rainfall" (Dinku et al., 2007; Kimani et al., 2017). In regions with a modest or short break between the rainy seasons, CHIRPS tends to overestimate rainfall during the break, leading to an overestimation of single-wet-season regimes. The agreement between stations and CHIRPS is best when high intensity rainfall periods can be detected. The new criterion can be adjusted and applied locally and requires solely a time series of about 30 years of precipitation for calibration. Thus, the method can also potentially be used in the context of identification and correction of biases in climate model simulations. The additional information on the onset and cessation of rainy seasons might allow identifications of possible season shifts in present and future climate scenarios.

5 Using seasonal rainfall clusters to explain the interannual variability of the rain belt over the Greater Horn of Africa

The intraseasonal to decadal variability of the four rainy seasons of the GHA can largely be understood as anomalies related to the location, intensity and width of the TRB. In an early approach, Riddle and Wilks (2013), introduced two statistical indices that describe the northward migration of the TRB, including its relevant meridional jumps, and allow for a relation to the development of the Somali Jet. In this study, the methodology of Riddle and Wilks (2013) for the full seasonal cycle to reassess the interannual variations and trends of seasonal cycle over the GHA region is used. Another focus is put on the circulation anomalies related to interannual variations of the Msimu and Long Rains.

Some of atmospheric features, which are relevant for the circulation of the Msimu and Long Rains are shown in Figure 5.1. The Msimu rains are part of the southern African solstitial rainy season. A main feature of the latter is the Angola Low (AL). The approximate locations of the TRB in January and the AL are given in Figure 5.1. On the synoptic scale, the AL is associated with increased westerly moisture fluxes from the southeast Atlantic and penetration of humid north-easterlies from the Indian Ocean deep into the outer tropics (black arrows in Figure 5.1, Munday and Washington (2017)), enhancing convection in the AL area. The above-mentioned westerly flow extends northward to the Congo Basin and can modulate the location of the meridional branch of the TRB (cf. Figure 5.1). In connection with a passing upper-level wave from the mid-latitudes, the AL can intensify and trigger the formation of TTTs (Todd and Washington, 1999). TTTs act as an important source of rainfall for southern Africa (Todd and Washington, 1999; Fauchereau et al., 2009). The associated convergence of moisture over southern Africa can suppress convection over Tanzania (Manhique et al., 2011).

The Long Rains show a weak spatio-temporal coherence, which also varies from month to month (Camberlin and Philippon, 2002; Zorita and Tilya, 2002; Nicholson, 2017). This may result from multiple jumps that are characteristic for the northward migration of the TRB from location during the Msimu Rains to the location at the end of April over eastern Africa (cf. Figure 5.1, Riddle and Cook, 2008; Riddle and Wilks, 2013). Both studies highlight that these jumps are connected with different stages of the development of the Somali Jet. Riddle and Cook (2008) showed that early stages of the Somali Jet (referred to as nascent) coincide with heavy rainfall over Ethiopia in April. Particularly in March and April, wet conditions are related to equatorial westerly wind anomalies in the middle and lower troposphere over the Congo Basin (e.g., Zorita and Tilya, 2002; Finney et al., 2019).

The present chapter will expand the Riddle and Wilks (2013) method to describe the mean TRB location and associated circulation and moisture transport anomalies during the full seasonal cycle. It will be demonstrated that the applied method is suitable to describe anomalous TRB locations and related circulations at intraseasonal to decadal time scales. By considering various synoptic- to large-scale atmospheric and SST fields, potential explanations for atypical Msimu and Long Rains are proposed. In Section 5.1, the applied method after Riddle and Wilks (2013) is explained. Section 5.2 discusses the seasonal mean evolution of the TRB and related circulations while Section 5.3 focusses on interannual variability for the entire seasons, as well as related anomalies of characteristic features of the Msimu and Long Rains. Section 5.4 provides conclusions and discussion.

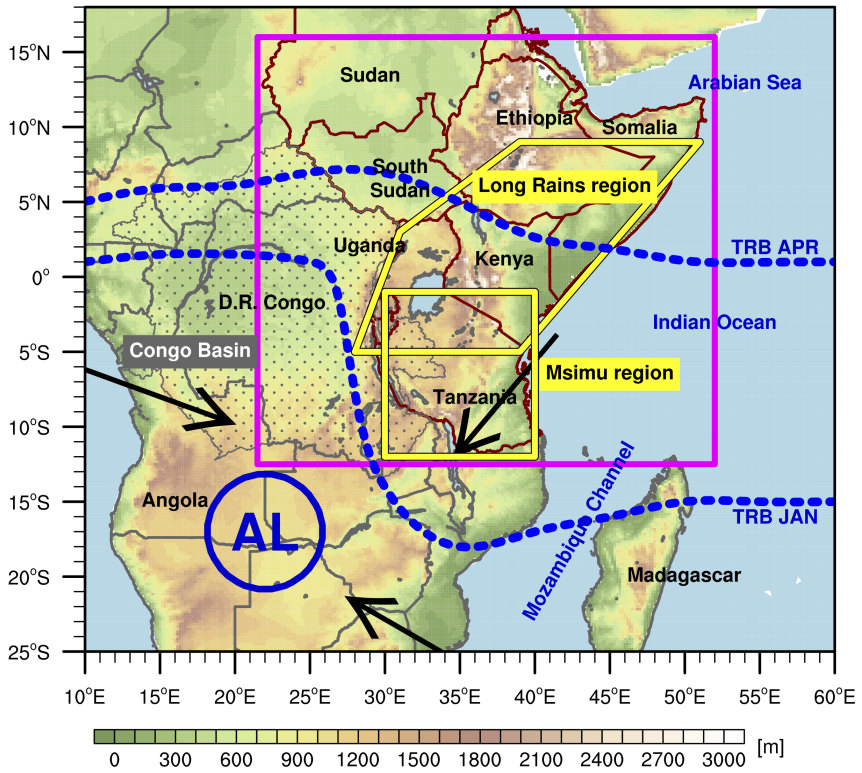

Figure 5.1: Topography of the study region (magenta rectangle) and its vicinity. Dark red lines mark the countries of the GHA. Yellow polygons delineate the regions used for the boreal winter Msimu rains and boreal spring Long Rains. The stippled area encircles the Congo Basin. The blue dashed lines indicate the locations of the TRB in January and April, respectively (adapted according to Laing and Evans (2008)). AL depicts the location of the Angola Low during the Msimu rains. Black arrows denote major moisture transport pathways in January (adapted from Munday and Washington (2017)). Topography was interpolated from the ETOPO1 1 Arc-Minute Global Relief Model Amante and Eakins (2009)

5.1 The Index Approach

The spatio-temporal characteristics of the TRB vary from year to year. Riddle and Wilks (2013) introduced two statistical indices to describe the rainfall distribution of the

TRB during its northward migration. Both indices are based on a principal component analysis of the rainfall time series to extract the most important patterns of variability. Riddle and Wilks (2013) used daily rainfall totals instead of anomalies and thus explicitly included the seasonal cycle. Since rainy seasons over the GHA are dominated by the migration of the TRB, the leading principal components capture large-scale variations associated with the seasonal modality of rainfall and TRB characteristics like location or intensity (Riddle and Wilks, 2013). In the present study, the first seven eigenvectors, which account for 34% of the total variance of rainfall (cf. Figures S7 and S8), were taken according to the Rule N significance test (Overland and Preisendorfer, 1982). The Rule N assumes that only a leading subset of the estimated eigenvalues reflects statistically significant patterns, while the remaining eigenvalues cannot be distinguished from uncorrelated random noise. This subset is determined by comparing test metrics of the estimated eigenvalues to test metrics of eigenvalues of randomly generated datasets of the same dimension. With this statistical approach, the TRB can be conceived as an smooth envelope encompassing the rainfall signatures of bulk activity of convective systems as a function of time in an area.

The Seasonal Location Index (SLI) is defined as a daily angle in radian between the first two principal components in clockwise direction to avoid a discontinuity at 2π. The index is constructed analogously to the phase component of the MJO index introduced by Wheeler and Hendon (2004). From an illustrative point of view, the evolution of the SLI can be depicted as a seasonal clock, where the vector resulting from the leading two principal components shows the seasonal 'time'. Low SLI values indicate that the TRB is located in a southern position. The SLI increases as the TRB progresses northward and decreases as the TRB migrates southward. By analyzing the annual distributions of SLI values and anomalies, impacts of anomalously fast or slow progressions of the TRB on GHA rainfall can be studied.

The Rainfall Cluster Index (RCI) is an integer-valued index that consists of clusters resulting from a cluster analysis. The input of the cluster analysis is the rainfall field reconstructed from the leading seven eigenvectors. Thus, each RCI value represents a typical spatial pattern of the daily precipitation over the GHA. The seasonal cycle can be conceived as a sequence of typical precipitation patterns identified by RCI values. Riddle and Wilks (2013) used six clusters, which were assigned by the k-means clustering algorithm according to the cosine metric. The advantage of this metric is that it reflects the (dis)similarity of two vectors, but it neglects the amplitude of the respective vectors.

The k-means algorithm requires predefined cluster centers as seeds or a predefined number of clusters, which is often subjectively determined. To minimize this aspect, a two-step approach to obtain the best-differentiated partition of clusters was used. First, we applied the agglomerative-hierarchical (AHC) approach which does not require a predefined number of clusters and always results in a single and reproducible partition (Wilks, 2011). This approach considers each observation as a 'micro' cluster and produces a multilevel hierarchy, where clusters at one level are joined pairwise as clusters at the next level. The number of clusters is obtained by determining the highest distance (dissimilarity) between two levels (difference between two clusters). A weakness of this approach is that the cluster members are fixed once they are included into a particular cluster even if a different cluster is more suitable in an advanced stage of the clustering procedure. To alleviate this disadvantage, a k-means clustering was applied subsequently with the number of clusters k 'proposed' by the AHC algorithm as

seeds. The k-means approach assigns each observation to one of k groups according to a distance measure (Wilks, 2011). When applied to the leading seven eigenvectors, the AHC algorithm proposed partitions of five to seven clusters. However, a comparison to other satellite products (e.g., GPM, Huffman et al., 2019) has shown that only the partition into six clusters revealed comparable results. Following several sensitivity tests, both regarding the separation between clusters and their physical interpretation, six clusters were chosen, which agrees with the choice of Riddle and Wilks (2013).
. In the context of trends and interannual variability, this approach offers several advantages. By construction, neither the value of SLI nor the presence of a particular RCI cluster is restricted to fixed calendar months. The composition of clusters during a specific month can indicate anomalous stages of the progression of the TRB. As clusters also reflect the spatial distribution of rainfall, changes in the temporal persistence of a cluster can provide hints towards trends of rainfall in particular regions.

5.2 Characterization of the annual cycle through SLI and RCI

In this section, the mean seasonal variability of the two indices SLI and RCI is examined and related to the different stages of the migration of the TRB. The daily climatological SLI values and percentages of the occurrences of RCI values are presented in Figure 5.2a. All series were smoothed by a 11-day running mean. Figure 5.2b–g shows the rainfall patterns associated with the six clusters. The rainfall patterns were calculated by averaging rainfall for all days belonging to a given RCI value. To highlight areas for which a cluster is associated with wet conditions, statistically significant positive differences between the rainfall distribution of a given cluster and the distribution of all rainy days were estimated using the Wilcoxon-Mann-Whitney-Test (Helsel and Hirsch, 2002). Note that instead of numbering the cluster from 1–6 as in Riddle and Wilks (2013), the clusters are addressed by two suggestive characters that reflected their region of maximum rainfall. For example, the first cluster is subsequently named "SE" since rainfall is concentrated in the southeastern part of the GHA. For this and the denomination of the remaining clusters, the reader is referred to the heading of panels (b)–(g) in Figure 5.2.
At the beginning of the year, the SLI values are close to 1, which corresponds to the Msimu rainy season. The northward migration of the TRB, characterized by an increase of the SLI, starts between the Julian Day (JD) 80 and 100 (i.e., between end of March and beginning of April), which can be attributed to the onset of the Long Rains. This northward movement goes along with a steady increase of the SLI until it reaches its maximum value of 5 in June. Until September, the SLI remains in the range between 4.5 and 5. The period June–September agrees with the timing of the Sahel/Kiremt rainy season. The following southward migration of the TRB and the corresponding Short Rains are captured by decreasing values of the SLI during JD 260–320 (i.e., mid-September to mid-November).
The frequent occurrence of the South-East (SE) and South-West (SW) RCI clusters dominates the Msimu Rains (turquoise and magenta lines in Figure 5.2a) between November and the beginning of April (JD 300 to JD 100 of the following year). Rainfall in cluster SE is concentrated at the southern and eastern edge of Tanzania

(Figure 5.2b). Figure 5.3 shows cluster-specific moisture flux vectors and moisture divergence. The former also represent the mean low-level flow due to the fact that the bulk of the moisture is concentrated in the lower troposphere. For cluster SE, northeasterly winds from the Arabian Sea and southeasterly flow southeast of Madagascar leads moisture convergence between 5 and 15°S, longitudinally stretching across the Tanzania-Mozambique border into the southernmost Congo Basin. For cluster SW, rainfall is concentrated over the southern hemispheric Congo Basin (Figure 5.2c). Cluster SW shows weaker north-easterlies over the Arabian Sea, stronger easterlies around the northern tip of Madagascar and Tanzania, thus leading to a much reduced moisture convergence over the southern GHA (Figure 5.3b). Rather, moisture convergence is concentrated over the southern Congo Basin.

The Equatorial East (EE) cluster occurs most frequently during both the increase of the SLI in April/May and the decrease in October/November (Figure 5.2a, red line). As indicated by the statistically significant region, this cluster reflects rainfall in equatorial East Africa (Figure 5.2d), and thus it can be attributed to the Long and Short Rains, respectively. During these periods, the northeasterlies over the Arabian Sea are absent (Figure 5.3c), but the southern-hemispheric branch of the Somali Jet is clearly discernible. It leads to a northwestward moisture flux directed and converging over equatorial eastern Africa including the Lake Victoria area.

The Equatorial West (EW) cluster shows increased frequencies in May/June and in September/October, and represents the equinoctial rainy seasons over the Congo Basin (Figure 5.2a, grey line, and Figure 5.2e). Figure 5.3d shows the interhemispheric moisture flux associated with the Somali Jet and moisture divergence over the GHA region, and convergence over the Congo Basin and Lake Victoria. The Indian-Ocean (IO) cluster shows a similar seasonal cycle as the EW (Figure 5.2a, yellow line), but the relative frequencies differ. Cluster IO occurs more frequently during May/June than in September/October, the opposite is true for cluster EW with lower percentages in May/June than IO and greater in September/October. The GHA region is overall dry (Figure 5.2f) and there is also moisture divergence over Uganda and the Congo Basin (Figure 5.3e). Cluster IO is peculiar in that it can occur in any month of the year (cf. Figure 5.4) and is not associated with wet anomalies anywhere in the study region (Figure 5.2f). The rainy season in the northern GHA starts with increasing frequency of cluster North (NO) in late May and June and is fully established in July and August (Figure 5.2g, blue line). The retreat starts in late September and ends at the beginning of October. Cluster NO represents the Kiremt rainy season. At this time, the Somali Jet is fully established and transports moisture away from the GHA region over the Arabian Sea towards India (Figure 5.3f). Apparent moisture sources for precipitation in northern Ethiopia and Sudan are the Congo Basin, but also the Red Sea area consistent with Viste and Sorteberg (2013).

In summary, the six RCI patterns reflect different stages of the seasonal cycle for both single-wet- and dual-wet-season regions. The results agree with Riddle and Wilks (2013) during the northward migration of the TRB within the first half-year. The southward migration can be described with the same set of clusters. Note, however, that a day with the same cluster value during the Long and Short Rains just signifies that the large?scale rainfall patterns are similar, yet spatial details, amplitudes, and the underlying dynamic forcings will usually differ. Nonetheless, the approach allows assigning rainfall clusters to the four major GHA rainy seasons. As will be shown below, anomalous dry or wet rainy seasons can be related to anomalous frequencies in

daily cluster occurrence and also be interpreted physically through the assignment of the large-scale circulation to seasonal clusters.

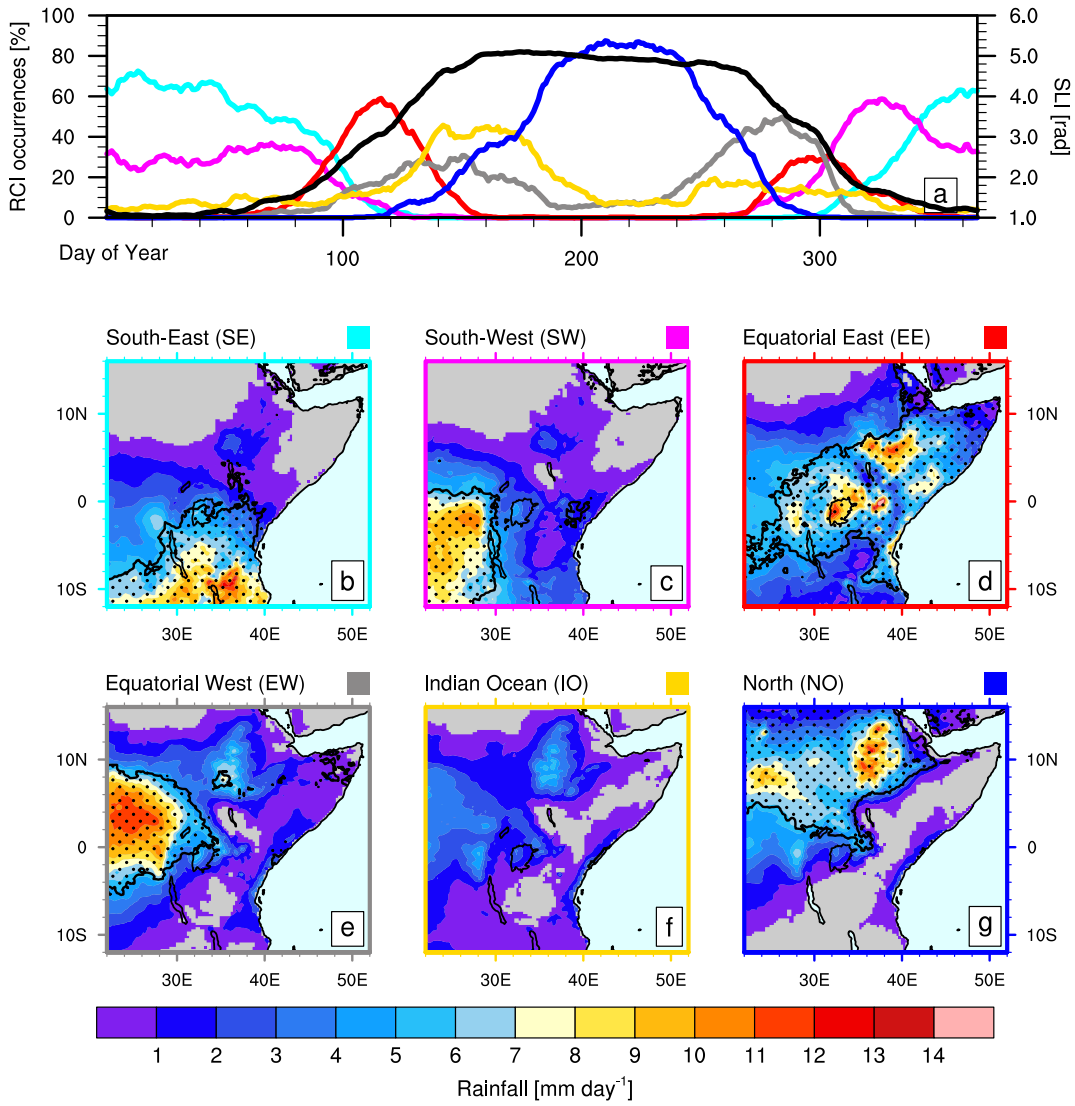

Figure 5.2: (a) Daily climatology of the SLI (black line) and relative climatological frequencies of the RCI (colored lines). The daily values are smoothed by 11-day running averages. Line colors in (a) refer to the colors of the clusters, which are denoted by the frames and squares in (b)–(g). (b)–(g) Mean daily rainfall in mm day^{-1} during each cluster (colors) for the period 1981–2018. The stippling marks areas, where the rainfall distributions differ significantly from climatology at the 5%-level according to the Wilcoxon-Mann-Whitney-Test.

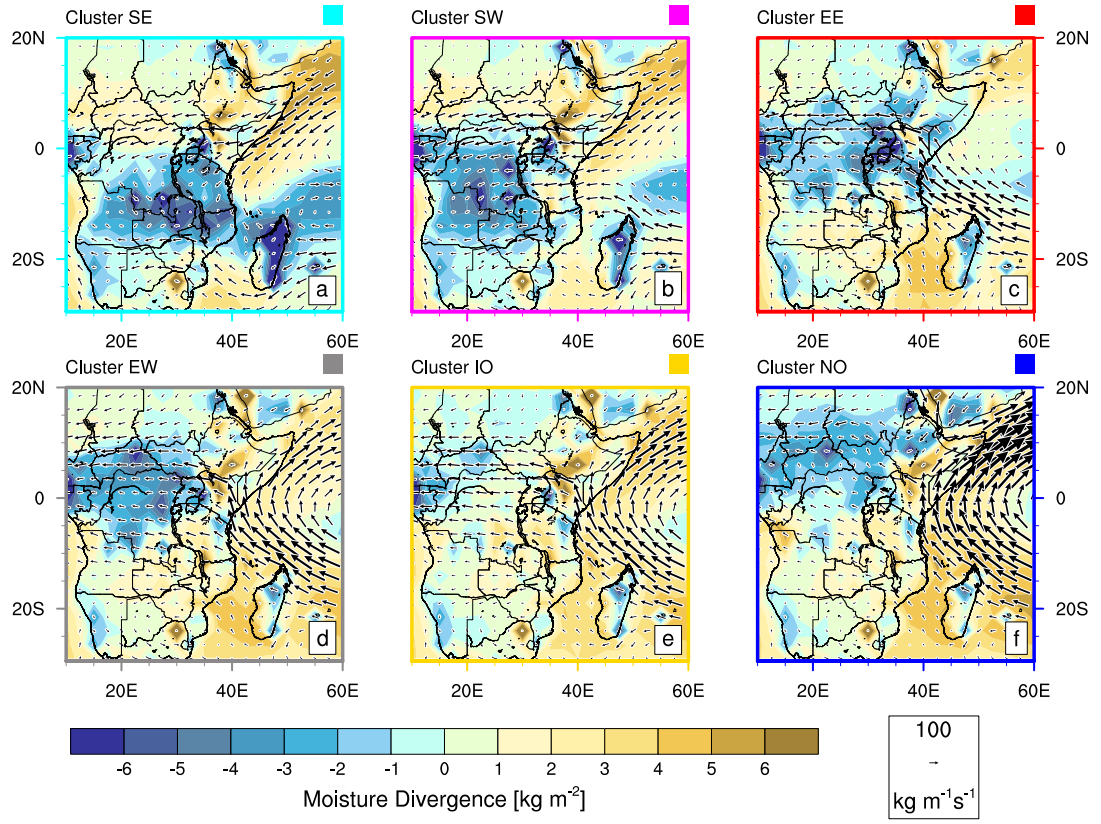

Figure 5.3: Average atmospheric circulation for each cluster (a)–(f). Colors show the vertically integrated moisture flux divergence, arrows mark the direction and strength of the vertically integrated moisture fluxes.

5.3 Interannual anomalies of seasonal progression and cluster-related circulation anomalies

In the following section, first the year-to-year variations of cluster frequencies are examined. In Sections 5.2 and 5.3, composite anomalies of the large-scale circulation associated with the occurrence of each cluster during the Msimu and Long Rains are analyzed, respectively.

5.3.1 Year-to-year variations in cluster frequency

The relative frequencies of the individual clusters per calendar month are shown in Figure 5.4 for all years between 1981 and 2018. A similar composition of clusters in consecutive months points to coherent seasons. This is, for example, the case for the Msimu Rains from December to March (Figure 5.4a-c, l). This rainy season can largely be explained by three clusters only; clusters SE and SW account for up to 90%, while around 6% can be attributed to cluster IO. July and August as part of the Sahel/Kiremt rainy season are also largely composed of three clusters (Figure 5.4g,h). Here, cluster NO is very dominant, more so than the prevailing SE cluster in the Msimu rainy season. June and September, usually also assigned to the Kiremt Rains, have

significantly different relative frequencies of the same clusters. These solstitial rains are characterized by a relative stationary location of the TRB in zones of unimodal rainfall distribution (). During the migratory phases of the TRB in boreal fall and spring, cluster composition changes progressively from month to month. Consequently, the Long Rains (MAM) and Short Rains (OND) are less coherent. Thus, while discussing the Msimu Rains for December–March, we restrict the analysis of the Long Rains to the wettest month April (Nicholson, 1996) in subsection 5.3.3.

Figure 5.4 also displays striking features of interannual variability for certain clusters in particular years. For example, the El Niño event in 1997 can be recognized by anomalous cluster composition in the months October to December (Figure 5.4j-l). In particular, this El Niño event reveals an anomalously frequent occurrence of cluster EE in October and November and of cluster SE in December (Figure 5.5a). Both clusters have in common that they favor rainfall in the eastern parts of GHA in the above-mentioned months (Figure 5.2). Contrarily, clusters leading to rainfall in the Congo Basin, that is, clusters SW and EW are suppressed in OND 1997. However, other El Niño events in the time series do not exhibit pronounced deviations from the mean cluster composition. Only in October 1982 an anomalously high proportion of cluster EE can be observed (Figure 5.5a).

Another example is the exceptional drought period during the Short Rains in 2010 and the following Long Rains in 2011 (Dutra et al., 2013; Lott et al., 2013) Stott, 2013. In October 2010, clusters EW, IO and NO dominate the rainfall distribution, while clusters SW and EE occur infrequently compared to the average October (Figure 5.5b). In November and December 2010, clusters SE and SW dominate the monthly rainfall, while cluster EE is suppressed (Figure 5.5b). In April 2011, the frequency of the wet cluster EE remains low, while clusters SE, SW, EW and IO prevail instead (Figure 5.5b). Overall, for both rainy seasons, clusters typical of earlier and later stages of the seasonal progression are anomalously frequent, while the occurrence of cluster EE is reduced. This is consistent with a delayed, but fast passage of the TRB from the northern into the southern hemisphere and vice versa during the 2010 Short and 2011 Long Rains, respectively. This pattern, which appears to be associated with recent La Niña events, represents a dangerous sequence of back-to-back East African droughts (Funk et al., 2018). For example, note that the sequence of small EE coverage in October and April was repeated in 1999/2000 and 2016/2017 (Figure 5.4).

For each month, the time series of cluster frequencies were tested for significant trends. In general, only a few trends in the cluster composition were found to be statistically significant (5%-level) according to the Mann-Kendall test (not shown). The only consistent trends occur for the Short Rains: Cluster EE occurs significantly more frequent in October and November in accordance with an observed wettening of the Short Rains, while cluster SW days are significantly reduced.

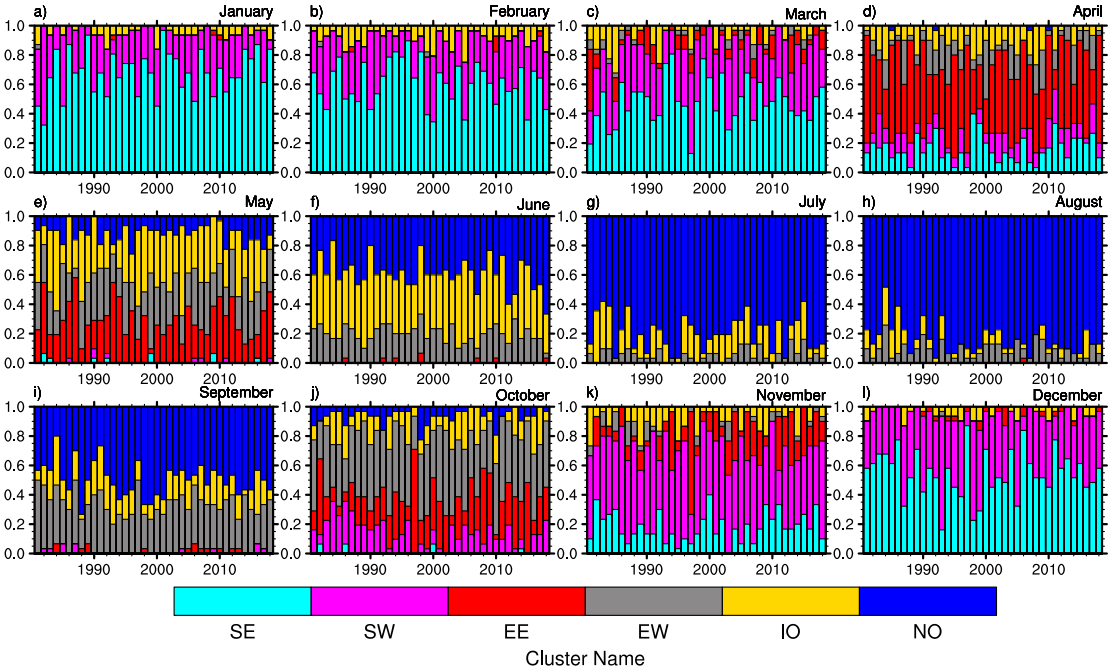

Figure 5.4: Relative frequency of clusters per year for each calendar month (a)–(l). The color of each cluster is indicated in the bar and corresponds to the colors in Figure 5.2.

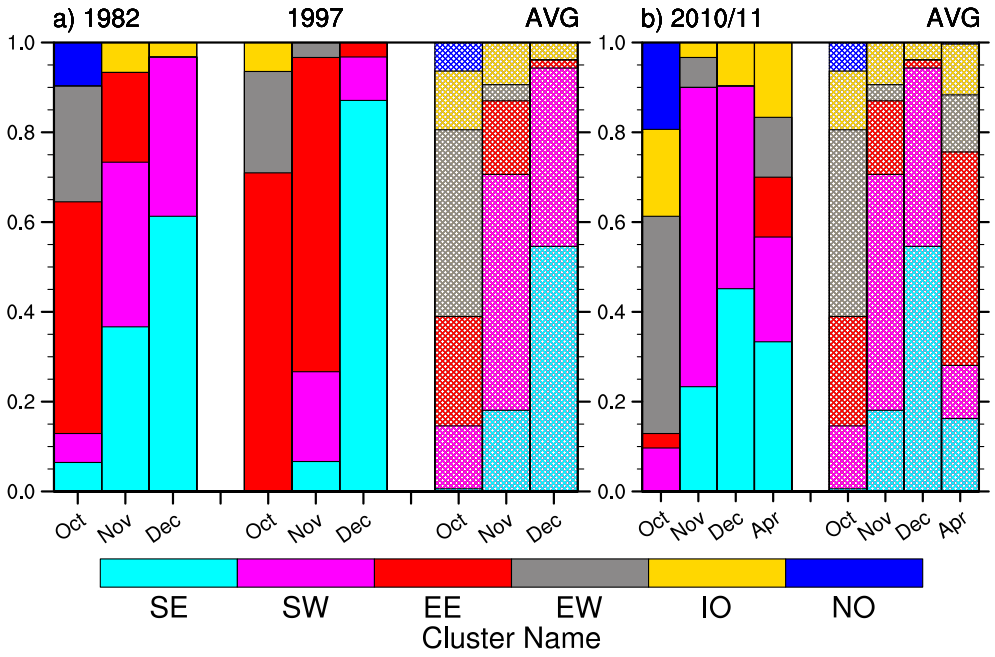

Figure 5.5: Comparison of relative frequencies of clusters during (a) El Niño events 1982 and 1997 and (b) the drought period 2010/2011 (solid bars) to the average cluster frequencies (hatched bars) for the months October, November, December, and April. The color of each cluster is indicated in the bar and corresponds to the colors in Figures 5.2–5.4.

5.3.2 The Msimu Rains

In this section, we will investigate the role of the frequency of occurrence of the clusters on rainfall anomalies during the Msimu Rains and the cluster-related circulation anomalies. Here, the period December–March (DJFM) during which mostly the three clusters SE, SW and IO occur will be considered. Figure 5.6 shows DJFM rainfall anomalies for southern GHA (see yellow rectangle in Figure 5.1 and Figure 5.6b), the anomalies of cluster frequencies, and three maps displaying differences in rainfall anomalies with respect to seasonal climatology between seasons exhibiting above- and below-average cluster occurrence. Clusters SE and SW reveal an anti-correlation to each other, which is strongest before 2010 (Figure 5.6b). The late 1990s show the strongest interannual variability of these two clusters. Msimu Rains with frequently occurring SE cluster lead to wetter conditions in Tanzania, while dryness prevails over the Congo Basin (Figure 5.6c). The Pearson linear correlation between anomalies of SE cluster occurrence and rainfall is 0.8 (Figure 5.6b). Vice versa, Msimu seasons with positive anomalies of SW cluster occurrences favor dry conditions in Tanzania (r=-0.8, cf. Figure 5.6b) and enhanced rainfall over the Congo Basin (Figure 5.6d). Cluster IO occurs less frequent than the previous two clusters (Figure 5.4a-c,l) but with pronounced positive anomalies in particular years (Figure 5.6b). Highest anomalies prevail in the 1980s and 1990s, while the magnitudes of the peaks are generally reduced after 2005. Frequent days in this cluster lead to dryness in most parts of Tanzania (r=-0.5, cf. Figure 5.6b), southern Kenya and Uganda (Figure 5.6e). In contrast to cluster SW, this cluster does not lead to extensive wetness over the Congo Basin.
To understand how anomalous frequencies of clusters are related to regional circulation anomalies, composite differences of vertically integrated moisture flux, flux divergence, and geopotential at the 700-hPa level between days in a particular cluster and seasonal climatology were calculated (Figure 5.7). Cluster SE is characterized by enhanced moisture convergence stretching south-eastwards from eastern Zambia and Tanzania to the Mozambique Channel (Figure 5.7a). This pattern is accompanied by a cyclonic anomaly of geopotential centered over the southern Mozambique Channel. Overall, the result suggests an anomalous eastward position of the meridionalTRBand an active zonal portion over the Mozambique Channel and adjacent land areas (cf. Figure 5.1, Figure S9a). Consequently, an increased occurrence of this cluster leads to above-average Msimu rainfall. In contrast, the Congo Basin experiences a drier season due to increased moisture flux divergence. Cluster SW shows an enhanced easterly divergent moisture flow from northern Madagascar crossing the Mozambique Channel, turning to more easterly anomalies, and affecting Tanzania and northeastern Zambia (Figure 5.7b, Figure S9b). This flux extends westward, converges over the Congo Basin, and is related to a near-climatological position of the meridional TRB. An anticyclonic anomaly of geopotential which is consistent with the easterlies and subsidence, is located over Madagascar. This suggests an anomalously northward position of the zonal TRB in the Madagascan region and a westerly position of the meridional TRB (cf. Figure 5.1). As a consequence, drier conditions are observed over southern GHA and wetter conditions over the Congo Basin. Stronger moisture flux divergence over large parts of eastern Africa is a striking feature of cluster IO (Figure 5.7c). This cluster reveals similarities to cluster SW, but divergence extends westward causing subsidence and drier conditions over the Congo Basin. An anticyclonic pattern of geopotential

extends from the southern hemisphere extratropics towards Angola (Figure 5.7c). This anticyclone is consistent with moisture flux anomalies around it. At its southwestern flank it appears to be associated with northwest-southeast oriented moisture flux convergence over southern Africa that is reminiscent of TTT locations (Fauchereau et al., 2009).

To better understand large-scale atmospheric and oceanic conditions associated with the cluster-specific rainfall anomalies, corresponding fields of SSTs and 200-hPa velocity potential are now discussed. Anomalous SSTs are known to impact tropical convection and upper-level divergence at larger spatial scales not instantaneously, but over a time span of a few weeks. To account for this, non-overlapping 14-day windows of the Msimu Rains were calculated and determined if the occurrence of a cluster had positive or negative anomalies with respect to the climatology. Two samples of SST anomalies of the previous fortnight were created and averaged; one for fortnights with subsequent 14?days with positive cluster occurrence frequencies, and one with negative cluster occurrence frequencies. Finally, the SST samples were subtracted. The SST anomalies associated with cluster SE show a gradient around Madagascar, which consists of a cold anomaly in the southwestern subtropical Indian Ocean and a warm anomaly that extends from the east African coast to the western coast of Australia (Figure 5.8a). The region of warm SSTs co-locates with negative anomalies of velocity potential in 200 hPa. The latter is equivalent to upper-level divergence and indicates anomalous large-scale ascent over the Indian Ocean. Anomalous subsidence is observed over western Africa and the Atlantic Ocean. The SST and velocity potential anomalies during cluster SW are largely mirroring those in cluster SE. SSTs south of Madagascar show positive anomalies, while the north-western tropical Indian Ocean is colder than the climatological average (Figure 5.8b). In addition, large parts of the tropical Atlantic reveal positive, partly significant SST anomalies and a pattern in the northern hemisphere Atlantic Ocean that mimics a positive phase of Atlantic Multidecadal Oscillation (Kerr, 2000). The anomalies of velocity potential reveal a consistent pattern with an ascending branch over the eastern Atlantic and a descending branch over the western Indian Ocean. The SST pattern of cluster IO reveals strong, largely significant negative anomalies over the western Indian Ocean (Figure 5.8c). Similar to cluster SW, the anomalies of velocity potential reveal a descending branch over the western Indian Ocean and an ascending counterpart over the equatorial Atlantic, which, is however, colder than average. Overall, the analysis in the section suggest that a complex interplay between changes in the tropical Walker circulation and interactions with the subtropics, as indicated by the significant geopotential anomalies in the Madagascan region, are responsible for cluster-specific changes in moisture transports and rainfall.

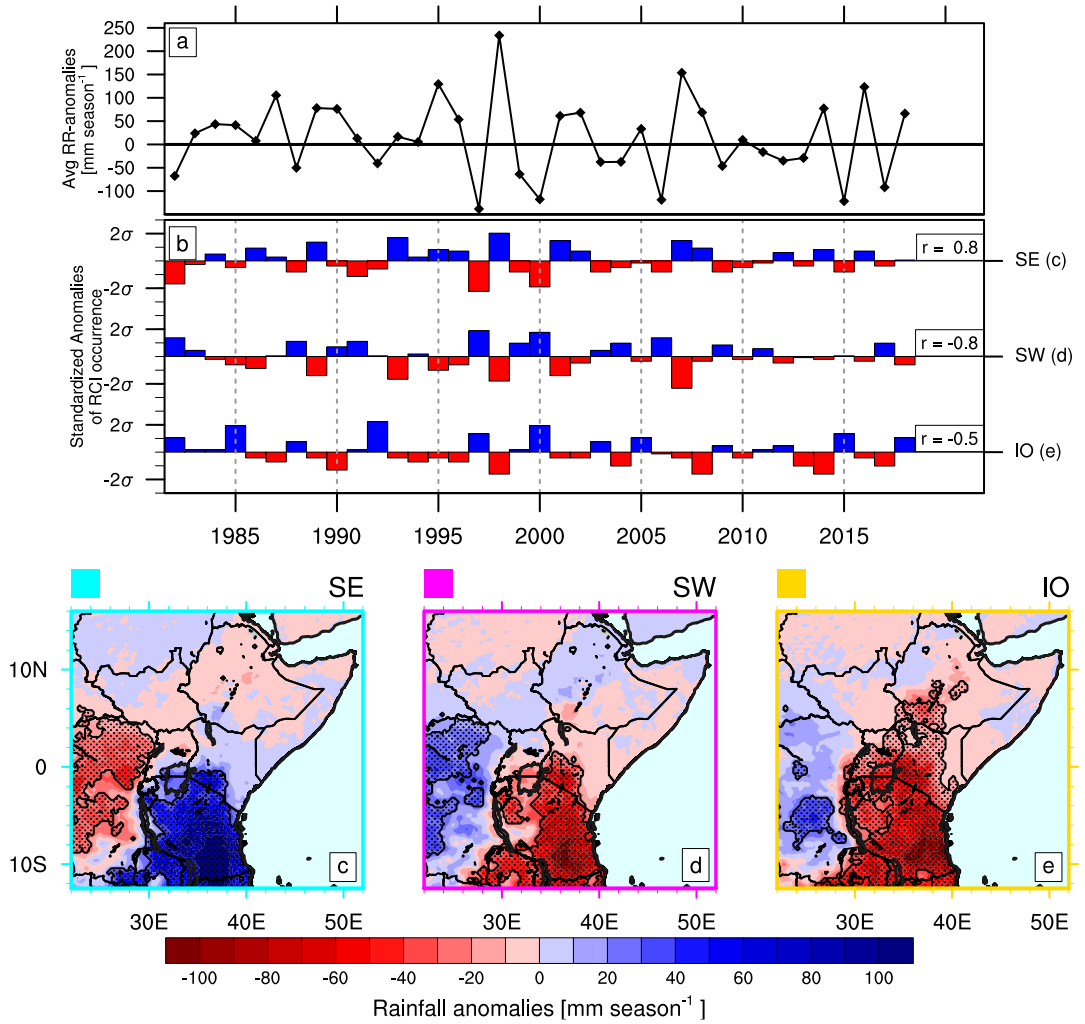

Figure 5.6: Temporal and spatial patterns of rainfall anomalies for the Msimu rainy season: (a) averaged seasonal rainfall anomalies over Tanzania (cf. yellow rectangle in Figure 5.1), (b) standardized anomalies of cluster occurrence, (c)–(e) composite maps of difference between seasonal rainfall anomalies across the region associated with (high-low) cluster occurrence. The Pearson correlation coefficients r between the time series in (a) and (b) are given on the right side of (b). Years in (a)–(b) refer to the major part of the rainy season, for example, for the year of 1982, the Msimu rainy season comprises December 1981 and January–March 1982. Statistically significant values compared to the climatology are stippled in (c)–(e).

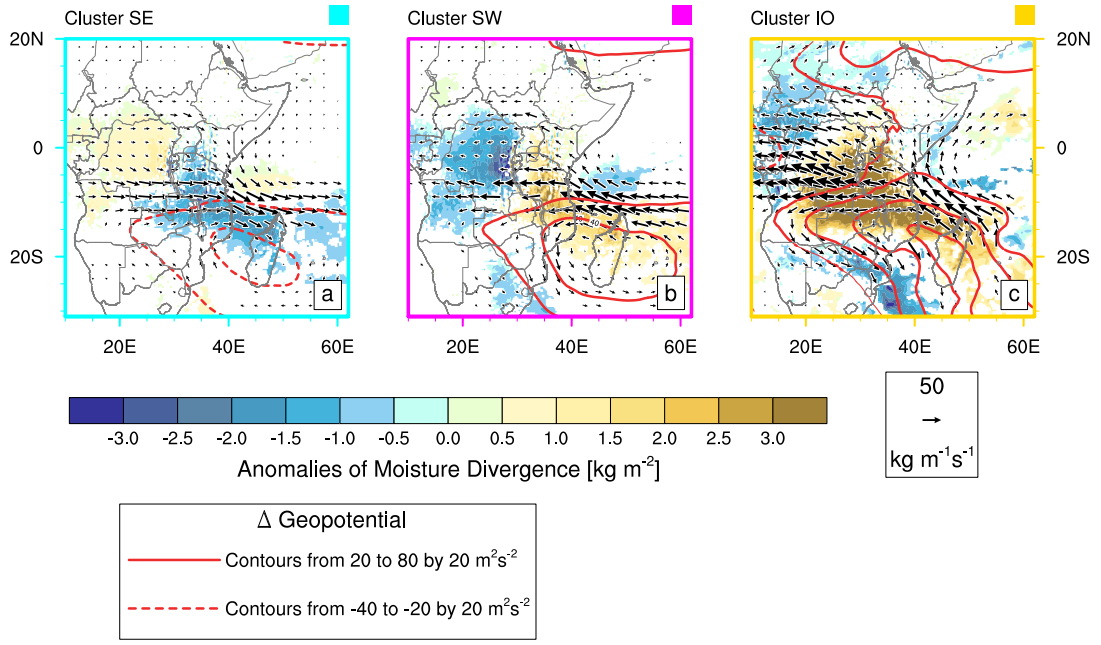

Figure 5.7: Anomalies of vertically integrated moisture flux divergence (colors), fluxes (vectors) and geopotential at the 700 hPa (contour lines) for the Msimu rainy season for the clusters (a) SE, (b) SW and (c) IO. Only statistically significant anomalies of moisture divergence and fluxes compared to the climatology at the 5% significance level are shown. Fluxes additionally require a persistence of at least 90%. Significant positive (negative) anomalies of geopotential are highlighted by red solid (dashed) contours.

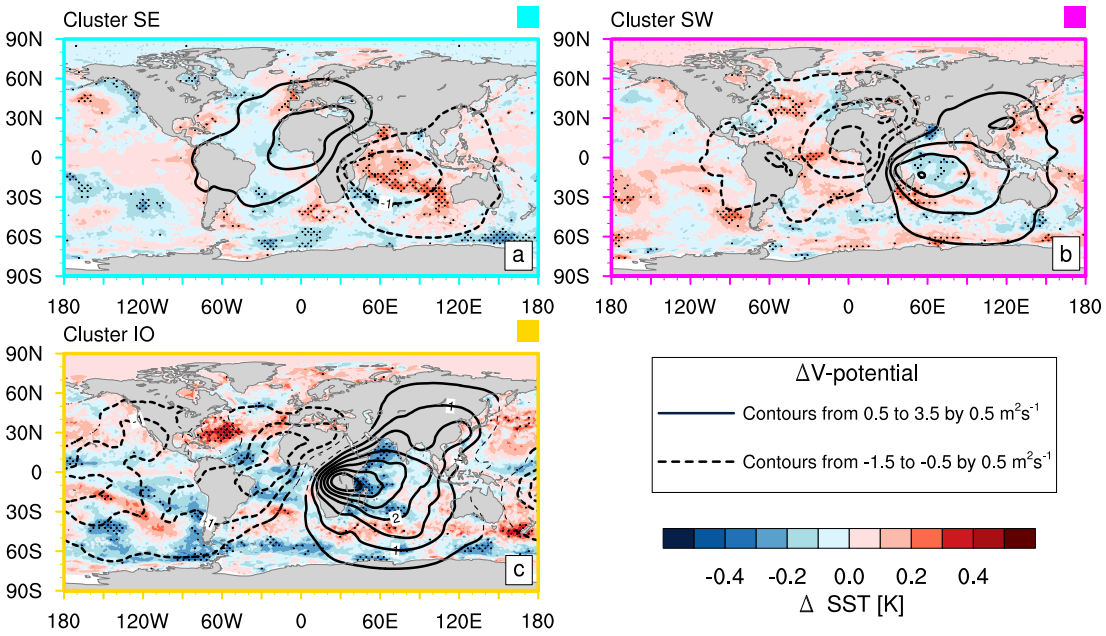

Figure 5.8: Velocity potential and SST anomalies for (a) SE, (b) SW, and (c) IO for the Msimu rainy season. Contours: Composite differences between 200-hPa velocity potential [m^2 s^{-1}] for the individual clusters and the seasonal mean. Solid lines mark positive anomalies, while dashed lines mark negative anomalies. Significant anomalies are highlighted in bold. Colours: Composite differences of 14-day lagged SST anomalies between periods of high and low cluster occurrence. Significant anomalies are stippled.

5.3.3 The April Month of the Long Rains

The transition month April is characterized by the northward progression of theTRB (Figure 5.2a). Thus, the latitudinal position of the TRB in this month plays an important role for the onset and persistence of the Long Rains over equatorial East Africa, and thus rainfall anomalies. Figure 5.9 shows the interannual variations of rainfall anomalies averaged over equatorial East Africa (see yellow polygon in Figure 5.1) and the mean SLI value and its daily distribution for April 1981–2018. The bold horizontal line marks the multi-year averaged SLI, while the solid curve and diamonds displays the average monthly SLI value for each year (Figure 5.9b). In addition, colors depict the frequency of the daily SLI value in 0.5 bins. Circles denote the monthly variance of SLI in each year. Overall, the average monthly SLI shows low interannual variability. The striking feature in Figure 5.9b is the intra-monthly variability of the SLI for given years. Low variance and a long period of TRB near the average latitudinal position occurred, for example, in 1981, 1988 and 2018. These years are mostly associated with wet conditions during the Long Rains over equatorial East Africa (Figure 5.9a, cf. Camberlin and Philippon, 2002; Kilavi et al., 2018). On the other hand, strong variations can be observed, e.g. in 1989, 1999, 2011 and 2014. In several of these Aprils, the maximum frequency of occurrence of SLI values is not observed at its long term mean, and in combination with a high latitudinal variability, these months are drier than normal (e.g. 1998–2001, 2011, 2014 in Figure 5.9a).
As revealed in Figure 5.2a, SLI values and the frequency of the six clusters have a characteristic seasonal dependence. In Figure 5.10, the focus lies on the anomalies

of cluster occurrence and the associated rainfall anomalies in April to shed light on this interdependence and on rainfall anomaly patterns. Positive anomalies in the occurrence of cluster EE match rather wet years in equatorial East Africa, while negative anomalies coincide with drought years (cf. Figures 5.9a and 5.10a). This cluster is related to positive rainfall anomalies over the Horn of Africa, most of Uganda and northern Tanzania, while negative rainfall anomalies can be observed in western Ethiopia and smaller parts of northern DR Congo (Figure 5.10d).

Although cluster EE dominates in April, its relative frequency shows high interannual variability (Figure 5.10a). Almost all positive rainfall anomalies, including the most extreme events in 1981, 1997 and 2018, coincide with above-average occurrence of cluster EE. Vice versa, negative rainfall anomalies coincide with years of below-average frequencies of cluster EE, particularly in 1998–2000, 2011, 2014, and 2017. The deficient occurrence of cluster EE is mostly balanced by higher percentages of clusters SE, EW, and IO. The occurrence of clusters SE and SW, can be interpreted as prolonged Msimu Rains (see section 5.3.2) in southern Tanzania and the southern Congo Basin and a delayed onset of the Long Rains in equatorial East Africa (Figure 5.10b-c). This observation is underlined by increased frequency of low SLI values during the respective years (e.g. 1998, 1999 and 2011, cf. Figure 5.9). Apart from 1998 and 1999, only single years show positive anomalies of SE prior to 2010, while most of the years reveal negative anomalies. Positive anomalies of these clusters in consecutive years occur predominately after 2010.

Cluster EW leads to positive rainfall anomalies over the northern Congo Basin and western Ethiopia, while dryness prevails in most parts of equatorial East Africa (Figure 5.10e). This cluster normally appears in May and June (cf. Figure 5.2a, Figure 5.4e-f), when SLI values are higher than 3.5. It is associated with a more north- and westward location of the TRB, mostly outside equatorial East Africa. This cluster frequently occurred in April during the early 1990s, but also in dry years, e.g. 1987, 2000, 2009, 2014 and 2017. The last cluster IO predominantly occurs during May and June. As it leads to rainfall outside of GHA, most of land areas remain dry (Figure 5.10f). Particularly in April, cluster IO leads to drier than normal conditions over equatorial East Africa. High positive anomalies of this cluster occurred concurrently with almost all strongest drought years. Interestingly, this cluster reveals a decadal variability including shifts around the mid-1990s and 2010, which corresponds to the time period of an abrupt decline of the Long Rains (Williams and Funk, 2011; Lyon and DeWitt, 2012). At the same time, the SLI shows particularly high variance values (Figure 5.9b). These results suggest that abundant rainfall in April is characterized by frequent EE clusters and related low SLI variability, whereas poor rainfall is associated with high SLI variability. The latter manifest itself in some years by frequent SE and SW cluster occurrence with the TRB predominantly south of the region or by frequent changes of cluster regimes and a wide latitudinal intra-monthly variability of the TRB causing intermittent wet spells in equatorial East Africa.

In the following, anomalies of moisture divergence, vertically integrated moisture fluxes and geopotential at 700 hPa are discussed in order to identify possible causes for anomalous cluster occurrences. Cluster EE can be regarded as the climatologically expected circulation type for the Long Rains (cf. Figure 5.2a, d). The climatological feature of this circulation is the 'nascent' Somali Jet, that is, a strong jet from the southeast but still without the zonal branch across the Arabian Sea (cf. Figure 5.3c). Over the latter, the wintertime northeasterlies already disappeared. The composite

differences in Figure 5.11c show a weakened easterly component of the nascent Somali Jet and weaker Turkana Jet leading to anomalous convergence of moisture and enhanced rainfall in the equatorial East Africa. The geopotential does not exhibit significant deviations except for a negative anomaly over the Arabian Peninsula, a region recently highlighted by Wainwright et al. (2019). Unlike most previous studies, Figure 5.11c emphasizes the potentially important role played by westerly moisture transports from the Congo Basin (cf. Finney et al., 2019).
In case of clusters SE and SW, strong northeasterly anomalies of moisture fluxes prevail and deflect the nascent Somali Jet towards the southern hemisphere. Cluster SE is characterized by northeasterlies over Somalia and the adjacent Indian Ocean that cross the equator while turning into northwesterlies (Figure 5.11a). As a consequence, the nascent Somali Jet does not reach the equatorial region, but converges in central-southern Tanzania. The geopotential shows positive anomalies over the northern GHA and southern Africa. The northwesterly component in the southern hemisphere are replaced by northeasterlies in cluster SW, while water vapor fluxes changes at the Somali coast are less pronounced (Figure 5.11b). As a consequence of wind changes south of the equator, maximum moisture convergence anomalies are found over the southern Congo Basin. Anomalies of geopotential indicate a cyclonic anomaly over the southwestern coast of Africa. For clusters EW and IO, the nascent Somali Jet is enhanced by an anomalous easterly to southeasterly component leading to anomalous moisture flux divergence and dryness over equatorial East Africa. In case of cluster EW, a strong convergence anomaly is observed over the Congo Basin (Figure 5.11d). During cluster IO, the western part of equatorial East Africa and the eastern Congo Basin are affected by much drier conditions when compared to EW. This is related to strong divergent moisture flow towards western equatorial Africa (Figure 5.11e) in accordance with lower geopotential in this region. Partly significant positive anomalies of geopotential are found in the southern hemisphere subtropics and the Arabian Peninsula.
The tropical large-scale divergent circulation is reflected in the velocity potential anomalies indicates anomalous divergent outflow over the GHA and adjacent Indian Ocean for cluster EE (Figure 5.12c). The significantly positive SSTs over the latter appear to be consistent with the enhanced upper level outflow. The SST anomalies in the equatorial central Pacific resemble the El Niño Modoki pattern (Ashok et al., 2007). Overall, the Indo-Pacific SST pattern appears to be associated with a complex Walker Circulation response that decreases divergence over the Warm Pool and south-western Pacific, while increasing divergence over the Arabian Sea. For cluster SE, the velocity potential map shows anomalous divergence from eastern Africa extending to the Maritime Continent (Figure 5.12a). SSTs over the southern Indian Ocean are above average. The SST pattern over the Pacific Ocean resembles a late stage of El Niño. The descending counterpart is located over the Gulf of Guinea. In case of cluster SW, the Indian Ocean is dominated by upper-level convergent flow, while divergence is observed over western equatorial Africa (Figure 5.12b). The tropical and subtropical Atlantic Ocean exhibit strongly positive SST anomalies. The southern hemisphere midlatitude ocean is cooler than normal, thus the SST anomalies bear some resemblance to the South Atlantic Meridional Overturning Circulation pattern as discussed in Lopez et al. (2017). Cluster EW is characterized by a dipole of upper-level convergence (divergence) over the GHA region/western Indian Ocean (central equatorial Africa) consistent with the observed rainfall anomalies (Figure

5.10 d,e). The former region is characterized by colder SSTs, which is one potential cause of the overlying anomalous convergence. Another potential cause is a wave train from the Mediterranean over the Arabian Peninsula into the Arabian Sea (Figure 5.13). Such a wave train has been discussed in Bekele-Biratu et al. (2018) in relation to the boreal spring Belg rainy season over Ethiopia. The final cluster IO shows a strong velocity potential dipole over East Africa and Gulf of Guinea (Figure 5.12e). In combination with Figure 5.11e, this suggests an anomalous Walker type circulation with an ascending (descending) branch over the Gulf of Guinea (East Africa). This circulation may be related to warmer (colder) SSTs in the Atlantic (Indian) Ocean (Figure 5.12e). Overall, the discussion of the composited anomalies allows insightful physical interpretations, that are complex due to concurrent tropical, subtropical and extratropical circulation anomalies.

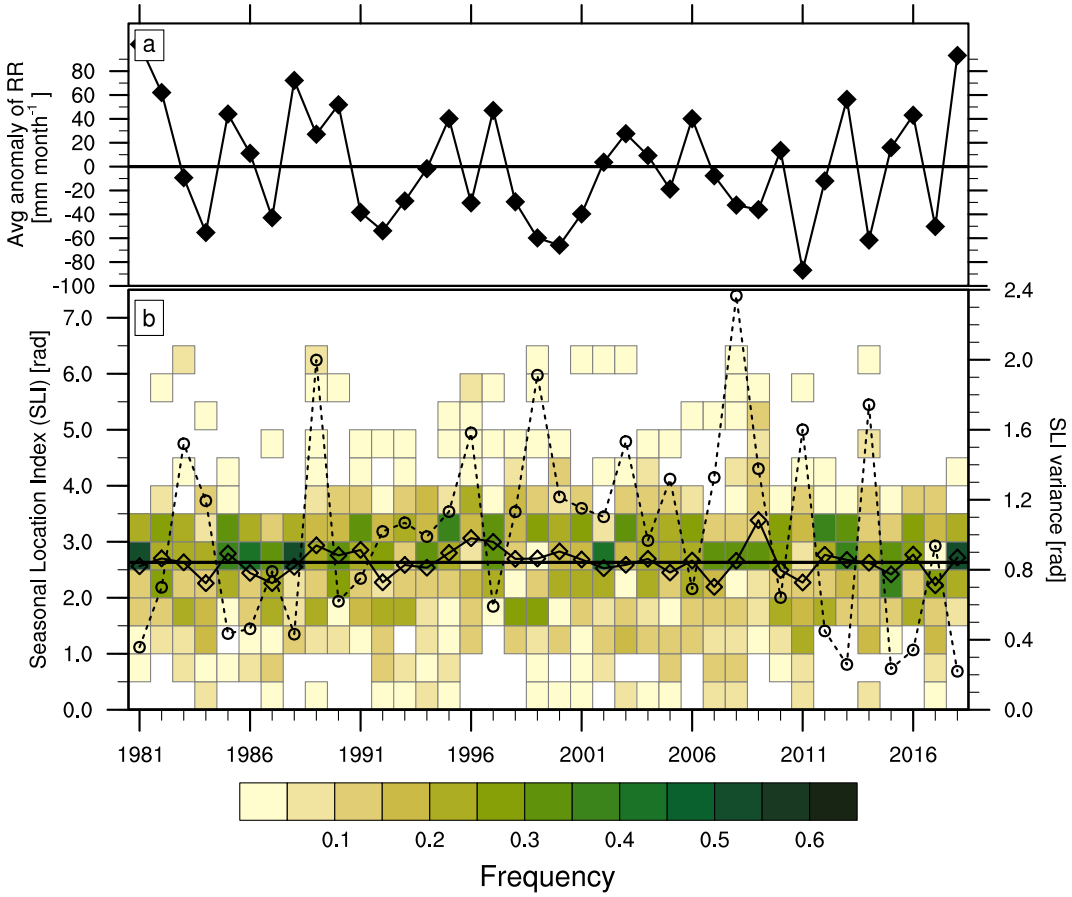

Figure 5.9: Interannual variability of rainfall over equatorial East Africa and the SLI as a proxy for the location of the TRB in April. (a) Averaged rainfall anomalies over equatorial East Africa (cf. yellow polygon in Figure 5.1). (b) Frequency of SLI values in April per year. The bold reference line marks the multi-year average of the SLI. Diamonds show the average value for each year, while circles highlight the respective monthly variance. The colored boxes denote the frequency of the SLI-values for the particular year.

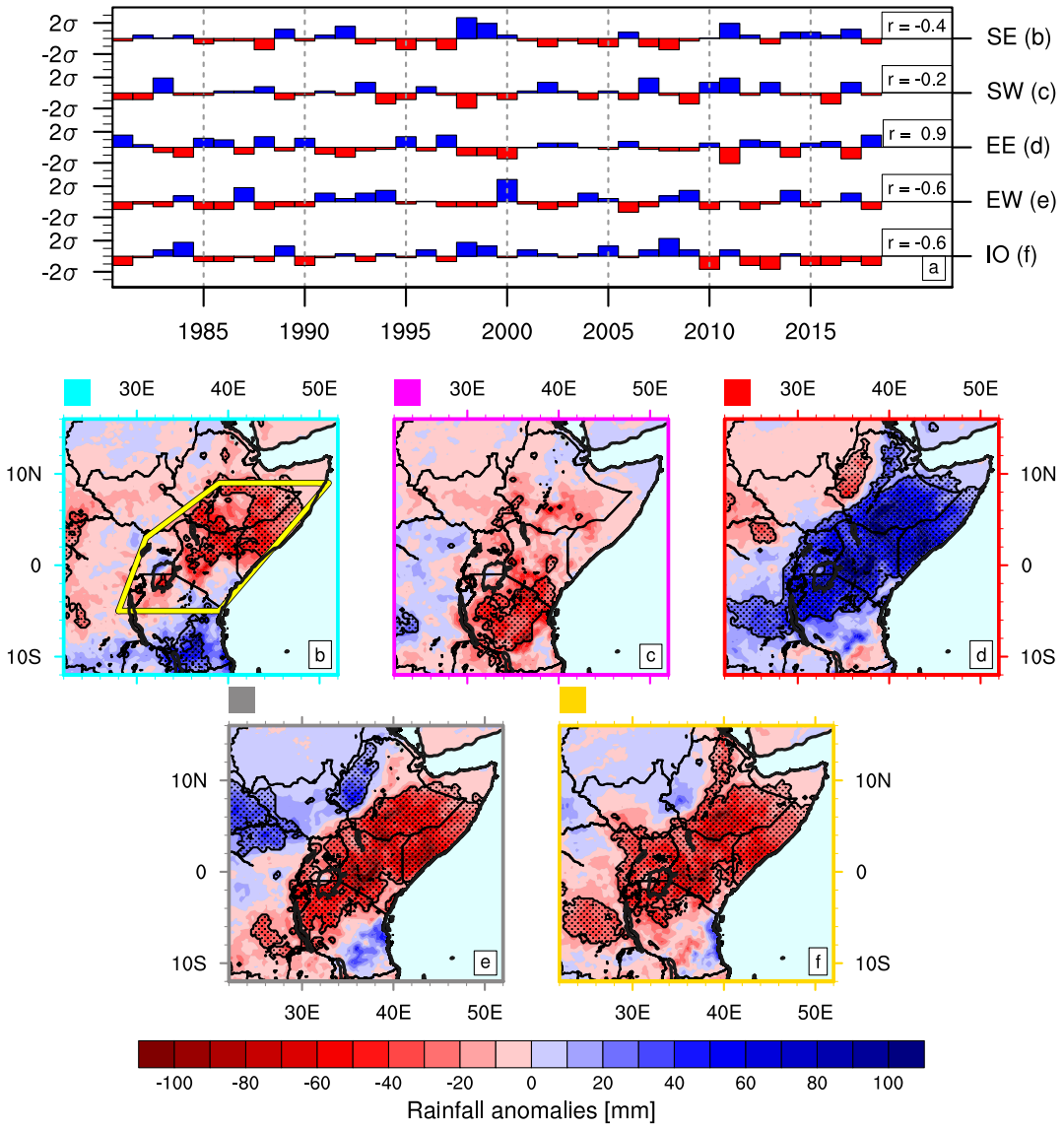

Figure 5.10: Temporal and spatial patterns of rainfall anomalies for April: (a) standardized anomalies of cluster occurrence, (b–f) composite maps of difference between seasonal rainfall anomalies across the region associated with (high-low) cluster occurrence. The Pearson correlation coefficients r between the time series in Figure 5.9a and Figure 5.10a are given on the right side of (a). Statistically significant values compared to the climatology are stippled in (b–f)

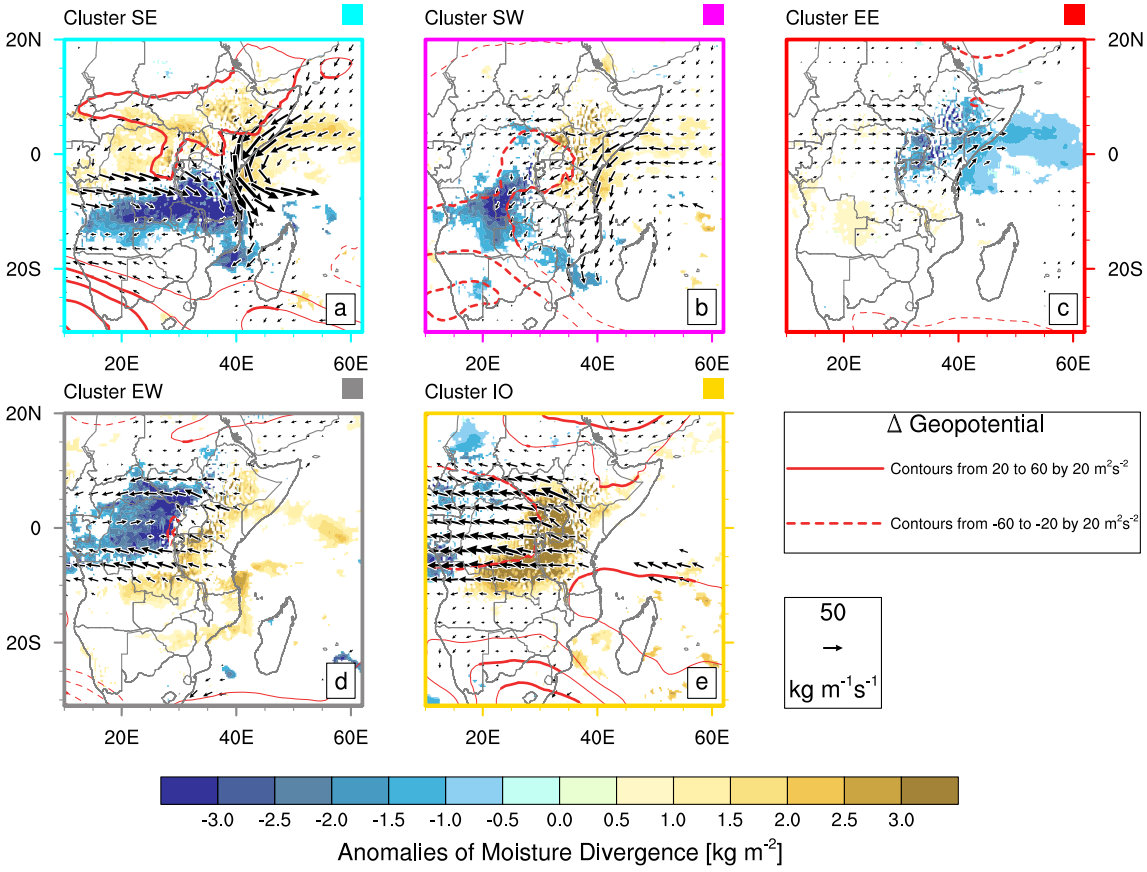

Figure 5.11: Same as Figure 5.7, but for those clusters which are important in April.

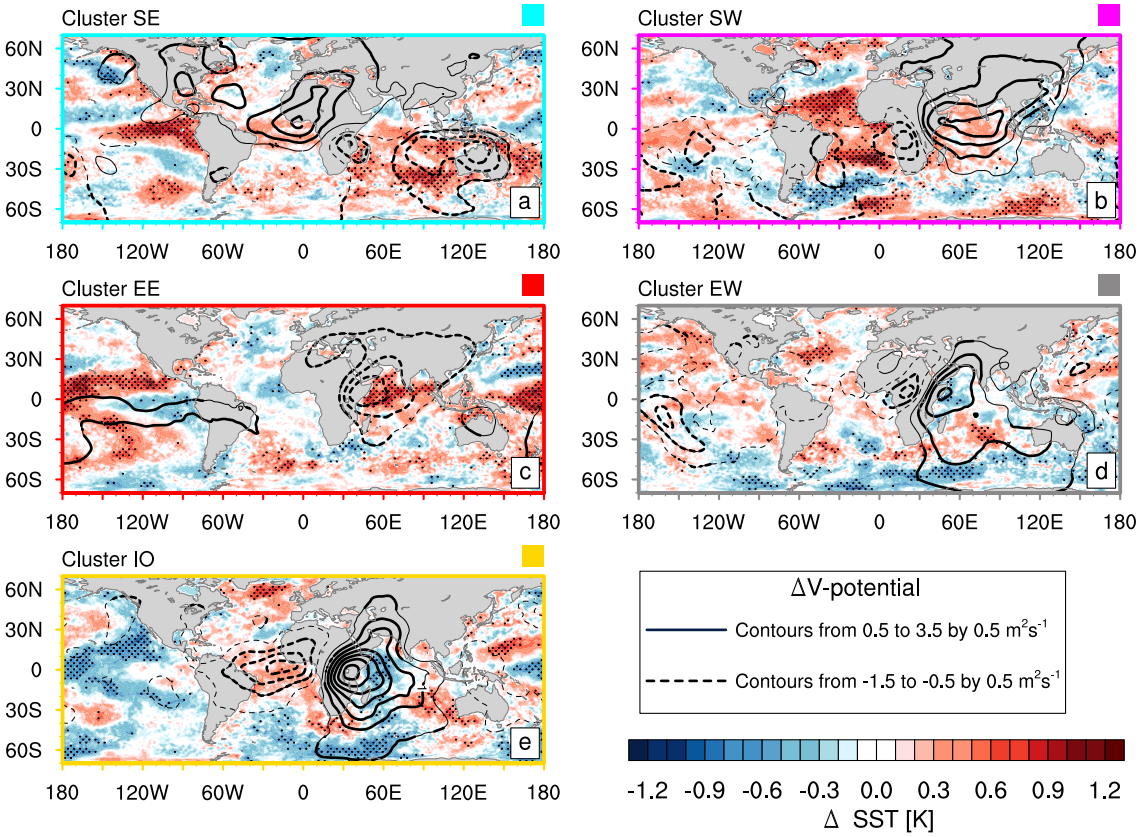

Figure 5.12: Same as Figure 5.8, but for those clusters which are important in April.

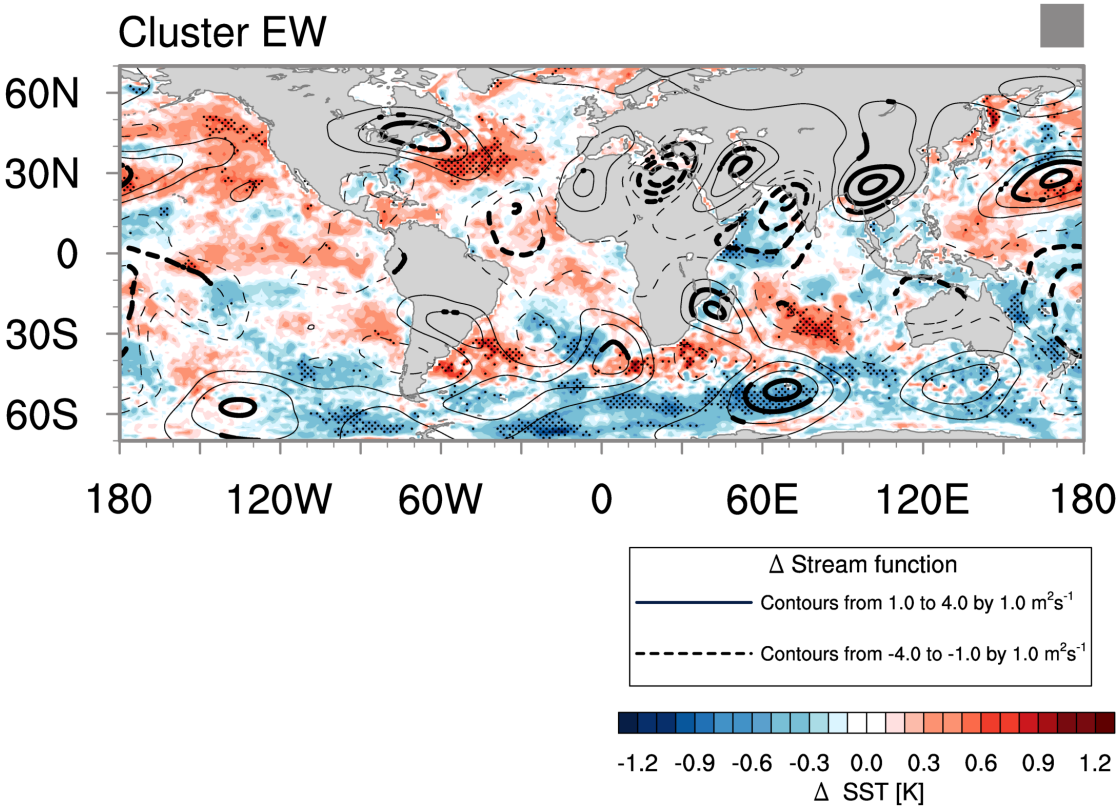

Figure 5.13: Stream function and SST anomalies for EW for April. Contours: composite differences between 200-hPa stream function [m^2 s^{-1}] for the individual clusters and the April mean. Solid lines mark positive anomalies, while dashed lines mark negative anomalies. Significant anomalies are highlighted in bold. Colors: composite differences of 14-day lagged SST anomalies between periods of high and low cluster occurrence. Significant anomalies are stippled.

5.4 Summary and Conclusions

In the present study, interannual variations of the seasonal cycle of rainfall over the GHA between 1981 and 2018 were analyzed using two statistical indices introduced by Riddle and Wilks (2013). The first index, the SLI, describes the daily north-south meandering of the TRB. The second index, the RCI, refers to six related rainfall clusters at daily time scales. Composite anomalies of moisture flux and flux convergence, geopotential heights and SSTs for clusters prevailing during the Msimu Rains in Tanzania, and during April, the core month of the Long Rains, were created to link the anomalous cluster occurrence to atypical atmospheric and oceanic conditions. The following main conclusions can be drawn:

1. Confirming and extending the results of Riddle and Wilks (2013), the SLI and RCI are powerful indices to capture the full seasonal cycle of the TRB. Mean monthly cluster composition indicate coherent parts of the rainy season and anomalous cluster occurrence helps to interpret interannual variations and trends, including some well-known ENSO extremes.

2. The Msimu Rains were dominated by two clusters with opposite rainfall char-

acteristics between the Congo Basin and Tanzania. The associated anomalies in moisture flux (divergence) indicate variations in the location of the TRB originating from an interplay between low-level air flows from the Atlantic and Indian Oceans, and tropical and subtropical teleconnections.

3. Abundant rainfall during the Msimu Rains resulted from a persistent 'zonalisation' of the climatological meridional branch of the TRB. This constellation is favored through westerly anomalies of moisture fluxes, a cyclonic anomaly of geopotential over the Mozambique Channel and large-scale anomalous ascent covering the east African coast and the Indian Ocean. Positive anomalies of SSTs over the equatorial Indian Ocean preceded these rain-favoring atmospheric conditions.

4. The peak period of the Long Rains shows a complex cluster composition, which is connected to intraseasonal and interannual variability of latitudinal locations of the TRB. In general, a persistent location of the TRB near the equator, evidenced in a frequent occurrence of cluster EE, is associated with wet conditions over East Africa, while dry Long Rains go along with strong and frequent latitudinal variations of the TRB position with a late onset and/or intermittent rainfall.

5. Rainfall anomalies at the height of the Long Rains were found to be related to anomalous stages of the Somali Jet and low-level, zonal wind anomalies over the Congo Basin. Tropical SSTs and large-scale upper-level divergence reveal links to the Walker circulation and SST anomalies over the Indian Ocean and equatorial central Pacific. Three clusters (SE, EE, and IO) showed links to El Niño variability in the Pacific Ocean, while cluster EW appeared to be related to an extratropical wave train over Mediterranean and Arabian Peninsula.

6. Drier than normal April months are often related to an anomalous occurrence of cluster EW and IO, both of which show significant geopotential height anomalies in the subtropics, thus suggesting tropical-subtropical interactions.

The results suggest that the SLI is particularly useful to analyze intraseasonal and interannual variations of the TRB during the periods of latitudinal migration, for example, Long Rains. It was shown that during wetter than normal Long Rains, SLI values show lower variability and a high percentage of days in the range of the seasonal mean, indicating a persistent location or a slow migration of the TRB. In years of drier than normal Long Rains, SLI values show higher variance, sometimes even a bimodal frequency distribution around the long-term mean. Strong variations of the SLI thus point towards frequent changes in circulation patterns, a strong intra-monthly north-south meandering of the TRB and resulting intermittent rainfall.
The two dominating clusters of the Msimu Rains reflect a dipole pattern between Tanzania and the southern Congo Basin. The third cluster shows strongly reduced rainfall over both poles. The patterns describe an interplay between northeasterlies from the Arabian Sea, the southeasterlies from the southwestern Indian Ocean and westerlies from the Atlantic. The cluster SE associated with substantial rainfall over Tanzania is characterized by westerly moisture flux anomalies and warmer SSTs over the northwestern Indian Ocean, consistent with for example, Zorita and Tilya (2002) and Mapande and Reason (2005). The circulation anomalies during the Msimu Rains agree with the latitudinal positions of the semi-permanent AL (cf. Crétat et al., 2019). In this context, the occurrence of cluster SE and rainfall over Tanzania is tightly

connected to a northerly position of the AL. Cluster IO and widespread dry conditions predominately occur during a southerly displacement of the AL.
Howard and Washington (2018) have shown that the characteristics of the AL can be separated into heat and tropical low phases. Howard et al. (2019) further investigated the relationship between the tropical low activity and precipitation over southern Africa. Their two circulation patterns of tropical low activity across the southern African continent agree with the two dominating clusters during the Msimu Rains in the current work. While current results indicate a relationship between a meridional SST dipole in the western Indian Ocean and the occurrence of rainfall clusters, no obvious link to ENSO variability was found unlike in Fauchereau et al. (2009) and Crétat et al. (2019). The circulation during Msimu rains with frequent co-occurrence of clusters SW and IO may be connected to the occurrence of TTTs over southwestern Africa (Todd and Washington, 1999; Fauchereau et al., 2009; Macron et al., 2014). A warm southwestern Indian Ocean, which is associated with cluster SW, is related to the formation of TTTs over southern Africa (Fauchereau et al., 2009). In addition, an interaction with extratropical Rossby wave activity, as described in Hart et al. (2013b); Manhique et al. (2011), and Macron et al. (2014), seems plausible for cluster IO.
In agreement with Vellinga and Milton (2018); Funk et al. (2018) and MacLeod and Caminade (2019), the rainfall-favoring cluster EE during the Long Rains positively correlates with SST anomalies in the Arabian Sea and central Pacific. Camberlin and Philippon (2002) found relationships of the Long Rains with lower sea level pressure, weakened easterlies and reduced divergence over the equatorial Indian Ocean, which agrees with the circulation of cluster EE. Finally, Wainwright et al. (2019) found that an earlier onset of the Long Rains is related to a warm Arabian Sea. In addition, a positive correlation is found to the SST anomalies in the central Pacific, suggesting an El Niño Modoki pattern (cf. Ashok et al., 2007; Preethi et al., 2015).
Dry conditions in April are characterized by higher relative frequencies of clusters related to moisture divergence and easterly anomalies of moisture fluxes, confirming the findings of Camberlin and Philippon (2002) and Zorita and Tilya (2002). The affected clusters can be separated into southern clusters SE and SW, and northern clusters EW and IO. The former clusters indicate a delayed onset of the Long Rains, while prolonging the Msimu rains. The occurrence of cluster SE in April is positively correlated with the SSTs in the southern Indian Ocean. This agrees with the results of Wainwright et al. (2019), who found a correlation between SSTs in the latter region and late onset dates of the Long Rains.
The northern clusters are associated with negative SST anomalies and subsidence over the northwestern Indian Ocean. Bekele-Biratu et al. (2018) emphasized that a tripolar pattern consisting of two anomalous mid- to upper-level cyclonic troughs and one anticyclone tends to enhance rainfall during the Ethiopian Belg Rains. Frequent occurrence of cluster EW goes along with a similar wave train from the northern subtropics. Cluster IO reveals a Walker-type circulation with cold SSTs and subsidence over East Africa and ascent over the Gulf of Guinea. A similar SST pattern correlating with cessation dates of the Long Rains was found by Wainwright et al. (2019) in May. In addition, a connection to SST anomalies in the central Pacific, suggesting a La Niña Modoki pattern (cf. Preethi et al., 2015) could be shown.
The current study highlights the role of the latitudinal position of the TRB and potential drivers related to the preponderance of five rainfall clusters during the Long Rains. Yet, the convective activity within the seasonal envelope of the TRB as well as

its width are also contributing to the clusters statistics, even if latitudinal anomalies would be small. The employed method does not allow a quantitative assessment of the relative roles of position, intensity, and width of the TRB. As a quick check, the relative contribution was estimated according to the formula given in for example, Clark et al. (2018) and Hauser et al. (2020) which has three terms: The first term describes the influence of the cluster frequency, the second term the influence of the rainfall intensity and the third term is a combination of both metrics. For grid points in the yellow polygon in Figure 5.1, the first term was twice as large as the second, whereas the third term was negligible for April for cluster EE days. This provided room for the interpretation that a 'subsidence cap' as a consequence of, for example, Walker cell anomalies or dry phases of the MJO (Vellinga and Milton, 2018), plays the dominant role. However, it can also be inferred that more dry days occur due to the TRB being outside the region. Anomalies of the seasonal progression of the TRB, as proposed in the present study, are consistent with recent results by Wainwright et al. (2019), who pointed out that the Long Rains decline was mostly associated with a shorter rainy season with late onset and early cessation dates rather than a decline in seasonal rainfall amounts.

The results of this study indicate that the employed methods not only shed light on the seasonal and interannual anomalies of the TRB, but can also contribute to a better description and potential causes of rainfall trends. For the Short Rains that show a wetting trend, significant changes in two clusters were found. For the Long Rains, the dry period 1995-2010 was marked by an anomalous occurrence of cluster IO that is overall dry over the GHA region and was related to Walker cell type anomaly encompassing the Indian and Atlantic Oceans. In summary, this work suggests to strengthen research into the role of SST anomalies in the oceans adjacent to Africa as well as of tropical-extratropical interactions in explaining interannual rainfall variations and trends.

6 Summary and Outlook

The economy of the GHA largely depends on rain-fed agriculture, which in turn affects both society and environment. For these reasons, future changes in rainfall over GHA may have potential for initiating negative socioeconomic developments. Therefor, an understanding of atmospheric and oceanic interactions and their influence on patterns of the seasonal rainfall variability over GHA is essential for estimating future changes and establishing appropriate adaptation strategies. This work provides a contribution to the description and understanding of seasonal and interannual variability of rainfall and its seasonality over the GHA. In particular, it attempted to disentangle the role of various remote forcing factors affecting the different rainy seasons and how they modulate the migration of the TRB.

6.1 Summary

Overall, the work was centered around the fundamental question, whether the observed negative rainfall trends were driven by an overall reduction of moisture or by changes in the migration of the TRB. The latter case would imply that a negative trend on a particular location results from a faster progression of the TRB associated with later onset and earlier cessation dates of the respective rainy season. This "acceleration" might be compensated by a prolonged and more intense rainfall in another part of the region and/or another rainy season.

The first step to answer this question was to objectively estimate the start and end dates for each of the rainy seasons and to determine the regions where these seasons account for substantial proportions of annual rainfall. This definition could be used to analyze trends in seasonal rainfall as well as trends of onset and cessation dates, which give potential first hints to solve the aforementioned fundamental question. The follow-up task was to investigate the corresponding atmospheric and oceanic conditions that contribute to the variability of the TRB migration and link them to large-scale modes of variability known from literature. These modes include variability at decadal and annual time scales, which include coupled atmosphere-ocean oscillations (e.g. El Niño Southern Oscillation), as well as at seasonal time scales (e.g. Madden-Julian Oscillation), or synoptic time scales (e.g. extratropical interactions, heat low variations). Particular attention was given to the abrupt decline of the Long Rains since the late 1990s and potential signals of this development in the TRB migration. The approach of the current work consisted of two steps.

Step 1: A new and flexible rainy season definition and estimation of rainfall trends

Generally, selected parts of the GHA (usually on national scale) with a known coherent seasonality are analyzed in terms of rainfall variability and trends. These approaches consider full-month periods to define the rainy seasons. However, these approaches neglect regional differences in rainy seasons and do not account for important aspects like seasonal stability, and onset and cessation dates. The first step to resolve the primary question was to develop an objective and flexible rainy season definition, which can be applied for the whole GHA and accounts for regions with one or more rainy seasons as well as for regions where two seasons merge into one. At the same time, the methodology should be able to identify interannual variability in onset and cessation dates and be applicable to different data sets. This definition was developed in chapter 4 in order to obtain an objective classification of the seasonality and timing of rainfall and rainy seasons. This classification enabled a more detailed mapping of the region independent of latitude, national borders or calendric definitions. The main advantage to commonly used threshold-based definitions is that this flexible definition determines an individual rainfall threshold for each location and thus allows the application independent of rainfall climates. Compared to its predecessor developed by Wang and LinHo (2002), this definition can be applied for multiple rainy seasons and also for a higher variety of rainfall climates. Whereas the definition of Dunning et al. (2016) requires an a priori estimation of the number of rainy seasons and can mostly be applied on past rainy seasons, the methodology developed in this work estimates the number of climatological rainy seasons, their onset and cessation dates in one step. With a few adaptations, this definition is also applicable in near-real time. The novel uncertainty estimation of modality, onset and cessation dates added further information about the temporal stability of the classification and also gave hints towards potential biases of different data sets. However, similar to Dunning et al. (2016), a pronounced rainfall gradient between dry and wet seasons is beneficial, since light rainfall at the beginning or end of the rainy seasons can lead to high uncertainties for the onset and cessation dates. First indications towards coherent local atmospheric features or circulations could be found, which potentially modify the onset or cessation dates. Since two kinds of rainfall data sets were used, namely a set of ground-based station measurements and gridded satellite-based rainfall estimates, a comparison between the two was also performed.

In the follow-up, the rainy season definition was used to estimate trends of rainfall within the seasonal bounds and trends of rainy season onset, cessation and length. Since all trends were calculated within seasonal bounds, the flexible rainy season definition also enables a comparison of trends over regions with different seasonality, i.e. regions with different numbers of climatological rainy seasons. Although there is a general agreement in the trend signs between the flexible and calendric rainy seasons, differences in amplitude and significance could be identified. As a general pattern, rainfall in the southern hemisphere and during the northward progression tends to decrease, whereas rainfall tends to increase in northern hemisphere and during the southward migration of the TRB.

A clear advantage of the flexible definition is its ability to evaluate trends in rainy season onset, cessation and length. In this context, trends towards a later cessation of the Kiremt Rains and the Short Rains in the northern hemisphere could be determined. On the other hand, Msimu and Long Rains exhibit an earlier cessation

and for the Msimu Rains in southern Tanzania also a later onset. It should be noted that shortening trends were found primarily for regions with climatological cessation dates in April, while lengthening trends are located in regions with a climatological cessation in October and November. The trends of onset and cessation dates are thus in agreement with trends of rainfall amounts, revealing a partitioning into a drying southern and a wetting northern hemisphere. Overall, the newly developed flexible rainy season definition helped to estimate long-term trends in rainfall amount more precisely, to distinguish between changes in rainfall amount versus changes in rainy season length, and to provide first important clues concerning changing points in the seasonal cycle.

Step 2:
In the second part, the results from step 1 were used in combination with an adopted approach to map the variability of the TRB migration. By applying the methodology of Riddle and Wilks (2013), the seasonal progression of the TRB from the southern to the northern hemisphere and back is represented as a sequence of distinct stages, which were expressed by two indices. The first index, the SLI, described the daily north-south meandering of the TRB. The second index, the RCI, refers to six related rainfall patterns at daily time scales.
Evidence was provided that rainfall anomalies go along with anomalies in the location of the TRB and in the proportions of particular rainfall/circulation patterns by marking seasons in the time series. Still, it should be emphasized that similar rainfall patterns in different seasons do not necessary arise from the same atmospheric or oceanic interactions. On the other hand, different seasonal forcing mechanisms may result in similar circulation features and spatial rainfall distributions. For the analysis of circulation anomalies, the focus was put on two periods of the seasonal cycle. First, the Msimu Rains over western and southern Tanzania are mostly underrepresented in the literature. Although some research has been carried out on the circulation features of the austral summer rainy season, the focus lied mostly on southern Africa. The second period in focus was the month April as the climatological peak month of the Long Rains. As indicated in step 1, April is apparently one of the turning points in the seasonal cycle, which is particularly expressed through earlier rainy season cessation dates in this month. Another interesting aspect is that correlations and predictability, that were studied in literature were lowest in April (Camberlin and Philippon, 2002; Nicholson, 2017).
The results for the Msimu Rains revealed three rainfall/circulation patterns, from which two of them dominate up to 90% of the season. The patterns describe an interplay between northeasterlies from the Arabian Sea, the southeasterlies from the southwestern Indian Ocean and westerlies from the Atlantic. These two major patterns can generally be classified as a seesaw between influences from the Congo Basin and the Indian Ocean, which can be interpreted as variations of the TRB along a northeasterly/southwesterly axis. These two patterns are associated with opposed anomalies of the zonal flow over Tanzania, which are in turn correlated with the circulation anomalies over the southwestern Indian Ocean. On synoptic time scales, such variations are connected to the different regimes of the Angola Low, and further modulated by SSTs in the equatorial and southwestern Indian Ocean. During the

Msimu Rains, the Angola Low can migrate into a rather northerly or a southerly position. Particularly, a northern position is favorable for rainfall over Tanzania. The rather rare third pattern corresponds to an extreme southward shift of the Angola Low and thus, a displacement of the TRB towards southern and southwestern Africa, away from Tanzania. A southward shift of the Angola Low can be favorable for the coupling with extra-tropical upper-tropospheric waves and the formation of TTTs. This circulation pattern is associated with a strong and divergent inflow from the southern extra-tropics towards the Gulf of Guinea and dry conditions over Tanzania. The analysis of April as the second period has shown a more complex compositions with five rainfall/circulation patterns. Such a wide variety of relevant rainfall patterns can only be identified for the months October and November. It should be emphasized that these two periods of the year were identified as turning points of the seasonal cycle in step 1, since significant trends of rainy season cessation dates occurred in these two periods of the year. The results have shown that the relative proportions of rainfall patterns strongly reflect the migration stages of the TRB. In particular, the composition includes patterns of the Msimu Rains, the early Kiremt Rains, and one rainfall pattern, which is characteristic for the rainy seasons over equatorial East Africa. Both indices, SLI and RCI, indicate that in abundant Long Rains, the latter pattern accounts for a high proportion of days, which is also in line with a persistent location of the TRB close to the equator. In years with deficient Long Rains, both indices indicate strong variations in the latitudinal location of the TRB and more days with rainfall patterns, which are characteristic for Msimu and/or early Kiremt Rains. Further analysis of regional and large-scale circulation revealed links to diverse regions and atmospheric and oceanic components, for example the Arabian Sea. Thus, this approach allows a partial disentangling and evaluation of the documented interactions and common hypotheses regarding the decline of the Long Rains. For the Long Rains, wetter than average conditions may arise when the TRB stalls over equatorial Africa, supported by westerly moisture transports coming from central Africa. Drier conditions are related to stronger TRB variations, supported by easterly moisture transports towards tropical western Africa and tropical-extratropical interactions.

In accordance with literature, the pattern associated with abundant Long Rains is linked to enhanced westerlies, but a strengthened Arabian Heat Low and warm Arabian Sea (c.f. Wainwright et al., 2019) was also identified. On the large scale, a connection to the central Mediterranean can be recognized, which might be linked to a trough pattern interacting with the Arabian Heat Low (c.f. Bekele-Biratu et al., 2018; Wainwright et al., 2019). Although several SST patterns in the Pacific Ocean in line with the Walker Cell hypothesis can be identified, the large-scale circulation does not show significant atmospheric links to these regions. A coherent Walker Cell with a descending pole over the Maritime Continent could not be clearly identified in April. The lack of a coherent large-scale circulation could be a reason for the poor predictability of the Long Rains.

Rainfall patterns associated with weaker Long Rains are partly linked to tropical-extratropical interactions in both hemispheres. In the southern hemisphere, positive SST anomalies in the Indian and Atlantic Oceans seem to delay the migration of the TRB to the north. In the northern hemisphere, an upper-tropospheric wave train with a trough over central North-Africa stretching towards the Guinea Coast and a second trough over India could be identified. The SST signals point towards a beginning upwelling along the African coast. This pattern could verify the connection to the

Indian monsoon system, but also the link to the extra-tropics documented for the Ethiopian Belg Rains (Camberlin and Philippon, 2002; Bekele-Biratu et al., 2018). The only large-scale circulation which resembles a Walker Cell-like response is rainfall pattern IO. This pattern is associated with dry conditions and an amplified easterly flow transporting moisture towards the Gulf of Guinea. Thus, the descending branch is located over the western Indian Ocean, whereas the ascent is connected with the equatorial Atlantic and West Africa. Although this pattern generally does not occur very frequently, its relative proportion in April exhibited a significant increase from the late 1980s until the end of the 2000s.
These results and interpretation are line with the explanation of Wainwright et al. (2019) concerning the decline of the Long Rains, implying that the increased SST gradient in the Arabian Sea and a stronger Arabian Heat Low lead to a faster migration of the TRB and shorter, but more intense Long Rains. However, the most common explanation for the decline of the Long Rains, referring to a shift of the Walker circulation, cannot be regarded as refuted. This is partly due to the focus on April, which is a rather short period of the seasonal cycle, but also on the day-to-day variability of the regional circulation. Trend estimations and interannual variability were accessed via accumulations of daily TRB positions and rainfall patterns. An extensive analysis of lagged correlations with particular regions of the Pacific or Atlantic Oceans were not performed in this work. From a different point of view, one can ask whether the enhanced tropical-extratropical interactions might also be a response to variations in the local Hadley circulation and/or indications of shifts of the Indian Ocean Walker Cell or the neighboring Congo Walker Cell. This question could be analyzed in future research.
The results highlight the role of the latitudinal position of the TRB during the Long Rains. Yet, further factors like the convective activity within the seasonal envelope of the TRB as well as its width also contribute to the clusters statistics. A quantitative assessment of the relative roles of position, intensity, and width of the TRB was not subject of this study. This has let room for the interpretation that a 'subsidence cap' as a consequence of, for example, Walker cell anomalies or dry phases of the MJO (Vellinga and Milton, 2018), plays the dominant role. However, it can also be inferred that more dry days occur due to the TRB being outside the region. Anomalies of the seasonal progression of the TRB, as proposed in the current results, are consistent with recent study by Wainwright et al. (2019), who pointed out that the Long Rains decline was mostly associated with a shorter rainy season with late onset and early cessation dates rather than a decline in seasonal rainfall amounts. Further research can analyze the quantitative assessment of the relative roles of position, intensity and width of the TRB and the associated atmospheric drivers.

6.2 Outlook

This work has shown that interannual variability of the TRB migration plays an important role for the rainfall climate and interannual variability of rainy seasons over the GHA. These atmospheric and oceanic dynamics can modify seasonal rainfall amounts as well as seasonal onset and cessation dates. Specific atmospheric and oceanic conditions could be attributed as being favorable for the development of

particular rainfall/circulation patterns. Depending on the amplitude and frequency of the respective pattern, it can contribute to enhanced rainfall or drought during any of the rainy seasons. The results and methods can serve as starting point for further research.
The methodology for the rainy season onset detection can generally be applied to other regions with a tropical seasonal rainfall cycle and to other data sets. Additionally to mapping the climatological rainfall seasonality, it can be applied in the context of evaluation of satellite products and climate models. Since it is also applicable in near-real time, it can also be potentially used for monitoring.
Still, most of the rainfall patterns reflect particular circulation anomalies in the areas around the GHA (e.g. Arabian Sea), which affect the local atmospheric stability. These patterns do not explicitly point towards one dominant large-scale mode of variability (e.g. IOD, MJO), that modulate the rainfall amounts of the respective rainy seasons. This implies that more complex interactions between multiple large-scale modes could lead to anomalies in the seasonal progression, which are reflected in anomalous occurrences of particular TRB stages. More detailed insights into these interactions could be subject of further research. These following pathways are particular promising:

- A lot of studies identified the MJO as an important driver of intraseasonal rainfall variability over the GHA (e.g. Pohl and Camberlin, 2006a,b; Vellinga and Milton, 2018; Finney et al., 2019). Possible links between the rainfall patterns and different MJO-phases can arise through modulations of rainfall amounts (amplitude) and/or by cluster occurrence. A preliminary analysis of rainfall anomalies and MJO-phase per cluster EE during the Long Rains (MAM) indicates enhanced rainfall over most of equatorial East Africa during MJO phases 3–4, while the coastal regions exhibit an increase of rainfall during the opposed phases 7–8 (Figure 6.1, MJO-phases according to Wheeler and Hendon (2004)). MJO-phases 1–2 are mostly associated with rainfall over the western and north-western parts of the GHA. Thus, there is evidence that MJO-phases modulate the magnitude and spatial pattern of rainfall of one particular cluster. The results also agree with Pohl and Camberlin (2006a,b) concerning the lag of rainfall anomalies relative to the passage of the active MJO-core. Further analysis could investigate if MJO-phases also affect the frequency of occurrence of a particular rainfall cluster and the latitudinal position of the TRB. In addition, the contribution to other parameters of the TRB, like intensity or width can be analyzed in detail.

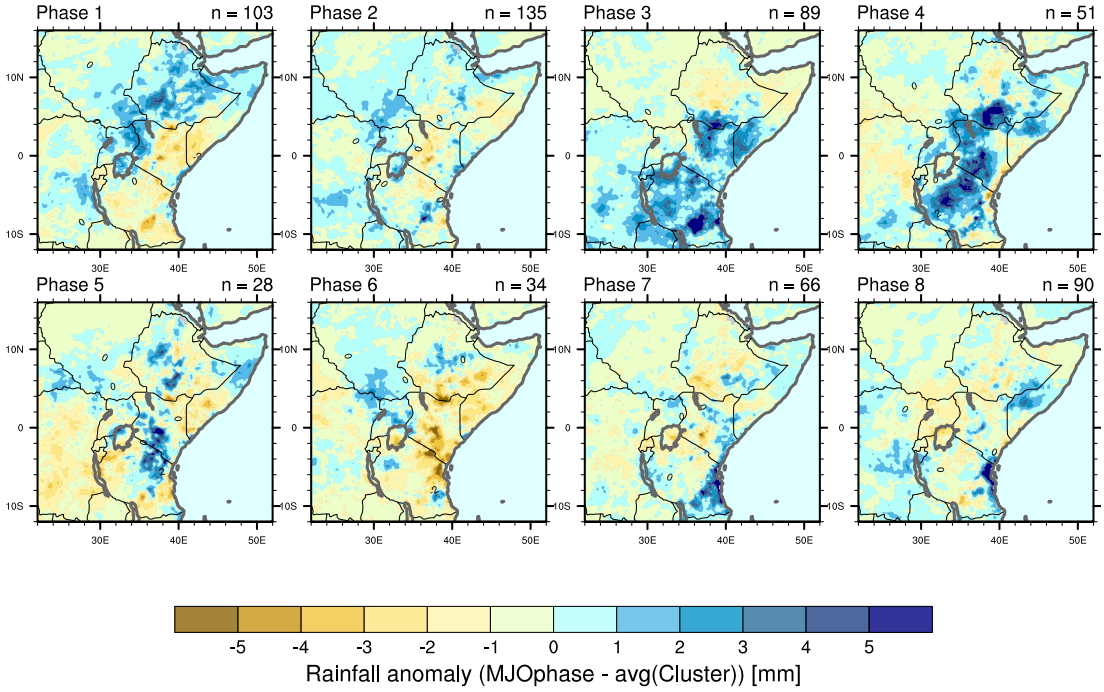

Figure 6.1: Rainfall anomalies for days in Cluster EE during the Long Rains (MAM) period for different MJO-phases. The MJO-phases were numbered according to Wheeler and Hendon (2004). Rainfall anomalies were obtained from CHIRPS for the period 1981–2018.

- Although not addressed in this work, tropical cyclones can also be a relevant factor for the wind variability over GHA, as their occurrence likely favors westerly flow over the GHA. Shanko and Camberlin (1998) have shown that frequent cyclone occurrences in the southwest Indian Ocean are related to drought conditions in Ethiopia. Finney et al. (2019) pointed out that the location of the tropical cyclone plays a role in initiating westerlies over equatorial East Africa. There is an increased likelihood of westerlies when tropical cyclones are located around northeast Madagascar, whereas they are less likely if tropical cyclones are located in the Mozambique Channel. Since tropical cyclones predominately form over higher SSTs in the western Indian Ocean, their occurrence and the associated circulation agrees with those of rainfall patterns SE and EE.

- The role of the large-scale circulation west of the GHA did not receive much attention yet in the literature. Three of the six rainfall/circulation patterns considered here involved interactions with the Atlantic Ocean and the Gulf of Guinea. Air masses from the Atlantic Ocean play an important role in the circulation of the Angola Low, which affects the Msimu Rains over Tanzania (c.f. e.g., Howard et al., 2019; Crétat et al., 2019). Partly, the role of air masses from the Gulf of Guinea was addressed in the context of the Kiremt Rains in Ethiopia (Diro et al., 2011; Bahaga et al., 2019). However, the build-up and phases of the Congo Walker Cell (Cook and Vizy, 2016), the deepening of the Saharan Heat Low (Evan et al., 2015) embedded in the amplified warming of the Sahara (Vizy and Cook, 2017) and its effect on the circulation over the GHA have not been studied systematically.

- Although the role of tropical-extratropical interactions has been studied for southern and western Africa, their role for the GHA has only marginally been issued. Rubin et al. (2007) analyzed the evolution and features of ten tropical plume events over eastern North Africa during the period 1988–2005 in which considerable rain over the Middle East was recorded. They noted that the preferred locations for tropical plume origin are located in the area of 5°– 15 °N, 5°W–15°E, which corresponds to the Guinea Coast. In line with Camberlin and Philippon (2002) and Bekele-Biratu et al. (2018) results for Ethiopia, Taylor et al. (2018) have shown that upper-tropospheric wave trains in the Mediterranean can modulate the development of mesoscale convective systems over the Congo Basin. Signatures of this kind of interactions were identified in multiple rainfall/circulation patterns in different rainy seasons and both hemispheres. Preliminary results analyzing rainfall anomalies over the GHA associated with upper-tropospheric troughs in the eastern Mediterranean and Arabian Peninsula show already promising results. Figure 6.2 shows anomalies of rainfall on days with an upper-tropospheric trough over the Arabian Peninsula and the following two days. A strip of positive anomalies from the eastern Ethiopian Highlands towards the Kenyan Highlands and northwestern Tanzania can be identified. In the following two days, the anomalies partly seem to propagate towards the lowlands in the east. However, a deeper analysis is required to quantify the effect of upper-level troughs on rainfall over the GHA. Since upper-tropospheric troughs are considerably slow-moving systems and are rather well captured by atmospheric models, their understanding and prediction could contribute to an improved weather prediction over the GHA.
  In summary, the results of this work contributed to the understanding of rainfall variability and the associated circulation patterns over the GHA. The various interactions with remote teleconnection patterns provide a wide range of pathways for further research. The statistical tools also allow application possibilities in an operational.

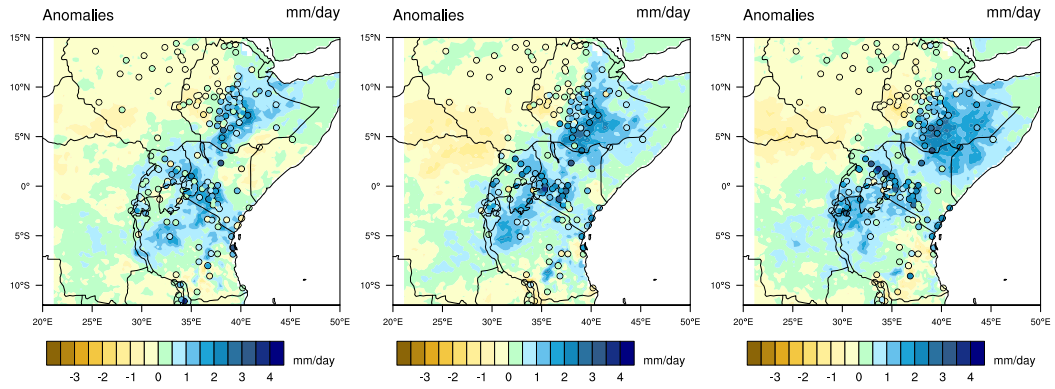

(a) day+0 (b) day+1 (c) day+2

Figure 6.2: Rainfall anomalies [mm/day] on days with upper-level trough occurrences and the following two days relative to the daily mean rainfall over the Arabian Peninsula for the month April in the period 1981–2018. Data were obtained from CHIRPS (grid points) and ground-based stations (circles).

Appendix

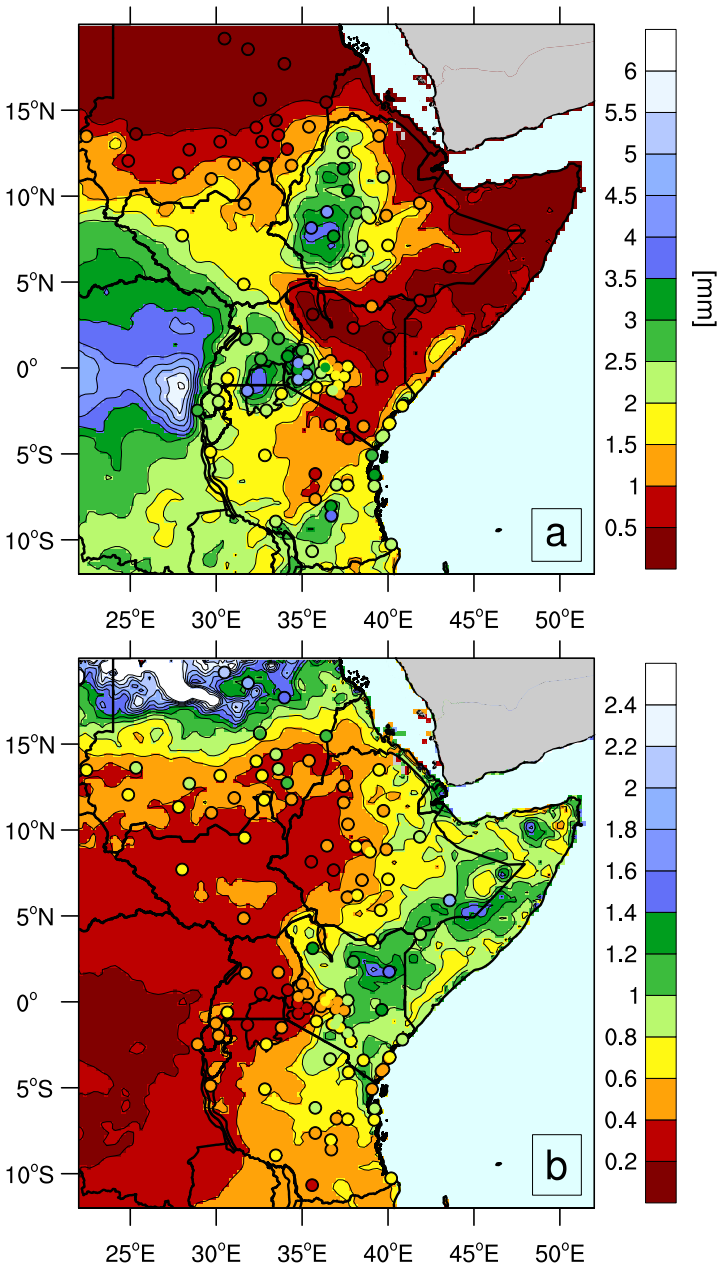

Figure S1: (a) Average threshold values, which are used to define the rainy seasons. (b) Quotient of variation, i.e. proportion of the threshold spread to the average threshold. Contours show the estimations based on the CHIRPS product. Station-based estimations are shown by colored circles.

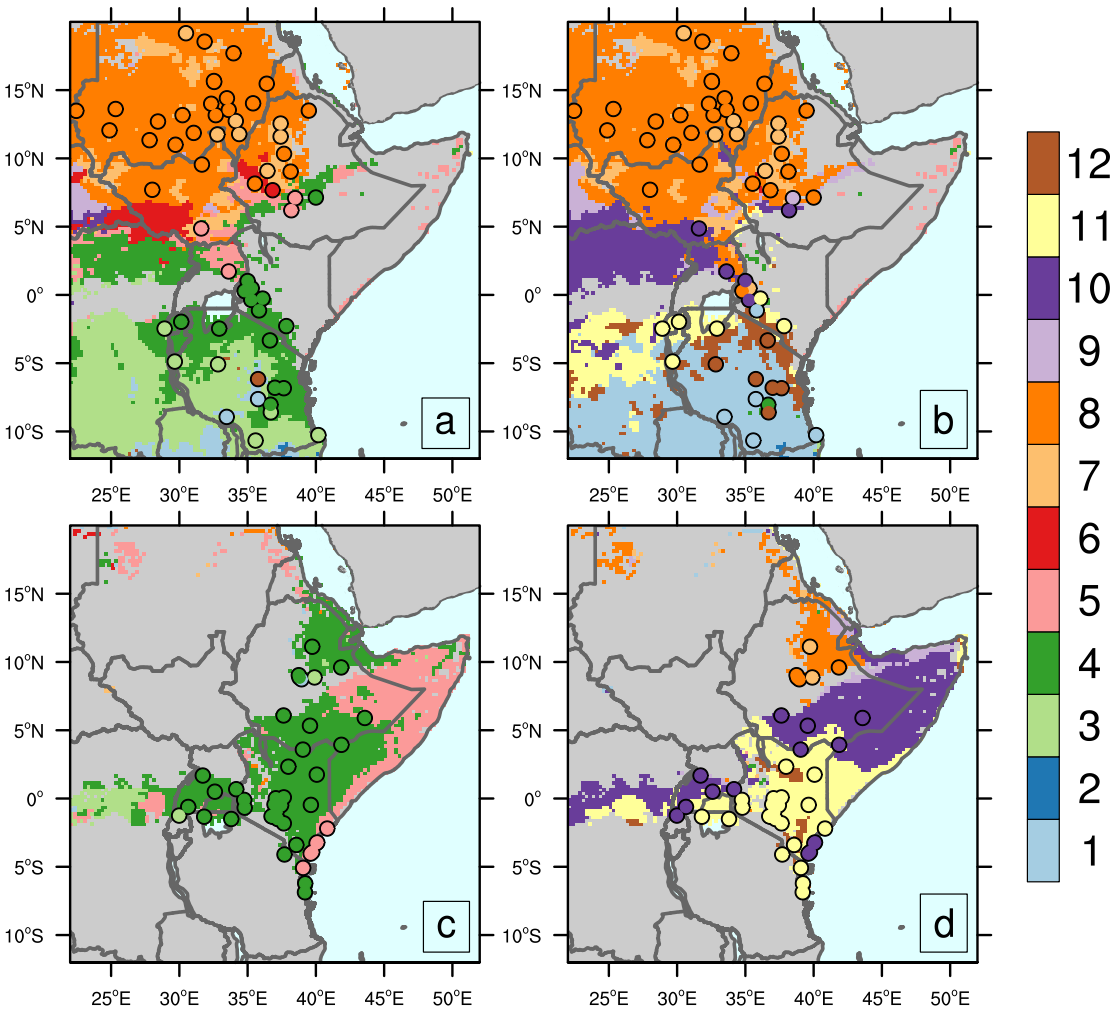

Figure S2: Peak months of the rainy seasons for the single-wet-season (a,b) and dual-wet-season (c,d) regimes: (a) and (c) during the northward progression in boreal spring, (b) and (d) during the southward progression during boreal autumn. Grid points show the estimations based on the CHIRPS product. Station-based estimations are shown by colored circles.

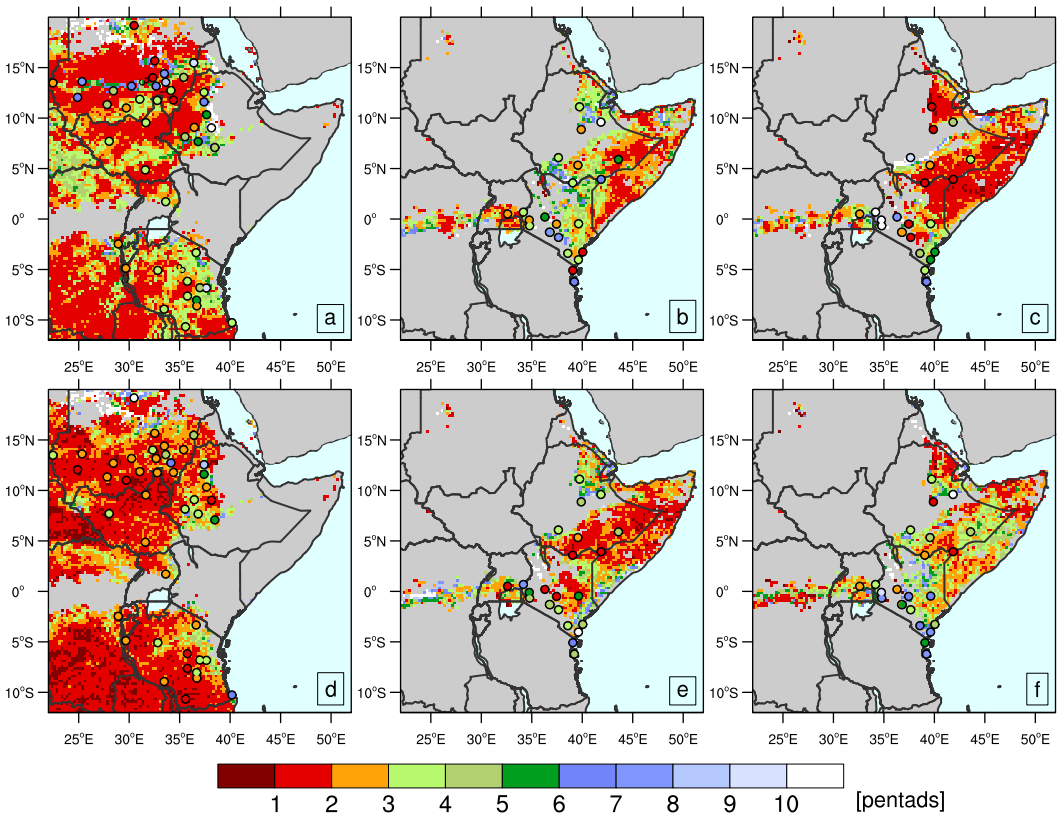

Figure S3: Time range [pentads] between the climatological onset and cessation dates based on the 5%- and 95%-thresholds for (a,d) single-wet-season regimes, (b,e) Long Rains and (c,f) Short Rains. Grid points show the estimations based on the CHIRPS product. Station-based estimations are shown by colored circles.

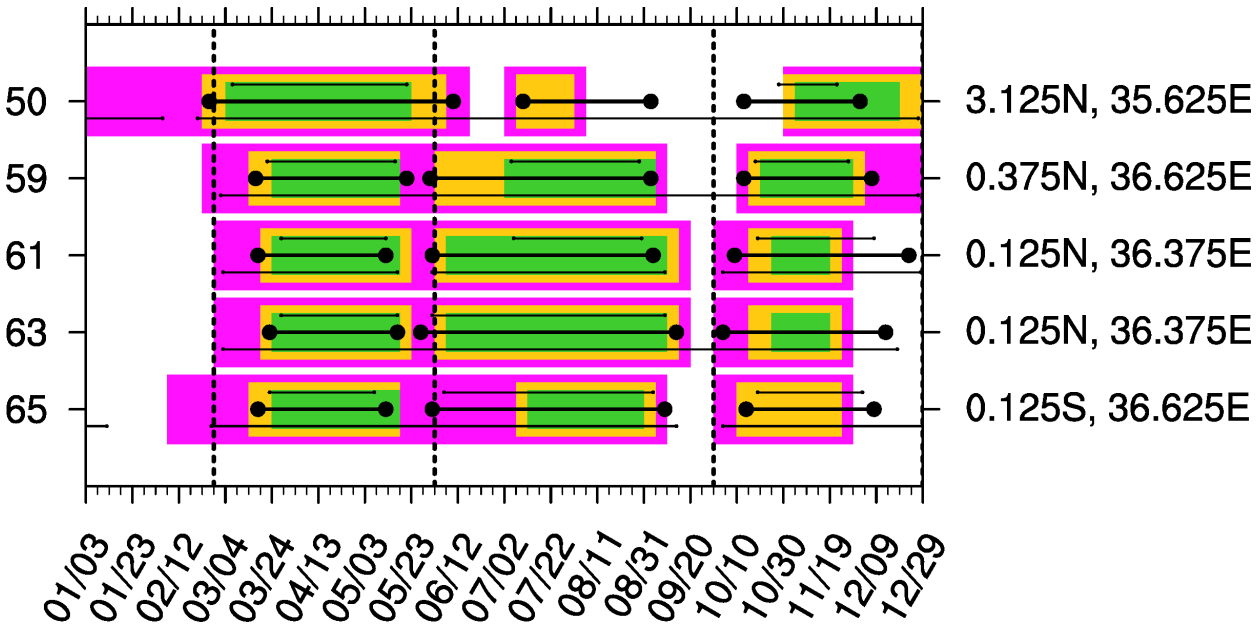

Figure S4: Same as Figure 8, but for the stations with a triple-wet-season regime.

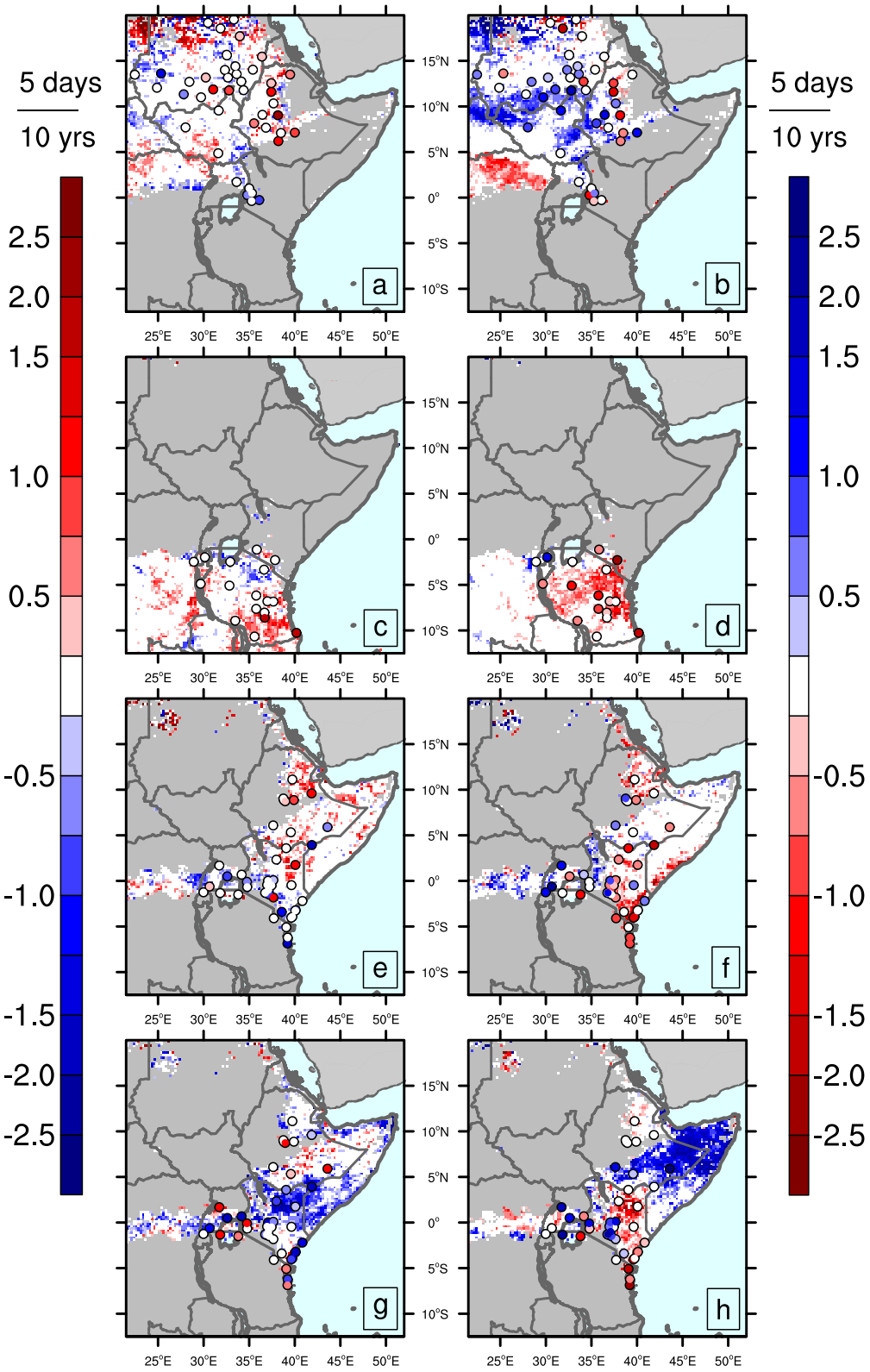

Figure S5: Trends of onset and cessation dates [5 days/10 years] for (a,b) the northern single-wet-season, (c,d) the southern single-wet-season regimes, (e,f) Long Rains and (g,h) Short Rains. Grid points show the estimations based on the CHIRPS product. Station-based estimations are shown by colored circles.

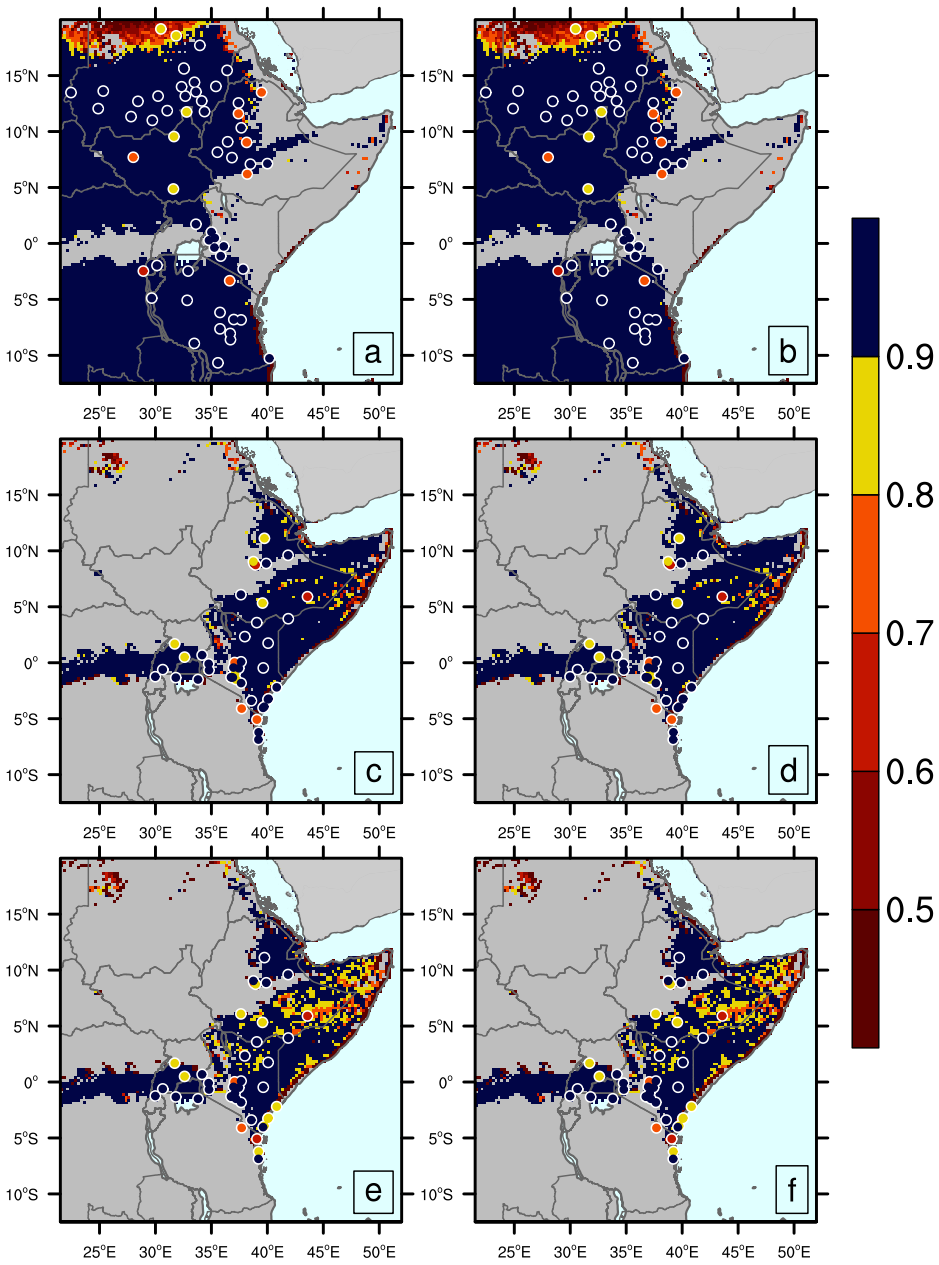

Figure S6: Proportion of detectable onset and cessation dates to the length of the time series. (a,b) onset and cessation for single-wet-season regimes, (c,d) Long Rains and (e,f) Short Rains, respectively. Grid points show the estimations based on the CHIRPS product. Station-based estimations are shown by colored circles.

Table S1: List of available stations from KASS-D. A map of the locations is shown in Figure 4.1. The numbers correspond to those in Figures 8, 12, S1 and S1. The names correspond to the names in the Integrated Surface Database (ISD), available at ftp://ftp.ncdc.noaa.gov/pub/data/noaa/isd-history.txt.

Nr.	Name	Lat	Lon	Altitude	Country
1	Port Sudan	19.6 N	37.2 E	42 m	Sudan
2	Abu Hamed	19.5 N	33.3 E	312 m	Sudan
3	Dongola	19.2 N	30.5 E	226 m	Sudan
4	Karima	18.6 N	31.9 E	249 m	Sudan
5	Atbara	17.7 N	34.0 E	345 m	Sudan
6	Shambat Observatory	15.7 N	32.5 E	380 m	Sudan
7	Khartoum	15.6 N	32.5 E	380 m	Sudan
8	Kassala	15.5 N	36.4 E	500 m	Sudan
9	Wad Medani	14.4 N	33.5 E	408 m	Sudan
10	Ed Duem	14.0 N	32.3 E	378 m	Sudan
11	Gedaref	14.0 N	35.4 E	599 m	Sudan
12	El Fasher	13.6 N	25.3 E	733 m	Sudan
13	Sennar	13.6 N	33.6 E	418 m	Sudan
14	Makale	13.5 N	39.5 E	2070 m	Ethiopia
15	Genina	13.5 N	22.5 E	805 m	Sudan
16	El Obeid	13.2 N	30.2 E	574 m	Sudan
17	Kosti Rabak	13.2 N	32.7 E	381 m	Sudan
18	Abu Na'ama	12.7 N	34.1 E	445 m	Sudan
19	En Nahud	12.7 N	28.4 E	564 m	Sudan
20	Gondar	12.6 N	37.4 E	1967 m	Ethiopia
21	Nyala	12.1 N	24.9 E	643 m	Sudan
22	Rashad	11.9 N	31.1 E	885 m	Sudan
23	Damazine	11.8 N	34.4 E	470 m	Sudan
24	Renk	11.8 N	32.8 E	282 m	Sudan
25	Bahar Dar	11.6 N	37.4 E	1770 m	Ethiopia
26	Babanusa	11.3 N	27.8 E	453 m	Sudan
27	Combolcha	11.1 N	39.7 E	1903 m	Ethiopia
28	Kadoglli	11.0 N	29.7 E	499 m	Sudan
29	Debre Marcos	10.3 N	37.7 E	2515 m	Ethiopia
30	Dire Dawa	9.6 N	41.9 E	1260 m	Ethiopia
31	Malakal	9.6 N	31.7 E	388 m	South Sudan
32	Lekemte	9.1 N	36.5 E	2080 m	Ethiopia
33	Addis Ababa-Bole	9.0 N	38.8 E	2354 m	Ethiopia
34	Ginchi	9.0 N	38.2 E	2236 m	Ethiopia
35	Metehara	8.9 N	40.0 E	930 m	Ethiopia
36	Akaki	8.9 N	38.8 E	2125 m	Ethiopia
37	Harar Meda	8.7 N	39.0 E	1900 m	Ethiopia
38	Gore	8.2 N	35.5 E	2002 m	Ethiopia
39	Wau	7.7 N	28.0 E	438 m	South Sudan
40	Jimma	7.7 N	36.8 E	1725 m	Ethiopia
41	Awassa	7.1 N	38.5 E	1750 m	Ethiopia
42	Robe/Bale	7.1 N	40.0 E	2480 m	Ethiopia
43	Yirga Cheffe	6.2 N	38.2 E	1890 m	Ethiopia
44	Gode	5.9 N	43.6 E	295 m	Ethiopia
45	Arba Minch	6.1 N	37.6 E	1290 m	Ethiopia
46	Neghelle	5.3 N	40.0 E	1544 m	Ethiopia
47	Juba	4.9 N	31.6 E	457 m	South Sudan
48	Mandera	3.9 N	41.9 E	231 m	Kenya
49	Moyale	3.5 N	39.1 E	1112 m	Ethiopia/Kenya
50	Lodwar	3.1 N	35.6 E	515 m	Kenya
51	Marsabit	2.3 N	38.0 E	1345 m	Kenya
52	Wajir	1.8 N	40.0 E	244 m	Kenya
53	Soroti	1.7 N	33.6 E	1123 m	Uganda
54	Masindi	1.7 N	31.7 E	1147 m	Uganda
55	Kitale	1.0 N	35.0 E	1875 m	Kenya

Nr.	Name	Lat	Lon	Altitude	Country
56	Tororo	0.7 N	34.2 E	1171 m	Uganda
57	Namulonge	0.5 N	32.6 E	1236 m	Uganda
58	Eldoret	0.5 N	35.3 E	2120 m	Kenya
59	Ol Maisor Farm	0.4 N	36.7 E	1803 m	Kenya
60	Kakamega	0.3 N	34.8 E	1530 m	Kenya
61	Rumuruti	0.3 N	36.5 E	1792 m	Kenya
62	Meru	0.1 N	37.7 E	1554 m	Kenya
63	Nyahururu	0.0 N	36.4 E	2378 m	Kenya
64	Nanyuki	0.0 N	37.1 E	1890 m	Kenya
65	Ndaragwa Forest	0.1 S	36.5 E	2281 m	Kenya
66	Kisumu	0.1 S	34.8 E	1146 m	Kenya
67	Nakuru	0.3 S	36.1 E	1901 m	Kenya
68	Kericho	0.4 S	35.3 E	1976 m	Kenya
69	Nyeri	0.4 S	37.0 E	1798 m	Kenya
70	Garissa	0.5 S	39.6 E	147 m	Kenya
71	Embu	0.5 S	37.5 E	1493 m	Kenya
72	Mbarara	0.6 S	30.7 E	1413 m	Uganda
73	Kisii	0.7 S	34.8 E	1493 m	Kenya
74	Nairobi Thika	1.0 S	37.1 E	1463 m	Kenya
75	Narok	1.1 S	35.8 E	1890 m	Kenya
76	Kabale	1.3 S	30.0 E	1869 m	Uganda
77	Nairobi Kabete	1.3 S	36.8 E	1820 m	Kenya
78	Nairobi Dagoretti Corner	1.3 S	36.8 E	1798 m	Kenya
79	Nairobi Wilson	1.3 S	36.8 E	1679 m	Kenya
80	Nairobi Kenyatta Airport	1.3 S	36.9 E	1624 m	Kenya
81	Bukoba	1.3 S	31.8 E	1143 m	Tanzania
82	Nairobi Machakos	1.5 S	37.2 E	1646 m	Kenya
83	Musoma	1.5 S	33.8 E	1147 m	Tanzania
84	Kampi Ya Mawe	1.8 S	37.7 E	1125 m	Kenya
85	Kigali	2.0 S	30.1 E	1481 m	Rwanda
86	Lamu	2.2 S	40.8 E	1 m	Kenya
87	Makindu	2.3 S	37.8 E	1000 m	Kenya
88	Mwanza	2.5 S	32.9 E	1140 m	Tanzania
89	Kamembe	2.5 S	28.9 E	1591 m	Rwanda
90	Voi	3.2 S	40.1 E	579 m	Kenya
91	Msabaha	3.3 S	40.1 E	91 m	Kenya
92	Arusha	3.3 S	36.6 E	1387 m	Tanzania
93	Malindi	3.4 S	38.6 E	19 m	Kenya
94	Mtwapa	3.9 S	39.7 E	200 m	Kenya
95	Mombasa	4.0 S	39.6 E	55 m	Kenya
96	Same	4.1 S	37.7 E	872 m	Tanzania
97	Kigoma	4.9 S	29.7 E	824 m	Tanzania
98	Tanga	5.1 S	39.1 E	35 m	Tanzania
99	Tabora Airport	5.1 S	32.8 E	1182 m	Tanzania
100	Dodoma	6.2 S	35.8 E	1120 m	Tanzania
101	Zanzibar/Kisauni	6.2 S	39.2 E	18 m	Tanzania
102	Ilonga	6.8 S	37.0 E	503 m	Tanzania
103	Morogoro	6.8 S	37.7 E	526 m	Tanzania
104	Dar Es Salaam Airport	6.9 S	39.2 E	53 m	Tanzania
105	Iringa	7.6 S	35.8 E	1428 m	Tanzania
106	Ifakara Katrin	8.0 S	36.7 E	274 m	Tanzania
107	Mahenge	8.6 S	36.7 E	1200 m	Tanzania
108	Mbeya	8.9 S	33.5 E	1758 m	Tanzania
109	Mtwara	10.3 S	40.2 E	113 m	Tanzania
110	Songea	10.7 S	35.6 E	1036 m	Tanzania

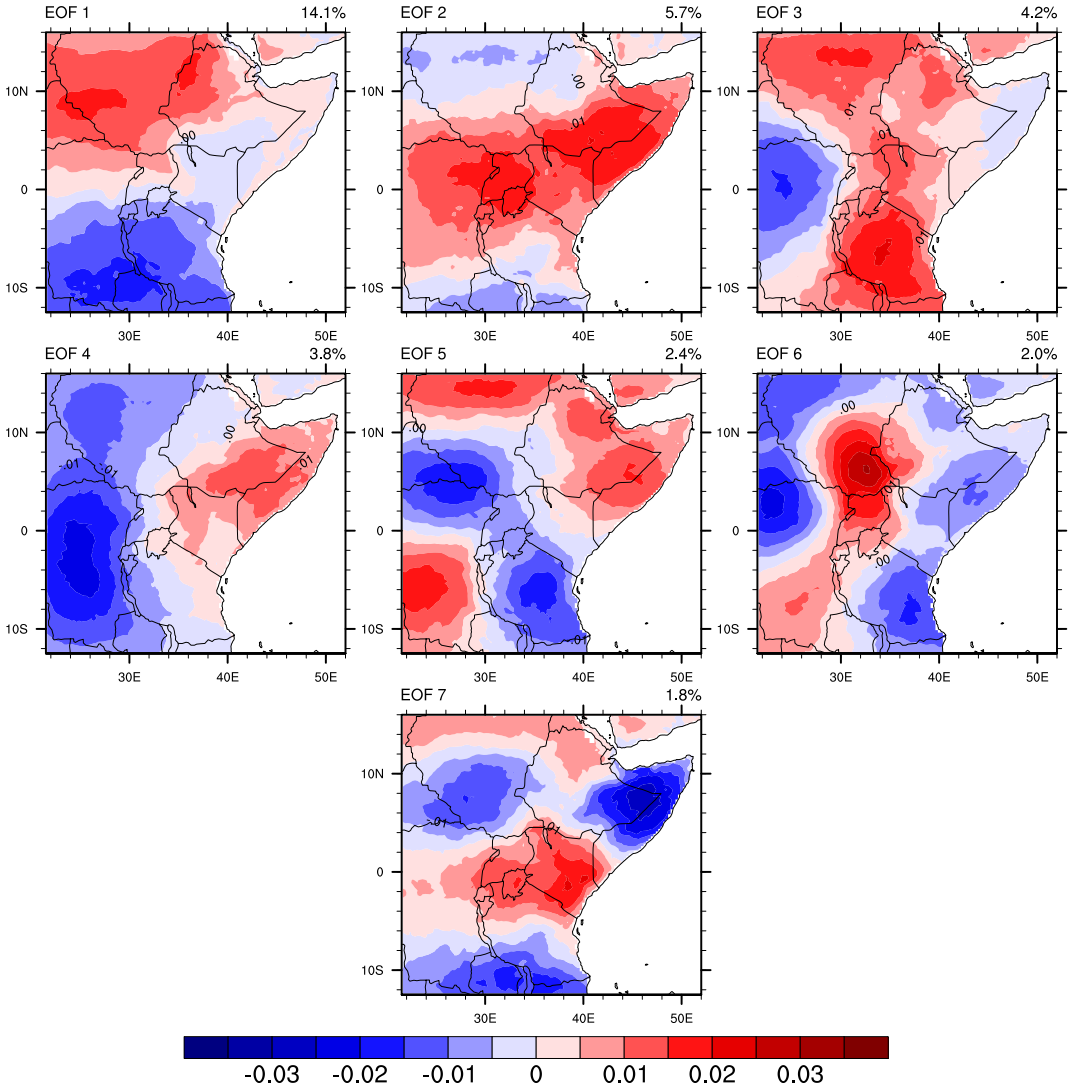

Figure S7: Spatial loadings of the leading seven eigenvectors associated with the leading principal components of CHIRPS daily rainfall for the period 1981 to 2018. Negative values are indicated with blue contours, while positive values are marked by red contours.

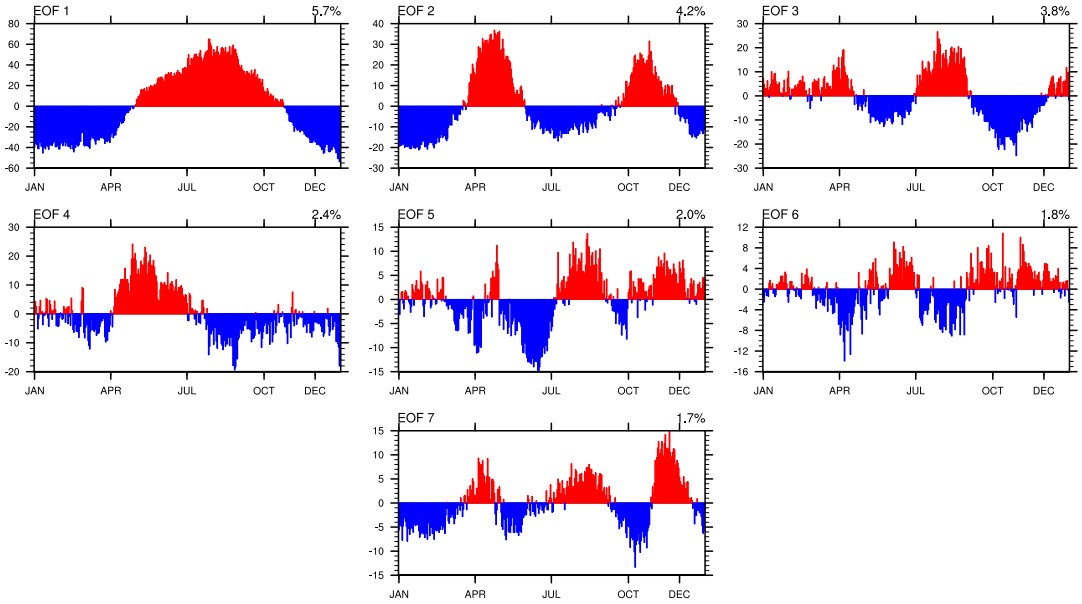

Figure S8: Multi-year average annual cycle of the leading seven scores of the principal components plotted versus the day of the year. Negative values are indicated with blue bars, while positive values are marked by red bars. © The authors and John Wiley & Sons Ltd, CC-BY.

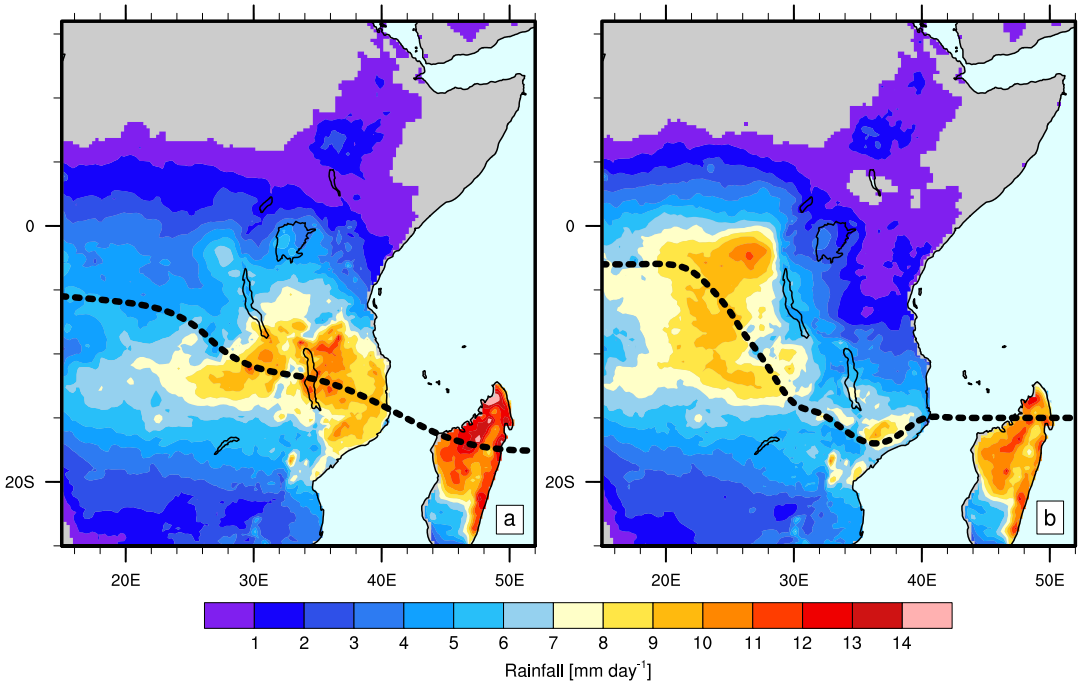

Figure S9: Mean daily rainfall and approximate positions of the tropical rain band (TRB) for days in (a) cluster SE and (b) cluster SW during the Msimu Rains. Colours denote rainfall amounts. The bold black lines show the approximate positions of the TRB). © The authors and John Wiley & Sons Ltd, CC-BY.

Bibliography

African Development Bank (ADBG), 2019: Eastern Africa Regional Integration Strategy Paper – 2018-2022. URL https://www.afdb.org/en/documents/document/eastern-africa-regional-integration-strategy-paper-2018-2022-106393.

Alexander, L. V., and Coauthors, 2006: Global observed changes in daily climate extremes of temperature and precipitation. *Journal of Geophysical Research: Atmospheres*, **111 (D5)**, doi:10.1029/2005JD006290.

Alexandersson, H., 1986: A homogeneity test applied to precipitation data. *Journal of Climatology*, **6 (6)**, 661–675, doi:10.1002/joc.3370060607.

Amante, C., and B. W. Eakins, 2009: ETOPO1 1 Arc-Minute Global Relief Model: Procedures, Data Sources and Analysis. URL https://data.nodc.noaa.gov/cgi-bin/iso?id=gov.noaa.ngdc.mgg.dem:316#, doi:10.7289/V5C8276M.

Ashok, K., S. K. Behera, S. A. Rao, H. Wenig, and T. Yamagata, 2007: El Niño Modoki and its possible teleconnection. *Journal of Geophysical Research*, **112**, C11 007, doi:10.1029/2006JC003798.

Bahaga, T., A. Fink, and P. Knippertz, 2019: Revisiting interannual to decadal teleconnections influencing seasonal rainfall in the Greater Horn of Africa during the 20th century. *International Journal of Climatology*, **39**, 2765–2785, doi:10.1002/joc.5986.

Baquero-Bernal, A., M. Latif, and S. Legutke, 2002: On dipolelike variability of sea surface temperature in the tropical indian ocean. *Journal of Climate*, **15 (11)**, 1358–1368, doi:10.1175/1520-0442(2002)015<1358:ODVOSS>2.0.CO;2.

Bayissa, Y., T. Tadesse, G. Demisse, and S. A., 2017: Evaluation of Satellite-Based Rainfall Estimates and Application to Monitor Meteorological Drought for the Upper Blue Nile Basin, Ethiopia. *Remote Sensing*, **9 (7)**, 669, doi:10.3390/rs9070669.

Beck, H., N. E. Zimmermann, T. R. McVicar, N. Vergopolan, A. Berg, and E. Wood, 2018: Present and future Köppen-Geiger climate classification maps at 1-km resolution. *Scientific Data*, **5**, 180 214, doi:10.1038/sdata.2018.214.

Behera, S. K., and T. Yamagata, 2001: Subtropical sst dipole events in the southern indian ocean. *Geophysical Research Letters*, **28 (2)**, 327–330, doi:10.1029/2000GL011451.

Bekele-Biratu, E., W. M. Thiaw, and D. Korecha, 2018: Sub-seasonal variability of the Belg rains in Ethiopia. *International Journal of Climatology*, **38**, 2940–2953, doi:10.1002/joc.5474.

Berhane, F., and B. Zaitchik, 2014: Modulation of daily precipitation over east africa by the madden-julian oscillation. *Journal of Climate*, **27 (15)**, 6016–6034, doi:10.1175/JCLI-D-13-00693.1.

Black, E., J. Slingo, and K. Sperber, 2003: An observational study of the relationship between excessively strong short rains in coastal East Africa and Indian Ocean SST. *Monthly Weather Review*, **131**, 74–94, doi:10.1175/1520-0493(2003)131<0074:AOSOTR>2.0.CO;2.

Blamey, R. C., S. R. Kolusu, M. P., M. C. Todd, and C. J. C. Reason, 2018: The role of regional circulation features in regulating El Niño climate impacts over southern Africa: A comparison of the 2015/2016 drought with previous events. *International Journal of Climatology*, **38**, 4276–4295, doi:10.1002/joc.5668.

Bombardi, R. J., V. Moron, and J. S. Goodnight, 2019: Detection, variability, and predictability of monsoon onset and withdrawal dates: A review. *International Journal of Climatology*, 1–27, doi:10.1002/joc.6264.

Boyard-Micheau, J., P. Camberlin, N. Philippon, and V. Moron, 2013: Regional-scale rainy season onset detection: A new approach based on multivariate analysis. *Journal of Climate*, **26**, 8916–8928, doi:10.1175/JCLI-D-12-00730.1.

Camberlin, P., 1995: June-september rainfall in north-eastern Africa and atmospheric signals over the tropics: A zonal perspective. *International Journal of Climatology*, **15 (7)**, 773–783, doi:10.1002/joc.3370150705.

Camberlin, P., and R. E. Okoola, 2003: The onset and cessation of the "long rains" in eastern Africa and their interannual variability. *Theoretical and Applied Climatology*, **75**, 43–54, doi:10.1007/s00704-002-0721-5.

Camberlin, P., and N. Philippon, 2002: The East African March-May Rainy Season : Associated Atmospheric Dynamics and Predictability over the 1968-97 Period. *Journal of Climate*, **15 (9)**, 1002–1019, doi:10.1175/1520-0442(2002)015<1002:TEAMMR>2.0.CO;2.

Camberlin, P., and O. Planchon, 1997: Coastal Precipitation Regimes in Kenya. *Geografiska Annaler, Series A: Physical Geography*, **79 (1-2)**, 109–119, doi:10.1111/j.0435-3676.1997.00010.x.

Camberlin, P., and J. G. Wairoto, 1997: Intraseasonal Wind Anomalies Related to Wet and Dry Spells During the "long" and "short" Rainy Seasons in Kenya. *Theoretical and Applied Climatology*, **58**, 57–69, doi:10.1007/BF0086743.

Cattani, E., A. Merino, J. A. Guijarro, and V. Levizzani, 2018: East Africa Rainfall Trends and Variability 1983–2015 Using Three Long-Term Satellite Products. *Remote Sensing*, **10 (6)**, 931, doi:10.3390/rs10060931.

Cattani, E., A. Merino, and V. Levizzani, 2016: Evaluation of Monthly Satellite-Derived Precipitation Products over East Africa. *Journal of Hydrometeorology*,

17 (10), 2555–2573, doi:10.1175/JHM-D-15-0042.1, URL http://journals.ametsoc.org/doi/10.1175/JHM-D-15-0042.1.

Chakraborty, A., R. S. Nanjundiah, and J. Srinivasan, 2009: Impact of african orography and the indian summer monsoon on the low-level somali jet. *International Journal of Climatology*, **29 (7)**, 983–992, doi:10.1002/joc.1720.

Chou, C., and J. D. Neelin, 2003: Mechanisms limiting the northward extent of the northern summer monsoons over north america, asia, and africa. *Journal of Climate*, **16 (3)**, 406–425, doi:10.1175/1520-0442(2003)016<0406:MLTNEO>2.0.CO;2.

Clark, S., M. Reeder, and C. Jakob, 2018: Rainfall regimes over northwestern australia. *Quarterly Journal of the Royal Meteorological Society*, **144 (711)**, 458–467, doi:https://doi.org/10.1002/qj.3217, URL https://rmets.onlinelibrary.wiley.com/doi/abs/10.1002/qj.3217, https://rmets.onlinelibrary.wiley.com/doi/pdf/10.1002/qj.3217.

Cook, C. C., C. J. C. Reason, and B. C. Hewitson, 2004: Wet and dry spells within particularly wet and dry summers in the South African summer rainfall region. *Climate Research*, **26 (1)**, 17–31, doi:10.3354/cr026017.

Cook, K. H., 2000: The south indian convergence zone and interannual rainfall variability over southern africa. *Journal of Climate*, **13 (21)**, 3789–3804, doi:10.1175/1520-0442(2000)013<3789:TSICZA>2.0.CO;2.

Cook, K. H., and E. K. Vizy, 2013: Projected Changes in East African Rainy Seasons. *Journal of Climate*, **26 (16)**, 5931–5948, doi:10.1175/JCLI-D-12-00455.1.

Cook, K. H., and E. K. Vizy, 2016: The Congo Basin Walker circulation: dynamics and connections to precipitation. *Climate Dynamics*, **47**, 697–717, doi:10.1007/s00382-015-2864-y.

Copernicus Climate Change Service (C3S), 2017: ERA5: Fifth generation of ECMWF atmospheric reanalyses of the global climate. URL https://cds.climate.copernicus.eu/cdsapp#!/home.

Cressman, K., 2016: *Desert Locust*, 87–105. doi:10.1016/B978-0-12-394847-2.00006-1.

Crétat, J., B. Pohl, B. Dieppois, S. Berthou, and J. Pergaud, 2019: The Angola Low: relationship with southern African rainfall and ENSO. *Climate Dynamics*, **52**, 1783–1803, doi:10.1007/s00382-018-4222-3.

Dee, D. P., S. M. Uppala, A. J. Simmons, P. Berrisford, P. Poli, S. Kobayashi, and Coauthors, 2011: The ERA-Interim reanalysis: configuration and performance of the data assimilation system. *Quaterly Journal of the Royal Meteorological Society*, **137**, 553–597, doi:10.1002/qj.828.

Diatta, S., and A. H. Fink, 2014: Statistical relationship between remote climate indices and west african monsoon variability. *International Journal of Climatology*, **34 (12)**, 3348–3367, doi:10.1002/joc.3912.

Diaz, H. F., and V. Markgraf, Eds., 2000: *El Niño and the Southern Oscillation*. Cambridge University Press.

Diem, J. E., J. Hartter, S. J. Ryan, and M. W. Palace, 2014a: Validation of Satellite Rainfall Products for Western Uganda. *Journal of Hydrometeorology*, **15 (5)**, 2030–2038, doi:10.1175/JHM-D-13-0193.1.

Diem, J. E., B. L. Konecky, J. Salerno, and J. Hartter, 2019: Is equatorial africa getting wetter or drier? insights from an evaluation of long-term, satellite-based rainfall estimates for western uganda. *International Journal of Climatology*, **39 (7)**, 3334–3347, doi:10.1002/joc.6023.

Diem, J. E., S. J. Ryan, J. Hartter, and M. W. Palace, 2014b: Satellite-based rainfall data reveal a recent drying trend in central equatorial Africa. *Climatic Change*, **126 (1-2)**, 263–272, doi:10.1007/s10584-014-1217-x.

Dinku, T., P. Ceccato, E. Grover-Kopec, M. Lemma, S. J. Connor, and C. F. Ropelewski, 2007: Validation of satellite rainfall products over East Africa's complex topography. *International Journal of Remote Sensing*, **28 (7)**, 1503–1526, doi:10.1080/01431160600954688.

Dinku, T., S. Chidzambwa, P. Ceccato, S. J. Connor, and C. F. Ropelewski, 2008: Validation of high-ĂŘresolution satellite rainfall products over complex terrain. *International Journal of Remote Sensing*, **29 (14)**, 4097–4110, doi:10.1080/01431160701772526.

Dinku, T., K. Hailemariam, R. Maidment, E. Tarnavsky, and S. Connor, 2014: Combined use of satellite estimates and rain gauge observations to generate high-quality historical rainfall time series over ethiopia. *International Journal of Climatology*, **34 (7)**, 2489–2504, doi:10.1002/joc.3855.

Diro, G. T., D. I. F. Grimes, and E. Black, 2011: Teleconnections between Ethiopian summer rainfall and sea surface temperature: part I – observation and modelling. *Climate Dynamics*, **37**, 103–119, doi:10.1007/s00382-010-0837-8.

Donald, A., H. Meinke, B. Power, A. d. H. N. Maia, M. C. Wheeler, N. White, R. C. Stone, and J. Ribbe, 2006: Near-global impact of the madden-julian oscillation on rainfall. *Geophysical Research Letters*, **33 (9)**, doi:10.1029/2005GL025155.

Duchon, C. E., 1979: Lanczos Filtering in One and Two Dimensions. *Journal of Applied Meteorology*, **18 (8)**, 1016–1022, doi:10.1175/1520-0450(1979)018<1016:LFIOAT>2.0.CO;2.

Dunning, C. M., E. Black, and R. P. Allan, 2018: Later wet seasons with more intense rainfall over africa under future climate change. *Journal of Climate*, **31 (23)**, 9719–9738, doi:10.1175/JCLI-D-18-0102.1.

Dunning, C. M., E. C. L. Black, and R. P. Allan, 2016: The onset and cessation of seasonal rainfall over Africa. *Journal of Geophysical Research: Atmospheres*, **121 (19)**, 11,405–11,424, doi:10.1002/2016JD025428.

Dutra, E., L. Magnusson, F. Wetterhall, H. L. Cloke, G. Balsamo, S. Boussetta, and F. Pappenberger, 2013: The 2010–2011 drought in the Horn of Africa in

ECMWF reanalysis and seasonal forecast products. *International Journal of Climatology*, **33 (7)**, 1720–1729, doi:10.1002/joc.3545.

Elagib, N. A., and M. M. Elhag, 2011: Major climate indicators of ongoing drought in sudan. *Journal of Hydrology*, **409 (3)**, 612 – 625, doi:10.1016/j.jhydrol.2011.08.047.

Emanuel, K. A., 1987: An air-sea interaction model of intraseasonal oscillations in the tropics. *Journal of the Atmospheric Sciences*, **44 (16)**, 2324–2340, doi:10.1175/1520-0469(1987)044<2324:AASIMO>2.0.CO;2.

Endo, S., and T. Tozuka, 2016: Two flavors of the Indian Ocean Dipole. *Climate Dynamics*, **46**, 3371–3385, doi:10.1007/s00382-015-2773-0.

Evan, A. T., C. Flamant, C. Lavaysse, C. Kocha, and A. Saci, 2015: Water vapor-ĂŞforced greenhouse warming over the sahara desert and the recent recovery from the sahelian drought. *Journal of Climate*, **28 (1)**, 108–123, doi:10.1175/JCLI-D-14-00039.1.

Fan, L. Q., L. C. Wang, and F. Guo, 2017: Indian Ocean Dipole Modes Associated with Different Types of ENSO Developments. *Journal of Climate*, **30**, 2233–2249, doi:10.1175/JCLI-D-16-0426.1.

Fauchereau, N., B. Pohl, C. J. C. Reason, M. Rouault, and Y. Richard, 2009: Recurrent daily OLR patterns in the Southern Africa/Southwest Indian Ocean region, implications for South African rainfall and teleconnections. *Climate Dynamics*, **32 (4)**, 575–591, doi:10.1007/s00382-008-0426-2.

Fenta, A. A., H. Yasuda, K. Shimizu, N. Haregeweyn, T. Kawai, D. Sultan, K. Ebabu, and A. S. Belay, 2017: Spatial distribution and temporal trends of rainfall and erosivity in the eastern africa region. *Hydrological Processes*, **31 (25)**, 4555–4567, doi:10.1002/hyp.11378.

Findlater, J., 1966: Cross-equatorial jet streams at low level over Kenya. *Meteorological Magazine*, **95**, 353–364.

Findlater, J., 1969: A major low-level air current near the indian ocean during the northern summer. *Quarterly Journal of the Royal Meteorological Society*, **95 (404)**, 362–380, doi:10.1002/qj.49709540409.

Findlater, J., 1977: Observational aspects of the low-level cross-equatorial jet stream of the western Indian Ocean. *Pure and Applied Geophysics*, **115**, 1251–1262, doi:10.1007/BF00874408.

Finney, D. L., J. H. Marsham, D. P. Walker, C. B. Birch, B. J. Woodhams, L. S. Jackson, and S. Hardy, 2019: The effect of westerlies on East African rainfall and the associated role of tropical cyclones and the Madden-Julian Oscillation. *Quarterly Journal of Royal Meteorological Society*, 1–18, doi:10.1002/qj.3698.

Fitzpatrick, R. G. J., C. L. Bain, P. Knippertz, J. H. Marsham, and D. J. Parker, 2015: The West African Monsoon Onset: A Concise Comparison of Definitions. *Journal of Climate*, **28 (22)**, 8673–8694, doi:10.1175/JCLI-D-15-0265.1.

Fontaine, B., and S. Louvet, 2006: Sudan-Sahel rainfall onset: Definition of an objective index, types of years, and experimental hindcasts. *Journal of Geophysical Research*, **111 (D20)**, D20 103, doi:10.1029/2005JD007019.

Freitas, A. C. V., L. Aímola, T. Ambrizzi, and C. P. de Oliveira, 2017: Extreme intertropical convergence zone shifts over southern maritime continent. *Atmospheric Science Letters*, **18 (1)**, 2–10, doi:10.1002/asl.716.

Funk, C., 2011: We thought trouble was coming. *Nature*, **476**, 7, doi:10.1038/476007a.

Funk, C., M. D. Dettinger, J. C. Michaelsen, J. P. Verdin, M. E. Brown, M. Barlow, and A. Hoell, 2008: Warming of the indian ocean threatens eastern and southern african food security but could be mitigated by agricultural development. *Proceedings of the National Academy of Sciences*, **105 (32)**, 11 081–11 086, doi:10.1073/pnas.0708196105.

Funk, C., A. Hoell, S. Shukla, I. Bladé, B. Liebmann, J. B. Roberts, F. R. Robertson, and G. Husak, 2014: Predicting east african spring droughts using pacific and indian ocean sea surface temperature indices. *Hydrology and Earth System Sciences*, **18 (12)**, 4965–4978, doi:10.5194/hess-18-4965-2014.

Funk, C., A. Verdin, J. Michaelsen, P. Peterson, D. Pedreros, and G. Husak, 2015a: A global satellite-assisted precipitation climatology. *Earth System Science Data*, **7 (2)**, 275–287, doi:10.5194/essd-7-275-2015.

Funk, C., and Coauthors, 2015b: The climate hazards infrared precipitation with stations - a new environmental record for monitoring extremes. *Scientific Data*, **2**, 150 066, doi:10.1038/sdata.2015.66.

Funk, C., and Coauthors, 2018: Examining the role of unusually warm Indo-Pacific sea-surface temperatures in recent African droughts. *Quarterly Journal of the Royal Meteorological Society*, **144 (Suppl. 1)**, 360–383, doi:DOI:10.1002/qj.3266.

Gadgil, S., 2003: The indian monsoon and its variability. *Annual Review of Earth and Planetary Sciences*, **31 (1)**, 429–467, doi:10.1146/annurev.earth.31.100901.141251.

Garcia, S., and M. Kayano, 2009: Determination of the onset dates of the rainy season in central Amazon with equatorially antisymmetric outgoing longwave radiation. *Theoretical and Applied Climatology*, **97**, 361–372, doi:10.1007/s00704-008-0080-y.

Goddard, L., and N. Graham, 1999: Importance of the Indian Ocean for simulating rainfall anomalies over eastern and southern Africa. *Journal of Geophysical Research*, **104**, 99–116, doi:10.1029/1999JD900326.

Grist, J. P., and S. E. Nicholson, 2001: A study of the dynamic factors influencing the rainfall variability in the west african sahel. *Journal of Climate*, **14 (7)**, 1337–1359, doi:10.1175/1520-0442(2001)014<1337:ASOTDF>2.0.CO;2.

Habtemichael, A., and D. Pegley, 1974: Synoptic case-study of spring rains in Er-

itrea. *Archiv für Meteorologie, Geophysik und Bioklimatologie, Serie A*, **23**, 285–296, doi:10.1007/BF02247268.

Halpern, D., and P. M. Woiceshyn, 1999: Onset of the somali jet in the arabian sea during june 1997. *Journal of Geophysical Research: Oceans*, **104 (C8)**, 18 041–18 046, doi:10.1029/1999JC900141.

Halpern, D., and P. M. Woiceshyn, 2001: Somali jet in the arabian sea, el niño, and india rainfall. *Journal of Climate*, **14 (3)**, 434–441, doi:10.1175/1520-0442(2001)014<0434:SJITAS>2.0.CO;2.

Harrison, L., C. Funk, A. McNally, S. Shukla, and G. Husak, 2019: Pacific sea surface temperature linkages with tanzania's multi-season drying trends. *International Journal of Climatology*, **39 (6)**, 3057–3075, doi:10.1002/joc.6003.

Hart, N. C. G., C. J. C. Reason, and N. Fauchereau, 2013a: Cloud bands over southern africa: seasonality, contribution to rainfall variability, and modulation by the mjo. *Climate Dynamics*, **41 (5-6)**, 1199–1212, doi:10.1007/s00382-012-1589-4.

Hart, N. C. G., C. J. C. Reason, and N. Fauchereau, 2013b: Tropical-extratropical interactions over southern africa: Three cases of heavy summer season rainfall. *Monthly Weather Review*, **138 (7)**, 2608–2623, doi:10.1175/2010MWR3070.1.

Hart, N. C. G., R. Washington, and C. J. C. Reason, 2018: On the likelihood of tropical-ĂŞextratropical cloud bands in the south indian convergence zone during enso events. *Journal of Climate*, **31 (7)**, 2797–2817, doi:10.1175/JCLI-D-17-0221.1.

Hastenrath, S., 2000: Zonal circulations over the equatorial indian ocean. *Journal of Climate*, **13 (15)**, 2746–2756, doi:10.1175/1520-0442(2000)013<2746:ZCOTEI>2.0.CO;2.

Hastenrath, S., A. Nicklis, and L. Greischar, 1993: Atmospheric-hydrospheric mechanisms of climate anomalies in the western equatorial indian ocean. *Journal of Geophysical Research: Oceans*, **98 (C11)**, 20 219–20 235, doi:10.1029/93JC02330.

Hauser, S., C. M. Grams, M. J. Reeder, S. McGregor, A. H. Fink, and J. F. Quinting, 2020: A weather system perspective on winter?spring rainfall variability in southeastern australia during el niño. *Quarterly Journal of the Royal Meteorological Society*, **146 (731)**, 2614–2633, doi:https://doi.org/10.1002/qj.3808.

Helsel, D. R., and R. M. Hirsch, 2002: Statistical methods in water resources. *Hydrologic Analysis and Interpretation*, Techniques of Water-Resources Investigations of the United States Geological Survey, Vol. 4, U.S. Geological Survey, Reston, VA, doi:10.3133/twri04A3.

Hendon, H. H., and M. L. Salby, 1994: The life cycle of the madden-julian oscillation. *Journal of the Atmospheric Sciences*, **51 (15)**, 2225–2237, doi:10.1175/1520-0469(1994)051<2225:TLCOTM>2.0.CO;2.

Hermes, J. C., and C. J. C. Reason, 2009: Variability in sea-surface temperature and winds in the tropical south-east atlantic ocean and regional rain-

fall relationships. *International Journal of Climatology*, **29 (1)**, 11–21, doi: 10.1002/joc.1711.

Herrmann, S. M., A. Anyamba, and C. J. Tucker, 2005: Recent trends in vegetation dynamics in the African Sahel and their relationship to climate. *Global Environmental Change*, **15 (4)**, 394–404, doi:10.1016/j.gloenvcha.2005.08.004.

Herrmann, S. M., and K. I. Mohr, 2011: A continental-scale classification of rainfall seasonality regimes in Africa based on gridded precipitation and land surface temperature products. *Journal of Applied Meteorology and Climatology*, **50 (12)**, 2504–2513, doi:10.1175/JAMC-D-11-024.1.

Hills, R. C., 1979: The Structure of the Inter-Tropical Convergence Zone in Equatorial Africa and Its Relationship to East African Rainfall. *Transactions of the Institute of British Geographers*, **4 (3)**, 329–352, doi:10.2307/622055.

Hirpa, F. A., M. Gebremichael, and T. Hopson, 2010: Evaluation of High-Resolution Satellite Precipitation Products over Very Complex Terrain in Ethiopia. *Journal of Applied Meteorology and Climatology*, **49 (5)**, 1044–1051, doi: 10.1175/2009JAMC2298.1.

Hirsch, R. M., J. R. Slack, and R. A. Smith, 1982: Techniques of trend analysis for monthly water quality data. *Water Resources Research*, **18 (1)**, 107–121, doi:10.1029/WR018i001p00107.

Hoell, A., M. Hoerling, J. Eischeid, X.-W. Quan, and B. Liebmann, 2017: Reconciling theories for human and natural attribution of recent east africa drying. *Journal of Climate*, **30 (6)**, 1939–1957, doi:10.1175/JCLI-D-16-0558.1.

Hogan, E., A. Shelly, and P. Xavier, 2015: The observed and modelled influence of the madden-ĂŞjulian oscillation on east african rainfall. *Meteorological Applications*, **22 (3)**, 459–469, doi:10.1002/met.1475.

Howard, E., and R. Washington, 2018: Characterizing the Synoptic Expression of the Angola Low. *Journal of Climate*, **31**, 7147–7165, doi:10.1175/JCLI-D-18-0017.1.

Howard, E., R. Washington, and K. I. Hodges, 2019: Characterizing the Synoptic Expression of the Angola Low. *Journal of Geophysical Research: Atmospheres*, **124**, 11,009–11,032, doi:10.1029/2019JD030803.

Hua, W., L. Zhou, H. Chen, S. E. Nicholson, Y. Jiang, and A. Raghavendra, 2018: Understanding the central equatorial african long-term drought using amip-type simulations. *Climate Dynamics*, **50**, 1115–1128, doi:10.1007/s00382-017-3665-2.

Hua, W., L. Zhou, H. Chen, S. E. Nicholson, A. Raghavendra, and Y. Jiang, 2016: Possible causes of the central equatorial african long-term drought. *Environmental Research Letters*, **11 (12)**, 124 002, doi:10.1088/1748-9326/11/12/124002.

Huffman, G. J., E. Stocker, D. Bolvin, E. Nelkin, and J. Tan, 2019: *GPM IMERG Final Precipitation L3 1 day 0.1 degree x 0.1 degree V06s*. Goddard Earth Sciences Data and Information Services Center (GES DISC), Greenbelt, MD, doi: 10.5067/GPM/IMERGDF/DAY/06.

Huffman, G. J., and Coauthors, 2007: The TRMM Multisatellite Precipitation Analysis (TMPA): Quasi-Global, Multiyear, Combined-Sensor Precipitation Estimates at Fine Scales. *Journal of Hydrometeorology*, **8 (1)**, 38–55, doi: 10.1175/JHM560.1.

Hurrell, J. W., Y. Kushnir, G. Ottersen, and M. Visbeck, 2013: *An Overview of the North Atlantic Oscillation*, 1–35. American Geophysical Union (AGU), doi: 10.1029/134GM01.

Indeje, M., F. H. M. Semazzi, and L. J. Ogallo, 2000: ENSO Signals in East African Rainfall Seasons. *International Journal of Climatology*, **20**, 19–46, doi: 10.3354/cr013231.

Inter-Agency Standing Comitee (IASC), 2012: *IASC Real-Time Evaluation of the Humanitarian Response to the Horn of Africa Drought Crisis in Somalia, Ethiopia and Kenya*. URL https://reliefweb.int/sites/reliefweb.int/files/resources/RTE_HoA_SynthesisReport_FINAL.pdf.

Kabanda, T. A., and M. R. Jury, 1999: Inter-annual variability of short rains over northern Tanzania. *Climate Research*, **13 (3)**, 231–241, doi:10.3354/cr013231.

Kang, S. M., Y. Shin, and S.-P. Xie, 2018: Extratropical forcing and tropical rainfall distribution: energetics framework and ocean ekman advection. *npj Climate and Atmospheric Science*, **1**, 20 172, doi:10.1038/s41612-017-0004-6.

Kao, H.-Y., and J.-Y. Yu, 2009: Contrasting eastern-pacific and central-pacific types of enso. *Journal of Climate*, **22 (3)**, 615–632, doi:10.1175/2008JCLI2309.1.

Keenlyside, N. S., and M. Latif, 2007: Understanding equatorial atlantic interannual variability. *Journal of Climate*, **20 (1)**, 131–142, doi:10.1175/JCLI3992.1.

Kerr, R., 2000: A North Atlantic Climate Pacemaker for the Centuries. *Climate Research*, **288 (5473)**, 1984–1985, doi:10.1126/science.288.5473.1984.

Khaliq, M. N., and T. B. M. J. Ouarda, 2007: On the critical values of the standard normal homogeneity test (SNHT). *International Journal of Climatology*, **27 (5)**, 681–687, doi:10.1002/joc.1438.

Kilavi, M., and Coauthors, 2018: Extreme Rainfall and Flooding over Central Kenya Including Nairobi City during the Long-Rains Season 2018: Causes, Predictability, and Potential for Early Warning and Actions. *Atmosphere*, **9 (12)**, 472, doi: 10.3390/atmos9120472.

Kimani, M. W., J. C. Hoedjes, and Z. Su, 2017: An Assessment of Satellite-Derived Rainfall Products Relative to Ground Observations over East Africa. *Remote Sensing*, **9 (5)**, 430, doi:10.3390/rs9050430.

Knutson, T. R., K. M. Weickmann, and J. E. Kutzbach, 1986: Global-scale intraseasonal oscillations of outgoing longwave radiation and 250 mb zonal wind during northern hemisphere summer. *Monthly Weather Review*, **114 (3)**, 605–623, doi:10.1175/1520-0493(1986)114<0605:GSIOOO>2.0.CO;2.

Korecha, D., and A. G. Barnston, 2007: Predictability of June?September Rainfall in Ethiopia. *Monthly Weather Review*, **135**, 628–650, doi:10.1175/MWR3304.1.

Kuete, G., W. Pokam, Mba, and R. Washington, 2020: African Easterly Jet South: control, maintenance mechanisms and link with Southern subtropical waves. *Climate Dynamics*, **54**, 1539–1552, doi:10.1007/s00382-019-05072-w.

Kug, J., M. Ahn, M. Sung, S.-W. Yeh, H.-S. Min, and Y.-H. Kim, 2010: Statistical relationship between two types of El Niño events and climate variation over the Korean Peninsula. *Asia-Pacific Journal of Atmospheric Sciences*, **46**, 467–474, doi:10.1007/s13143-010-0027-y.

Kug, J.-S., F.-F. Jin, and S.-I. An, 2009: Two types of el niño events: Cold tongue el niño and warm pool el niño. *Journal of Climate*, **22 (6)**, 1499–1515, doi:10.1175/2008JCLI2624.1.

Kumar, K. K., B. Rajagopalan, M. Hoerling, G. Bates, and M. Cane, 2006: Unraveling the mystery of indian monsoon failure during el niño. *Science*, **314 (5796)**, 115–119, doi:10.1126/science.1131152.

Laing, A., and J.-L. Evans, 2008: *Introduction to Tropical Meteorology. A comprehensive online & print textbook*. 2nd ed., University Corporation for Atmospheric Research (UCAR), version 4.0, March 2016.

Larkin, N. K., and D. E. Harrison, 2005: On the definition of el niño and associated seasonal average u.s. weather anomalies. *Geophysical Research Letters*, **32 (13)**, L13 705, doi:10.1029/2005GL022738.

Latif, M., D. Dommenget, M. Dima, and A. Grötzner, 1999: The Role of Indian Ocean Sea Surface Temperature in Forcing East African Rainfall Anomalies during December–January 1997/98. *Journal of Climate*, **12**, 3497–3504, doi:10.1175/1520-0442(1999)012<3497:TROIOS>2.0.CO;2.

Lavaysse, C., C. Flamant, S. Janicot, D. J. Parker, J.-P. Lafore, B. Sultan, and J. Pelon, 2009: Seasonal evolution of the West African heat low: a climatological perspective. *Climate Dynamics*, **33**, 313–330, doi:10.1007/s00382-009-0553-4.

Liebmann, B., I. Bladé, G. N. Kiladis, L. M. V. Carvalho, G. B. Senay, D. Allured, S. Leroux, and C. Funk, 2012: Seasonality of African precipitation from 1996 to 2009. *Journal of Climate*, **25 (12)**, 4304–4322, doi:10.1175/JCLI-D-11-00157.1.

Liebmann, B., and J. A. Marengo, 2001: Interannual variability of the rainy season and rainfall in the Brazilian Amazon Basin. *Journal of Climate*, **14 (22)**, 4308–4318, doi:10.1175/1520-0442(2001)014<4308:IVOTRS>2.0.CO;2.

Liebmann, B., and Coauthors, 2014: Understanding recent eastern Horn of Africa rainfall variability and change. *Journal of Climate*, **27 (23)**, 8630–8645, doi:10.1175/JCLI-D-13-00714.1.

Liebmann, B., and Coauthors, 2017: Climatology and interannual variability of boreal spring wet season precipitation in the eastern horn of africa and implications for its recent decline. *Journal of Climate*, **30 (10)**, 3867–3886.

Lopez, H., G. Goni, and S. Dong, 2017: A reconstructed South Atlantic Meridional Overturning Circulation time series since 1870. *Geophysical Research Letters*, **44**, 3309–3318, doi:10.1002/2017GL073227.

Lott, F. C., N. Christidis, and P. A. Stott, 2013: Can the 2011 east african drought be attributed to human-induced climate change? *Geophysical Research Letters*, **40 (6)**, 1177–1181, doi:10.1002/grl.50235.

Lyon, B., 2014a: Seasonal Drought in the Greater Horn of Africa and Its Recent Increase during the March–May Long Rains. *Journal of Climate*, **27**, 7953–7975, doi:10.1175/JCLI-D-13-00459.1.

Lyon, B., A. Barnston, and D. G. DeWitt, 2014b: Tropical pacific forcing of a 1998–1999 climate shift: observational analysis and climate model results for the boreal spring season. *Climate Dynamics*, **43**, 893–909, doi:10.1007/s00382-013-1891-9.

Lyon, B., and D. G. DeWitt, 2012: A recent and abrupt decline in the East African long rains. *Geophysical Research Letters*, **39 (2)**, doi:10.1029/2011GL050337.

Lyon, B., and N. Vigaud, 2017: Unraveling East Africa's Climate Paradox. *Climate Extremes: Patterns and Mechanisms*, Geophysical Monograph Series, Vol. 226, 1st ed., John Wiley and Sons, Inc., 7953–7975.

MacLeod, D., and C. Caminade, 2019: The moderate impact of the 2015 el niño over east africa and its representation in seasonal reforecasts. *Journal of Climate*, **32 (22)**, 7989–8001, doi:10.1175/JCLI-D-19-0201.1.

Macron, C., B. Pohl, and Y. Richard, 2014: How do Tropical Temperate Troughs Form and Develop over Southern Africa? *Journal of Climate*, **27**, 1633–1647, doi:10.1175/JCLI-D-13-00175.1.

Madden, R. A., and P. R. Julian, 1971: Detection of a 40Ă-50 day oscillation in the zonal wind in the tropical pacific. *Journal of the Atmospheric Sciences*, **28 (5)**, 702–708, doi:10.1175/1520-0469(1971)028<0702:DOADOI>2.0.CO;2.

Madden, R. A., and P. R. Julian, 1972: Description of global-scale circulation cells in the tropics with a 40-50 day period. *Journal of the Atmospheric Sciences*, **29 (6)**, 1109–1123, doi:10.1175/1520-0469(1972)029<1109:DOGSCC>2.0.CO;2.

Madden, R. A., and P. R. Julian, 1994: Observations of the 40-50-day tropical oscillation – a review. *Monthly Weather Review*, **122 (5)**, 814–837, doi:10.1175/1520-0493(1994)122<0814:OOTDTO>2.0.CO;2.

Maidment, R. I., R. P. Allan, and E. Black, 2015: Recent observed and simulated changes in precipitation over africa. *Geophysical Research Letters*, **42 (19)**, 8155–8164, doi:10.1002/2015GL065765.

Maidment, R. I., D. I. F. Grimes, R. P. Allan, H. Greatrex, O. Rojas, and O. Leo, 2013: Evaluation of satellite-based and model re-analysis rainfall estimates for Uganda. *Meteorological Applications*, **20 (3)**, 308–317, doi:10.1002/met.1283.

Manatsa, D., C. Mudavanhu, T. D. Mushore, and E. Mavhura, 2016: Linking major shifts in east africa ?short rains? to the southern annular mode. *International Journal of Climatology*, **36 (4)**, 1590–1599, doi:10.1002/joc.4443.

Manhique, A. J., C. J. C. Reason, L. Rydberg, and L. Fauchereau, 2011: How do Tropical Temperate Troughs Form and Develop over Southern Africa? *International Journal of Climatology*, **31**, 1–13, doi:10.1002/joc.2050.

Mapande, A. T., and C. J. C. Reason, 2005: Links between rainfall variability on intraseasonal and interannual scales over western Tanzania and regional circulation and SST patterns. *Meteorology and Atmospheric Physics*, **89**, 215–234, doi:10.1007/s00703-005-0130-2.

Marteau, R., V. Moron, and N. Philippon, 2009: Spatial Coherence of Monsoon Onset over Western and Central Sahel (1950-2000). *Journal of Climate*, **22 (5)**, 1313–1324, doi:10.1175/2008JCLI2383.1.

Matsuno, T., 1966: Quasi-geostrophic motions in the equatorial area. *Journal of the Meteorological Society of Japan. Ser. II*, **44 (1)**, 25–43, doi:10.2151/jmsj1965.44.1_25.

Mei, S. L., T. Li, and W. Chen, 2015: Three-type MJO Initiation processes over the Western Equatorial Indian Ocean. *Advances in Atmospheric Sciences*, **32 (9)**, 1208–1216, doi:10.1007/s00376-015-4201-0.

Munday, C., and R. Washington, 2017: Circulation controls on southern African precipitation in coupled models: The role of the Angola Low. *Journal of Geophysical Research Atmospheres*, **122**, 861–877, doi:10.1002/2016JD025736.

Mutai, C. C., and M. N. Ward, 2000: East African Rainfall and the Tropical Circulation/Convection on Intraseasonal to Interannual Timescales. *Journal of Climate*, **13**, 3915–3939, doi:10.1175/1520-0442(2000)013<3915:EARATT>2.0.CO;2.

Neelin, J. D., I. M. Held, and K. H. Cook, 1987: Evaporation-wind feedback and low-frequency variability in the tropical atmosphere. *Journal of the Atmospheric Sciences*, **44 (16)**, 2341–2348, doi:10.1175/1520-0469(1987)044<2341:EWFALF>2.0.CO;2.

Nguyen, H., C. D. Thorncroft, and C. Zhang, 2011: Guinean coastal rainfall of the West African Monsoon. *Quarterly Journal of the Royal Meteorological Society*, **137 (660)**, 1828–1840, doi:10.1002/qj.867.

Nicholson, S., 1996: A Review of Climate Dynamics and Climate Variability in Eastern Africa. *The limnology, climatology and paleoclimatology of the East African Lakes*, I. A. Johnson, and Odada, Eds., CRC Press, chap. The East African Climate, 25–56.

Nicholson, S., 2016: The turkana low-level jet: mean climatology and association with regional aridity. *International Journal of Climatology*, **36 (6)**, 2598–2614, doi:10.1002/joc.4515.

Nicholson, S. E., 2017: Climate and climatic variability of rainfall over eastern Africa. *Reviews of Geophysics*, **55 (3)**, 590–635, doi:10.1002/2016RG000544.

Nicholson, S. E., 2018: The itcz and the seasonal cycle over equatorial africa. *Bulletin of the American Meteorological Society*, **99 (2)**, 337–348, doi:10.1175/BAMS-D-16-0287.1.

Nicholson, S. E., and J. P. Grist, 2003: The seasonal evolution of the atmospheric circulation over west africa and equatorial africa. *Journal of Climate*, **16 (7)**, 1013–1030, doi:10.1175/1520-0442(2003)016<1013:TSEOTA>2.0.CO;2.

Nicholson, S. E., and J. Kim, 1997: The relationship of the el niño–southern oscillation to african rainfall. *International Journal of Climatology*, **17 (2)**, 117–135, doi:10.1002/(SICI)1097-0088(199702)17:2<117::AID-JOC84>3.0.CO;2-O.

Nikulin, G., and Coauthors, 2012: Precipitation climatology in an ensemble of CORDEX-Africa regional climate simulations. *Journal of Climate*, **25 (18)**, 6057–6078, doi:10.1175/JCLI-D-11-00375.1.

Oettli, P., T. Tozuka, T. Izumo, F. Engelbrecht, and T. Yamagata, 2014: The self-organizing map, a new approach to apprehend the madden-ĂŞjulian oscillation influence on the intraseasonal variability of rainfall in the southern african region. *Climate Dynamics*, **43**, 1557–1573, doi:10.1007/s00382-013-1985-4.

Ogallo, L. J., 1988: Relationships between seasonal rainfall in east africa and the southern oscillation. *Journal of Climatology*, **8 (1)**, 31–43, doi:10.1002/joc.3370080104.

Okoola, R. E., 1999: A diagnostic study of the eastern Africa monsoon circulation during the northern hemisphere spring season. *International Journal of Climatology*, **19**, 143–168, doi:10.1002/(SICI)1097-0088(199902)19:2<143::AID-JOC342>3.0.CO;2-U.

Osman, O. E., and S. L. Hastenrath, 1969: On the synoptic climatology of summer rainfall over central Sudan. *Archiv für Meteorologie, Geophysik und Bioklimatologie Serie B*, **17 (4)**, 297–324, doi:10.1007/BF02243371.

Osman, Y. Z., and A. Y. Shamseldin, 2002: Qualitative rainfall prediction models for central and southern Sudan using El Niño-southern oscillation and Indian Ocean sea surface temperature Indices. *International Journal of Climatology*, **22 (15)**, 1861–1878, doi:10.1002/joc.860.

Overland, J. E., and R. W. Preisendorfer, 1982: A Significance Test applied to a Cyclone Climatology. *Monthly Weather Review*, **110 (1)**, 1–4, doi:10.1175/1520-0493(1982)110<0001:ASTFPC>2.0.CO;2.

Peel, M. C., B. L. Finlayson, and T. A. McMahon, 2006: Updated world map of the Köppen-Geiger climate classification. *Hydrology and Earth System Sciences*, **11**, 1633–1644, doi:10.5194/hess-11-1633-2007.

Peixoto, J. P., and A. H. Oort, 1992: *Physics of Climate*. Springer.

Philander, S. G. H., D. Gu, G. Lambert, T. Li, D. Halpern, N.-C. Lau, and R. C. Pacanowski, 1996: Why the itcz is mostly north of the equator. *Journal of Climate*, **9 (12)**, 2958–2972, doi:10.1175/1520-0442(1996)009<2958:WTIIMN>2.0.CO;2.

Philippon, N., P. Camberlin, V. Moron, and J. Boyard-Micheau, 2015: Anomalously wet and dry rainy seasons in Equatorial East Africa and associated differences in intra-seasonal characteristics. *Climate Dynamics*, **45 (7)**, 2101–2121, doi:10.1007/s00382-014-2460-6.

Phillips, J., and B. McIntyre, 2000: Enso and interannual rainfall variability in uganda: implications for agricultural management. *International Journal of Climatology*, **20 (2)**, 171–182, doi:10.1002/(SICI)1097-0088(200002)20:2<171::AID-JOC471>3.0.CO;2-O.

Poccard, I., S. Janicot, and P. Camberlin, 2000: Comparison of rainfall structures between NCEP/NCAR reanalyses and observed data over tropical Africa. *Climate Dynamics*, **16 (12)**, 897–915, doi:10.1007/s003820000087.

Pohl, B., and P. Camberlin, 2006a: Influence of the Madden-Julian Oscillation on East African rainfall. I: Intraseasonal variability and regional dependency. *Quarterly Journal of the Royal Meteorological Society*, **132 (621)**, 2521–2539, doi:10.1256/qj.05.104.

Pohl, B., and P. Camberlin, 2006b: Influence of the Madden-Julian Oscillation on East African rainfall: II. March–May season extremes and interannual variability. *Quarterly Journal of the Royal Meteorological Society*, **132 (621)**, 2541–2558, doi:10.1256/qj.05.223.

Pohl, B., Y. Richard, and N. Fauchereau, 2007: Influence of the madden-ĂŞjulian oscillation on southern african summer rainfall. *Journal of Climate*, **20 (16)**, 4227–4242, doi:10.1175/JCLI4231.1.

Preethi, B., T. P. Sabin, J. A. Adedoyin, and K. Ashok, 2015: Impacts of the ENSO Modoki and other Tropical Indo- Pacific Climate-Drivers on African Rainfall. *Scientific Reports*, **5**, 16 653, doi:10.1038/srep16653.

Rashki, A., D. Kaskaoutis, A. Mofidi, F. Minvielle, I. Chiapello, M. Legrand, U. Dumka, and P. Francois, 2019: Effects of monsoon, shamal and levar winds on dust accumulation over the arabian sea during summer – the july 2016 case. *Aeolian Research*, **36**, 27 – 44, doi:10.1016/j.aeolia.2018.11.002.

Reason, C. J. C., and D. Jagadheesha, 2005: A model investigation of recent ENSO impacts over southern Africa. *Meteorology and Atmospheric Physics*, **89 (1–4)**, 181–205, doi:10.1007/s00703-005-0128-9.

Riddle, E. E., and K. H. Cook, 2008: Abrupt transitions in rainfall over the Greater Horn of Africa: observations and regional climate simulations. *Journal of Geophysical Research*, **113**, D15 109, doi:10.1029/2007JD009202.

Riddle, E. E., and D. S. Wilks, 2013: Statistical indices of the northward rainfall progression over eastern Africa. *International Journal of Climatology*, **33 (2)**, 356–375, doi:10.1002/joc.3429.

Ropelewski, C. F., and M. S. Halpert, 1987: Global and regional scale precipitation patterns associated with the el niño/southern oscillation. *Monthly Weather Review*, **115 (8)**, 1606–1626, doi:10.1175/1520-0493(1987)115<1606:GARSPP>2.0.CO;2.

Rouault, M., P. Florenchie, N. Fauchereau, and C. J. C. Reason, 2003: South east tropical atlantic warm events and southern african rainfall. *Geophysical Research Letters*, **30 (5)**, doi:10.1029/2002GL014840.

Rubin, S., B. Ziv, and N. Paldor, 2007: Tropical plumes over eastern north africa as a source of rain in the middle east. *Monthly Weather Review*, **135 (12)**, 4135–4148, doi:10.1175/2007MWR1919.1.

Rácz, Z., and R. K. Smith, 1999: The dynamics of heat lows. *Quarterly Journal of the Royal Meteorological Society*, **125 (553)**, 225–252, doi:10.1002/qj.49712555313.

Saha, S., and Coauthors, 2010: The NCEP Climate Forecast System Reanalysis. *Bulletin of the American Meteorological Society*, **91 (8)**, 1015–1058, doi:10.1175/2010BAMS3001.1.

Saji, N. H., B. N. Goswami, P. N. Vinayachandran, and T. Yamagata, 1999: A dipole mode in the tropical Indian Ocean. *Nature*, **401**, 360–363, doi:10.1038/43854.

Salih, A. A., N. A. Elagib, M. Tjernström, and Q. Zhang, 2018: Characterization of the Sahelian-Sudan rainfall based on observations and regional climate models. *Atmospheric Research*, **202**, 205–218, doi:10.1016/j.atmosres.2017.12.001.

Sanogo, S., A. H. Fink, J. A. Omotosho, A. Ba, R. Redl, and V. Ermert, 2015: Spatio-temporal characteristics of the recent rainfall recovery in West Africa. *International Journal of Climatology*, **35 (15)**, doi:10.1002/joc.4309.

Saria, E., E. Calais, D. S. Stamps, D. Delvaux, and C. J. H. Hartnady, 2014: Present-day kinematics of the east african rift. *Journal of Geophysical Research: Solid Earth*, **119 (4)**, 3584–3600, doi:10.1002/2013JB010901.

Schmocker, J., H. P. Liniger, J. N. Ngeru, Y. Brugnara, R. Auchmann, and S. Brönnimann, 2016: Trends in mean and extreme precipitation in the mount kenya region from observations and reanalyses. *International Journal of Climatology*, **36 (3)**, 1500–1514, doi:10.1002/joc.4438.

Schneider, T., T. Bischoff, and G. Haug, 2014: Migrations and dynamics of the intertropical convergence zone. . *Nature*, **513**, 45–53, doi:110.1038/nature13636.

Schoenwiese, C.-D., 2003: *Klimatologie*. Verlag Eugen Ulmer.

Schwendike, J., G. J. Berry, M. J. Reeder, C. Jakob, P. Govekar, and R. Wardle, 2015: Trends in the local hadley and local walker circulations. *Journal of Geophysical Research: Atmospheres*, **120 (15)**, 7599–7618, doi:10.1002/2014JD022652.

Segele, Z. T., and P. J. Lamb, 2005: Characterization and variability of Kiremt rainy season over Ethiopia. *Meteorology and Atmospheric Physics*, **89 (1-4)**, 153–180, doi:10.1007/s00703-005-0127-x.

Segele, Z. T., P. J. Lamb, and L. M. Leslie, 2009: Large-scale atmospheric circulation and global sea surface temperature associations with horn of africa june-

september rainfall. *International Journal of Climatology*, **29 (8)**, 1075–1100, doi:10.1002/joc.1751.

Seleshi, Y., and U. Zanke, 2004: Recent changes in rainfall and rainy days in Ethiopia. *International Journal of Climatology*, **24 (8)**, 973–983, doi:10.1002/joc.1052.

Shanko, D., and P. Camberlin, 1998: The effects of the southwest indian ocean tropical cyclones on ethiopian drought. *International Journal of Climatology*, **18 (12)**, 1373–1388, doi:10.1002/(SICI)1097-0088(1998100)18:12<1373::AID-JOC313>3.0.CO;2-K.

Shongwe, M. E., G. J. van Oldenborgh, B. J. J. M. van den Hurk, B. de Boer, C. A. S. Coelho, and M. K. van Aalst, 2009: Projected changes in mean and extreme precipitation in africa under global warming. part i: Southern africa. *Journal of Climate*, **22 (13)**, 3819–3837, doi:10.1175/2009JCLI2317.1.

Spengler, T., and R. K. Smith, 2008: The dynamics of heat lows over flat terrain. *Quarterly Journal of the Royal Meteorological Society*, **134 (637)**, 2157–2172, doi:10.1002/qj.342.

Steedman, A., Ed., 1990: *Locust handbook*. 3rd ed., Chatham: Natural Resources Institute.

Stern, R. D., M. D. Dennett, and I. C. Dale, 1982: Analysing Daily Rainfall Measurements to Give Agronomically Useful Results. I. Direct Methods. *Experimental Agriculture*, **18 (03)**, 223, doi:10.1017/S001447970001379X.

Straub, K. H., 2013: Mjo initiation in the real-time multivariate mjo index. *Journal of Climate*, **26 (4)**, 1130–1151, doi:10.1175/JCLI-D-12-00074.1.

Stuecker, M. F., A. Timmermann, F.-F. Jin, Y. Chikamoto, W. Zhang, A. T. Wittenberg, E. Widiasih, and S. Zhao, 2017: Revisiting enso/indian ocean dipole phase relationships. *Geophysical Research Letters*, **44 (5)**, 2481–.2492, doi:10.1002/2016GL072308.

Sylla, M. B., F. Giorgi, E. Coppola, and L. Mariotti, 2013: Uncertainties in daily rainfall over Africa: Assessment of gridded observation products and evaluation of a regional climate model simulation. *International Journal of Climatology*, **33 (7)**, 1805–1817, doi:10.1002/joc.3551.

Taylor, C. M., A. H. Fink, C. Klein, D. J. Parker, F. Guichard, P. P. Harris, and K. R. Knapp, 2018: Earlier seasonal onset of intense mesoscale convective systems in the congo basin since 1999. *Geophysical Research Letters*, **45 (24)**, 13,458–13,467, doi:10.1029/2018GL080516.

Thiemig, V., R. Rojas, M. Zambrano-Bigiarini, V. Levizzani, and A. De Roo, 2012: Validation of Satellite-Based Precipitation Products over Sparsely Gauged African River Basins. *Journal of Hydrometeorology*, **13 (6)**, 1760–1783, doi:10.1175/JHM-D-12-032.1.

Thorncroft, C. D., and M. Blackburn, 1999: Maintenance of the african easterly jet. *Quarterly Journal of the Royal Meteorological Society*, **125 (555)**, 763–786, doi:10.1002/qj.49712555502.

Tierney, J. E., J. E. Smerdon, K. J. Anchukaitis, and R. Seager, 2013: Multidecadal variability in east african hydroclimate controlled by the indian ocean. *Nature*, **493**, 389–392, doi:10.1038/nature11785.

Todd, M., and R. Washington, 1999: Circulation anomalies associated with tropical-temperate troughs in southern Africa and the south west Indian Ocean. *Climate Dynamics*, **15 (15)**, 937–951, doi:10.1007/s003820050323.

Toté, C., D. Patricio, H. Boogaard, R. van der Wijngaart, E. Tarnavsky, and C. Funk, 2015: Evaluation of Satellite Rainfall Estimates for Drought and Flood Monitoring in Mozambique. *Remote Sensing*, **7 (2)**, 1758–1776, doi:10.3390/rs70201758.

Tsidu, G. M., 2012: High-resolution monthly rainfall database for ethiopia: Homogenization, reconstruction, and gridding. *Journal of Climate*, **25 (24)**, 8422–8443, doi:10.1175/JCLI-D-12-00027.1.

Ummenhofer, C. C., M. Kulüke, and J. E. Tierney, 2018: Extremes in East African hydroclimate and links to Indo-Pacific variability on interannual to decadal timescales. *Climate Dynamics*, **50**, 2971–2991, doi:10.1007/s00382-017-3786-7.

United Nations, 2019: Department of Economic and Social Affairs, Population Division (2019). Data retrieved from World Population Prospects 2019, URL https://population.un.org/wpp/DataQuery/.

UN Office for the Coordination of Humanitarian Affairs (UNOCHA), 2017: Horn of africa: Humanitarian impacts of drought – issue 11 (3 november 2017). URL https://reliefweb.int/report/somalia/horn-africa-humanitarian-impacts-drought-issue-11-3-november-2017.

UN Office for the Coordination of Humanitarian Affairs (UNOCHA), 2020: Greater horn of africa region: Humanitarian snapshot (february 2020). URL https://reliefweb.int/report/ethiopia/greater-horn-africa-region-humanitarian-snapshot-february-2020.

Vellinga, M., A. Arribas, and R. Graham, 2013: Seasonal forecasts for regional onset of the West African monsoon. *Climate Dynamics*, **40 (11)**, 3047–3070, doi:10.1007/s00382-012-1520-z.

Vellinga, M., and S. F. Milton, 2018: Drivers of interannual variability of the East African "Long Rains". *Quarterly Journal of Royal Meteorological Society*, **144**, 861–876, doi:10.1002/qj.3263.

Vigaud, N., B. Lyon, and A. Giannini, 2017: Sub-seasonal teleconnections between convection over the indian ocean, the east african long rains and tropical pacific surface temperatures. *International Journal of Climatology*, **37 (3)**, 1167–1180, doi:10.1002/joc.4765.

Vigaud, N., Y. Richard, M. Rouault, and N. Fauchereau, 2007: Water vapour transport from the tropical Atlantic and summer rainfall in tropical southern Africa. *Climate Dynamics*, **28**, 113–123, doi:10.1007/s00382-008-0377-7.

Vigaud, N., Y. Richard, M. Rouault, and N. Fauchereau, 2009: Moisture transport between the South Atlantic Ocean and southern Africa: relationships with

summer rainfall and associated dynamics. *Climate Dynamics*, **32**, 113–123, doi:10.1007/s00382-008-0377-7.

Viste, E., and A. Sorteberg, 2013: Moisture transport into the Ethiopian highlands. *International Journal of Climatology*, **33**, 249–263, doi:10.1002/joc.3409.

Vizy, E. K., and K. H. Cook, 2017: Seasonality of the observed amplified sahara warming trend and implications for sahel rainfall. *Journal of Climate*, **30 (9)**, 3073–3094, doi:10.1175/JCLI-D-16-0687.1.

Vogel, P., P. Knippertz, A. H. Fink, A. Schlueter, and T. Gneiting, 2018: Skill of Global Raw and Postprocessed Ensemble Predictions of Rainfall over Northern Tropical Africa. *Weather and Forecasting*, **33 (2)**, 369–388, doi:10.1175/WAF-D-17-0127.1.

Wainwright, C. M., J. H. Marsham, R. J. Keane, D. P. Rowell, D. L. Finnay, E. Black, and R. P. Allan, 2019: 'Eastern African Paradox' rainfall decline due to shorter not less intense Long Rains. *npj Climate and Atmospheric Science*, **2**, 34, doi:10.1038/s41612-019-0091-7.

Wallace, J. M., and P. V. Hobbs, 2006: *Atmospheric science: an introductory survey*. Academic Press.

Wang, B., and LinHo, 2002: Rainy season of the Asian-Pacific summer monsoon. *Journal of Climate*, **15 (4)**, 386–398, doi:10.1175/1520-0442(2002)015<0386:RSOTAP>2.0.CO;2.

Washington, R., R. James, H. Pearce, W. M. Pokam, and W. Moufouma-Okia, 2013: Congo basin rainfall climatology: can we believe the climate models? *Philosophical Transactions of the Royal Society B: Biological Sciences*, **368 (1625)**, 20120 296, doi:10.1098/rstb.2012.0296.

Weickmann, K. M., G. R. Lussky, and J. E. Kutzbach, 1985: Intraseasonal (30-ĂŞ60 day) fluctuations of outgoing longwave radiation and 250 mb streamfunction during northern winter. *Monthly Weather Review*, **113 (6)**, 941–961, doi:10.1175/1520-0493(1985)113<0941:IDFOOL>2.0.CO;2.

Weng, H., K. Ashok, S. K. Behera, S. A. Rao, and T. Yamagata, 2007: Impacts of recent El Niño Modoki on dry/wet conditions in the Pacific rim during boreal summer. *Climate Dynamics*, **29**, 113–129, doi:10.1007/s00382-007-0234-0.

Wheeler, M. C., and H. H. Hendon, 2004: An all-season real-time multivariate mjo index: Development of an index for monitoring and prediction. *Monthly Weather Review*, **132 (8)**, 1917–1932, doi:10.1175/1520-0493(2004)132<1917:AARMMI>2.0.CO;2.

Wilks, D., Ed., 2011: *Statistical Methods in the Atmospheric Sciences*, Vol. 100, chap. Chapter 15 - Cluster Analysis, 603–616. Academic Press.

Williams, A. P., and C. Funk, 2011: A westward extension of the warm pool leads to a westward extension of the Walker circulation, drying eastern Africa. *Climate Dynamics*, **37**, 2417–2435, doi:10.1007/s00382-010-0984-y.

Williams, A. P., and Coauthors, 2012: Recent summer precipitation trends in the Greater Horn of Africa and the emerging role of Indian Ocean sea surface temperature. *Climate Dynamics*, **39**, 2307–2328, doi:10.1007/s00382-011-1222-y.

World Bank, 2020: The world bank group and the locust crisis. URL https://www.worldbank.org/en/topic/the-world-bank-group-and-the-desert-locust-outbreak#1.

World Meteorological Organization (WMO), 2016: *The Global Climate in 2011–2015*. URL https://reliefweb.int/report/world/global-climate-2011-2015.

World Meteorological Organization (WMO) and Food and Agriculture Organization of the United Nations (FAO), 2016: *Weather and Desert Locusts*. URL https://library.wmo.int/doc_num.php?explnum_id=3213.

Yamada, T. J., S. Kanae, T. Oki, and R. D. Koster, 2013: Seasonal variation of land-atmosphere coupling strength over the West African monsoon region in an atmospheric general circulation model. *Hydrological Sciences Journal*, **58 (6)**, 1276–1286, doi:10.1080/02626667.2013.814914.

Yamagata, T., and Y. Hayashi, 1984: A simple diagnostic model for the 30-50 day oscillation in the tropics. *Journal of the Meteorological Society of Japan. Ser. II*, **62**, 709–717, doi:10.2151/jmsj1965.62.5_709.

Yang, W., R. Seager, M. A. Cane, and B. Lyon, 2014: The east african long rains in observations and models. *Journal of Climate*, **27 (19)**, 7185–7202, doi:10.1175/JCLI-D-13-00447.1.

Yang, W., R. Seager, M. A. Cane, and B. Lyon, 2015: The Annual Cycle of East African Precipitation. *Journal of Climate*, **28 (6)**, 2385–2404, doi:10.1175/JCLI-D-14-00484.1.

Yasunari, T., 1979: Cloudiness fluctuations associated with the northern hemisphere summer monsoon. *Journal of the Meteorological Society of Japan. Ser. II*, **57 (3)**, 227–242, doi:10.2151/jmsj1965.57.3_227.

Yeh, S.-W., J.-S. Kug, B. Dewitte, M.-H. Kwon, B. P. Kirtman, and F.-F. Jin, 2009: El Niño in a changing climate. *Nature*, **461**, 511–514, doi:10.1038/nature08316.

Yu, J.-Y., and S. T. Kim, 2010a: Identification of central-pacific and eastern-pacific types of enso in cmip3 models. *Geophysical Research Letters*, **37 (15)**, L15 705, doi:10.1029/2010GL044082.

Yu, J.-Y., and S. T. Kim, 2010b: Three evolution patterns of central-pacific el niño. *Geophysical Research Letters*, **37 (8)**, L08 706, doi:10.1029/2010GL042810.

Yun, K.-S., K.-J. Ha, B. Wang, and R. Ding, 2010: Decadal cooling in the Indian summer monsoon after 1997/1998 El Niño and its impact on the East Asian summer monsoon. *Geophysical Research Letters*, **37**, L01 805, doi:10.1029/2009GL041539.

Zaitchik, B. F., 2017: Madden-julian oscillation impacts on tropical african precipitation. *Atmospheric Research*, **184**, 88–102, doi:10.1016/j.atmosres.2016.10.002.

Zebiak, S. E., 1993: Air-ĂŞsea interaction in the equatorial atlantic region. *Journal of Climate*, **6 (8)**, 1567–1586, doi:10.1175/1520-0442(1993)006<1567:AIITEA>2.0.CO;2.

Zhang, C., 2005: Madden-Julian Oscillation. *Reviews of Geophysics*, **43 (2)**, doi:10.1029/2004RG000158.

Zhang, C., 2013: Madden-Julian Oscillation: Bridging Weather and Climate. *Bulletin of the American Meteorological Society*, **94 (12)**, 1849–1870, doi:10.1175/BAMS-D-12-00026.1.

Zhang, C., and M. Dong, 2004: Seasonality in the Madden-Julian Oscillation. *Journal of Climate*, **17 (16)**, 3169–3180, doi:10.1175/1520-0442(2004)017<3169:SITMO>2.0.CO;2.

Zhang, X., L. Alexander, G. C. Hegerl, P. Jones, A. K. Tank, T. C. Peterson, B. Trewin, and F. W. Zwiers, 2011: Indices for monitoring changes in extremes based on daily temperature and precipitation data. *WIREs Climate Change*, **2 (6)**, 851–870, doi:10.1002/wcc.147.

Zhang, Z., B. Ren, and J. Zheng, 2019: A unified complex index to characterize two types of enso simultaneously. *Scientific Reports*, **9**, 8373, doi:10.1038/s41598-019-44617-1.

Zhao, C., T. Li, and T. Zhou, 2013: Precursor signals and processes associated with mjo initiation over the tropical indian ocean. *Journal of Climate*, **26 (1)**, 291–307, doi:10.1175/JCLI-D-12-00113.1.

Zhou, L., and Coauthors, 2014: Widespread decline of Congo rainforest greenness in the past decade. *Nature*, **509 (7498)**, 86–90, doi:10.1038/nature13265.

Zorita, E., and F. Tilya, 2002: Rainfall variability in Northern Tanzania in the March-May season (long rains) and its links to large-scale climate forcing. *Climate Research*, **20 (1)**, 31–40, doi:10.3354/cr020031.

Glossary

AHC agglomerative-hierarchical clustering. 77, 78

AL Angola Low. 75, 76, 96, 97

CHIRPS Climate Hazards InfraRed Precipitation with Stations. 17, 40, 43, 44, 47, 55, 57, 58, 62, 67, 69, 71, 72, 74, 105, 106, 108–112, 114

DR Democratic Republic. 42, 55, 57, 66, 69, 73, 74, 89

ENSO El Niño Southern Oscillation. 26–30, 36–41, 95, 97, 138

FEWS NET Famine Early Warning Systems Network. 10

FMAM February-March-April-May. 13

GHA Greater Horn of Africa. 10–22, 24, 26, 29, 30, 34–37, 39, 40, 42, 45–47, 49, 56, 69, 72, 74–79, 82, 84, 89, 90, 95, 98–100, 103–106, 138

IOD Indian Ocean Dipole, also known as Indian Ocean Zonal Mode. 24, 29, 30, 38, 45, 104, 138

ISD Integrated Surface Database. 113

ITCZ Intertropical Convergence Zone. 11–13, 16, 18, 20, 22–24

JD Julian Day. 78

JJAS June-July-August-September. 13, 56, 57

KASS-D Karlsruhe African Surface Station Database. 43, 47, 48, 141

MAM March-April-May. 13, 22, 35, 45, 57, 61, 66, 72, 73, 82, 104, 105

MJO Madden-Julian Oscillation. 24, 30–33, 36, 38, 77, 98, 103–105, 138

NAO North-Atlantic Oscillation. 34, 36

OND October-November-December. 13, 16, 45, 57, 61, 62, 66, 70, 72, 73, 82

RCI Rainfall Cluster Index. 9, 77–80, 95, 101, 102, 139

SLI Seasonal Location Index. 9, 77–80, 88, 89, 91, 95, 96, 101, 102, 139

SST sea surface temperature. 12, 13, 22, 24, 26, 27, 29, 30, 35–40, 44, 74, 76, 85, 88, 90, 91, 95–98, 101–103, 105, 139

TRB Tropical Rain Band, referred as the zone of maximum rainfall. 12, 23, 24, 35–40, 45, 53, 55, 57, 73, 75–79, 82, 84, 88, 89, 91, 95–104, 115, 139, 140

TTT tropical-temperate trough. 34, 35, 40, 41, 75, 85, 97, 102

List of Figures

List of Tables

Acknowledgements

I would like to thank my supervisors, Prof. Joaquim Pinto and Prof. Andreas Fink for the possibility to work on this PHD-Thesis and the insight in this complex but really thrilling topic. Also, I would like to thank for the continuous support despite of a lot of obstacles and challenges on this long way to the finish. In particular, I would to thank Prof. Andreas Fink for suggestions, knowledge, constructive criticism, and useful discussions. I also thank Prof. Joaquim Pinto and Prof. Peter Knippertz for offering me the opportunity to work in their working groups, providing infrastructure and research facilities.

I would also like to thank Nadir Elagib for collaboration on the publication on the rainy season onset over the Greater Horn of Africa and for sharing his experience on rainfall variability over Sudan. Also, I would like to thank Chris Funk for providing valuable advice concerning the atmospheric circulation and rainfall variability over East Africa and for co-authoring the publication on the variability of the Tropical Rain Band.
I acknowledge support by the "GlobE – Wetlands for East Africa" project funded by the German Federal Ministry of Education and Research (BMBF) under Grant 031A250F.